Structure and Durability of UK Simulated High Level Nuclear Waste Glasses

Nathan J. Cassingham

A Thesis submitted to the Department of Materials Science and Engineering at the University of Sheffield in partial fulfilment of the requirement for the Degree of Doctor of Philosophy.

18th June 2013

Acknowledgements

I would like to first and foremost thank my family for their continual support during my PhD. Without them and their encouragement to continue with my education I wouldn't have been able to accomplish this goal. I made some close friends during my stint at Sheffield and I would like to thank them for putting up with my insistent pestering when I had little motivation for work and making them go to the pub to relax.

Thanks to my main supervisor; Dr. Neil Hyatt, who made it possible for me to come to Sheffield to pursue my PhD in glass durability with the international funding from EPSRC and DIAMOND. To my second supervisor, Dr. Paul Bingham, who gave constant feedback on ideas that I threw at him. To the technicians at Sheffield such as Mouldy, Mr. I. P. Alots, Mr. D. Weld-a-lock, Mr. P. Statton, and Mrs. B. Lane, who were able to put up with me during the not so kid friendly conversations at coffee breaks. To the Post Doctoral Research Associates; Dr. Stennett, Dr. Utton and Dr. Corkhill who all helped with experiments and revisions to chapters and papers.

For the ability to go to PNNL and perform SPFT and VHT, I am grateful to Dr. J. Vienna and Dr. J. Ryan who helped make it possible and for Dr. D. Wellman, Dr. E. Cordova, C. Boviard and W. Lepry for teaching me the experimental set-up of the experiments.

Abstract

The understanding of dissolution of the British nuclear waste glass, as compared to other nuclear waste glasses, is limited. The few studies that have been performed were generally done in static leach tests with the exception of the single pass flow through test performed by Abratis during his PhD, producing a number of papers (Abraitis, P.K., Univ. Manchester, 1999; Abraitis, P.K. *et. al.*, Applied Geochemistry 15 (2000) 1399; Abraitis, P.K. *et. al.*, Mat. Res. Soc. Sym. Pro. 556 (1999) 401). In order to gain further insight to the British nuclear waste glasses X-ray absorption spectroscopy was used along with dissolution studies of British simulated nuclear waste glasses to determine the role of Zn and to ascertain the mechanisms of corrosion. Both baseline glasses along with a Blend simulated nuclear waste glass were studied to give better comparisons with previous results by other authors. The Blend waste glass is composed of a mixture of Magnox reactor waste and thorium oxide reprocessing (ThORP) waste at a wt% of 25wt% Magnox waste and 75 wt% ThORP.

Zn K edge X-ray absorption spectroscopy was applied to determine the Zn coordination environment in model inactive UK high level waste (HLW) glasses. Quantitative analysis of the X-ray absorption fine structure (EXAFS) data provided conclusive evidence for the presence of ZnO_4 species participating in network formation, linking, on average, to 2 ± 1 SiO_4 units *via* bridging oxygen atoms. Excellent quantitative agreement was observed between the Zn-O contact distance and coordination number determined from EXAFS and previous Molecular Dynamics simulations of glasses with the same nominal composition. Analysis also provided evidence in support of the network forming role of Zn as predicted from Molecular Dynamics simulation, but it was not possible to confirm the predicted clustering of Zn species at high Zn concentration in simple soda lime silica glasses.

The single pass flow through (SPFT) work in this study has shown that the steady state dissolution of a base glass with 25 wt% waste loading (MW+25wt%) and a base glass with 30 wt% waste loading (MW+30wt%) of Blend simulated nuclear waste glasses is similar to that of previous studies. The SPFT flow per surface area (Q/S) results are consistent with previous studies. The dissolution rate dependency on temperature and pH of was also consistent with similar glasses. The NR_i with respect to B, Si, Na and Al, of the glasses in this study increased with an increase in solution pH. The average activation energy with respect to Si was consistent for a surface controlled reaction with these glasses as was shown in previous studies on MW+Magnox, a similar glass.

One of the current designs for a geological repository of HLW is a co-located repository with intermediate level waste (ILW). At long times, there is the possibility of hyper alkaline

solution from the ILW repository interacting with the vitrified HLW glass wasteforms. Dissolution studies were performed to understand the mechanisms by which the UK HLW glasses will corrode under hyper alkaline solutions. The addition of an alkali buffer to high purity H_2O resulted in a decrease of the dissolution rate for the MW Blend glasses during the product consistency type tests. The concentration of Si in solution for all of the samples suggests that Ca and Si are co-precipitating as was evident from the decrease in Ca concentrations at short times. It is suggested that the presence of Ca in solution forms a passive reactive interface (PRI) which decreases the rate of formation of a hydrated surface layer decreasing the overall dissolution rate.

The results from the geochemical modelling of the product consistency type tests showed that Ca and Si are co-precipitating at short times decreasing the normalised mass loss. This is evident from the Ca and Si phases which are most probable to precipitate out of solution as suggested by the geochemical modelling results from PhREEQC

In order to understand the mechanisms of alteration layer formation of the UK HLW glasses, vapour hydration tests (VHT) were performed. Results from the time dependant VHT experiments have shown changes in the mechanisms of alteration layer formation with the addition of the simulated Blend waste to the base glasses. It was also shown that iron may be a suppressor to zinc dissolution. Both a Ca and Zn doped Blend waste glass and a base glass doped with Fe Zn and Zr did not show significant layers of zinc in the alteration layer as shown in the Ca and Zn doped base glass in both the reproducibility or time-dependant VHT experiments.

Giesler *et al.* have similar results to the VHT results in this study, which correlate to an interface-coupled dissolution-reprecipitation mechanism when simulated Blend waste is added to the base glasses (Giesler, T. *et. al.*, J. Non-Cryst. Solids 356 (2010) 1458). However, further work needs to be performed in order to prove this second mechanism of waste glasses.

Table of Contents

1.0 Introduction

In 1956, the first commercial nuclear reactor connected to a grid for generation of electricity was commissioned at Calder Hall in Sellafield, England. Up until approximately three decades ago, much of the research in the nuclear industry has concentrated on power generation; however, there has been a large increase internationally on research for the safe immobilisation and disposal of radioactive nuclear waste.

There is an international consensus to dispose of radioactive nuclear waste in geological repositories. [1; 2; 3] Several options have been studied for immobilisation of nuclear waste, and in particular, heat generating highly radioactive wastes. [1; 3; 4] Cementation of the intermediate level wastes and vitrification of the high level radioactive wastes that generate heat have proven to be the leading options internationally. [4]

Currently in the UK, the Radioactive Waste Management Directorate (RWMD) suggests vitrifying the high level nuclear waste (HLW) for immobilisation followed by disposal in a geological storage facility. [4; 3] The current concepts for a geological facility contain engineered multi barrier systems, which include but are not limited to, the waste form, the waste container, a buffer or backfill, a mass backfill and sealing systems. [5]

Vitrification of HLW for immobilisation and interim storage is performed using various methods such as the Atelier de Vitrification de La Hague (AVH), the Atelier de Vitrification de Marcoule (AVM) in France, and the joule heated melter in the USA. [6] Each operation uses evaporation, decomposition, and melting of the HLW followed by casting of the melt in stainless steel containers. The UK uses a similar approach as the AVH process where the liquid HLW is calcined, melted with a borosilicate glass frit and then cast into a stainless steel canister.

Recently, vitrification of HLW has increased the need to gain an understanding of glass dissolution due to the effects of the biosphere caused by corrosion of the vitrified HLW package when placed in a geological disposal facility. Early experiments were performed on glasses in a closed or static system; however, more recent work has been performed on open systems in order to gain an understanding of the mechanisms of glass dissolution in various solutions such as different temperatures and pH levels. [7; 8]

Although the methods of vitrification of HLW are similar, the compositions of the liquid HLW streams differ significantly between countries. The base glass frit used to vitrify the HLW streams is based on a borosilicate glass; however, the French composition utilises an addition of CaO and ZnO. [9] Recent work by Short *et al.* has shown an increase in durability

and ease of processing of the UK HLW glasses with a small addition of ZnO to the composition of the borosilicate base glass. [10] Durability experiments performed on simulated waste glasses in a static leach tests gave evidence of a glass with better durability; however, the mechanisms in which ZnO increase the durability of glass are not yet fully understood.

Several durability studies on the UK HLW glasses have been performed in order to understand the final dissolution rate. However, many of these studies have been performed using static leach tests which can be affected by saturation of the solution by ion exchanged elements from the bulk glass.

The alteration product formation on the surface of glasses during corrosion is also of interest due to little agreement in the kinetics of formation of the alteration layers. Studies have shown the formation of secondary phases on the surface of the glass serve as a protective barrier and decrease the overall dissolution rate of the glass. [11] Controversial studies suggest gel-layer formation decreases the final dissolution rate of glass through transfer of insoluble components from the glass surface. [12; 13]

Research conducted in this project was performed to assess: the local structure of glasses considered for vitrifying UK HLW streams, the alteration layers formed during dissolution of the glass network with a main goal of determining the role of the gel layer and alteration products formed during dissolution, and determination of the intrinsic dissolution rate of UK HLW glass compositions being considered for vitrification of UK HLW nuclear waste.

X-ray absorption spectroscopy was used to examine the key mechanism of increased durability and processing ability of simulated UK HLW glasses with small additions of ZnO. The effects of changes in temperature and pH on the final dissolution rate of UK simulated HLW glasses were studied using the single pass flow through test (SPFT) and semi-static durability tests to understand how these glasses behave in different geological environments. Studies were also performed on the alteration layer formation during glass dissolution to understand the mechanisms of the formation of secondary products on these glasses.

In Chapter 4, X-ray absorption studies were performed in order to understand if Zn performs as a network intermediate or network former in UK HLW glasses. Further structural modelling of these glasses through the use of X-ray absorption fine structure studies were carried out to determine the role of Zn in the processing ability of the UK HLW glasses. Chapter 5 utilized SPFT to understand the temperature and pH dependency on the dissolution rate of the UK HLW glasses to help predict the dissolution rate of the UK HLW glasses in different repository environments. In order to determine feasibility of a co-located ILW/HLW geological repository, product consistency type tests were performed under hyper

alkaline solutions on simulated UK HLW glasses in Chapter 6. The final results chapter, Chapter 7, gives the results of vapour hydration tests performed on simulated UK HLW glasses to study the mechanisms of alteration layer formation.

The combination of the structural studies about Zn in the UK HLW glasses with the dissolution experiments performed in these works aims to give a broad understanding, through careful experimentation, of the fundamental science of UK HLW glasses in different geological environments.

2.0 Literature Review

Glass dissolution has been studied for many years and its effects are of particular interest due to the potential of contamination of the biosphere from radioactive waste currently in interim storage awaiting final geological disposal. [14; 15; 16; 17; 18; 19; 20; 21; 22; 23] Dissolution behaviour of nuclear waste glasses has been a key focus of international research in radioactive waste management. More recent work has tried to address the effects of a geological repository on the biosphere and to define a source term for the release of radionuclides from glass under assumed conditions of a geological disposal site.

There is general agreement on the basic mechanisms of glass dissolution, which involve: hydration of the glass surface, interdiffusion of the alkali cations and H_3O^+, network hydrolysis forming a gel-layer, network dissolution and finally precipitation of alteration products from solution. [22; 23] However, retention of key fission products and actinides in the gel-layer and alteration products during the dissolution process are yet to be identified.

Understanding of the structure, properties and leaching behaviour of UK High Level Waste (HLW) glasses is presently limited. Initial studies of the dissolution rate, pH dependence, and activation energies for dissolution of the UK HLW glasses have been studied; however, the composition and role of the gel-layer and alteration products is still to be fully understood. [15; 21; 24]

The Radioactive Waste Management Directorate (RWMD) has suggested two general options for disposal of HLW. [20] The first is a concept for HLW and spent fuel based on the Swedish KBS-3V repository concept and the second, a co-located geological disposal facility of both ILW and HLW. [25] Currently, the general consensus is to vitrify HLW and place the product in interim storage awaiting final disposal in a deep geological disposal site. A major focus of the RWMD is currently on establishing criteria for a final geological site. Radionuclide migration will be of great interest during characterization of the final geological site in order to understand the site-specific processes.

The engineered barrier system (EBS) can be defined as the man-made engineered materials placed in a repository, which include the waste form, waste canister, buffer materials, backfill, and the final seal of the repository. [5] In the UK, the EBS is considered as a short-term physical containment of most fission products in the waste form. It should also limit the level of dissolved radionuclides and the release from the near-field through the use of a buffering material and have the ability for gas release without over pressurization. [5] The waste form (currently thought to be a vitrified product) is the last barrier before migration of

radionuclide migration occurs. Because of this, the durability of the vitrified wasteform needs to be well understood.

Glass durability has been studied for many decades with a few studies dating back to the 1600's. [26] More recent studies have provided a better understanding of reactions of a glass surface in a solution. [15; 22; 23; 27; 28; 29] Other studies, such as the Compendium of Glass Corrosion, considered glass dissolution models in order to compare final dissolution rates for the overall performance assessment of sites suggested for final geological disposal of a vitrified product. [30; 14]

2.1 The Nuclear Fuel Cycle

The nuclear fuel cycle covers mining and processing of uranium ore through discharge of the fuel used for power generation in the civil nuclear industry. Initially, the fuel cycle comprises of: mining and milling the ore. It is then converted (purifying the ore) and enriched (if necessary). Fabrication of the fuel is performed after enrichment, and finally utilization of the fuel in reactors. [31] Once the fuel reaches the end of its use in the reactor, it can either be recycled (closed fuel cycle), or disposed of through the use of immobilisation (open fuel cycle). Figure 2.1 illustrates a general fuel cycle for both the open and closed loops.

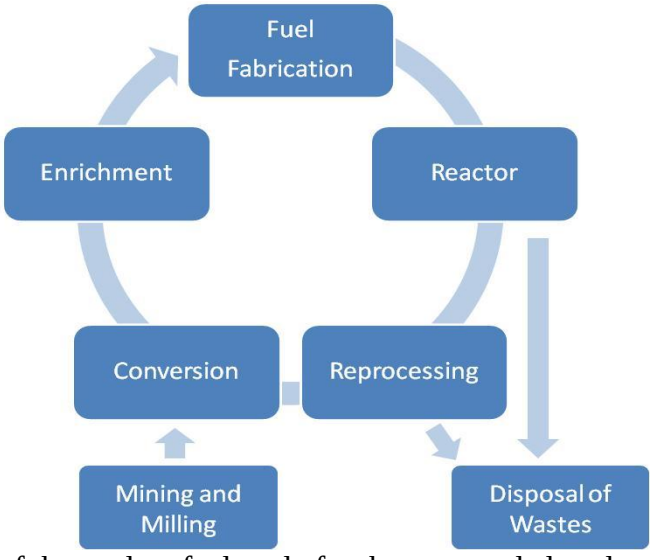

Figure 2.1 Illustration of the nuclear fuel cycle for the open and closed cycles.

The UK currently operates, what is effectively, a closed fuel cycle where spent nuclear fuel is reprocessed and the recovered U and Pu stored to be recycled as MOX fuel; although this has not yet been used in UK reactors. This process limits the amount of waste generated from spent nuclear fuel; however, it is susceptible to proliferation of the fissile material. An open fuel cycle, where spent nuclear fuel is disposed of and not reprocessed, occurs in the USA. The benefit of an open fuel cycle is to reduce the risk of nuclear proliferation.

2.1.1 Generation of Waste in the Nuclear Industry

Nuclear waste is generated from a number of sources. These sources are generally, mining of the natural ore, processing of the ore for fuel rod fabrication, waste from a nuclear reactor, and waste from reprocessing of the spent nuclear fuel. Uranium materials, such as pitchblende, were reported as early as the mid 1500's; however, it was not until the 1960's when uranium ore became a highly sought after material for the manufacture of energy and weapons. [32; 33] A variety of methods such as; open cast or open pit, underground mines, *in situ* leaching (ISL), heap leaching and also recovery from sea water have been used for the recovery of uranium ore. [32; 34; 35; 36; 37; 38] All the methods mentioned create large amounts of waste which have an impact on the environment.

Ore retrieved from the mines is sent to a mill where it is turned into 'yellowcake' (U_3O_8). This is performed by crushing the ore and leaching it in order to extract uranium and other deposits. Separation of the uranium and constituents such as molybdenum, vanadium, selenium, iron, and lead occurs at the mill. After separation, the 'yellow cake' is transported to the processing plants for enrichment. Large amounts of waste are generated from the mine and mill which are known as tailings.

Early methods for disposal of tailings were to place it in large ponds or piles which were subsequently abandoned. [34] Potential hazards from the ponds or piles containing the tailings consist of radon-exhalation, gamma-radiation, seepage of hazardous materials into the aquifer, and a failure of the dam containing the tailings. [34] In recent years, reclamation of the tailings deposits have started; however, each site requires an in depth investigation in order to assess the site for safe disposal of the tailings previously created.

In order to enrich 'yellow cake,' refining, conversion and enrichment are first performed before fabrication of the fuel. Refining the uranium ore from 'yellow cake' to UO_3 or UO_2 is completed by one of three processes; thermal denitration (TDN), ammonium diuranate (ADU), or ammonium uranyl carbonate (AUC). [39] Converting the 'yellow cake' to UO_2 or

UO_3 by one of these methods for 1000 t of uranium produces over 600 t of solid waste and up to 10,000 m^3 of liquid effluent. [39]

After refinement, conversion from UO_3 or UO_2 to uranium hexafluoride (UF_6) is performed. Because UF_6 is thermally stable and has a high volatility, it is the only compound generally suitable for enrichment. [39] This process (if necessary) reduces the UO_3 to UO_2 through the use of hydrogen or cracked ammonia followed by hydrofluorination where UO_2 is converted to UF_4 by either an aqueous hydrofluoric acid or with gaseous HF. [39] Fluorination is performed in order to convert UF_4 to UF_6 by exposing UF_4 to fluorine. Typical waste for production of 1000 t of uranium during the conversion process is approximately 90 t consisting of both solids and sludges. [39]

After conversion of UO_3 and UO_2 to UF_6, enrichment of ^{235}U from its natural abundance to 3-5 At% in UF_6 can be performed. The majority of current methods performed in industry involve gaseous diffusion or centrifuges; however, other technologies do exist. [39; 40] Waste arising from gaseous diffusion or centrifuges is minimal. This is attributed to no additions of material or rejects of intermediate or waste products. Waste which does occur from the diffusion or centrifuge process is a result of gas that is passed through scrubbers before being released into the atmosphere. However, a by-product from the production of 1000 t of enriched uranium is approximately 850 t of depleted uranium. [39]

Fabrication of the fuel for use in reactors utilizes production of uranium dioxide through similar methods as refinement followed by pellet manufacture. Processes similar to refinement are ADU, AUC or the integrated dry route (IDR) for production of uranium dioxide. [39] The ADU process is primarily used for production of natural UO_2 powder for use in CANDU reactors. Fabrication of fuel by the IDR process is used for enriched UO_2. The AUC process is used to fabricate both natural and enriched UO_2.

Pelletizing the uranium dioxide and assembly of the fuel elements is performed in several steps. [39] The first step is blending of the UO_2 powder for homogenisation followed by additions of U_3O_8 or other additives, such as neutron poisons. Pre-compaction of the powder followed by granulation is performed by some facilities; however, it is not used all the time. Granulated powder is pressed into a pellet and sintered in a reducing atmosphere. After sintering, the pellets are ground and loaded into zirconium alloy tubes with a helium atmosphere awaiting assembly. The fuel elements (zirconium alloy tubes with pellets) are assembled to make the fuel assemblies. In the case of Magnox reactors as used in the United Kingdom, the process is as follows; blending, pelletizing, reduction (MgF_2 as a by-product), billet cleaning, vacuum casting, machining, uranium metallic rods, canning and then fuel assembly. [39]

Waste generated from manufacturing of fuel assemblies is different depending on which fabrication process is used. The AUC process generates approximately 9500 m^3 of solutions, sludges, residues and about 40 t of miscellaneous metal scrap for 1000 t of uranium throughput. [39] The ADU process generates approximately 4000 m^3 of solution less than the AUC process for 1000 t of uranium throughput due to ammonium fluoride solution not being present. [39] The IDR process creates approximately: 1000 t of hydrogen fluoride, 40 t of miscellaneous metal scrap and 500 m^3 of combustibles and filters for 1000 t of uranium throughput. [39] In the case of the Magnox reactors in the United Kingdom there is about 450 t of magnesium fluoride, 300 t of graphite and 500 m^3 of combustibles and filters for 1000 t of uranium throughput. [41]

In general, nuclear reactors currently in use today rely on fissioning of the ^{235}U isotope by neutrons which have passed through a moderator. [1] The moderator can be water, heavy water, or graphite and is used to slow down the neutrons needed for fission of ^{235}U. When fission occurs it releases heat used to produce steam. The steam produced generates electricity by turning a turbine. The fuel assemblies contain the enriched ^{235}U (excluding Magnox or the CANDU reactors which use natural uranium) in the form or rods or fuel assemblies. The reactor design determines the type of fuel assembly required. Advanced gas cooled reactors (AGR) use oxide pellets in stainless steel rods while fuel is enclosed in zirconium alloy fuel rods for pressurized water reactors (PWR), boiling water reactors (BWR) and CANDU reactors. In the case of the UK Magnox reactors, uranium metal rods are encased in magnesium alloy fuel rods with cooling fins. [41]

The waste from the reactors is mainly from the spent fuel (used fuel assemblies) and the reactor itself. The composition of the spent fuel depends on the fuel assembly used; however, the fission products obtained from the spent fuel are very similar. The used fuel assemblies in the UK are reprocessed in order to retrieve unused uranium. Waste from reprocessing fuel assemblies at Sellafield comes from the Magnox and the uranium dioxide fuels. [1] In order to reprocess the spent fuel, the cladding surrounding the fuel has to be removed. The PUREX (plutonium and uranium extraction) process is one method for reprocessing spent nuclear fuel. After removal of the fuel cladding, the uranium and plutonium fuel is dissolved in nitric acid, and Pu and U are separated and recovered by chemical solvent extraction. The solution can be concentrated by evaporation, or neutralized by additions of alkali such as sodium hydroxide. The composition of the waste solution from chemical solvent extraction comprises of fission products, fuel alloying elements, trans-uranic (TRU) elements formed by neutron capture, elements from the fuel cladding, and also process chemicals. This resulting solution is known as high level liquid waste (HLLW) and is calcined for de-nitration. At

Sellafield, the calcined waste has been vitrified for immobilisation awaiting final geological disposal.

2.1.2 Waste Classifications

There are currently four major classifications of solid wastes in the UK. [31] These are; high, intermediate, low, and very low level wastes (HLW, ILW, LLW, and VLLW, respectively). These classifications for the UK only take into account the current radioactivity and neglect the radionuclide half-life, while the US classifies waste based on the source of the material. Liquid wastes are also divided into high, medium, and low level wastes. Table 2.1 lists the classification and the activity level for each waste.

Table 2.1 Current UK solid waste classifications.

Classification	Activity level
HLW	> 4 GBq/t α-radiation or 12 GBq/t β-/γ-radiation and heat generating
ILW	> 4 GBq/t α-radiation or 12 GBq/t β-/γ-radiation
LLW	< 4 GBq/t α-radiation or 12 GBq/t β-/γ-radiation
VLLW	Each 0.1 m^3 of material containing < 400 KBq β-/γ-radiation

2.1.2.1 LLW Classification

Building materials, miscellaneous organic and inorganic materials, protective clothing and equipment used in and around radioactive facilities are classified as LLW. Activity levels set in the UK for LLW are < 4 GBq/t α-radiation or 12 GBq/t β-/γ-radiation. This waste, although seemingly ordinary, cannot be disposed of as normal civil waste due to possible exposure to low levels of radiation.

2.1.2.2 ILW Classification

Intermediate level wastes are those with radioactivity levels greater than 4 GBq/t α-radiation or 12 GBq/t β-/γ-radiation. As defined by Donald, ILW may also be heat generating but to a lesser degree than HLW; specifically < 2 kW m^{-3} of material. [1] ILW is generally comprised from components inside the nuclear reactor such as reactor cores, fuel cladding and fuel

element debris. Other sources of ILW are medical equipment, experimental instruments, filters, and chemical sludges.

2.1.2.3 HLW Classification

High level waste is classified as such due to radiogenic heating; specifically > 2 kW m^{-3}. [1] Because of this, disposal methods need to take into account the temperature changes during storage. To date, there is no international consensus on the definition of the HLW classification. [1] Sources of HLW from the civil industry include liquid wastes from spent fuel reprocessing containing short-lived fission products, long-lived fission products, and actinides. Weapons manufacture creates HLW from the production of plutonium metal and tritium.

2.1.3 Immobilisation of Radioactive Wastes

Due to the difference in the radioactive inventory the wastes generated from nuclear facilities, various classification schemes have been incorporated. There are different classifications between countries such as those put forward by the UK National Decommissioning Authority (NDA), International Atomic Energy Agency (IAEA), and the US Nuclear Regulatory Commission (NRC). [41; 42; 43] Each classification of waste whether it be LLW, ILW, or HLW involves a different method of immobilisation and / or disposal. This is due to the difference in inventory associated to each classification or in the case of UK HLW, radiogenic heating.

In the UK, LLW is super-compacted using a force of up to 2,000 tonnes per square metre in either drums or boxes. The compacted drums are loaded into freight containers which are subsequently filled with cement and placed into vaults. [31; 41] The containers are sent to sites near Dounreay or Drigg for final geological disposal in near surface concrete lined vaults. The Low Level Waste Repository near Drigg has a limited capacity and either an alternative disposal means or facility will need to be found. [41] Similar methods are used in the US where LLW is disposed of in low level repositories. [43]

ILW is immobilised before it is sent for interim storage in the UK. Current practice in the UK is to encapsulate ILW in cement because it is currently the most suitable method. [31] The choice of cement is based on mixes of blast furnace slag (BFS), ordinary Portland cement (OPC) or pulverised fuel ash (PFA). The two main matrices for ILW immobilisation are

BFS/OPC and PFA/OPC. [31] An advantage the BFS/OPC mix has over OPC is that BFS (a cementitious material) reacts with water to produce a completely hydrated system. Additions of PFA improve the rheological properties and it is used when high fluidity is required. The encapsulation process of ILW has 8 major steps: (i) load swarf, (ii) install anti-flotation device, (iii) de-water and grout, (iv) cure, (v) cap and cure, (vi) fit lid, (vii) decontaminate, and (viii) monitor and store. The immobilised ILW should be robust and stable until final disposal; usually up to 100 years and onward.

2.1.3.3 Vitrification of HLW

There are three main full scale operations used for immobilisation of HLW in use today: Atelier de Vitrification de La Hague (AVH), Atelier de Vitrification de Marcoule (AVM), and the Joule Heated melter. [6] In each of the operations, evaporation, decomposition, melting and casting steps are needed to immobilise the liquid high level waste. [2]

The first and second step, evaporation of the free nitric acid and water along with decomposition of the nitrates and calcinations of the waste components to oxides is generally performed using a calciner, or rotary kiln in which the off-gasses are sent to scrubbers and condensers. From the calciner, melting is performed. This can be done using pot melters, or through a continuous process in which the melt flows to a stainless steel container. After casting, the final vessel can be stored before final geological disposal.

The UK currently employs a similar method to the two stage AVH process. [2] The two stage process consists of calcining the waste followed by melting. Before waste is calcined it is fully characterized by chemical analysis and a quantity of lithium nitrate is added, which inhibits refractory oxides from forming during the calcination process. Without additions of lithium nitrate to the liquid HLW stream; aluminium, chromium and iron oxides could form causing an increase in melting temperature, or worse, blockage of the drain tube during melting. After characterization and additions of lithium nitrate the HLW is sent to a calciner for de-nitration: the first stage of the two-step vitrification process.

The calciner is a large rotating inclined (at 1.7°) cylinder heated up to 850 ºC in a reducing atmosphere. [31] Rumble bars (tumbling large iron bars) are used inside the calciner to prevent caking of the waste. HLW solution is fed into the top portion of the calciner. During calcination, the waste is de-nitrated and liquid is evaporated leaving a fine powder. Reagents are used in order to suppress volatilisation of ruthenium and to prevent caking. The calcined waste is then mixed with a glass frit of a specified composition (which can change depending

on the waste being calcined) and subsequently fed into the melter: the second stage of the two-step process, via an air lock system.

The calcine and frit are fed into an induction furnace at a temperature of ~1100 ºC. During melting residual nitrates decompose. Waste is added typically to 25 wt% of a borosilicate base glass; however, there have been studies showing higher waste loadings are possible with phosphate glasses. [44] After approximately 8 hours, the melter is drained into a stainless steel container which is subsequently washed and placed into interim storage to cool before final disposal.

2.1.3.4 UK Nuclear Waste Glass Compositions

From the beginning of the British nuclear program, the Highly Active Storage Tanks (HASTs) have been used to store various HLW waste streams. [45] These waste streams were comprised, mainly, of the Magnox waste with changing amounts of U, Al, Fe, and Cr. Simplified compositions of different UK HLW waste streams are given in Table 2.2. [45]

Table 2.2 Simplified compositions in mol % of the UK HLW waste streams.

Oxide	Magnox	Blend	HAST A	HAST B
Al_2O_3	16.62	0.84	43.22	30.20
Cr_2O_3	1.44	1.53	0.70	1.91
Fe_2O_3	4.31	3.44	10.13	10.81
Gd_2O_3	0.49	4.33	--	--
MgO	45.53	18.56	16.37	37.95
MoO_3	4.38	10.81	1.45	1.04
NiO	--	--	1.25	1.93
UO_3	Trace	Trace	14.24	6.83
ZrO_2	4.95	12.3	1.68	1.32
Others	22.28	48.19	10.96	7.91

The base glass composition, “MW Base,” currently considered for vitrification of the UK high level nuclear wastes is based on a four component borosilicate glass with the nominal composition of 61.7 wt% SiO_2, 21.9 wt% B_2O_3, 11.1 wt% Na_2O, and 5.3 wt% Li_2O. There are two major waste compositions from the UK: Magnox and Blended wastes. [2] Magnox waste arises from reprocessing of only Magnox fuel, whereas the Blend waste is a mixture of the Magnox HLW and HLW from the Thermal Oxide Reprocessing Plant (ThORP) at a ratio

of 25 wt% and 75 wt%, respectively. [10] General compositions of the base glass and the base glass with additions of the waste calcine at a 25 wt% waste loading are given in Table 2.3.

Table 2.3 Nominal compositions of MW Base glass, MW Base glass with the Magnox HLW (MW Magnox), and the MW base glass with the Blend HLW (MW Blend) glass in wt%.

Oxide	MW Blend (wt%)	MW Magnox (wt%)	MW Base (wt%)
SiO_2	46.28	46.28	61.70
B_2O_3	16.43	16.43	21.90
Na_2O	8.33	8.33	11.10
Li_2O	3.98	3.98	5.30
Al_2O_3	1.91	4.86	--
BaO	0.47	0.40	--
CeO_2	1.45	2.25	--
Cr_2O_3	0.51	0.68	--
Cs_2O	1.59	1.17	--
Fe_2O_3	2.06	3.15	--
Gd_2O_3	4.16	0.12	--
La_2O_3	0.73	0.66	--
MgO	1.61	5.05	--
MoO_3	2.49	1.52	--
Nd_2O_3	2.17	1.94	--
NiO	0.34	0.45	--
Pr_2O_3	0.66	0.61	--
RuO_2	0.55	0.42	--
Sm_2O_3	0.49	0.43	--
SrO	0.41	0.31	--
TeO_2	0.28	0.18	--
Y_2O_3	0.31	0.20	--
ZrO_2	2.82	1.59	--
Total	100.0	101.0	100.0

2.2 Silicate Glass Structure

Current knowledge of glass structure has increased significantly since Zachariasen's theory in 1932. [46] Since then, other scientists have challenged or expanded upon his model of glass structure. Structural theories such as Zachariasen's random network theory and Goldschmidt's radius ratio criterion are based on a co-ordination number concept while Smekal's mixed bonding rule, Stanworth's electronegativity rule and Sun's single bond strength criterion are all based on aspects of bonding. [47] Other theories include Dietzel's

field strength criterion and Phillips' topological constraint model. However, Zachariasen's random network theory can still be thought to be broadly correct, but with many criticisms.

2.2.1 Zachariasen Theory

Zachariasen compared the mechanical properties of glasses to those of crystals. In his paper, he states all bonds or atoms are not structurally equal which explains a non-abrupt melting point in glasses since the energy required to detach an atom from the network will be different for each bond or atom. [46] As in the case of a crystal, all bonds or atoms are equivalent and at an exact temperature there is enough thermal energy to detach all the bonds or atoms simultaneously causing the crystal network to break down abruptly. Zachariasen also states that glasses and crystals are linked together by forces that are almost equivalent and atoms oscillate about definite equilibrium positions.

The results from Zachariasen's X-ray diffraction (XRD) experiments show the glass network is not periodic and symmetrical as in crystals, however, atoms in glasses must form extended three dimensional networks. A crystal lattice must contain an integral number of stoichiometric molecules since all unit cells are alike and since there is no periodicity in glass, the glass unit cell can be thought of as being infinitely large, having an extended three dimensional network lacking symmetry and periodicity. [46] Because the crystal and glass have similar interatomic forces, Zachariasen postulated the glass networks should have polyhedra of oxygen atoms around atoms similar to that of crystals. It is also known that when atoms are ionized, cations are surrounded by as many anions as possible, as long as the anions do not contact one other.

This is also true for a glass network; however, conditions to which this applies need to be specified. In the case of SiO_2, linking silicon atoms to oxygen atoms yields oxygen polyhedra surrounding the silicon atom. The oxygen polyhedra share corners and are linked by two silicon atoms (atom A). Zachariasen describes the glass as a network of oxygen polyhedra with a set of rules: [46; 47; 48; 49]

1. Oxygen atoms are linked to no more than two atoms.
2. The coordination of oxygen atoms surrounding atom A is small.
3. The oxygen polyhedra share corners, but not edges or faces.
4. At least three of the four corners of the oxygen polyhedra must be shared.

Some oxides readily satisfy these four rules of glass network and some do not. Oxides which do not satisfy these requirements are based on X_2O or XO oxides. Zachariasen concludes in his studies that a glass can be expressed as A_mB_nO, where B represents one of the cations from the fore mentioned oxides, A represents all other cations present, and *m* and *n* are the number of cations A and B per oxygen atom respectively.

2.2.1.1 Random Network Theory

The radial distribution function (RDF) was used by Warren supporting Zachariasen's theory of the random network theory and four rules of glass formation. [49] Warren showed that the RDF of vitreous silica gives the same pair correlation as that of the crystal, SiO_2; however, the peak widths differ indicating the structure of the glass is random and not ordered. Warren also suggests strong evidence of a continuous glass structure due to an absence of small angle scattering in the XRD pattern.

It was proposed, on the basis of what was later termed non-bridging oxygen's (NBOs) that the total number of oxygen atoms is greater than twice the number of silicon atoms. If the number of oxygen atoms is twice that of silicon atoms, there are oxygen atoms only bonded to one silicon atom. In the case of alkali or alkaline earth silicate glasses the alkali or alkaline earth atoms are assumed to be randomly situated in the 'holes' of the silicon and oxygen network.

2.2.2 Other Theories

Since Zachariasen presented his rules of glass formation there have been several criticisms. One other theory of glass formation is the single bond criterion from K.-H. Sun. [50] Sun based the conditions of glass formation on the bond strength of the glass components. Bond strengths are calculated using co-ordination numbers for the metals in the oxides and are obtained by dividing the dissociation energy of the oxide by the oxygen co-ordination number of the metal. The bond strengths are said to give a representation of network formers ($\Delta H > 80$ kcal), intermediates ($80 > \Delta H > 60$ kcal), and modifiers ($60 > \Delta H$ kcal); however, the transition between the formers, intermediates, and modifiers is gradual so the classifications can be thought of as being rather arbitrary. Sun summarizes a glass structure, which he postulates as being a liquid structure cooled below the melting point, by saying:

> *"To secure such long chains or large networks, (1) the bond strength of atoms in the chains or networks must be very strong; (2) small ring formation of these strongly bonded atoms should be at a minimum; (3) the relative numbers of various atoms in the chains or networks should be such that at least a continuous chain is configuratively and structurally possible; and (4) at the same time, the coordination numbers of the glass-forming atoms should be as small as possible to keep the bond strong."* [(50)]

Almost at the same time as Zachariasen published his theory in 1931, Randall *et al.* suggested that a glass structure is made up of small crystallites of the stoichiometric equivalent crystal. [(51)] By exposing liquids to X-Rays Randall *et al.* were able to achieve XRD patterns similar to that of glasses. It was proposed that atoms in the liquid were trying to arrange themselves into a crystal structure; however, the atoms were only able to succeed for short time periods and in very small groups of atoms. [(51)]

Another similar approach to the work by Randall *et al.*, which suggested evidence of short-range order similar to that found in crystals, was published by Lebedev several years before Zachariasen's theory of glass structure. [(52; 47)] Lebedev's work suggested an accumulation of crystallites of different silicates with a definite chemical composition. He also proposed the crystallites are separated by amorphous layers which become increasingly random the thicker the amorphous layer gets and that the crystallites are a deformed structural formation with pronounced features of a crystal lattice. Lebedev's theory implied the RDF of a borosilicate glass could be constructed through the use of individual RDF's of both B_2O_3 and SiO_2 in appropriately weighted proportions. [(53)] Experimental evidence of the construction of the glass's RDF showed that the use of the $xNa_2O{\cdot}ySiO_2$ system where the SiO_2 RDF was multiplied by 'y' and subtracted out of the RDF of the system $xNa_2O{\bullet}ySiO_2$, gives a similar shape to that of the experimentally produced Na_2O RDF. [(52; 47)]

Further development of the crystallite theory by Hägg states that in borate glass the structure is made up of chains of borate groups and not small groups of crystals in a random network. [(54)] The borate groups, when lined up next to each other, are considered to be an unlimited radical and are kept together by strong bonding. Hägg theorised that in a glass melt, atom groups are kept together due to strong forces. When cooling a liquid, if the groups of atoms are large enough, the further addition of atom groups to the crystal lattice is difficult which leads to a random network formation of the crystal lattice (i.e. a glass). If however, an addition to a crystal lattice from a group of atoms is easy, where these groups are formed by single atoms or small radicals, crystallization is very likely. As the irregularity of

the groups increase the tendency towards glass formation also increases, as in the case with nearly all inorganic glasses.

More recent work on the structure of glass by Greaves *et al.* studied the local order in silicate glasses around the sodium and silicon atoms. [55; 56] The work presented agrees with that of Lebedev where ". . . the structure of silicate glasses [is] to be a natural extension of the structure of crystalline silicates. As such it will be made up of two interpenetrating sub-lattices: a covalent network consisting of the SiO_2 component 'inter-calated' by an ionic fraction made up of the modifier component (such as Na_2O)." [55] Greaves also used X-ray absorption spectroscopy (XAS) to study the Na and Ca environments in silicate glasses to support his theory of the modified random network (MRN). [56] The MRN is suggested to be made up of two regions. The first region is 'islands' or 'lakes' of network formers surrounded by an inter-network or 'channels' of modifiers. [56] The islands are a network which follows the rules presented by Zachariasen. The channels of modifier ions contain network modifier cations and non-bridging oxygen (NBO).

2.3 Borate and Borosilicate Glass Structure

Many of the current ideas of glass structure previously discussed are for silicate glasses. These structural ideas are not suitable for borate and borosilicate glasses due to the different co-ordination number in which boron takes in the glass network. Bray and his colleagues postulated on the structure of borate glasses in the late 70's, although the earliest studies were published in 1962. [54; 57; 58]

2.3.1 Krogh-Moe Model of Borate Glasses

Krogh-Moe suggested that boron changes its speciation with a change in alkali content through different boron groupings. These groupings are a boroxol, pentaborate, triborate, and a diborate grouping. At low alkali percentages the boroxol group is prevalent; however, an increase of alkali initiates formation of tetraborate (tri- and pentaborate groups) and diborate groups. At approximately 40 mol % the number of NBO's becomes significant in the glass structure. Krogh-Moe gives an example of viscous flow of a boron oxide glass comparing it to that of a silicon oxide glass: even though the bonds of B-O and Si-O are similar in strength, the viscosity of the boron oxide glass is less than the silicon oxide glass. Krogh-Moe suggests this is due to the ability of boron oxide to change between three-fold and four-

fold co-ordination by bonding with available oxygen in the glass network. Boron atoms become less likely to change co-ordination with an addition of alkali due to the more polarisable oxygen. This polarisation of the oxygen atom would normally increase the viscosity; however, the addition of alkali weakens the structure subsequently decreasing the viscosity resulting in a maximum and minimum in the viscosity curve of an alkali borate glass. [59] This work led to the work on the 'boron oxide anomaly' by Krogh Moe. [60]

2.3.2 Boron Oxide Anomaly

Both Warren and Krogh-Moe suggest the 'boron anomaly' can be attributed to additions of alkali to the boron oxide glass. [49; 57] The addition of alkali changes the co-ordination of the boron structure from three-fold to four-fold co-ordination. [49; 57] For alkali additions up to ~13 mol % in the glass, the fraction of boron in tetrahedral co-ordination can be easily calculated; however, above this the extra oxygens introduced from the alkali do not all bond with boron. It is widely accepted that there is a maximum number of four co-ordinated boron units around 15 mol % alkali (theory of saturation); however, Krogh-Moe disagreed and later work by Bray *et al.* gave experimental evidence of saturation of four-fold co-ordinated boron units near 35 mol%. [57; 61; 60]

Early work by Bray *et al.* developed a model giving four different regimes of alkali (Na_2O) borate glasses. [58; 62] These regimes are dependent on two molar ratios; R and K, where $R = Na_2O/B_2O_3$ and $K = SiO_2/B_2O_3$. [63]

- The first region; ($R < 0.5$), the boron groups are either trigonal or tetrahedral. This is due to the modifier ion being consumed and converting the trigonal boron units into tetrahedral boron units. The modifier ion compensates the total negative charge of the boron units in the tetrahedral groups.
- The second region; ($0.5 < R < 0.5 + K/16$), is the linear increase of K to the maximum value of the 4 co-ordinated boron with respect to R.
- The third region; ($0.5 + K/16 < R < 0.5 + K/4$), is when the 4 co-ordinated boron becomes constant and independent of alkali content.
- And the fourth region; ($0.5 + K/4 < R < 2 + K$), is the decrease in the 4 co-ordinated boron units due to an excess of alkali.

The classic theory suggested the alkali or modifier goes into the voids in the glass network and does not contribute to the total volume; however, it has also been suggested that the modifiers may contribute to the final volume due to "strict demands on their surroundings." [60] The work Krogh-Moe presented gives evidence that the oxygen volume is independent of alkali and decreases with increasing alkali content up to 30 mol %. [57] After 30 mol % of alkali additions the oxygen volume increases significantly suggesting a reversion in the co-ordination of boron.

Since borate glasses have an anomaly with additions of alkali, additions of silica make the structure more complex. Much of the early work performed on silicate glasses and boric glasses can be used to describe the structure of boro-silicate glasses; however, the structure of the boro-silicate glasses is still under discussion due to the boron anomaly.

2.3.3 Dell-Bray Models of Borosilicate Glasses

Some of the earlier work on boro-silicate glass structure was performed by Bray, Yun, and Dell. [58; 64] The work performed by Yun et al. in 1978 and 1979 proposed 4 different regions of the structure of the boron units similar to that of the four regions of a boron glass by Krogh-Moe. The basis of this model demonstrated that an increase in alkali up to an R value of 0.5 ($R = Na_2O/B_2O_3$) destroyed diborate groups. These diborate groups then form reedmergnerite groups by combining with existing SiO_2. The reedmergnerite groups are made up of a boron tetrahedron surrounded by 4 silica tetrahedra. Additions of alkali in the borosilicate network break up remaining diborate groups which form other borate units while leftover alkali form NBOs on reedmergnerite groups.

In a later paper, Xaio revisited this model suggesting a modification which better correlates to the experimental data presented by Yun *et al.* [65] In Xiao's paper, the model suggested $R \geq R_0$, and $K \leq 8$, where $R = Na_2O/B_2O_3$ and $K = SiO_2/B_2O_3$. Xiao concludes that after the depletion of available diborate units the un-bonded tetrahedron boron units may react subsequently rather than all at once. It was also proposed that the initiation of orthoborate units may start at lower boric oxide concentrations (higher R values).

Collaboration between Xiao, Dell, and Bray continued the modelling of an alkali-boro-silicate glass structure through the use of ^{11}B nuclear magnetic resonance (NMR). [66] The new model presented by Dell, Bray, and Xiao still contains 4 regions; however, they are slightly changed from the original work by Yun *et al*. These regions, as shown in Figure 2.2, are:

1) $R < 0.5$: The alkali forms four co-ordinated boron units, and the number of four co-ordinated boron units is equal to R ($R = Na_2O/B_2O_3$).

2) $0.5 \leq R \leq R_{max}$ ($R_{max} = 1/2 + 1/16K$): The additional alkali form reedmergnerite groups.

3) $R_{max} \leq R \leq R_{D1}$ ($R_{D1} = 1/2 + 1/4K$): Formation of NBOs on the silicate tetrahedra starts to occur from the reedmergnerite groups absorbing all additional alkali in the system.

4) $R_{D1} \leq R \leq R_{D3}$ ($R_{D3} = 2 + K$): A fraction of the additional alkali ((K - K/4)/(2 + K)) combine with left over diborate groups to form borons with two NBOs and the other fraction, ((K + K/4)/(2 + K)), combine with reedmergnerite groups.

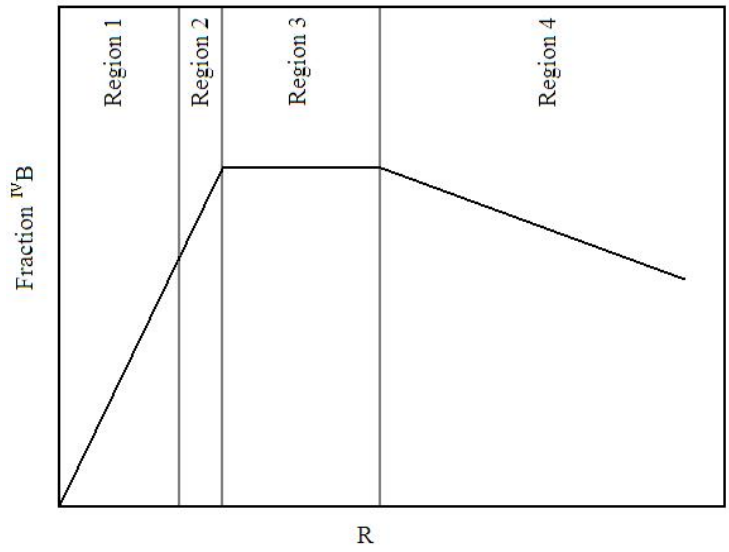

Figure 2.2 The 4 regions of formation for borosilicate glasses as given by Dell *et al.* [66]

The structures of silicate, borate, and borosilicate glasses are still studied today. Many methods have been employed to develop models of these structures. Early methods such as diffractometry and spectrometry have been used to explain the differences seen between bonding of the different species within these glasses. Current methods used today are still through the use of spectrometry and diffractometry methods; however, these methods have been developed further.

More current work on glasses has been in the corrosion and dissolution mechanism in order to study how glass reacts to a solution. These reactions are important in nuclear waste

management due to final geological disposal depending on the conditions and durability of the glass wasteforms used.

2.4 Structural Role of Zn in Silicate Glasses

Zn has been shown to improve the mechanical properties of silicate and borosilicate glasses and to decrease the softening point of phosphate glasses. [67] In particular, the increased chemical durability from small additions of ZnO to silicate glasses is of interest for long term dissolution behaviour of nuclear waste glasses; however, the role of Zn in silicate glasses is the subject of controversy due to findings of both four- or six-fold co-ordinations of Zn in the glass network. [10; 68] The crystal field theory classifies Zn^{2+} as an intermediate due the ability of Zn to adopt either four- or six-fold co-ordination. [47]

Several structural studies of Zn in silicate glasses have been performed using X-ray absorption spectroscopy (XAS). [68; 69] Recent work by McKeown *et al.* modelled the short range structure around Zn of several borosilicate glasses used for vitrification of nuclear waste and conclude that Zn acts as a network modifier. [69] This was supported by work from Le Grand *et al.* modelling silicate glasses with small additions of ZnO ($ZnO \leq 2.5$ wt%) to the compositions of borosilicate glasses which are, again, derived from glass compositions for use in vitrification of nuclear waste. [68] Le Grand *et al.* conclude that Zn performs as a network former with low additions of ZnO to borosilicate glasses. [68] Other studies suggesting Zn performs as a network former and not as a network modifier were performed by Lusvardi *et al.* in 1987 and Rosenthal and Garofalini in 2004. [70; 71]

XAS has been a useful tool in determination of the local structure around Zn in oxide glasses. Other methods to study the local structure of Zn are Raman spectroscopy molecular dynamic (MD) simulations. [67; 72] Lusvardi *et al.* suggest that Zn performs as a weak network former independent of the alkali concentration in glasses; however, Minser *et al* give conflicting evidence that Zn performed as a simple network modifier in sodium silicate glasses doped with ZnO. [67; 72] The contrasting evidence of Zn performing as a network former or modifier, along with studies suggesting small additions of ZnO to silicate glasses increases the durability, lead to work being undertaken to study the mechanisms by which ZnO increases the durability of glass through the use of structural modelling by XAS and durability tests. [73]

2.5 Durability of Glass

The mechanisms of glass corrosion have been studied for several decades; however, it was not until recently it has become important to understand the rates of corrosion, mainly due to the use of glass as a waste form for vitrification of nuclear waste. When used as a vitrified nuclear waste form, the glass needs to be chemically durable, immobilise a wide variety of elements, must not crystallize after being poured into the final stainless steel canister and must remain stable for many thousands of years. [7] Other reasons for understanding chemical durability are; for preserving artefact glasses, making fibre optic interfaces reliable, bonding of bio-glasses to living tissue, and prediction of serviceable lifetimes of glass and ceramic materials. [7]

The surface chemistry of glasses during water/glass reactions have been studied and several models have been developed in order to predict the behaviour of glass corrosion. [8] Different methods of modelling glass corrosion are based on geochemical or thermodynamic approaches. [8; 74] Most models base dissolution of glass on the breakdown of the glass network. However, saturation effects, formation of alteration layers, diffusion processes and the composition of the solution reacting with the glass need to be taken into account. [8]

Surfaces of glass from reactions between the glass matrix and solution have been described by Hench and Clark. [7] These authors suggest that at any point in its lifetime a glass has one of five types of surfaces. [7] These surfaces depend largely on the environment surrounding the glass. A Type I glass does not have any significant change in the surface composition. The surface of the glass has undergone slight hydration; however, this layer is typically less than 50 Å in thickness. Type II surfaces have undergone selective leaching of the alkali on the surface and this layer acts as a protective film or gel layer. The selective leaching causes dealkalization on the surface and an increase in concentration of silica in this area. Glasses which have Al_2O_3 or P_2O_5 additions will normally show a Type III surface. These are glasses which show a dual protective gel layer. This occurs due to a silica rich layer between the bulk of the glass and an alumina-silicate or calcium phosphate layer in the gel. The dual gel layer is usually from dealkalization, surface structural modifications, or precipitation in or on the gel layer. Glasses which contain low concentrations of silica will normally have a Type IV surface. This surface is similar to that of a Type II surface; however, the gel layer does not act as a protective film due to the concentration of silica being too low. The low concentration of silica leads to rapid dealkalization or network dissolution. Glasses which exhibit congruent dissolution exhibit a Type V surface. Silica concentrations on the surface and the bulk show little to no difference. Normally, this type of

surface will lead to frosting and crazing of the surface. Figure 2.3 (modelled after from Hench & Clark, 1978) illustrates the five types of glass surfaces. [7]

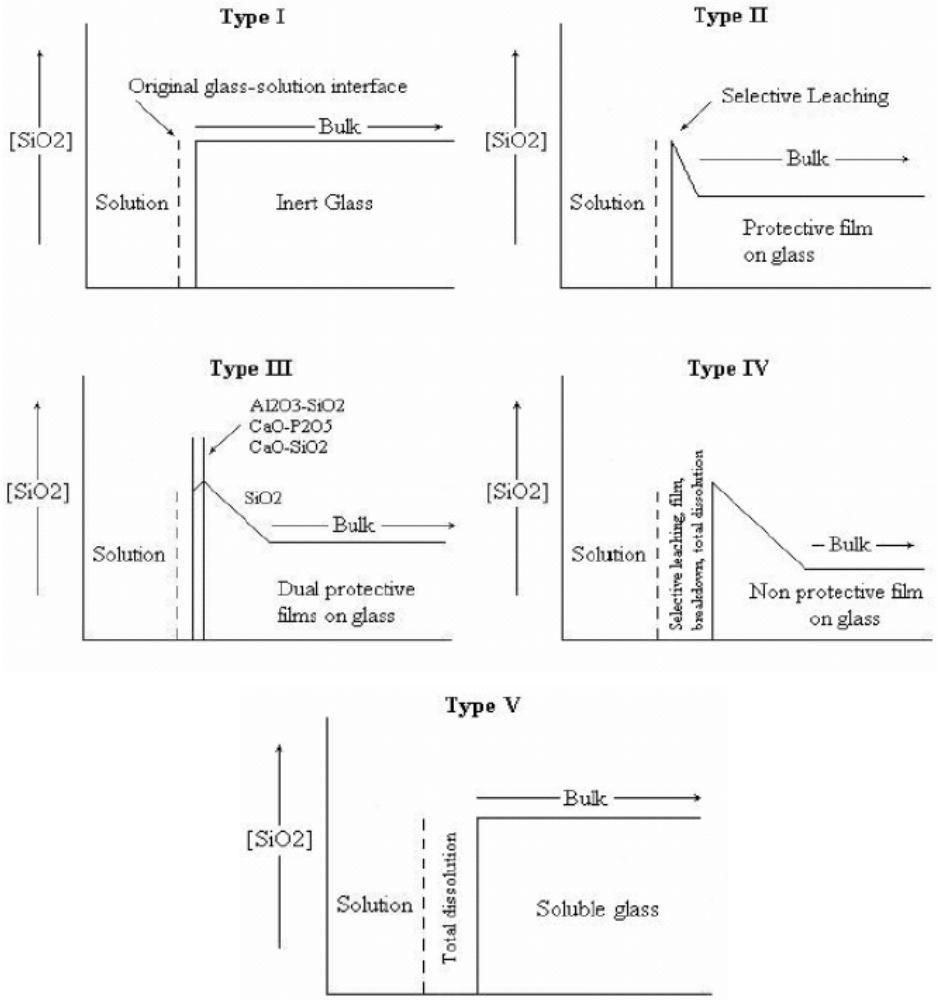

Figure 2.3. The five types of glass surfaces after exposure to water. After Hench & Clark, 1978. [7]

Initial reactions of the glass surface with an aqueous solution are suggested to be from two independent processes; ion-exchange of the alkali into solution and dissolution of the glass matrix. [7; 26] The rate of exchange of the alkali into solution follows a parabolic shape. [26] As the exchange of the alkali into solution progresses, the rate of exchange decreases and matrix dissolution becomes dominant. [23] Figure 2.4 shows the rate of corrosion with the concentration of species in solution. As the reaction proceeds with time, the concentration of the species starts to increase. This causes the rate of corrosion to decrease. However, if another species starts to exchange out into solution, the rate of corrosion abruptly increases and will then continue to decrease as the concentration of that species increases. [19; 23]

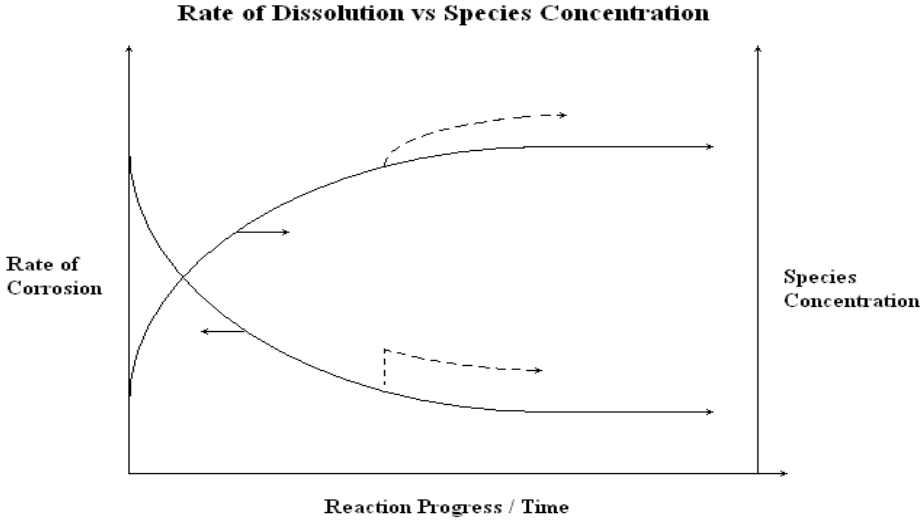

Figure 2.4. Rate of glass dissolution versus species concentration in solution.

This co-existence of the exchange between the alkali ions and hydrogen protons and matrix dissolution can be described mathematically by the solution to Fick's law for moving boundary conditions. [8] The overall rate of corrosion of glass depends on the diffusion coefficient, D (m^2 sec^{-1}), and matrix dissolution, a (m sec^{-1}). [8] At very short times, t << a^2/D, the corrosion rate is controlled by the exchange of the alkali ions with hydrogen protons. The amount of alkali released, Q, can be determined by the initial concentration of alkali in the glass, C_o, and multiplied by the square root of the diffusion coefficient, D, and time, t (Equation 2.1). [8]

Equation 2.1 $$Q = C_o 2\sqrt{D * t/\pi}$$

At longer times, t >> a^2/D, matrix dissolution becomes dominant and the amount of alkali in solution then follows equation 2.2. [8] The term 'a t' describes the depth of glass network breakdown and 'D/a' describes the depth of water penetration.

Equation 2.2 $$Q = C_o(a\,t + \frac{D}{a})$$

At short times, the alkali can also be described by equations 2.3 through equation 2.5, where 'M' is an alkali or monovalent metal ion. [74; 75]

Equation 2.3 $\equiv$Si-OM + H_2O $\Leftrightarrow$ Si-OH + M^+ + OH^-

In Equation 2.3, the cations released are from the ion exchange with the protons in solution. The forward reaction of equation 2.3 gives a release of silica into solution as the siloxane bonds are broken by OH^- ions in solution (Equation 2.4).

Equation 2.4 $\equiv Si\text{-}O\text{-}Si\equiv + OH^- \Leftrightarrow \equiv Si\text{-}OH + NBO$

During attack of the siloxane bonds, non-bridging oxygen's (NBOs) are formed. These NBOs then react with water forming additional silanol bonds on the glass surface which release other hydroxyl ions (Equation 2.5).

Equation 2.5 $NBO + H_2O \Leftrightarrow \equiv Si\text{-}OH + OH^-$

These reactions, however, can be simplified through a simple reaction equation (equation 2.6) which represents forward dissolution and a reverse condensation reaction, both of which are responsible for silica in solution and the gel layer. [74]

Equation 2.6 $SiO_2 + H_2O \Leftrightarrow H_2SiO_3$

Because glass is relatively inert, most chemical durability tests involve reactivity with water, aqueous solutions, and weathering. These reactions include ion exchange of the hydrogen protons from water and dissolution of glass into solution. The dissolution rate of the glass is affected by glass composition, solution pH, temperature of the environment, and solution chemistry.

The rate of glass dissolution has been studied by several authors in order to model the durability of glasses which will be used for vitrification of nuclear waste. [17; 19; 27; 8; 74] Early modelling of glass dissolution was based on diffusion kinetics; however, this did not take into account changes in the rate of corrosion due to formation of alteration layers. [19] Recent work based on the kinetic rate equation for mineral dissolution by Aagaard and Helgeson has been performed by Grambow and further developed by Strachan and Croak. [19; 8; 76]

2.5.1 Derivation of the Kinetic Rate Equation of Glass Corrosion

Early investigations of silicate mineral dissolution tests have lead to theories about the formation of a protective film, or residual surface layer during corrosion of minerals. [76] This was due to early results demonstrating that dissolution of silicates resulted in molar ratios of ions in solution differing from that of the mineral under study. [77; 78] It was also discovered that components of minerals were exchanged as ionic species rather than colloidal gels. [76]

According to Aagaard and Helgeson, this protective film has become the basis for many current theoretical models of silicate hydrolysis. [76] Aagaard and Helgeson, among others, also suggest that precipitation of a gel layer from reaction products is consistent with incongruent silicate hydrolysis; however, the ability of a gel layer to decrease diffusion of material through an aqueous phase in the interstitial pore areas of the film has not been experimentally verified. [76]

Several authors have failed to find supporting evidence of a protective gel. Other studies have confirmed, through the use of scanning electron microscopy and X-ray photo electron spectroscopy, the absence of a coherent coating on the surface of a mineral, ruling out the theory of a gel layer thicker than ~17 Å. [76; 79; 80] The confirmation of the absence of a coherent and continuous surface layer suggests that the observed rates of hydrolysis are not fast enough for the rate-limiting step to be interstitial aqueous diffusion. [81; 76]

Work performed by Wollast determined that the rate of hydrolysis was affected by the incongruent nature of feldspar dissolution processes which are described by: (1) diffusion of species through a precipitated surface layer and (2) later formation of an amorphous phase of a different chemistry. [82] It has since been confirmed that changes in solution composition, which accompany silicate hydrolysis, are consistent with a later formation of a gel layer. [76]

Aagaard and Helgeson suggest sequential changes in the rate of hydrolysis with time can also be attributed to methods of sample preparation. Lagache, Wyart, and Sabatier first suggested surface reactions were the rate-limiting mechanism of feldspar hydrolysis, which led to recognition between the time and surface area dependence for both of the integrated forms of the rate equation for diffusion and surface-reaction control of the kinetics of the hydrolytic processes. [83] However, it has also been shown that stirring decreases the thickness of the boundary at the solution/grain interface, increasing the rate of diffusion. [76]

It is proposed that with a high surface area, surface reactions control the dissolution rate at high stirring rates; however, lowering the stirring rate causes diffusion transfer through the aqueous phases to become rate-limiting. [76] This has been shown for calcite at room temperature and low pressure (1 bar) by Sjöberg, but for silicates the stirring rate is negligible due to the low rate of hydrolysis. [76; 84] Stirring rates will; however, affect the rate of precipitation of reaction products for silicates. [76]

The above has demonstrated that the rate of hydrolysis of silicates is controlled by kinetics of reactions at activated sites and not by diffusion and also that stable or metastable reaction products formed during dissolution of silicates do not form a coherent and continuous layer on the surface of reactant minerals. They do; however, affect the apparent rate of silicate dissolution. [76]

Early work performed by Aagaard and Helgeson derived a general rate equation for mineral dissolution, which was based on activated surface complexes and solution chemistry. [76; 85] Later work, performed by Grambow applied the work by Aagaard and Helgeson to silicate glasses which included steady state chemistry within the reaction zone on the surface of glasses. [76; 85] Grambow's work focused on bulk solution chemistry allowing the use of a reaction path model to calculate pH variations, solution composition and precipitation of solid reaction products as a function of reaction progress. [85] Below is a summary of the derivation of the general rate equation by Aagaard and Helgeson and the application of the rate equation to silicate glasses by Grambow. [76; 85]

2.5.1.1 A General Kinetic Rate Equation of Mineral Corrosion

Transition state theory (TST) is based on chemical equilibrium being maintained from the reactants and activated complexes during any reaction. [76; 86] In TST, the critical complex, which is the decomposition of one activated complex, is rate-limiting. Initially, the rate of dissolution can be described by the concentration of the critical activated complex in the transition state and increases linearly with reaction progress. [76; 85] Near equilibrium, the rate of dissolution is proportional to the overall reaction chemical affinity of the *j*th reaction, A_j (Equation 2.7). In Equation 2.7, dQ_{irrev} is the inexact differential of the heat associated with all irreversible reactions, G is the Gibbs free energy of the system, ξ_i is the extent of the reaction, ξ_k is the constant progress variable for all reactions other than the *j*th reaction, μ_i is the chemical potential of the *i*th species, $\hat{n}_{i,j}$ is the stoichiometric reaction coefficient of the *i*th species in the *j*th reaction, K_j is the equilibrium constant for the *j*th reaction and Q_j corresponds to the reaction quotient. [76; 85]

Equation 2.7
$$A_j = \frac{dQ_{irrev}}{d\xi_j} = -\left(\frac{\delta G}{\delta \xi_j}\right)_{\mathrm{P,T},\xi_k} = -\sum_i \mu_i \hat{n}_{i,j} = RTln\left(K_j/Q_j\right)$$

Equation 2.7 takes into consideration the conservation of mass for stoichiometric reaction coefficients that are independent of reaction progress, pressure, temperature, the total chemical affinity at a given pressure and temperature of hydrolysis of a silicate glass, and the effect of surface area.

The overall dissolution process at constant temperature and pressure can be expressed by, Equation 2.8, where $r_{\phi r}$ is the dissolution rate at constant temperature and pressure, r_j is the total rate of the *j*th elementary step of hydrolysis, and σ_j is the rate of the *j*th intermediate reaction step relative to the overall reaction.

Equation 2.8 $$r_{\phi_r} = r_j/\sigma_j$$

Activated complexes, according to absolute reaction rate theory, form during each step in an irreversible reaction. [76] The activated complexes can be described by a cluster of atoms similar to a known molecule; however, they have a high tendency to dissociate. The dissociation corresponds to the energy of the activated complexes in a transition state at the top of an energy barrier separating the reactants and products. [76; 86] The rate at which this occurs can be calculated from Equation 2.9 where $\vec{r}_j$ is the forward rate of the *j*th elementary reaction in a hydrolytic process, α_j is the transmission coefficient, f is the frequency of dissociation, and $c^{\ddagger}_j$ is the concentration of the *j*th activated complex on the surface of the reactant mineral.

Equation 2.9 $$\vec{r}_j = \alpha_j f c^{\ddagger}_j$$

Assuming each activated complex is in equilibrium with the reactants, Equation 2.9 can be expressed as Equation 2.10, where $\overleftarrow{r}_j$ is the backward rate of the *j*th elementary reaction in a hydrolytic process and A is the chemical affinity of the *j*th elementary reaction.

Equation 2.10 $$\vec{r}_j/\overleftarrow{r}_j = \exp\left(A_j/\mathrm{RT}\right)$$

The addition of the average stoichiometric number (σ) for the overall reaction process as defined by Temkin and given in Equation 2.11 leads to Equation 2.12 where $\vec{r}_{\phi_r}$ is the forward rate of reaction for the ϕ_rth mineral and $\overleftarrow{r}_{\phi_r}$ is the backward rate of reaction for the ϕ_rth mineral. [87; 76]

Equation 2.11 $$\sigma \equiv \frac{\sum_j \sigma_j A_j}{\sum_j A_j} = \frac{A}{\sum_j A_j}$$

Equation 2.12 $$\vec{r}_{\phi_r}/\overleftarrow{r}_{\phi_r} = \exp(A/\sigma\mathrm{RT})$$

The overall reaction rate ($r_{\phi r}$) can also be written as a ratio of the forward and backward rates as given in Equation 2.13, which relates the chemical affinity and the overall rate of reaction and, hence, it constitutes a link between the kinetic and thermodynamic rates.

Equation 2.13 $$r_{\phi_r} = \vec{r}_{\phi_r} - \overleftarrow{r}_{\phi_r} = \vec{r}_{\phi_r}\left(1 - \left(\overleftarrow{r}_{\phi_r}/\vec{r}_{\phi_r}\right)\right) = \vec{r}_{\phi_r}\left(1 - \exp(-A/\sigma\mathrm{RT})\right)$$

Equation 2.13 suggests that near equilibrium the chemical affinity on the reaction rates increases; therefore, becoming rate-limiting. The exponential term in Equation 2.13 can be re-written as Equation 2.14 where $l = 1, 2, 3, \ldots l$.

Equation 2.14 $$\exp(-\mathrm{A}/\sigma\mathrm{RT}) = 1 + \sum_l \frac{(-\mathrm{A}/\sigma\mathrm{RT})^l}{l!}$$

At l = 1, the error for the reactions near equilibrium is negligible leading to the overall reaction rate (combination of Eq. 2.14 at l = 1 and the final term in Eq. 2.13), given in Equation 2.15 where $\vec{r}^*_{\phi_r}$ corresponds to the forward rate of reaction at equilibrium. As equilibrium is approached, the effect of the chemical affinity on the reaction rate increases and becomes rate limiting.

Equation 2.15 $$r_{\phi_r} = \vec{r}^*_{\phi_r}(\mathrm{A}/\sigma\mathrm{RT})$$

For geochemical processes which involve minerals and an aqueous phase, the reaction rate is proportional to the chemical affinity near saturation. Far from saturation, the chemical affinity becomes insignificant and $\overleftarrow{r}_j \gg \vec{r}_j$ for all *j* species, which gives Equation 2.16.

Equation 2.16 $$r_{\phi_r} = \vec{r}_r = \frac{\vec{r}_j}{\sigma_j}$$

If one *j*th reaction becomes rate limiting the chemical affinities of the other reactions become negligible resulting in Equation 2.16 reducing to Equation 2.17. According to reaction rate theory, the rate limiting step in the overall reaction process corresponds to decomposition of the *j*th activated complex. [76]

Equation 2.17 $$r_{\phi_r} = \vec{r}_{\phi_r} = \frac{\alpha_j f c_j^{\ddagger}}{\sigma_j}$$

The formation constant for the *j*th activated complex can be described by Equation 2.18, where $a_j^{\ddagger}$ is the activity of the *j*th activated complex on the surface of reactant mineral, $\gamma_j^{\ddagger}$ is the activity coefficient of the *j*th activated complex on the surface of reactant mineral, a_i is the activity of the *i*th species in the system, $\hat{n}_{i,j}$ is the stoichiometric reaction coefficient of the *i*th reaction representing the reversible formation of the *j*th activated complex, and $K_j^{\ddagger}$ is the equilibrium constant for the reaction.

Equation 2.18 $$a_j^{\ddagger} \prod_i a_i \hat{n}_{i,j} = c_j^{\ddagger} \gamma_j^{\ddagger} \prod_i a_i \hat{n}_{i,j} = K_j^{\ddagger}$$

Since the *j*th elementary reaction step which corresponds to decomposition of the *j*th activated complex is rate limiting, assuming $\gamma_j^{\ddagger}$ is constant, $\sigma_j = \sigma$ and $\Sigma_j A_j = A_j$, Equation 2.18 can be combined with Equation 2.15 to give the general rate equation for hydrolysis of minerals at a constant temperature and pressure, $r_{\phi r}$, as given in Equation 2.19, where $k_{\phi r}$ is the steady state rate constant, $S_{\phi r}$ is the effective surface area, ξ is the overall reaction progress and t is time.

Equation 2.19 $$r_{\phi_r} = k_{\phi_r} \prod_i a_i^{-\hat{n}_{i,j}} \left(1 - exp\left(\frac{-A}{\sigma RT}\right)\right) = \frac{d\xi}{dt} / S_{\phi_r}$$

The steady state rate constant, $k_{\phi r}$, is defined by Equation 2.20 and reduces Equation 2.19 to Equation 2.21.

Equation 2.20 $$k_{\phi_r} = \frac{\alpha_j f K_j^{\ddagger}}{\sigma \gamma_j^{\ddagger}}$$

Equation 2.21 $$\frac{d\xi}{dt} = kS \prod_i a_i^{-\hat{n}_{i,j}} \left(1 - exp\left(\frac{-A}{\sigma RT}\right)\right)$$

Far from equilibrium the chemical affinity is insignificant and, therefore, the general rate equation can be given as Equation 2.22.

Equation 2.22 $$r_{\phi_r} = \vec{r}_{\phi_r} = k_{\phi_r} \prod_i a_i^{-\hat{n}_{i,j}}$$

Near equilibrium, however, the general rate equation reduces to Equation 2.23, where $C_j^{*\ddagger}$ is the equilibrium concentration of the *j*th activated complex on the surface of the reactant mineral.

Equation 2.23 $$r_{\phi_r} = \frac{\alpha_j f C_j^{*\ddagger}}{\sigma}$$

Equations 2.13, 2.15, and 2.19 take into consideration the non-detachment related surface reactions which are analogous to Dibble, and Dibble and Tiller. [88; 89] Dibble and Tiller attempted to couple interface and transport kinetics to incorporate the possible roles from; the fluid boundary layer, electrostatic potential, fluid motion, diffusion transport through the boundary layer, interface attachment, surface reconstruction, layer-edge generation and excess surface energy. [89; 76]

Far from equilibrium, where the degree of interfacial undersaturation is high, the roles of the interface attachment, surface reconstruction, layer-edge generation and excess surface energy have an insignificant effect on dissolution suggesting that early precipitation of reaction products during dissolution prolong interfacial undersaturation. At $T \leq 200$ °C in acidic solutions, diffusion rates in solution are faster than the rates of silicate hydrolysis. In the acidic solutions, transport through the fluid boundary layer has a negligible effect on the rate of hydrolysis; therefore, a small degree of interfacial undersaturation occurs in the vicinity of equilibrium. Assuming the chemical affinities of the non-detachment related reactions on the surfaces of reactant minerals are negligible compared to the chemical affinities of the overall reactions, the rate that a given silicate dissolves in the vicinity of equilibrium is proportional to the chemical affinity of the overall hydrolysis reaction. [76] The

stoichiometry of the activated complex on the reactant surface may be affected by the electrostatic potential in the reaction zone suggesting that Equation 2.23 is only valid if diffusion rates through the reaction zone are faster than the rate of reaction at the activated sites on the surface. (76)

The relative rate at which two minerals react with an aqueous phase can be described by Equation 2.24.

Equation 2.24

$$\frac{r_{\phi r}}{r_{\phi \vec{r}}} = \frac{k_{\phi r} \prod_i a_i^{-\hat{n}_{i,j,r}} \left(1 - exp\left(\frac{-A_r}{\sigma_r RT}\right)\right)}{k_{\phi \vec{r}} \prod_i a_i^{-\hat{n}_{i,j,r}} \left(1 - exp\left(\frac{-A_{\vec{r}}}{\sigma_{\vec{r}} RT}\right)\right)}$$

If the same activated complex controls the dissolution rate of both minerals, Equation 2.24 reduces to Equation 2.25. (76)

Equation 2.25

$$\frac{r_{\phi r}}{r_{\phi \vec{r}}} = \frac{k_{\phi r} \left(1 - exp\left(\frac{-A_r}{\sigma_r RT}\right)\right)}{k_{\phi \vec{r}} \left(1 - exp\left(\frac{-A_{\vec{r}}}{\sigma_{\vec{r}} RT}\right)\right)}$$

Near equilibrium, the relative rate of dissolution is proportional to the ratio of the chemical affinities of the independent overall reactions. (76) Far from equilibrium, the dissolution rate becomes constant as given in Equation 2.26, which is controlled by the same activated complex.

Equation 2.26

$$\frac{r_{\phi r}}{r_{\phi \vec{r}}} = \frac{k_{\phi r}}{k_{\phi \vec{r}}}$$

Aagaard and Helgeson propose that modelling the stoichiometry of the *j*th activated complex for values of $k_{\phi r}$ and $\hat{n}_{i,j}$, suggests that many activated complexes may form, but only the decomposition of the *j*th complex is rate limiting. (76) The identity of the *j*th complex may change as the reaction proceeds and the aqueous solution changes composition.

The configuration and stoichiometry of the *j*th activated complex varies between minerals and the identity of the *j*th complex on the surface may vary under different conditions. Formation of the *j*th activated complex is from H^+, H_3O^+, H_2O, and possibly OH^-. As is internationally accepted, the main mechanism of silicate dissolution are breaking of bridging oxygens to form hydroxyl groups, which are formed by direct action of H^+, or H_3O^+ to form OH^- and the 1:1 reaction of water dipoles with bridging oxygen to form two hydroxyls.

2.5.1.2 Application of the General Rate Equation to Glasses

The general equation of kinetic mineral dissolution derived by Aagaard and Helgeson was applied to silicate glasses by Grambow. [76; 85] In order for dissolution of glasses to take place, complete hydrolysis of Si has to occur and the concentration of the activated complex is, therefore, dependent on the crosslink density of the reaction zone. [85] The interaction of water and the glass matrix in the reaction zone, can be described by two reversible equations and one non-reversible equation; Equations 2.27, 2.28, and 2.29, respectively, where the glass matrix is designated as 'matrix.'

Equation 2.27 matrix + aqueous species ↔ matrix-O-Si(OH)$_3$

Equation 2.28 matrix-O-Si(OH)$_3$ + H_2O ↔ matrix-OH + OH-Si(OH)$_3$

Equation 2.29 matrix-OH + OH-Si(OH)$_3$ → $H_4SiO_{4\,(aq)}$

If there is a large amount of crosslinking within the glass matrix, the more dissolution will tend towards Eq. 2.27. The Gibbs free energy of reaction, $\Delta G_R(\xi)$, can be expressed as Equation 2.30 where Q is the ion activity product in solution at reaction progress ξ, K_L is the solubility product which includes the solid activity of the end member, ϕ, and the activity of water in the reaction zone and ε_ϕ is the stoichiometric sum of the species constituting the mineral and is defined by Equation 2.31. [85]

Equation 2.30
$$\Delta G_{R,\phi}(\xi) = 2.3\ \mathrm{RT}\left(\log\frac{Q_\xi}{K_L} - \varepsilon_\phi \log \xi\right)$$

Equation 2.31
$$\varepsilon_\phi = \sum_i \hat{n}_{i,\xi}$$

The Gibbs free energy of reaction of the glass with the solution, $\Delta G_R(\xi)$, is the sum of the free energy of reaction of the end members of the glass solid solution model and can be expressed as Equation 2.32, where σ is the fraction of the mineral in the solid solution. As $\Delta G_R(\xi)$ becomes dominant, the activity of the surface silanol groups, a_{Sim}, is governed by the Gibbs free energy (Equation 2.33). [85]

Equation 2.32
$$\Delta G_R(\xi) = \sum_\sigma \sigma_\phi \Delta G_{R,\phi}(\xi)$$

Equation 2.33
$$a_{Si_m} = \mathrm{B}\exp\left(\frac{-\Delta G_R(\xi)}{RT}\right)$$

Combining equation 2.33 with 2.19 yields a general rate equation for matrix dissolution, Equation 2.34, which assumes that matrix bound silanol groups and water molecules are the only reactants participating in formation of activated complexes, where $r_m(t)$ is the rate of matrix dissolution, X is a proportionality constant that takes into account entropy of activation, the activity of water and the constant B (Eq 2.33), E_A is the activation energy and A_j is the chemical affinity of the rate limiting reaction and is described by Equation 2.7. [85; 76]

Equation 2.34 $$r_m(t) = \mathrm{X} * \exp\left(\frac{-\Delta G_R(\xi)}{RT}\right) \exp\left(\frac{-E_A}{RT}\right) \left(1 - \exp\left(\frac{-A_j}{RT}\right)\right)$$

At the onset of glass dissolution, far from saturation, A_j is large and the reaction proceeds forward. The continuation of the reaction increases the concentration of silica in solution and decreases the affinity of the rate limiting reaction. [85] For glasses, A_j cannot become zero since saturation only involves reacting surfaces. [85] For a simple silicate glass, the rate limiting reaction can be written as Equation 2.35 where the desorbing silanol group may be bound to another silicon atom on the reacting surface.

Equation 2.35 $$SiO_2 + 2H_2O \rightarrow H_4SiO_4$$

In dilute systems, the activity of water is one and for Equation 2.35, the degree of saturation is described by Equation 2.36, where Q is the ion activity product and K is the equilibrium constant

Equation 2.36 $$\frac{Q}{K} = \frac{a_{H_4SiO_4}}{a_{H_4SiO_4}(sat.)}$$

When transport processes are neglected, silicic acid concentrations in the bulk solution can be used, which allows Equation 2.34 to be reduced to Equation 2.37, where k^+ is the forward rate constant. [85]

Equation 2.37 $$r_m(t) = k^+(\xi)\left(1 - \exp\left(\frac{-A_j}{RT}\right)\right)$$

Combining Equation 2.37 with Equation 2.35 gives the current general rate equation for glass dissolution, Equation 2.38.

Equation 2.38 $$r_m(t) = k^+(\xi)\left(1 - \left(\frac{Q}{K}\right)\right)$$

The reactions of water with an alkali silicate glass is the exchange of alkali ions in the glass with hydronium ions from the water; equations 2.3-2.6. In the case of a soda-lime silica (SLS) glass, the forward reaction of sodium hydroxide dissolving in water increases the

alkalinity and; therefore, the pH of the solution increases. If the volume of the solution is small compared to that of the glass surface area, the pH will increase rapidly.

For a silicate glass, as silicic acid (H_4SiO_4) continues to be formed by breaking the Si-O-Si bonds from interactions with H_2O, the pH of the solution increases and will increase the dissolution rate. If, however, the volume of the solution is low compared to the surface area of glass, the solution becomes saturated with silicic acid and the dissolution rate decreases due to the probability of the Si-O-Si bond being re-established (Figure 2.4). If a phase such as analcime precipitates rapidly, the demand for silicic acid increases and the reaction becomes more irreversible. The more irreversible the reaction, the more the dissolution rate increases due to the ion activity product, Q, as given by Strachan in Equation 2.39;

Equation 2.39 $$k = k_0 10^{\eta pH} e^{-E_a/RT}\left(1 - \frac{Q}{K}\right)$$

Where *k* is the rate of glass dissolution (g m^{-2} d^{-1}), k_0 is the intrinsic rate constant of dissolution (g m^{-2} d^{-1}), η is the power law coefficient for solution pH, E_a is the activation energy (J mol^{-1}), R is the gas constant (J mol^{-1}),), T the temperature (K) and K is the equilibrium constant of the dissolution reaction. [23] If it is assumed a chemical reaction is rate-limiting, the limiting factor in Equation 2.4 involves the breaking of the Si-O-Si bonds and formation of silicic acid. As put by Strachan and Croak ". . . there is always a driving force for the reaction of glass with water, [and] Q can never equal k." [19] The ion activity product, Q is generally given by Equation 2.40;

Equation 2.40 $$\log Q = b_{h_2O}\log_{a_{H_2O}} + b_{O_2}\log f_{O_2} + \sum_{s=1}^{M} b_s \log \gamma_s m_s$$

where b_s is the stoichiometric coefficient, a_{H2O} the activity of water, f_{O2} is the oxygen fugacity, M the number of aqueous species in reaction, γ_s is the activity coefficient of species s, and m_s is the molar concentration of species, s. [19] In dilute solutions, the first two terms of Equation 2.40 become constants, and only H_4SiO_4 is involved in the rate-limiting step for silicate glasses. [19] If H_4SiO_4 formation becomes the rate-limiting step, Q becomes the activity of silicic acid (H_4SiO_4) due to the terms on the left side of Equation 2.40 becoming constants. During the reaction, if Q/K starts to approach one, the probability that the Si-O-Si bond will be re-established will increase and the dissolution rate decreases. [19]

Figure 2.5a shows the total concentration of silica increasing as the reaction continues with a corroding glass. At lower concentrations of cations in solution, secondary phases start to precipitate (Figure 2.5b). At each major slope change in the total Si concentration, a new phase begins to precipitate. When analcime becomes the only Si-bearing precipitating phase the dissolution rate decreases due to the solution becoming saturated with silica. Once the

solution becomes saturated, the Si-O-Si bonds have a higher probability of being re-established.

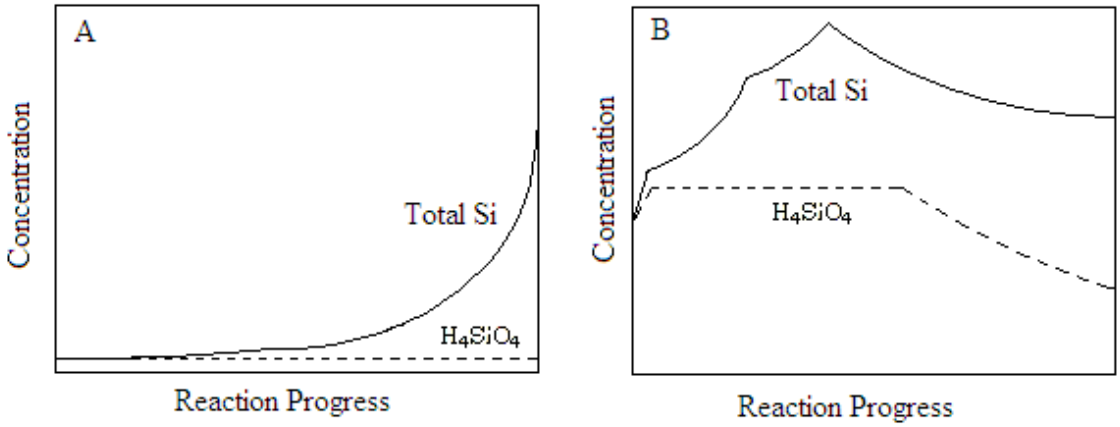

Figure 2.5 A) Concentration of Si in solution from a corroding glass and B) the concentration of Si in solution from a corroding glass which results in changes of H_4SiO_4 concentration. Modelled after Strachan and Croak. [19]

It has been shown, in the presence of clays, the glass dissolution rate increases. [90] This is due to silica in solution being taken up by the clay so that the driving force for dissolution continues. Lemmens suggests the species transferred to the clay such as Si and Al decrease the protectiveness of the gel-layer. [90] This would be due to the gel-layer being deficient in protective species and allowing further diffusion of these species out of the bulk glass. Conclusions from the work of Lemmens are that clay will initially delay the reduction in the dissolution rate, however, a decrease in the corrosion rate to very low long-term rates have been observed which can be attributed to the high concentrations of silica in the interstitial solution between the clay and the bulk glass. [90]

It has been shown that in a simulated Magnox nuclear waste glass the dissolution rate is dependent on both silicic acid and species of Al in solution. [15] Abraitis *et al.* suggested for systems with a low Al species activity, glass dissolution decreases as the activity of Si species increases to saturation and that removal of Al by formation of secondary phases gives rise to a decrease in saturation limits for Al with respect to the glass. [16] Abraitis *et al.* also suggest that the formation of surface gels may function as a transport barrier which could moderate the rate of dissolution. [16]

2.6 Alteration Product and Gel-layer Formation

Early studies of natural analogues to nuclear waste glasses, such as basaltic glasses have shown formation of alteration layers on the surface. [91] These alteration products, or gel-layers, are in general, a result of water permeation and alkali interdiffusion formed by a process of co-precipitation of dissolved elements from the glass. [91; 92] Studies of the French SON68 glass, a R7T7-type nuclear glass, have observed formation of alteration products on the surface, similar to that formed on the natural analogues. [92]

Formation of the gel-layer occurs after interdiffusion of the alkali cations in the surface of the glass. [92] At short times, after formation of the interdiffusion layer, a collapsed gel with a density similar to that of the glass without alkaline elements is formed. This is followed by formation of a homogeneous gel-layer on the surface of the glass. At longer times, a gradient in the density of the alteration layer has been observed. [92] Observations by Cailleteau *et al.* suggest similar results as Rebiscoul *et al.* where the density of the gel-layer decreases with time. [92; 12] Cailleteau *et al.* propose that insoluble oxides in the glass, such as ZrO_2, prevent reorganization of the alteration layer, which inhibits pore ripening leading to higher corrosion rates. [12]

It has been suggested that the decrease in the dissolution rate at longer times is attributed, in part, to the formation of alteration products on the surface of the glass. [93] Advocat *et al.* have observed a decrease in the dissolution rate for both radioactive and non-radioactive glasses; however, they observed a significantly different behaviour between the active and inactive glasses with similar compositions. [94] The radioactive glass at short times resulted in a higher dissolution rate than the non-radioactive glass. The formation of a gel-layer was observed in both glasses; however, the alteration layer on the active glass was not as protective. It is suggested that the gel-layer on the surface of the radioactive glass is less protective due to a difference in the microstructure allowing enhanced diffusion as compared to the non-radioactive glass. [94]

Several studies have shown changes in the dissolution rate with the formation of a gel-layer on the surface of the glass samples. [90; 93; 92; 12] Contrasting studies suggest either the alteration layer on the surface, or saturation effects in the solution are responsible for the decrease in the corrosion rate. Xing *et al.* suggest that there is a large range of glass composition that vary in corrosion rates and thicknesses of the gel-layer and that the reaction rate is strongly affected by the formation of the gel-layer. [13] Experimental results from Gin indicate that the gel-layer formed under saturation conditions controls the kinetics of glass

alteration. [95] Contrasting results by Advocat *et al.* suggest the alteration products do not constitute a short-term kinetic barrier. [96]

Early results from the vapour phase hydration tests (VHT) of the Magnox waste glasses by Hyatt *et al.* indicate that the durability, according to the generalised Avrami equation, is less than that of the French SON68 glass. [97] Further VHT experiments on a blended Oxide / Magnox simulant HLW glass exhibited similar results where the thickness of the alteration layer were several orders of magnitude greater than that of the French SON68 glass after 21 days in a humid environment at 200 °C. [98]

2.7 Current State of Knowledge Regarding HLW Glass Dissolution

Currently, there are several countries considering vitrification to immobilise spent fuel from the civil nuclear industry and also from the weapons programs. [99] These countries are the UK, USA, France, Russia, Belgium, Germany and Japan. As mentioned previously, glass is a suitable host matrix due to the ability to accommodate a wide range of waste compositions while sustaining a suitable durability. The base glass used for vitrification is a borosilicate with a waste loadings ranging from a few weight percent up to greater than 20 weight percent depending on the composition of the waste added to the base glass. [99]

2.7.1 International Understanding of HLW Glass Corrosion

Several studies have been performed on silicate glasses in order to understand the general dissolution kinetics of nuclear waste glasses. This has been achieved using both static and flow through tests. Earlier studies by Vernaz *et al.* have shown that the final corrosion rate decreases from 83 x 10^{-4} g m^{-2} d^{-1} to much less than 3 x 10^{-4} g m^{-2} d^{-1} in solutions at 90 ° as the surface area to volume (SA/V) ratio increases. [100] It was suggested by Grambow that ". . . a slight difference in the chemical potential between the hydrated gel and a gel formed under saturation conditions maintains a residual affinity for the dissolution reaction." [9; 101] It was later suggested by Vernaz and Dussossoy that the final rate of dissolution is only affected by precipitation of silicate phases which renew corrosion by diminishing the activity of silicic acid. [9]

Early work has suggested 5 regions of glass dissolution; initial diffusion or interdiffusion, initial or forward rate, a decrease in the initial rate, the residual rate, and precipitation of

alteration phases. [102] These regions are illustrated in Figure 2.5 which represents the concentration of ions in solution with time.

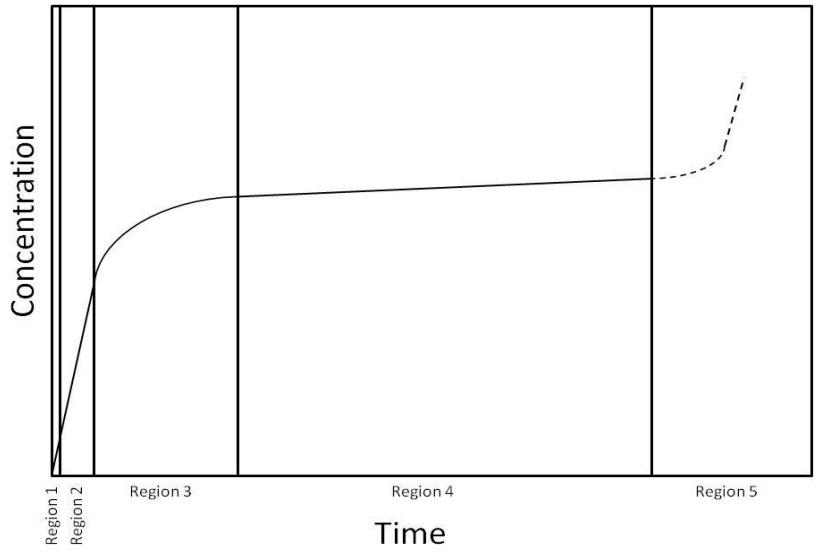

Figure 2.5 The 5 regions of dissolution for a silicate glass.

As mentioned previously in section 2.5, interdiffusion is the ion exchange process between the modifier cations in the glass network and protons in solution. Recent work on silicate glasses have proposed that the dissolution of these glasses can be characterised by the immediate release of boron in solution following the inverse √t, where t is time, when leaching in solutions saturated in silica in order to prevent region 1 of glass dissolution. [103; 104]

The second region, the forward rate, is from hydrolysis of the glass network forming cations and breaking the bridging oxygen bonds in the inter-phase which were created from the exchange of the mobile glass modifiers.‡ The layer formed during region 1 quickly reaches a constant thickness under the initial dissolution rate, which depends on the temperature and pH of the solution and the composition of the glass. Oelkers suggests the initial dissolution rate depends on the concentration of aluminium and iron in solution, while others suggests ions can catalyze or inhibit the corrosion kinetics. [105; 106] Several models on the initial dissolution rate have been made in order to relate the initial dissolution rate to various structural properties of the glass. These models are based on thermodynamics of the free enthalpy of glass hydration and the standard enthalpy of formation of the oxide. [102]

‡ See section 2.5 for a basic review on silicate glass network hydrolysis.

The third region occurs when the concentration of silicon in solution reaches saturation and then begins to condense to form a gel layer on the surface of the pristine glass. Previously, there have been two approaches to account for the decrease in the initial dissolution rate (region 3); one based on a passivating effect on the gel layer, and the other based on the chemical affinity with respect to the pristine glass. [107; 108] Early work on the dissolution rate, as reviewed in section 2.5, was based on mechanistic models from Aagaard and Helgeson and later modified for glasses by Grambow. [76; 85] However, it has recently been established that the decrease in the dissolution rate (region 3) is attributed to the effects of the affinity and passivation of the gel layer.

The residual rate (region 4) differs between a closed and open system. In a closed system, the alteration kinetics decrease over an extended time and become linear, however, in an open or reactive system, the residual rate depends on the near field materials, diffusion elements, and on the solution chemistry. In the case of nuclear waste glasses, the residual rate is generally referred to as the long term dissolution rate in a geological repository taking into account the effects of hydrolysis and condensation mechanisms.

The large increase in concentration after the residual rate of dissolution is defined as a resumption of alteration, or precipitation of secondary phases (region 5). The difference between region 2 and region 5 is that in region 5 precipitation occurs rapidly after extended times. As suggested by Frugier *et al.*, region 5 is kinetically limited or highly activated when either the pH or an activity threshold is exceeded in the solution. [102]

The French have observed several different amorphous phases in their simulated waste glass, SON68, after corrosion. These regions, as shown in Figure 2.6, are an amorphous layer consisting of a water interdiffusion region, a hydrated glass region, a zone of proton/alkali ion exchange, a passive reactive interphase (PRI), and a depleted gel. [102]

The first layer in the amorphous phase on the pristine glass after dissolution is from interdiffusion of water and solvated ions and is known as a hydration layer. The second layer is the exchange reaction between the protons and the alkali and alkaline earth ions in the glass that follows hydration of the surface of the pristine glass. The third layer, the PRI, occurs when the solution becomes saturated and all the alteration layer forming elements are preserved. This layer can be characterised by a concentration gradient for the mobile elements such as boron and for the elements such as zinc which limit the formation of crystalline phases. A depleted gel is finally formed on the surface and occurs when the glass is significantly altered.

Recent work on the dissolution kinetics of glass by Frugier *et al*. have suggested a mechanistic model known as the glass reactivity with allowance for the alteration layer, or

the GRAAL model. [102; 109] As given in the name, this model takes into account the alteration layers formed during dissolution of the glass network. The GRAAL model is based on simplified hypothesis along with predominant dissolution mechanisms that have been identified.

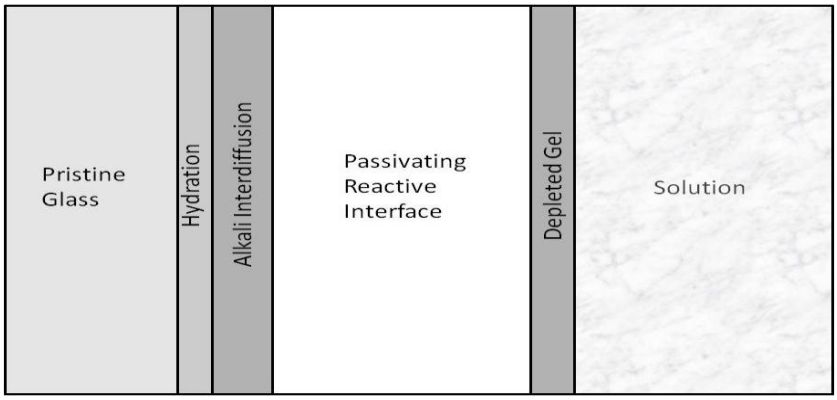

Figure 2.6 The amorphous layers on SON68 after corrosion. Figure modelled after Frugier *et al.* [102]

The simplified hypotheses of the GRAAL model are that only water diffusion in the PRI is considered to be the rate-limiting factor, the hydration, alkali interdiffusion and depleted gel layers are ignored and the reactivity of the PRI with the leaching solution is described through thermodynamic equilibrium. [109] Currently, the GRAAL model is available in two forms, an analytical GRAAL and a geochemical GRAAL. The analytical GRAAL is a solution with very simplified chemistry suitable for sensitive calculations. Currently, only silicon and boron are specifically described. [102] The geochemical GRAAL is a numerical solution using a geochemical calculation code. It will provide a chemical description such as the pH and speciation in potentially complicated geometry and possibly with materials other than glass. [109]

Frugier *et al.* propose that the GRAAL modelling is valid for any surface area to volume (SA/V) and flow rate per surface area (Q/S) ratio for different experimental geometries. [109] It is also suggested that the current models do not account for the SA/V effect without modifying their parameter values, however, the GRAAL model results by Frugier *et. al.* have shown when the element speciation in solution and with an allowance for ion diffusion in the PRI that a simple hypothesis is sufficient to explain the effects with a set of single parameters. [109]

2.7.2 Current State of UK HLW Glass Dissolution Understanding

Currently, there is little known about the dissolution of UK HLW glasses. Some of the most current work on the UK HLW glasses has been performed by Abraitis, Abraitis *et al.* and Hyatt *et al.* on the dissolution and alteration layers of the Magnox waste glasses. [14; 15; 16; 110; 97; 98; 111] Little work has been performed on the dissolution of the blended waste (25 wt% Magnox waste and 75 wt% ThORP waste) HLW glasses; however, Hyatt *et al.* have looked at the alteration phases which form at high temperature. [98]

Initial work by Abraitis *et al.* on the Magnox UK HLW glass suggests that there are different mechanisms that govern the glass dissolution. [110] It was observed that at in the absence of buffers, the dissolution rates are lower than the dissolution rate in buffered solutions during short term experiments. It was also proposed that the dissolution of glass at low pH occurs by a proton-promoted process, which leads to a selective release of boron and network modifiers and the formation of a gel layer rich in silicon. At high pH levels, the release of soluble components in the glass have been shown to occur in approximately equal molar proportions, which result in an apparent congruent dissolution. [110]

Later work by Abraitis *et al.* use static leach tests in order to observe the effect of silicic acid, aluminate ion activity and hydro-silicate gel development on the dissolution rate of UK HLW glass. [16] It was shown that the dissolution rate of a Magnox HLW glass that the dissolution rate is dependent on both the silicic acid activity and the aqueous aluminate species.

Abraitis *et al*. go on to study the kinetics and mechanisms of UK HLW glass dissolution. They conclude that there are pH and temperature dependent molecular processes that govern the Magnox HLW glass dissolution. [15] This is in agreement with their earlier work where they suggest two mechanisms for the corrosion of a Magnox waste glass; a selective release of boron at low and intermediate pH levels, and congruent dissolution in alkaline solutions. [110; 15]

Continuing work by Abraitis *et al.* proposes that aluminium in solution has a more significant influence than silicon in solution on the corrosion rate. [111] It is suggested that the solubility of aluminium is limited due to the formation of alteration layers and this gives an indication there are processes which will influence the solubility or speciation of aluminium leading to an influence in the dissolution of the Magnox HLW glass. [111]

Dissolution of Magnox HLW glass at high temperatures in order to study the crystallisation under deep borehole disposal conditions was performed by Hyatt *et al.* [112] Conclusions suggest that there is partial crystallisation of the Magnox HLW glass; however, it does not impose any detriment to the disposal of HLW glasses *via* this disposal scheme as long as there is no infiltration of hydrous fluids. [112]

Studies using the vapour hydration test (VHT) in order to analyze the alteration layers which form on the surface of the glass were performed on both the Magnox waste glass and a blended Oxide / Magnox waste glass by Hyatt *et al.* [97; 98] It was found that within the alteration layer of both glasses, there is a distribution of elements in the gel layer from the pristine glass. On the Magnox waste glass, a magnesium sodium aluminosilicate phase formed which does not form on the French waste glass, SON68.

From the literature review above, it can be deduced that there is still much needed work in the area of nuclear waste glass dissolution; both for prediction of the overall dissolution rate, but also in understanding the thermodynamic and/or kinetic mechanisms in which glass corrodes. The work presented below will help to understand the mechanisms of current UK simulated HLW glass dissolution by using static and flow through dissolution experiments. It will also help to underpin the role of zinc in increasing durability of these glasses.

One of the concepts currently being considered for disposal of the UK nuclear waste glasses is in a co-located geological disposal facility (GDF) where ILW will be placed in a hyper alkaline backfill. The resulting phase may encounter regions of the GDF containing HLW vitrified wasteforms. Few studies have been performed on UK simulated HLW waste glasses in hyper alkaline solutions giving rise for the need to understand the rate and mechanisms that the UK HLW glasses corrode. Part of this Thesis aims to understand some of the dissolution mechanisms of simulated UK nuclear waste glasses under hyper alkaline environments.

The Nuclear Decommissioning Authority (NDA) strategic priorities include the development of waste solutions and final disposal of radioactive wastes. [113] The NDA also carries out activities and research to support the development of waste solutions. [113] The Radioactive Waste Management Directorate (RWMD), which is part of the NDA, was put together to deliver a GDF and provide radioactive waste management solutions. [113] Both the NDA and RWMD strategy has detailed concepts regarding a GDF which will is currently considered to host all of the wastes and materials in the baseline inventory and what type of environments are expected for a co-located disposal site. [5; 4]

Previous work on dissolution mechanisms of ILW glass in high pH solutions by SERCO show the dissolution rate of simulant ILW glass is lower in alkaline solutions as compared to neutral solutions. [114] It is believed that a protective layer forms on the surface of the glass (alteration layer formation) reducing the forward rate of dissolution of the glass. The final chapter gives results from a study on the mechanisms of alteration layer formation in order to understand how an alteration layer may decrease the forward rate of dissolution.

3.0 Experimental Techniques

3.1 Preparation of Glasses

All glasses were prepared, in general, by batching, mixing, melting, casting, and then annealing. Batch constituents were either from raw oxides measured out and mixed, or from a supplied simulated waste calcine and a base glass frit from the National Nuclear Laboratory, which is similar in composition to what is currently in use at the research melter at Sellafield, UK. Nominal compositions of the glasses used for experiments in the work presented in later chapters are given in Table 3.1. Compositions of each glass were analysed using inductively coupled plasma (ICP) and X-ray fluoresence (XRF) spectroscopic methods by the Sheffield Assay Office in Sheffield, UK.

Table 3.1 Nominal glass compositions in wt% of all glasses used for experiments in this thesis.

Oxide	NCZS 3	NCZS 3.5	NCZS 4	NCZS 5	CaZn Base	MW Base	FeZnZr	CaZn Magnox	CaZn Blend	MW Magnox	MW 25 Blend	MW 30 Blend
SiO_2	45.40	44.00	42.60	60.00	55.92	61.70	49.47	44.26	45.42	45.28	46.28	44.10
B_2O_3					22.68	21.90	17.56	17.95	18.42	16.43	16.43	14.24
Na_2O	23.40	22.60	21.40	20.00	11.38	11.10	8.90	9.01	9.24	8.33	8.33	7.22
CaO	23.20	22.40	21.50		1.76			1.39	1.43			
ZnO	8.00	11.00	14.50	20.00	5.60		3.08	4.43	4.55			
Li_2O					2.67	5.30	4.25	2.11	2.17	3.98	3.98	3.45
Al_2O_3								4.11	1.49	4.86	1.91	2.67
BaO								0.40	0.34	0.40	0.47	0.66
CeO_2								0.96	1.12	2.25	1.45	2.03
Cr_2O_3								0.63	0.41	0.68	0.51	0.71
Cs_2O								0.89	1.33	1.17	1.59	2.23
Fe_2O_3							12.08	2.79	1.68	3.15	2.06	2.88
Gd_2O_3								0.06	3.29	0.12	4.16	5.82
La_2O_3								0.52	0.55	0.66	0.73	1.02
MgO								4.10	1.21	5.05	1.61	2.25
MoO_3								1.32	1.77	1.52	2.49	3.49
Nd_2O_3								1.53	1.71	1.94	2.17	3.04
NiO								0.39	0.27	0.45	0.34	0.48
Pr_2O_3								0.52	0.52	0.61	0.66	0.92
RuO_2								0.52	0.00	0.42	0.55	0.77
Sm_2O_3								0.32	0.38	0.43	0.49	0.69
SrO								0.24	0.27	0.31	0.41	0.57
TeO_2								0.15	0.21	0.18	0.28	0.39
Y_2O_3								0.16	0.24	0.20	0.31	0.43
ZrO_2							4.66	1.24	1.96	1.59	2.82	3.95
Total	100.0	100.0	100.0	100.0	100.0	100.0	100.0	100.0	100.0	100.0	100.0	100.0

Batching of NCZS 3, NCZS 3.5, NCZS 4, NCZS 5, and the FeZnZr irradiation glasses were prepared by measuring out the raw chemicals (oxides, and carbonates), from Alpha Aesar at 99.9% purity, to specified amounts and mixing for approximately 2 min. After mixing, half of the batch was added to a platinum crucible, which was then placed in the

furnace for melting. Once the batch in the Pt crucible was melted (after ~10 min.), the Pt crucible was charged with the rest of the batch. Charging of the batch is performed in order to keep the batch from foaming over the top of the crucible, damaging the furnace, and having to re-melt the batch due to a large change from the nominal composition. After the final charge of batch to the Pt crucible, the batch was melted for 1 h before a Pt stirrer was inserted into the melt and the melt stirred for 3 h at 60 rpm. After stirring, the stirrer was removed and allowed to rest above the melt for ~10 min in order for any melt from the stirrer to drip back into the melt. The melt was then removed and cast into a block using a pre heated stainless steel mould and allowed to cool until the melt would not flow. Once cooled, it was placed into an annealing oven at 500 °C for 1 h and then the oven was cooled at 1 °C min^{-1} to room temperature.

The simulated high level waste (HLW) glasses; CaZn Base, CaZn Magnox, CaZn Blend, MW Base, MW Magnox, MW 25 Blend, and MW 30 Blend, were all melted using mullite crucibles. This was performed due to several oxides of the simulated waste can oxidise the Pt crucible which produces holes allowing the melt to flow out of the crucible and onto the floor of the furnace. Although melting in mullite crucibles introduces small amounts of SiO_2 and Al_2O_3 into the melt from corrosion of the crucible during melting, these amounts were taken into account during melting and, hence, one of the reasons for analysing the composition of the glass after melting.

All the glasses, with the exception of the NCZS series of glasses were melted at 1060 °C. The NCZS series glasses were all melted at 1200 °C. The batch was melted for 1 h without stirring (batch free), and then stirred for three hours with either a Pt stirrer, or a mullite stirrer. The stirrer used depended on the type of crucible used. If a Pt crucible was used, a Pt stirrer was then used to stir the melt. If a mullite crucible was used for melting the glass, a mullite stirrer was used to stir the melt.

All glasses were annealed at 500 °C in order to relieve any stresses in the glass. Sci-Glass was used to find a suitable annealing temperature for all the glasses made. [115] Annealing was performed for fabrication of monoliths of the glass sample. If the glasses were not annealed, the glass could fracture during processing of the samples.

3.1.1 Fabrication of Glass Powder and Monoliths

Preparation of glass powder for both X-ray spectroscopic measurements and durability tests was performed by crushing the annealed glass samples with a stainless steel percussion mortar. After crushing, the glass powder was size fractioned using a stainless steel sieve.

For X-ray spectroscopic measurements, glass powder less than 75 μm (-100 mesh) were collected. Due to small fragments of stainless steel in the glass powder from the percussion mortar, a magnet was passed through the powder for approximately 3 min to collect magnetic particles from the glass powder.

Glass monoliths were prepared by cutting the annealed glass blocks with a diamond impregnated blade in an Isomet low speed saw (Model #111280). The speed was set to speed 8 and approximately 75 g of mass was placed on top of the cantilever to give a small amount of pressure on the sample against the blade. If too much mass is used on top of the cantilever, the pressure against the blade will cause the blade to warp and possibly catastrophically fail.

3.2 X-ray Spectroscopy

3.2.1 X-ray Absorption Spectroscopy

X-ray Absorption Spectroscopy (XAS) is a useful technique to attain detailed information on non-periodic systems such as the co-ordination environment of a core atom, atom types, and contact distances to neighbouring atoms. XAS covers both XANES (X-ray Absorption Near Edge Spectroscopy), which is approximately 100 eV below the absorption edge to 100 eV above the absorption edge, and XAFS (X-ray Absorption Fine Structure), which encompasses XANES data up to 800 eV above the absorption edge.

XAS is the modulation of the X-ray absorption coefficient at energies just below and above the absorption edge. As the energy of the X-ray bombarding the sample is increased, the energy at which the X-ray becomes absorbed is known as the absorption edge and gives rise to the large peak in the XAS spectrum as seen in Figure 3.1.

X-ray absorption occurs when an X-ray is absorbed by an atom and ejects a core-level electron into the continuum, leaving the atom in an excited state. After excitation, an electron from a higher energy will ‘relax’ to fill the core hole releasing either a fluorescent X-ray, or an Auger electron. X-ray fluorescence and Auger emission occurs at discrete energies depending on the absorbing atom and is used to identify the atom of interest.

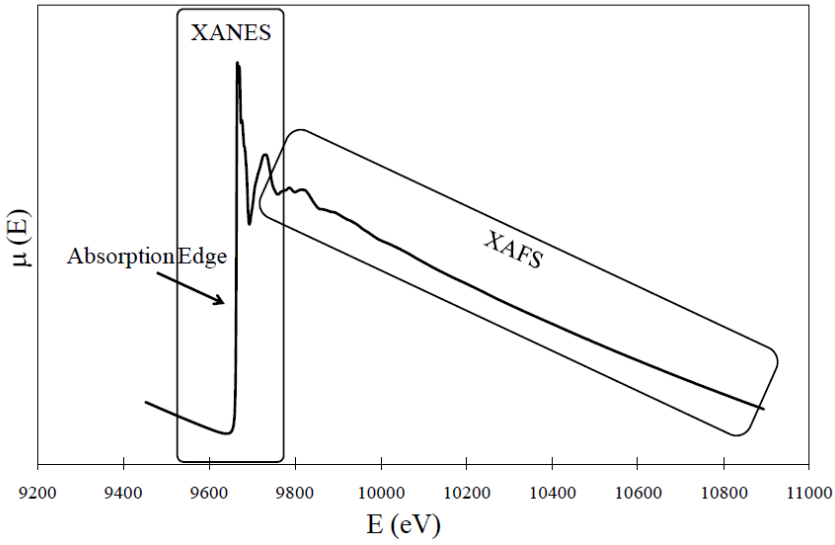

Figure 3.1 Zn K-edge XAS spectrum of hemimorphite, a natural mineral with the composition, $Zn_4Si_2O_7{\bullet}H_2O$. Both XANES and XAFS regions are circled and the absorption edge is labelled.

Generally, XAS measurements are performed at a synchrotron with the use of mirrors and monochromators to measure the XAS spectrum from below to above the selected absorption edge of the absorbing atom. In the case of Figure 3.1, the Zn K-edge energy of 9659 eV is the absorption edge. The spectrum can be gathered in one of two ways: transmission or fluorescence. In transmission mode, the intensity of the transmitted beam is measured (Equation 3.1), while in fluorescence mode, the intensity of released X-rays from secondary X-ray emission is measured (Equation 3.2).

Equation 3.1 $\mu(E)\, t = -\ln(I_t/I_0)$

where I_t is the transmitted beam intensity, I_0 is the initial beam intensity, and t is thickness of the sample.

Equation 3.2 $\mu(E) \approx I_f / I_0$

where I_f is the fluorescence intensity off of the sample.

The absorption coefficient is strongly related to the core-level energies of the absorbing atom and, therefore, information on the absorbing atom can be obtained. The energy dependent oscillations in μ(E) can be described by X-ray energy, or the interference effect with respect to energy (χ(E)), Equation 3.3,

Equation 3.3 $$\chi(E) = \frac{\mu(E) - \mu_0(E)}{\Delta\mu_0(E)}$$

where $\mu_0(E)$ is the bare atom background energy, and $\Delta\mu_0(E)$ is the edge step. This normalises the oscillations in the XAFS signal to one absorption event. In order to model the XAFS signal, it is useful to express the interference effect, χ, in terms of the photo-electron wave number, *k*, which is described by Equation 3.4.

Equation 3.4

$$k = \sqrt{\frac{2m(E-E_0)}{\hbar^2}}$$

where *m* is the mass of the electron, ħ is Planck's constant, and $(E - E_0)$ is energy.

The photo-electron wave number, *k*, can be thought of in terms of an outgoing wave propagating away from the core atom and interacting with neighbouring atoms which reflect the photo-electron wave back towards the core atom.

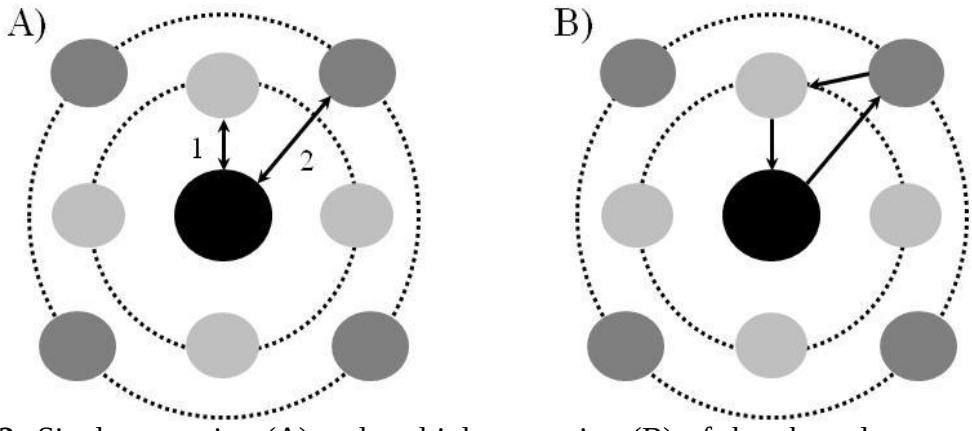

Figure 3.2 Single scattering (A) and multiple scattering (B) of the photoelectron spherical wave from the absorbing atom with the next nearest atom. For the closest scattering the label 1 represents the closest shell and the label 2 represents a further shell. The black sphere represents the core atom, the light grey spheres represent the first nearest neighbouring atoms, and the dark grey spheres represent the second nearest neighbouring atoms.

Figure 3.2 illustrates a representation of a core atom with a photo-electron wave propagating out and interacting with neighbouring atoms. The wave is reflected back either by single scattering, or multiple scattering. Single scattering, as shown in Figure 3.2 A, occurs when the photo-electron wave is reflected straight back to the core atom. Multiple scattering, as given in Figure 3.2 B, occurs when the reflected photo-electron wave interacts with a neighbouring atom before being reflected back to the core atom. The oscillations in the XAFS signal occur from constructive (a maximum in the spectra) and destructive (a minimum in the spectrum) interference from the outgoing and reflected photo-electron waves.

The XAFS equation is written in terms of the sum of all the contributing photo-electron waves, or scattering paths. The probability of X-ray absorption is determined by the interference of the outgoing and backscattered wave, and thus, the absorption coefficient ($\chi(k)$) can be expressed as Equation 3.5.

Equation 3.5 $$\chi(k) = \sum_i \chi_i(k)$$

where $\chi_i(k)$ is a single photo-electron wave.

Each of the photo-electron waves, can be described by Equation 3.6,

Equation 3.6 $$\chi_i(k) = \frac{(N_i S_0^2) F_{eff_i}(k)}{kR_i} sin[2kR_i + \varphi_i(k)] e^{-2\sigma_i^2 k^2} e^{\frac{-2R_i}{\lambda(k)}}$$

where N_i is the number of co-ordinating atoms within a particular shell, S_0^2 is the passive electron reduction factor, $F_{effi}(k)$ is the effective scattering amplitude, $\varphi_i(k)$ is the phase shift of the photo-electron, σ_i^2 is the thermal and static disorder, and $\lambda(k)$ is the mean free path of the photo-electron. R_i is the distance to neighbouring atoms and is described by Equation 3.7,

Equation 3.7 $$R_i = R_{0i} + \Delta R_i$$

where ΔR_i represents a change to the interatomic distance relative to the initial distance to the neighbouring atom, R_{0i}.

Both N_i and S_0^2 modify the amplitude of the XAFS signal. N_i represents the co-ordination number for a particular shell of atoms for single scattering events. If multiple scattering occurs, N_i represents the number of identical paths. The passive electron reduction factor, S_0^2, accounts for the presence of a core hole which has been vacated by the photo-electron. Typical values of S_0^2 are between 0.7 and 1.0. [116] The effective scattering amplitude, $F_{effi}(k)$, accounts for the element sensitivity in the XAFS signal. For single scattering paths, it is the atomic scattering factor; however, for multiple scattering paths, it is an effective scattering amplitude in terms of a single scattering formalism. The oscillation wavelength is accounted for by the term, $\sin[2kR_i + \varphi_i(k)]$. The phase is determined by the path of the photo-electron, R_i, and its wave vector, k. The phase shift of the photo-electron caused by the interaction between the photo-electron of the nuclei of the absorbing atom and co-ordinating atoms of the photo-electron path is $\varphi_i(k)$. Static (structural heterogeneity) and dynamic (thermal) disorder are taken into account by the term, $\exp[-2\sigma_i^2 k^2]$, where σ^2 takes into account the disorder in the interatomic distances between the absorbing and the co-ordinating atoms. The distance that a photo-electron travels before scattering in-elastically and before a core hole is

filled, is the mean free path of the photo-electron, $\lambda(k)$. The mean free path of the photo-electron is accounted for in the term, $\exp[-2R_i / \lambda(k]$, and is the reason why the XAFS signal is dominated by the scattering contributions from atoms within approximately 10 Å of the absorbing atom.

3.2.1.2 XAS Experimental Setup

Data collected for this work was performed at a variety of synchrotron beam lines; BL 11.1 X-ray Absorption Fine Structure at ELETTRA, X23A2 of the National Synchrotron Light Source, B18 at the Diamond Light Source, and KMC-2 at the Helmholtz-Zentrum Berline Fur Materialien und Energie HZB on the third generation synchrotron source, BESSY II.

A general beam line set up from the synchrotron source is illustrated in Figure 3.3. The high energy X-rays travel from the source to the monochromator, which scans the energy of the X-rays between the desired energies, through slits to the first ion chamber which measures the intensity of the incident beam. The sample is placed between the first ion chamber, a second ion chamber which measures the transmitted X-rays and also a fluorescence ion chamber generally situated at 45 ° to the face of the sample.

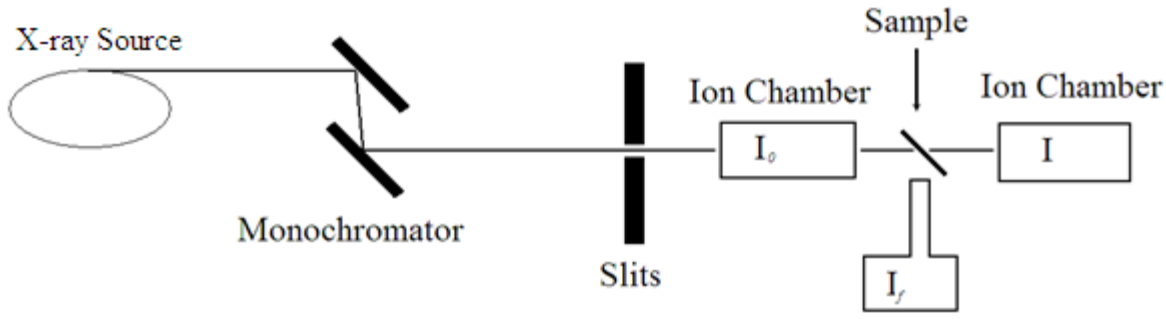

Figure 3.3 A general XAS experimental setup from the synchrotron source through to the ionisation chambers.

All beam lines utilised for the work presented in later chapters utilised a Si(311) double crystal monochromator that was detuned for harmonic rejection. The K-edge of interest was calibrated *in situ* using a metal foil for the energy of interest placed in front of a reference ion chamber. Data was acquired in both transmission and fluorescence mode at room temperature. Generally, unless otherwise specified in later chapters, finely ground samples of glass powder (< 75 μm particles) were used and dispersed in poly-ethyl-glycol (PEG) to

achieve one absorption length and then pressed into 13 mm diameter pellets using a stainless steel uni-axial hydraulic press. The pellets improve sample homogeneity and therefore, improve data quality and reliability. The *k*-range normally scanned during acquisition was typically 3 $Å^{-1}$ to 18 $Å^{-1}$.

3.2.1.3 XAS Data Analysis

Data acquired in this work was analysed using the programs Athena and Artemis in the IFEFFIT package. [117] Normalisation of the measured absorption spectra performed in Athena of the data given in Figure 3.1 is shown in Figure 3.4. This is performed by accounting for the effects of concentration of the absorber element, sample preparation, sample thickness, and response of the detectors (ion chambers).

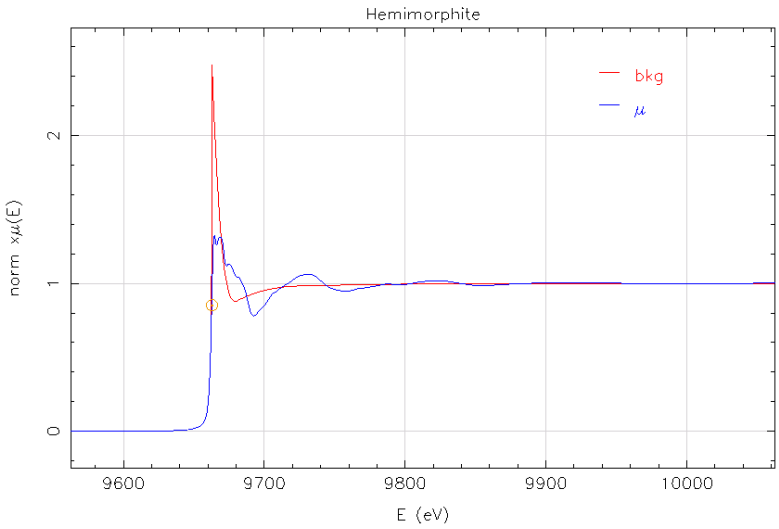

Figure 3.4 Normalised Zn K-edge XAS signal of Hemimorphite (blue) and the subtracted background (red) as performed in Athena of the IFEFFIT package. [117]

As shown earlier, Figure 3.1 is a K-edge spectra obtained for hemimorphite. After normalisation, Figure 3.4, the resulting XAFS spectra, $\chi(k)$, can be plotted as given in Figure 3.5. The Fourier transform (FT) from the data in Figure 3.5 is written as FT $[k^x \chi(k)]$, which indicates a multiplication of *k* by a weighting of x. A multiplication of *k* is performed on the data due to the dependence of *k* on the mean free path of the photo-electron, $\lambda(k)$. The mean free path of the photo-electron decreases from ~15 $Å^{-1}$ to a minimum at short wave

numbers of ~1 Å^{-1}, and then increases up to ~30 Å^{-1} at a wave number of 15 Å^{-1}. This causes the XAFS signal to be a local structural probe.

Figure 3.6 illustrates the FT [k^3 $\chi(k)$] for the Zn K-edge of hemimorphite. As mentioned earlier, the XAFS equation is the sum of the photo-electron waves, or scattering paths. Fitting the $\chi(k)$ data collected for work in this thesis was performed using Artemis in the IFEFFIT package utilising single and multiple scattering paths. As shown in Figure 3.5 and 3.6, the fitted spectrum was performed using several single scattering paths; a Zn-O path, three Zn-Si paths, and three Zn-Zn paths.

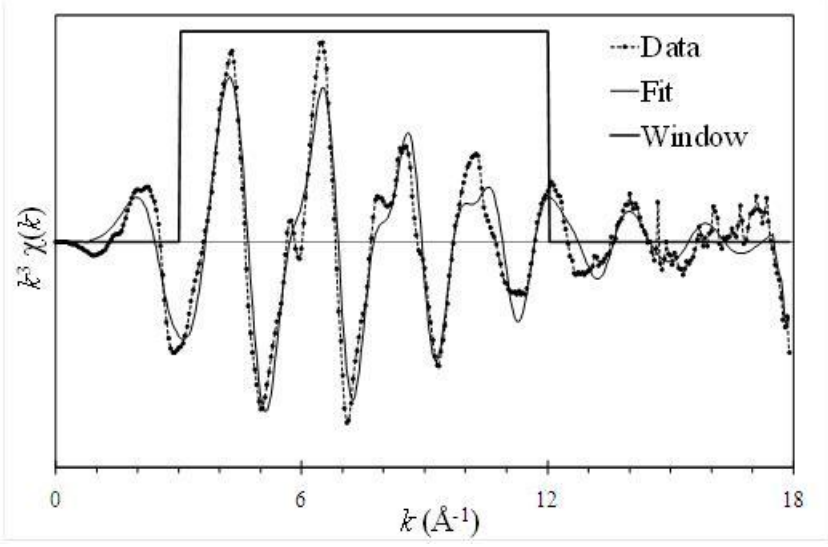

Figure 3.5 As obtained Zn K-edge $\chi(k)$ spectra (dotted) and fitted spectra (solid) of hemimorphite.

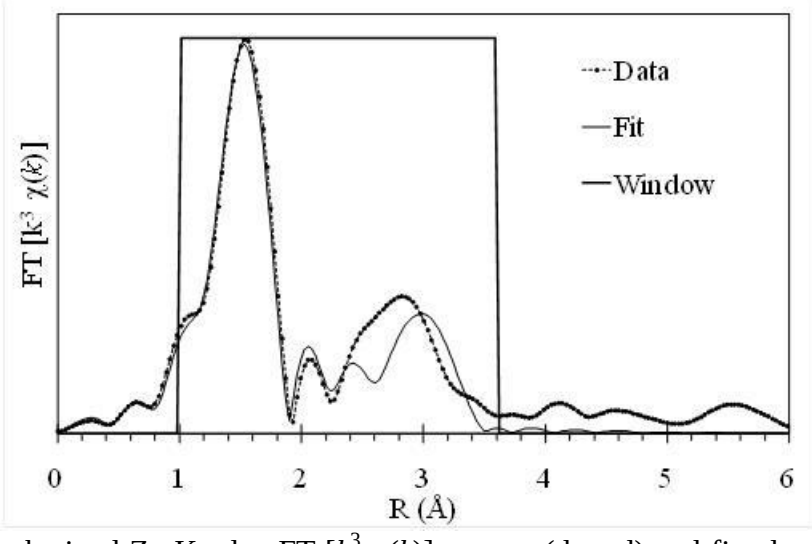

Figure 3.6 As obtained Zn K-edge FT [k^3 $\chi(k)$] spectra (dotted) and fitted spectra (solid) of hemimorphite.

The general approach to fitting data obtained in this work was by building structural models from known chemical species and using Artemis to adjust the parameters in the structural model to fit the experimental (obtained) spectra. The model parameters were adjusted as needed (different scattering paths and different neighbouring atom types) until the most plausible fit to the data was obtained. The quality of the fit, R-factor, is the sum of squares of the differences between the data and the fit at each point per the sum of the squares of the data and is given by Equation 3.8. In general, the R-factor should be less than 0.05 to be considered as a plausible fit.

Equation 3.8 $$R - \text{factor} = \frac{\sum_i (data_i - fit_i)^2}{\sum_i data_i^2}$$

3.2.2 X-ray Diffraction

X-ray diffraction was used in order to ensure glass samples were homogenous and amorphous in nature. This was performed using a Siemens D5000 X-ray Powder Diffractometer with Cu Kα radiation. X-ray diffraction is based on Bragg's Law (Equation 3.9) where the intensity and angle of the diffracted beam from the sample is measured.

Equation 3.9 $$n\lambda = 2d\sin\theta$$

Where n is an integer, λ is the wavelength of the incident X-ray beam, d is the crystalline lattice spacing and θ is the angle of diffraction.

Unless otherwise noted in later chapters, all glass samples were also finely ground powders (< 75 μm average particle size) and, in general, all glass samples were measured from 5 to 70 °2θ with a step size of 0.02 at 0.1 ° min^{-1}.

3.3 Scanning Electron Microscopy

Scanning electron microscopy (SEM) is a useful technique for microstructural analysis of materials. Its usefulness increases with the addition of a backscattered electron (BSE) detector and an energy dispersive X-ray spectrometer (EDS) detector. The basis of SEM analysis is performed by introducing a sample to an electron beam and allowing the electrons

to interact with the surface of the sample. Signals are produced through the interaction between the incident electron beam and approximately 2 μm into the sample surface. Figure 3.7 illustrates a typical SEM microscope.

The electron beam is produced by a tungsten filament generally operated at 20 keV. The electron beam first passes through a set of apertures and then through the first and second condenser lenses. The condenser lenses increase or decrease the spot size of the electron beam. The objective lens, located after the condenser lenses, focuses the electron beam on the sample. In the case of Figure 3.7, scan coils which direct the electron beam over the sample are included in the objective lens. The apertures limit the size of the electron beam passing to the sample. The first aperture, just after the filament, is used to condense the electron beam, while the second aperture, just after the objective lens, is used to control the contrast in the electron image.

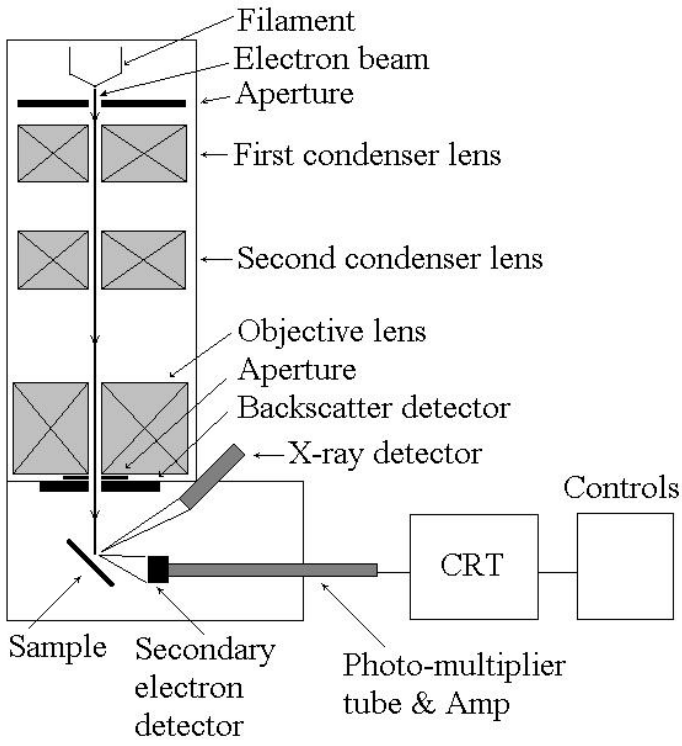

Figure 3.7 A typical SEM microscope layout.

The interaction between the sample and the incident electron beam causes secondary electrons to be emitted within the excitation volume of the sample. The excitation volume is generally only ~2 μm in depth from the surface of the sample. As shown in Figure 3.8, the interaction of the incident electron beam and the sample emits Auger electrons, secondary electrons, backscatter electrons, characteristic X-rays and photons.

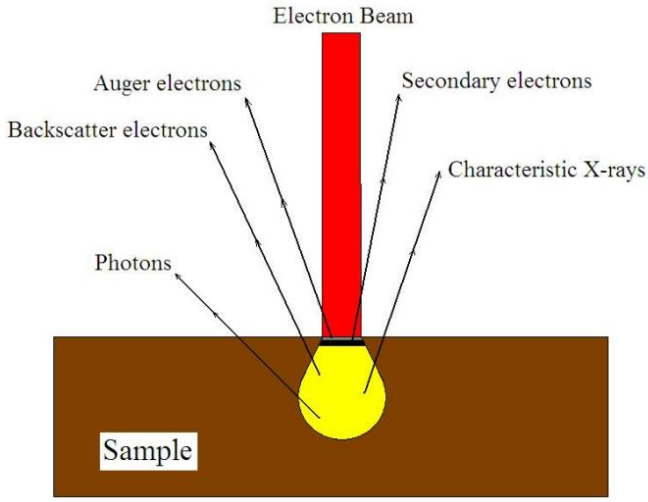

Figure 3.8 Excitation volume generated from an electron beam interacting with a sample.

The emitted secondary electrons are attracted to the secondary electron detector by a corona placed over a scintillator plate. The scintillator place sends the signal through a photomultiplier tube which is sent through an amplifier and then to the monitors which show the image of the sample. The backscatter electron detector, as shown in Figure 3.7 is generally located after the final aperture and the objective lens and is a disk surrounding the electron beam. As the backscatter electrons are emitted, the detector above the sample collects the emitted backscatter electrons as a function of sample composition.

The X-ray detector for EDS analysis, as shown in Figure 3.7, makes used of the emitted X-rays when the incident electron beam interacts with the surface of the sample. Characteristic X-rays are produced when the incident electron beam excites electrons in the sample surface to higher energy shells. When the electrons relax back to their initial energy state they release characteristic X-rays which are detected using the X-ray detector. The X-ray detector measures the energy of the X-ray photon which is equal to the difference of the initial energy state and the excited energy state of the sample. Because each element has discrete energy level changes it allows qualitative and quantitative analysis of the sample.

3.3.1 SEM Sample Preparation

Samples used for SEM analysis were first polished to a median grit size of 15 μm using SiC polishing paper with water as a lubricant. After using the SiC polishing paper, diamond paste with an average particle size of six, three and one micron with an oil based lubricant

was used. In order to decrease electron build-up (charging) on the surface of the sample, samples should be coated with a conducting coating, such as gold or carbon, using a vacuum sputter coater. Samples used in this work were coated with carbon. After coating, silver paste was painted on to allow flow of the electrons from the sample to the grounded sample holder.

3.4 Glass Durability Testing

Several durability experiments are used for determining the final dissolution rate of glass. These experiments contain both powder and monolithic samples. Experiments such as the product consistency test (PCT) and the materials characterisation centre (MCC-1) tests are static tests while the single pass flow through (SPFT) and the micro-channel flow through (MCFT) tests make use of a flow through solution to negate the effects from solution saturation. [118] Several glass durability experiments were performed in these works and are discussed below.

3.4.1 Single Pass Flow Through

The single pass flow through (SPTF) test was conducted at the Pacific Northwest National Laboratory in Richland, WA, USA. Glass powders of compositions MW+25 wt% Blend and MW+30 wt%f Blend (compositions given in Table 3.1) were prepared as in section 3.1.1 for use in the SPFT tests. Cleaning of the powders was performed as given in the ASTM standard for the PCT. [118] The method of cleaning the powders is to rinse the powder in deionised water and then to decant the water. This is repeated three times. After rinsing the glass powder with deionised water, it is then cleaned ultrasonically with deionised water for 2 min. and then the water decanted. This is repeated three times. The glass powder is then ultrasonically cleaned with ethanol for 2 min. and the ethanol decanted. This is repeated two times. After cleaning with ethanol, the glass powder is dried in an oven at 90 °C overnight (>16 h) and then placed in a desicator until further use.

3.4.1.1 Buffer Solutions

Three water based buffer solutions were used for the SPFT measurements; pH = 8.00, pH = 10.00 and pH = 12.00. For pH = 8.00 and pH = 10.00, Tris(hydroxymethyl)aminomethane (TRIS) from Fisher Scientific at 99.9% purity was added to high purity H_2O to make 0.05 M TRIS. These solutions were pH balanced with concentrated HNO_3 to either pH = 8.00 ± 0.05, or pH = 10.00 ± 0.05. For pH = 12.00, LiOH and LiCl from Alpha Aesar at 99.99% purity were added to high purity H_2O to make a solution of 0.01 M LiOH and 0.01 M LiCl which was then pH balanced with 0.01 M LiOH to pH = 12.00 ± 0.05. After pH balancing, solutions were allowed to sit overnight and the pH was measured again. If the pH drifted away from the target pH, the pH was balanced again and the solution allowed to sit overnight. This was performed in order to confirm the buffer solutions would not have a drift in pH during the measurements.

3.4.1.2 SPFT Setup and Calibration

The SPFT experimental setup, as pictured in Figure 3.9, shows the buffer solution in a HDPE vessel connected to a Kloehn V6 syringe pump which pumps the solution to a Savillex Teflon digestion vessel located inside an oven. The solution is then passed on to a HDPE collection vessel located outside of the oven. The connection tubing in the setup is PTFE tubing with an inner diameter of 1/8 in. Figure 3.9A is an illustration of the SPFT setup and Figure 3.9B is a picture of the actual setup used where the buffer solution is contained in the oven at the same temperature as the reaction vessel. This allows the buffer solution to be at the same temperature as the reaction vessel solution in order to diminish effects of a varying temperature outside the oven.

Before starting the SPFT experiments, a flow rate calibration of the pumps being used is performed. To do this, the reaction vessels were filled 80 % with the solution to be used for the test. For calibration of the pumps in this study, 0.05 M TRIS at pH = 8 was used. After filling reaction vessels with the buffer solution, vessels were sealed and the pumps started at the desired flow rates. Flow rates used for the Q/S study were 5, 10 (for two vessels), 20, 40, 80 (for two vessels) and 125 mL d^{-1}.

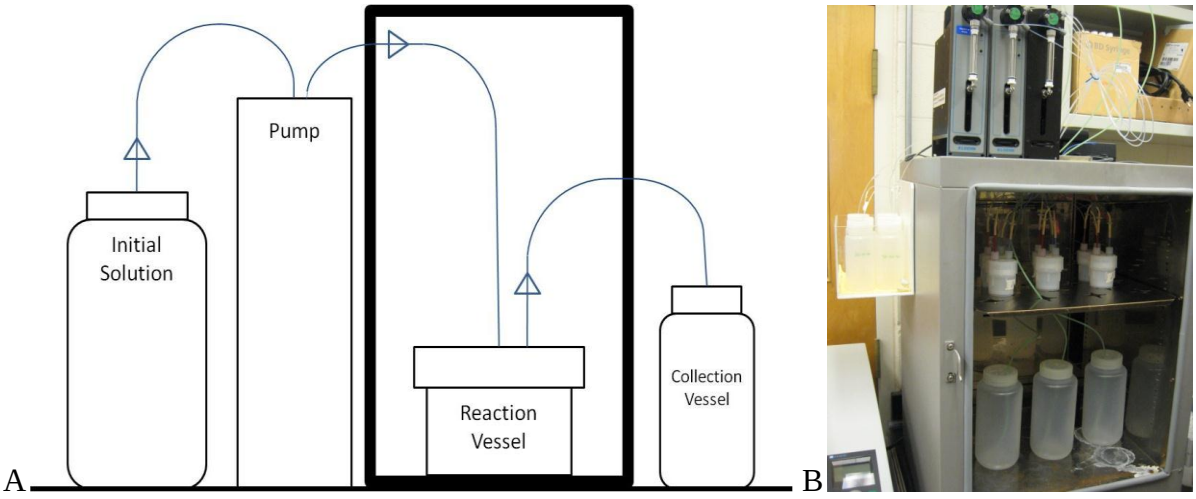

Figure 3.9 A) SPFT setup illustration B) Actual SPFT setup with the oven door open for refilling of buffer solution bottles.

Solutions were collected in collection vessels outside the oven and then weighed after every 24 h. This enabled calculation of the flow rate by assuming the density of the solution to be equal to that of H_2O and measuring the mass of the solution per solution collection time. Once each pump was calibrated to within 10% of the desired flow rate, the flow rate per surface area (Q/S) measurements was started.

3.4.1.3 Flow Rate per Surface Area (Q/S) Measurements

After calibrating the flow of the pumps, the clean glass powder was added to the reaction vessels and then the reaction vessels sealed and placed back into the oven set at 40 ± 2 °C. The addition of glass powder with a particle size of 75 μm < X < 150 μm was added to each vessel to give Q/S values of 6.00×10^{-7}, 2.40×10^{-6}, 6.00×10^{-6}, 1.60×10^{-5}, 4.80×10^{-5}, 9.60×10^{-5}, 3.20×10^{-4} and 5.00×10^{-4} m s^{-1}, respectively. Table 3.2 gives the flow rate and the mass of glass needed for each Q/S measurement performed for the full Q/S sweep.

Solutions in the collection vessel during the measurement were collected every 24 h and the mass of the solution measured in order to confirm the flow rate was on target. Aliquots of 10-20 mL were there taken and subsequently acidified with 100 μL of concentrated HNO_3 before being submitted for ICP analysis. For the Q/S measurements, solutions were collected every 24 h until a steady state dissolution rate was achieved. Depending on the flow rate and amount of glass powder added to the vessel, this can take anywhere between 5 and 60 days. Once the final dissolution rate for each Q/S measurement was attained, a plot of the concentration of ions as a function of log (Q/S) is plotted. At steady state conditions, the

concentration of Si, B, and Na will not significantly change with an increase of Q/S. At the Q/S where steady state conditions are reached, a pH-Temperature sweep can be performed. Acidified solutions were submitted for ICP analysis for concentrations of Al, B, Fe, Li, Mg, Mo, Si, Na and Zr for the Q/S measurements.

Table 3.2 Flow rates and mass of glass powder for each Q/S measurement performed on glasses MW 25 Blend and MW 30 Blend.

Flow (mL d^{-1})	Mass (g)	Q/S (m s^{-1})
5	5.00	6.00E-07
10	2.50	2.40E-06
10	1.00	6.00E-06
20	0.75	1.60E-05
40	0.50	4.80E-05
80	0.50	9.60E-05
80	0.15	3.20E-04
125	0.15	5.00E-04

3.4.1.4 Temperature and pH SPFT Measurements

The pH-Temperature sweep for the SPFT experiment is performed after the constant Q/S is attained from the Q/S measurement. This allows information on the final dissolution rate with changes in pH and temperature to be acquired. Buffer solutions made as per section 3.4.1.1 of pH of 8.00, 10.00, and 12.00 were used at temperatures of 25 °C (room temperature), 40 ± 2 °C, 70 ± 2 °C and 90 ± 2 °C were used for the pH-Temperature sweep. Both MW 25 Blend and MW 30 Blend attained steady state conditions at a Q/S of 9.60 x 10^{-5} m s^{-1} which was used for the pH-Temperature sweep measurements.

Setup of the pH-Temperature sweep experiments was, in general, the same as the Q/S measurements. The only difference was the temperature of the oven, the buffer solution used, and the amount of glass powder placed in the reaction vessel during the experiment. To achieve a Q/S of 9.60 x 10^{-5} m s^{-1}, a flow rate of 80 mL d^{-1} with 0.5 g of 75 μm < X < 150 μm glass powder was used for both the MW 25 Blend and MW 30 Blend glasses.

Once the pH-Temperature sweep was started, solutions from the collection vessel were collected, measured, acidified and analysed as in section 3.4.1.3. This measurement was continued until steady state conditions were met for each pH at the different temperatures. Acidified solutions of the pH-Temperature sweep measurements were submitted for ICP analysis for concentrations of Al, B, Fe, Li, Mg, Mo, Si, Na and Zr.

3.4.2 Product Consistency Type Test

Co-disposal of UK HLW glass with ILW wastes may induce hyper alkaline solutions which can interact with the HLW glass after long periods of time. The Product Consistency Type Test (PCT-t) was performed in order to study the dissolution rates of UK simulated HLW glasses under the hyper alkaline solutions, which they may encounter at long times. The glass composition used for the long term durability tests in hyperalkaline solution was MW 25 Blend. The glass for the long term powder durability tests was crushed using a stainless steel percussion mortar and sieved to two different size fractions; 150 μm > X > 75 μm and 53 μm > X > 35 μm. After sieving, the powder was rinsed with high purity H_2O three times. The glass powder was then cleaned with high purity H_2O ultrasonically for 2 min and the high purity H_2O decanted. This was repeated three times. Cleaning the powder ultrasonically using ethanol and decanting the ethanol was also repeated three times. After cleaning, the powder was placed in a drying oven at 90 °C for 24 h and then placed in a desicator until use.

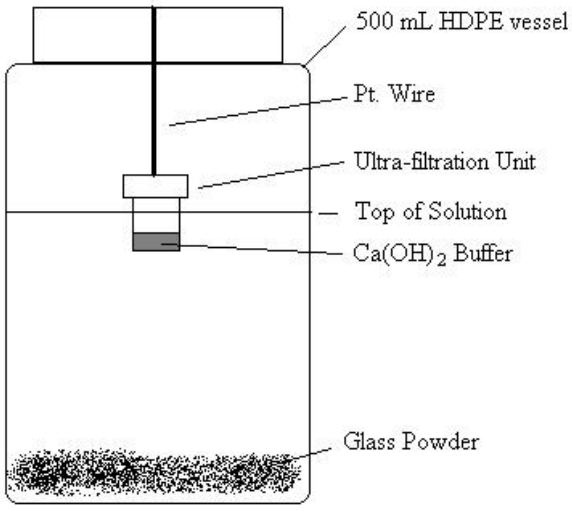

Figure 3.10 Vessel used for the PCT-t durability study with the $Ca(OH)_2$ saturated solution. For the PCT-t with high purity H_2O, the platinum wire, Ultra-filtration Unit with the $Ca(OH)_2$ buffer was not used.

The long term durability test performed is similar to the ASTM standard for the product consistency test (PCT). [118] The PCT generally uses several small vessels (volume = 50 mL) which are removed at specific time intervals in order to characterise the normalised mass loss (NL_x) of species, x, in the glass at a constant temperature. [118] The PCT type (PCT-t) test performed in this work used one large vessel with 400 mL of solution in which aliquots of

5 mL were removed at specific time intervals. Two solutions were used for the PCT-t at 50 °C in this study; de-aerated high purity H_2O and a de-aerated $Ca(OH)_2$ saturated solution buffered with a $Ca(OH)_2$ slurry. Two SA/V ratios were also used; 1200 m^{-1} and 10,000 m^{-1}. The PCT-t vessel, as shown in Figure 3.10, is a 500 mL HDPE with an Ultra-filtration Unit (UFU) attached to the lid with platinum wire. The mass of the powder added to 400 mL of solution was determined by the SA/V ratio used for the test; 95.23 g for SA/V = 10,000 m^{-1} and 24.87 g for SA/V = 1200 m^{-1}. The $Ca(OH)_2$ buffer was a slurry of $Ca(OH)_2$ with a small addition of de-aerated high purity water.

In order to keep CO_2 from reacting with the $Ca(OH)_2$ buffered solution, forming $CaCO_3$ precipitates and also reducing the pH of the solution, the durability tests were performed in a glove-box under a N_2 atmosphere. A slow flow of N_2 gas was used to keep a positive pressure inside the glove-box. The inline N_2 gas system was filtered with soda lime pellets before entering the glove-box and in the glove-box to filter CO_2. Oxygen content was monitored using a Dräger Pac 3000 O_2 sensor in order to monitor the atmosphere. Typically the oxygen percent was less 0.2 vol% except during short periods of time when items were transferred in or out of the glove-box. The furnace (LT Scientific OP39-UF) inside the glove box was kept at a constant 50 ± 2 °C throughout the experiments.

The ASTM Type II H_2O with >18 MΩ (high purity H_2O) and $Ca(OH)_2$ saturated solution were both prepared from de-aerated high purity H_2O. De-aerating the high purity H_2O was performed by boiling high purity H_2O for 10 min under a blanket of N_2 gas. Once de-aerated, the high purity H_2O was transferred into the glove-box. For the PCT-t experiments performed with high purity H_2O, the de-aerated high purity H_2O was measured and transferred to the vessels. The $Ca(OH)_2$ saturated solutions were prepared in the glove-box using the de-aerated high purity H_2O and adding $Ca(OH)_2$ up to the saturation point at 50 °C which was calculated using solubility limits from Bassett and Taylor. [119; 120] The pH of the de-aerated high purity H_2O and the $Ca(OH)_2$ saturated solution were measured prior to adding the powder to the vessels to start the PCT-t test. The pH measurements were performed with 1 mL aliquots at room temperature using a Fisher semi-micro pH probe.

After the glass powder was added to the PCT-t vessels, aliquots were removed from the PCT-t vessels for the 75 μm < X < 150 μm particle size powder at 1, 3, 7, 14, 21, 28, 35, and 42 days. For the 35 μm < X < 53 μm particle size powders, aliquots were removed at 1, 3, 7, 14, 21, 28, 42, 56, 70, 84, 112, 140, and 168 days. After removing aliquots, 4 mL was filtered through Fisher Scientific 45 μm filters and acidified with 40 μL of concentrated HNO_3. The 1 mL leftover solution was then used to measure the pH.

After collection of the solutions and acidifying, samples were submitted for ICP analysis by the Sheffield Assay Office to analyse concentrations of selected ions in solution. These ions were; Li, Na, Mg, Al, Cr, Fe, Ni, Sr, Y Zr, Mo, Ru, Te, Cs, Ba, La, Ce, Pr, Nd, Sm, Gd, S, Ca, and B.

3.4.3 Long Term Monolithic Durability Tests

Long term durability test using monolithic samples from the Materials Characterization Center (MCC-1) test were performed on the MW 25 Blend glass. [121] The MCC-1 test was also performed at 50 °C using the $Ca(OH)_2$ buffered solution with excess $Ca(OH)_2$ (> 1 g) added to the vessel before the monolith and $Ca(OH)_2$ solution were added and the vessel sealed. The MCC-1 test was performed under a N_2 atmosphere in a glove box. The SA/V ratio used was 10 m^{-1} as is specified in the PCT ASTM standard. [118] Figure 3.11 illustrates the MCC-1 test vessel setup. Monolithic samples were cut to 10 mm x 10 mm x 4 mm and then polished with a median grit size of 3 μm with diamond paste and ethanol as a lubricant. The monolithic samples were cleaned as the powder samples in section 3.4.1. After cleaning, the monolithic sample was placed on a Teflon cradle in the de-aerated $Ca(OH)_2$ saturated solution situated above excess $Ca(OH)_2$ powder. Blank MCC-1 vessels were also used and contained everything as shown in Figure 2 except the monolithic sample. Samples were removed from the oven at 1, 3, 7, 14, 21, 28, 42, 56, 70, 84, 112, 140, and 168 days.

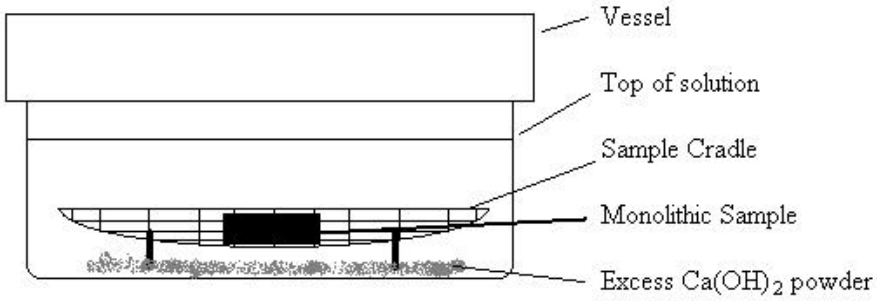

Figure 3.11. Vessel used for the MCC-1 test with the $Ca(OH)_2$ saturated solution with excess $Ca(OH)_2$.

After removal of the samples from the vessel, samples were dried and stored in a desicator in the glove box until further analysis. Aliquots of the solution were taken as per section 3.4.2, and acidified with 40 μL of HNO_3. The remaining 1 mL of solution was used to measure the pH of the solution as per section 3.4.2. After collection of the solutions and

acidifying, samples of the solution were submitted for ICP analysis by the Sheffield Assay Office to analyse concentrations of selected ions in solution. These ions were; Li, Na, Mg, Al, Cr, Fe, Ni, Sr, Y Zr, Mo, Ru, Te, Cs, Ba, La, Ce, Pr, Nd, Sm, Gd, S, Ca, and B.

3.4.4 Vapour Hydration Test

Glass samples were cut to a size of 10mm x 10mm x 1.5mm using a diamond impregnated saw and polished with SiC paper using paper designations of P220, P600, P800, and P1200. Water was used as a lubricating agent while polishing with the SiC paper. After polishing to P1200 with SiC paper, further polishing using diamond paste with median grit sizes of 6μm, 3μm, and 1μm paste was performed using a water based lubricant. Once polished, samples were cleaned.

Samples were cleaned by rinsing with deionized water twice and again with deionized water in an ultrasonic bath for 2 min. and the water decanted. This was repeated twice. After cleaning with DI water, samples were cleaned with ethanol ultrasonically for 2 min. and the liquid decanted. This was repeated once. After cleaning, samples were placed into a drying oven at 90 ºC for 1 h. After drying, samples were placed in a desicator until further use.

Figure 3.12 Vapour Hydration Test sample vessel and sample holder. The Left column shows the sample holder and sample, the middle column shows the vessel un-sealed, and the right column shows the sealed vessel.

Vapour hydration test (VHT) vessels and sample holders were cleaned in the same manner as the samples. After cleaning, the vessels and sample holders were placed in a desicator

until use. Figure 3.12 shows the VHT vessel, sample holder and sample. Stainless steel wire with a diameter of 5.0 x 10^{-3} in. was used to hold the samples in place during the test. After the sample was placed into the vessel, 200 μL of high purity water was placed in the vessel. The amount of water used was sufficient to give a saturated water vapour atmosphere without dripping water from the specimen which could lead to transport of leached species from the sample. After placing the water into the vessels, the vessels were sealed and placed into an oven at 200 ºC (± 1 ºC) for 3, 5, 7 and 14 days. Different times were used in order to investigate the rate of dissolution and change in hydration layers.

4.0 The Structural Role of Zn in Model UK Nuclear Waste Glasses Studied by X-ray Absorption Spectroscopy*

4.1 Introduction

In the UK, and elsewhere, alkali borosilicate glasses are the current material of choice for vitrification of high level radioactive waste (HLW) arising from reprocessing of spent nuclear fuel by the Plutonium and Uranium Recovery by Extraction (PUREX) process. [1; 2] Alkali borosilicate glasses have been selected on the basis of their ability to chemically and physically incorporate most waste stream elements and their acceptable processing temperature, chemical durability, radiation tolerance and mechanical stability. [2] The Sellafield Waste Vitrification Plant (WVP) employs the Atelier de Vitrification Marcoule (AVM) process, similar to that operated at Cap de la Hague in France. [2] In this process, a nitric acid solution of HLW is partially denitrated in a rotary calciner and the product is combined with an alkali borosilicate frit, and then vitrified in an induction melter operating at ~1060 ^{o}C. Although the operational processes at Sellafield and la Hague are broadly similar, the vitrified products differ in three crucial respects. First, the waste loading of UK HLW glass product is typically in the range 25-28wt% (on the basis of metal oxides), with a possible move toward higher incorporation levels in the future. In comparison, the waste loading of the comparable French product is typically 15-18 wt%. [122; 10; 21] Second, although both processes employ a sodium lithium borosilicate glass frit, the composition employed at la Hague contains different amounts of SiO_2, B_2O_3, Li_2O and Na_2O to the UK glass and crucially, also contains additions of ZnO and CaO which are believed to confer certain beneficial effects, as summarized below. [21; 68] Third, the UK HLW glasses typically incorporate a significant quantity of MgO and Al_2O_3 derived from partial dissolution of Magnox fuel cladding during reprocessing; in comparison the French HLW composition is deficient in Al_2O_3 and contains no MgO. [21] As a result, the compositions of the French and UK wastes being vitrified differ considerably from one another.

The addition of ZnO to alkali borosilicate glasses at low concentrations (typically < 5 wt % ZnO) is reported to confer several beneficial effects, including improved chemical durability and mechanical processing ability. [10; 123; 124] In contrast, ZnO is reported to act as a nucleating agent when present at low concentrations in both alkali silicate and aluminosilicate glasses. [125] In general, Zn has been shown to exhibit a marked preference

* This chapter is presented in a modified version of a published paper; Cassingham, N.J., Stennett, M.C., Bingham, P.A., Hyatt, N.C., Aquilanti, G., *International Journal of Applied Glass Science*, 2 [4] (2011) 343.

for tetrahedral coordination in simple alkali silicate glasses. [68; 69] However, with increasing Zn / modifier ratio, the ratio of 6- to 4- fold coordinate Zn species is reported to increase due to the availability of charge compensating modifier cations. [68; 126] Furthermore, comparison of crystalline alkali and alkaline earth silicates, shows that 6-fold coordinate Zn species are stabilized by high field strength cations (e.g. Mg), whereas the lower field strength cations (e.g. Li, Na, Ca) stabilize 4-fold coordinate Zn species. [126]

The UK glass frit, commonly known as "MW" glass, is a simple mixed-alkali borosilicate, with a nominal composition (wt %): 61.7 SiO_2, 21.9 B_2O_3, 11.1 Na_2O, 5.3 Li_2O. [1; 2; 10] Modification of the UK "MW" frit composition to incorporate both CaO and ZnO is currently under consideration, with the aim of improving the waste incorporation rate and improving long term chemical durability. [10] ZnO additions are also reported to reduce melt viscosity, thus facilitating better melt homogenization and increased levels of waste loading at lower processing temperatures. [10] This potentially offers the combined benefits of reduced melter corrosion rate, a reduction in the number of waste packages required and hence accelerated immobilization of UK hazardous liquid HLW stocks. The motivation for the current study was to develop an understanding of the structural role of Zn in model UK HLW glasses in order to scientifically underpin possible future modification to the "MW" base glass composition. A particular point of interest was the potential role of ZnO as a network modifier, intermediate or former in modified matrix compositions relatively rich in Mg which is unique to the chemistry of UK HLW.

X-ray Absorption Near Edge (XANES) and Extended X-ray Absorption Fine Structure (EXAFS) are useful techniques for the study of amorphous, aperiodic and metamict materials, providing information on the local structure around an absorber atom (i.e. number, distance and type of coordinating atoms - for a recent overview see Kelly *et al.*). [116] Previous EXAFS studies of Zn speciation in French laboratory-prepared and full-scale model nuclear waste glasses, incorporating simulant HLW derived from PUREX and advanced reprocessing flowsheets, have determined the presence of tetrahedral ZnO_4 species. [68] These ZnO_4 units may possibly form part of the glass network, as evidenced by (weak) next-nearest neighbour scattering paths. [68] In this investigation we confirm the presence of ZnO_4 species in UK nuclear waste glass compositions and, by comparison with simple soda-lime-silica compositions, we conclude that ZnO_4 species indeed participate in network formation.

4.2 Experimental Procedure

4.2.1 Preparation of Glasses

Simple soda-lime-silica (SLS) glasses doped with ZnO were prepared as model glass compositions to aid in fitting the EXAFS data of simulated, inactive, UK HLW glasses and comparison to previous molecular dynamics simulations. [127; 67] Three sodium calcium zinc silicate (NCZS) glasses were prepared for this study with 8.0 - 14.5 mol% ZnO. The compositions of these glasses are given in Table 4.1. Additionally, an alkali zinc silicate glass was prepared with a stoichiometry equivalent to $Na_2ZnSi_3O_8$, which has been previously reported in crystalline form. [128] Compositions were analysed by quantitative EDS (simple glasses) ICP (simulant waste glasses) and XRF (simulant waste glasses) did not deviate significantly from nominal compositions. It should be noted that there is a limitation to analysis of compositions using EDS analysis due to excitation of Na within the electron beam. This may produce a false measurement that is higher in Na than in the bulk glass. For the EDS analysis, three spots were measured and the average used.

Table 4.1 Analysed compositions of the simple sodium calcium zinc silicate and zinc silicate glasses. The error in the EDS analysis was 0.5 wt % based on analyzing three regions

Glass	SiO_2 (wt %)	Na_2O (wt %)	CaO (wt %)	ZnO (wt %)
NCZS 3	44.19	23.29	20.85	11.67
NCZS 3.5	41.58	18.55	19.89	19.98
NCZS 4	39.81	20.83	18.65	20.72
NCZS 5	53.52	18.28	0	28.20

Glass batches were melted in a dispersion hardened Pt crucible at 1350 ºC. The glass was melted for 1 h after the final charge and stirred with a dispersion hardened Pt stirrer for 4 h. Glasses were cast into blocks using a pre-heated stainless steel mould, allowed to cool until the melt would not flow and then placed into an annealing furnace at 450 ºC and held at this temperature for 1 h, where upon the furnace was cooled at 1 ºC min^{-1} to room temperature.

Three simulated, inactive, UK HLW glasses were prepared to aid the understanding of ZnO speciation in model UK HLW glasses and their nominal compositions are given in Table 4.2. All three glasses were melted in re-crystallized alumina crucibles at 1060 ºC with 1 h batch free time after the final charge and then stirred for 4 h with a re-crystallized

alumina stirrer (platinum-ware was avoided due to partial reaction with the glass during batch reactions and melting). After melting, the glass melt was poured into a block using a pre-heated stainless steel mould and annealed at 500 ºC for 1 h before being cooled at 1 ºC min^{-1} to room temperature.

Table 4.2 Analysed compositions of the three model UK simulated HLW glasses. Compositions were analyzed using XRF Uniquant and ICP-MS with an error of 0.1 wt %.

Oxide	CaZn Base (wt %)	Magnox (wt %)	Blend (wt %)
SiO_2	56.10	44.27	46.44
B_2O_3	21.54	18.45	18.95
Na_2O	11.48	8.8	9.32
CaO	1.94	1.70	1.54
ZnO	6.03	4.53	4.28
Li_2O	2.92	2.24	2.27
Al_2O_3	--	3.65	0.11
BaO	--	0.90	1.67
CeO_2	--	1.40	1.28
Cr_2O_3	--	0.18	0.19
Cs_2O	--	0.89	1.42
Fe_2O_3	--	1.44	0.49
Gd_2O_3	--	0.68	2.62
La_2O_3	--	0.76	0.71
MgO	--	3.2	0.11
MoO_3	--	1.33	2.41
Nd_2O_3	--	1.9	1.69
NiO	--	0.29	0.18
Pr_2O_3	--	0.50	0.46
RuO_2	--	0.39	0.46
Sm_2O_3	--	0.32	0.28
SrO	--	0.24	0.43
TeO_2	--	0.09	0.12
Y_2O_3	--	0.1	0.11
ZrO_2	--	1.72	2.48
Total	100.0	100.0	100.0

4.2.2 X-Ray Absorption Spectroscopy (XAS) Measurements

Zn K-edge XAS spectra were acquired on beam line BL 11.1 X-ray Absorption Fine Structure at ELETTRA in Basovizza, Italy and beam line X23A2 of the National Synchrotron Light Source, Brookhaven National Laboratory, Upton, NY, USA. Beam lines utilize either a Si (311) or SI (111) double crystal monochromator, detuned for the purpose of harmonic rejection. The Zn K-edge energy was calibrated *in situ* using a Zn foil placed in front of the reference ion chamber. Data were acquired in transmission mode, at room temperature, using finely ground sample dispersed in poly-ethyleneglycol (PEG) to achieve one absorption length. To improve sample homogeneity, and hence data quality, the powders were pressed into 13 mm diameter pellets using a stainless steel uni-axial hydraulic press. The *k*-range scanned during acquisition was typically 3 $Å^{-1}$ to 18 $Å^{-1}$. Data analysis was performed using the programs Athena, Artemis and Hephaestus. [117]

4.2.3 X-Ray Diffraction (XRD) Analysis

The mineral standard was analyzed using a STOE IP-PSD X-Ray diffractometer with Cu Kα radiation while the glass samples were measured using a Siemens D5000 X-ray diffractometer with Cu Kα radiation. Glass samples were measured in powdered form (< 75 μm) in order to ensure they were homogeneous and amorphous in nature (Figure 4.1). This was confirmed by SEM and EDS analysis. The mineral standard was analyzed and verified to be hemimorphite ($Zn_4Si_2O_7(OH)_2•H_2O$).

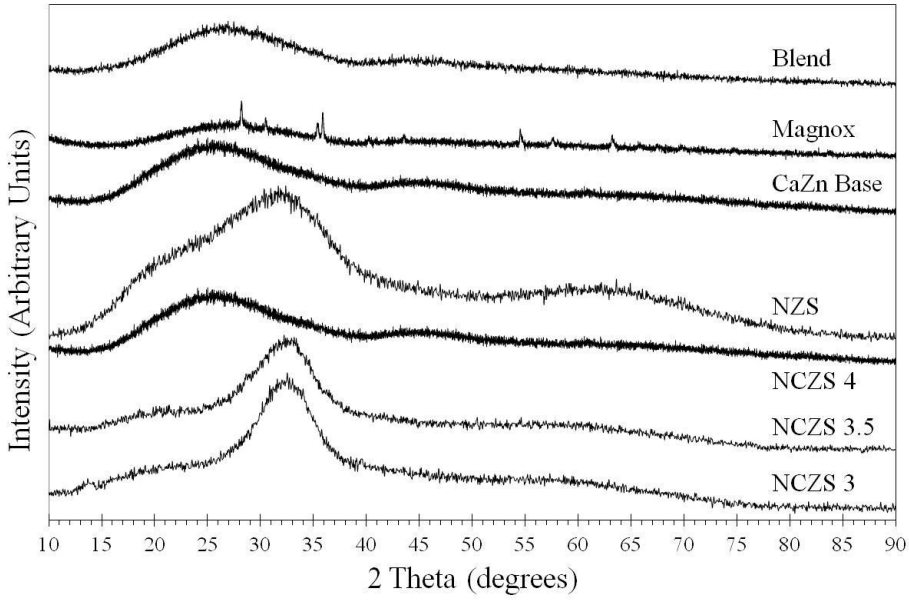

Figure 4.1 X-ray diffraction patterns of the glass samples analysed by X-ray absorption spectroscopy.

4.2.4 Property Measurements of Glasses

Glass powder was used to perform differential thermal analysis (DTA) in order to determine the glass transition temperature (T_g) of each glass studied in this chapter. A Metler Toledo DTA was used at a heating rate of 10 °C min^{-1} up to 1200 °C and the difference in temperature between a blank reference crucible and the sample was measured.

Density measurements were also performed using the Archimedes method. Several different monolithic samples of each glass were measured and the average of the density measurements calculated and used as the density.

4.3 Results

4.3.1 X-Ray Absorption Near-Edge Structure (XANES) Analysis

Zinc K-edge XANES data for the glasses and hemimorphite are compared in Figure 4.2. As expected for oxidized Zn samples, the Zn K-edge is shifted to a higher energy than that of a

(non-oxidized) Zn metal (E_0 = 9659 eV). [129] Edge energies measured as the maximum in first derivative for all samples in this study, were 9664.0 ± 0.5 eV, which is generally typical for Zn^{2+}. [68; 69]

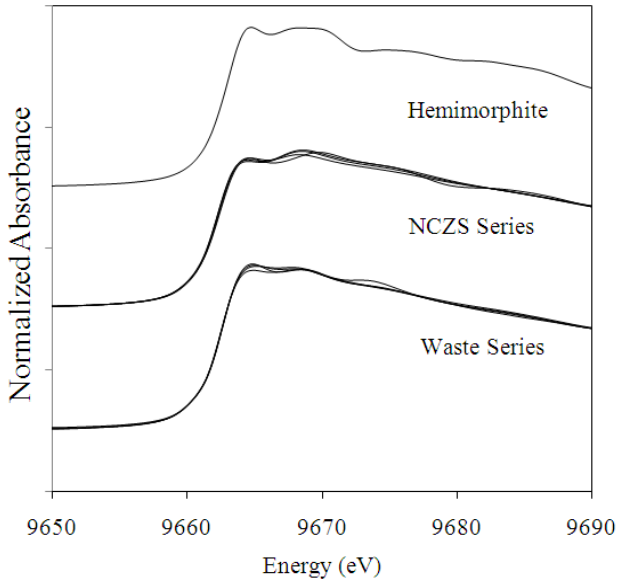

Figure 4.2. Normalized Zn K-edge XANES data for the crystallographic mineral standard (Hemimorphite), the NCZS glasses (NCZS Series) and model UK simulated HLW glasses (Waste Series).

4.3.2 Extended X-Ray Absorption Fine Structure (EXAFS) Analysis

As previously mentioned in Chapter 3, the EXAFS signal is calculated as the sum over all paths by which the excited photoelectron may be scattered by the atoms surrounding the absorber, according to Equation 4.1. [67; 130]

Equation 4.1

$$\chi(k) = \sum_i \chi_i(k)$$

For each scattering path, *i*, $\chi_i(k)$ is evaluated as Equation 4.2:

Equation 4.2

$$\chi_i(k) = \frac{\left(N_i S_0^2\right) F_i(k)}{kR_i^2} \sin\left[2kR_i + \varphi_i(k)\right] e^{-2\sigma_i^2 k^2} e^{\frac{-2R_i}{\lambda(k)}}$$

with

Equation 4.3 $$R_i = R_{0i} + \Delta R_i$$

where, $F_i(k)$ and $\varphi_i(k)$ represent the effective scattering amplitude and phase shift of the photo-electron, for each scattering path *i*, $\lambda(k)$ is the photo-electron mean free path, and R_{0i} is the nominal path length used in the computation. These terms were calculated using the theory FEFF 6. [117]

The parametric terms in Equation 4.2, which must be evaluated for each scattering path are: N_i, the number of geometrically equivalent paths; S_0^2 commonly referred to as the amplitude reduction factor, which accounts for relaxation of the passive electrons on the absorber atom following photo excitation of a core shell electron; ΔR_i, the difference between the input (R_{0i}) and calculated (R_i) scattering path distance; σ_i^2, the root mean variation in distance between absorber and scatterer; and E_0, an adjustment to zero the kinetic energy of the photo-electron.

EXAFS data were analyzed by constructing local scattering clusters based on the known crystal structures of $Zn_4Si_2O_7(OH)_2 \cdot H_2O$ (hemimorphite), $Na_2ZnSi_3O_8$ (disodium zincosilicate), Zn_2SiO_4 (willemite), $Ca_2ZnSi_2O_7$ (hardysonite) and $Na_2ZnSi_2O_6$ (zinc chkalovite). [128; 131] These compounds are all characterized by ZnO_4 tetrahedra linked to SiO_4 groups, and are chemically similar (as far as reasonably possible) to the glass compositions under study. Single scattering (SS) and multiple scattering (MS) paths were calculated over all possible scattering geometries, within a specified radius of the absorber atom. In general, the summation of Equation 4.1 is dominated by a small number of short SS and MS paths, as was found to be the case in this study. Paths were selected from the FEFF calculation based on the significance of the effective scattering amplitude; where possible paths between atom pairs with similar phase were grouped into a single path in order to minimize the number of independent variables.

A key aim of the current study was to determine, with confidence, the coordination number of Zn species within the glass matrix, corresponding to the number of geometrically equivalent Zn-O paths ($N_{Zn\text{-}O}$). However, the parametric terms N_i and S_0^2 both appear in the product of the amplitude term, given in Equation 4.2. These terms are, therefore, completely correlated, and reliable determination of N_i requires independent determination of S_0^2. It is typically assumed the value of S_0^2 is transferable between different species from the same element and the same edge when measured at the same beam line. [116] In the present study, S_0^2 was determined independently by fitting EXAFS data from a mineral specimen of hemimorphite, with the number of geometrically equivalent paths, N_i, constrained according to the known crystal structure.

The EXAFS data for hemimorphite and the glass samples were background subtracted and converted to k (Å^{-1}), and the resulting $\chi(k)$ data were k^3 weighted and Fourier transformed using a 0.5 Å^{-1} Hanning window over the range $2.25 \leq k \leq 12$ Å. The amplitude reduction factor, S_0^2, was determined by modelling the mineral standard, hemimorphite, using the crystallographic model of Libowitzky *et al.* [132] Three paths from the FEFF calculation were selected; Zn-O, Zn-Si, and Zn-Zn; unique paths between these atom pairs were grouped into a single path with an appropriate degeneracy since the path lengths determined by fitting unique distances were identical within the estimated precision of the analysis. The global parameters S_0^2 and E_0, and for each path, R_i and σ_i^2, were allowed to refine. Table 4.3 gives the results of the fitted model for hemimorphite, determined with $S_0^2 = 0.90 \pm 0.15$ and $E_0 = 2.2 \pm 2.3$ eV. In general, it is considered that S_0^2 should fall in the range $0.70 \leq S_0^2 \leq 1.05$, as determined here. [117] Inspection of the fit to the EXAFS data in Figure 4.3, and the resulting R-factor of 0.036, demonstrate an acceptable fit of the model to the data, and comparison of path lengths determined by EXAFS and crystallography showed these to be identical within the mutual precision of measurement. The Zn bond valence sum was calculated to be 2.1 ± 0.1 valence units (v.u.), demonstrating the refined Zn-O contact distance to be consistent with tetrahedral ZnO_4 species.

Table 4.3. Fitted model parameters from analysis of EXAFS data for hemimorphite ($Zn_4Si_2O_7(OH)_2 \cdot H_2O$). The degeneracy of the paths, N_i, was held constant while allowing S_0^2, R_i, and σ_i^2 to refine. The resulting S_0^2, E_0 and R-factor are 0.90 ± 0.15, 2.21 ± 2.29 and 0.38, respectively. The number of independent variables (N_v) and data points (N_{ip}, determined from the Nyquist theorem) was $N_v = 8$ and $N_{ip} = 12$, respectively.

Path	**Model**	**R_i (Å)**	**±**	**σ_i^2 (Å^2)**	**±**	**N_i**
Zn-O	1.95	1.94	0.02	0.006	0.002	4.0
Zn-Si	3.11	2.96	0.08	0.03	0.02	3.0
Zn-Zn	3.38	3.28	0.03	0.009	0.003	4.0

Determination of the local Zn environment in the glass samples followed the same strategy as the hemimorphite standard taking $S_0^2 = 0.90$ (as previously determined). The crystallographic model used to fit the glasses was that of $Na_2ZnSi_3O_8$ reported by Hesse *et al.* which has a similar structure to sodic plagioclase feldspars [128]; note, this compound has the same stoichiometry as glass NCZS 5. The EXAFS data were fitted using a single Zn-O and Zn-Si path, with N_i, R_i and σ_i^2 allowed to refine. This model provided an acceptable fit to all data sets as shown by the R-factors reported in Table 4.4 and demonstrated by the $k^3\,\chi(k)$ and FT [$k^3\,\chi(k)$] plots shown in Figure 4.4. Inclusion of the Zn-Si path always improved the fit to the data, typically reducing the R-factor by a factor of 2 or more. Examination of the fitted

parameters in Table 4.4 shows, conclusively, that zinc is fourfold coordinated in all the glasses analyzed in this study based on consideration of the refined Zn-O contact distance and coordination number (corresponding to the path degeneracy). The coordination number for all the glasses analysed is the same as minerals found in nature containing zinc, within error. This is further supported by the Zn-O contact distance which is, within error, similar to the same natural minerals containing zinc.

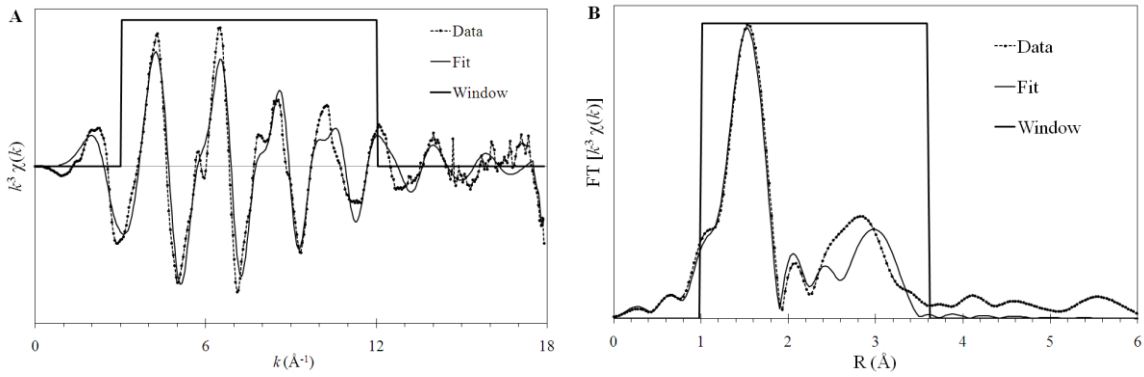

Figure 4.3. Model fit (solid line) to EXAFS data (points and dashed line) for the mineral standard, hemimorphite: (A) k^3 weighted $\chi(k)$ data, and (B) the Fourier Transform of $k^3(\chi(k)$, not corrected for phase shift. The vertical lines indicate the Fourier transform range in k and the fitting range in R.

Table 4.4. Fitted model parameters from analysis of EXAFS data for glass compositions. S_0^2 = 0.90 was held constant while E_0, R_i and σ^2 were refined. N_i was initially allowed to refine freely and then constrained in further fits. The number of independent variables (N_v) and data points (N_{ip}, determined from the Nyquist theorem) was N_v = 7 and N_{ip} = 12, respectively.

Glass	R-factor	E_0 (eV)	±	R_O (Å)	±	σ^2_O (Å^2)	±	N_O	±	R_{Si} (Å)	±	σ^2_{Si} (Å^2)	±	N_{Si}	±	v_{Zn} (± 0.1 v.u.)
NCZS 3	0.006	4.1	0.5	1.95	0.01	0.005	0.001	3.9	0.2	3.58	0.02	0.010	0.007	2.6	1.0	2.1
NCZS 3.5	0.004	4.1	0.5	1.95	0.01	0.005	0.001	3.7	0.2	3.58	0.02	0.009	0.006	2.3	0.9	2.1
NCZS 4	0.005	4.2	0.5	1.95	0.01	0.005	0.001	3.9	0.2	3.56	0.02	0.008	0.005	1.7	0.7	2.1
NCZS 5	0.010	4.0	0.6	1.95	0.01	0.006	0.001	3.7	0.2	3.58	0.03	0.008	0.007	2.1	1.0	2.1
CaZn Base	0.006	4.1	0.6	1.95	0.01	0.006	0.001	4.0	0.2	3.56	0.03	0.009	0.008	1.7	0.9	2.1
Magnox	0.007	4.1	0.5	1.96	0.01	0.006	0.001	4.0	0.2	3.61	0.03	0.011	0.010	1.9	1.1	2.0
Blend	0.007	4.0	0.6	1.96	0.01	0.006	0.001	4.0	0.2	3.57	0.03	0.011	0.009	1.6	0.9	2.0

The bond valence model can be used to test the validity of EXAFS determined bond lengths, where the sum of the valence contribution (v) from each metal oxygen bond, Equation 4.4, should equate to the formal charge on a cation: [133; 134; 135]

Equation 4.4 $$v = exp\left[\frac{(R_o - R)}{0.37}\right]$$

where, R_o is the tabulated reference metal-oxygen bond length and R is the experimentally determined value. [68; 133; 134; 135; 136] As shown in Table 4.4, the Zn bond valence sums are consistent with the formation of tetrahedral ZnO_4 species in all glasses. Our results are thus in broad agreement with those of McKeown *et al.* and Le Grand *et al.;* [68; 69] however, in the present study, the relative precision associated with the refined Zn-Si path degeneracies provides strong evidence to support the presence of Si next nearest neighbour species.

4.3.3 Property Measurements of the Glasses

The T_g of each glass measured by DTA is given in Table 4.5. There is a resulting decrease in the T_g with an increase of zinc for the NCZS glasses. The T_g of the waste glasses does not change (within a ± 5 °C error) when the simulated waste is added to the CaZn Base glass.

The density of these glasses was also measured by the Archimedes method and the results are given in Table 4.5. There is an increase in the density with the increase of zinc in the NCZS glasses; however, the density then drops when the calcium is removed from the system. As expected, the density of the waste glasses increases with the addition of the simulated waste to the glasses.

Table 4.5 Glass transition temperature measured by DTA and density of each glass studied in this chapter.

Glass	T_g (°C) ± 5	Density (g-cm^{-3}) ± 0.02
NCZS 3	496	2.99
NCZS 3.5	518	3.03
NCZS 4	533	2.96
NCZS 5	547	2.96
CaZn Base	514	2.61
Magnox	510	2.79
Blend	517	2.81

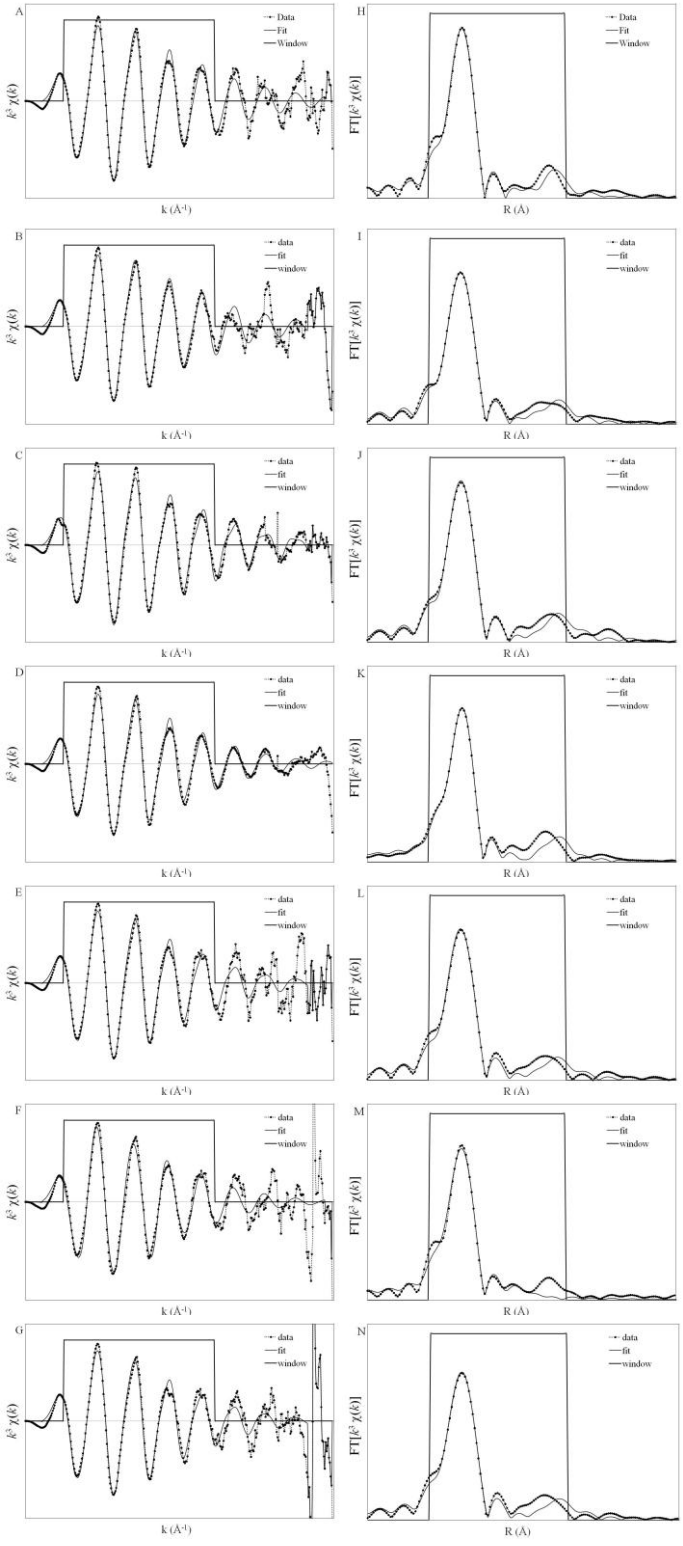

Figure 4.4 Model fit (solid line) to EXAFS data (points and dashed line) for glass compositions: (A-G) k^3 weighted $\chi(k)$ data, and (H-N) the Fourier Transform of $k^3(\chi(k))$, not corrected for phase shift. The vertical lines indicate the Fourier transform range in k and the fitting range in R. A through G are; NCZS 3, NCZS 3.5, NCZS 4, CaZn Base, Magnox and Blend glasses, respectively. H through N are also; NCZS 3, NCZS 3.5, NCZS 4, CaZn Base, Magnox and Blend glasses, respectively. Compositions of the glasses can be found in Tables I and II.

4.4 Discussion

4.4.1 Interpretation of XANES Data

Figure 4.2 illustrates that all of the glass spectra obtained exhibit XANES spectral features and edge positions consistent with that of hemimorphite, where Zn occurs solely in tetrahedral sites. This indicates that the local environment of Zn in the glasses is comparable to that in hemimorphite and thus Zn is present in the glasses in tetrahedral coordination. This conclusion is supported by previously published Zn K-edge XANES for hardystonite, $Ca_2ZnSi_2O_7$, a mineral in which Zn is also 4 coordinated, and for which the XANES exhibits an absorption edge at the same energy (9659 eV) as the glasses and the mineral standard, hemimorphite, studied here. [69]

4.4.2 Interpretation of EXAFS Data

Figures 4.3 and 4.4 allow comparison of both $k^3\chi(k)$ and FT $k^3\chi(k)$ data of the mineral standard, hemimorphite, and glass materials. The $k^3\chi(k)$ data of the glass materials show smooth oscillations, whereas that of hemimorphite exhibits more complex oscillations indicative of constructive and destructive interference arising from the presence of long range periodicity. [116] In the case of hemimorphite, close examination of Figure 4.3 reveals two distinct oscillations as shown by the split features between 5.5 - 7.0 $Å^{-1}$ and 7.5 - 9.0 $Å^{-1}$ which are contributions from next nearest neighbours in the mineral standard. As shown in Figure 4.4, this feature is not clearly resolved in the $k^3\chi(k)$ data from the glasses, indicating disorder in the interatomic distance of next nearest neighbours (as expected for an amorphous material). These results are comparable to those obtained by McKeown *et al*. who compared Zn K-edge EXAFS for hardystonite and borosilicate glasses. [69]

The FT $k^3\chi(k)$ data of the hemimorphite and the glass materials are similar at distances below 2.0 Å, as shown in Figures 4.3 and 4.4, comprising a single feature located at 1.5 Å associated with four Zn-O scattering paths (note: radial distances uncorrected for phase shift). However, considerable differences between the FT $k^3\chi(k)$ data of the hemimorphite and the glass materials are observed near 3.0 Å, the magnitude of this feature is consistently greater than that of the Fourier transform ripples and is associated with scattering by next nearest neighbour species, as discussed above. In the case of hemimorphite, both Zn-Si and Zn-Zn scattering paths were required to fit this feature, whereas only Zn-Si scattering paths could be

fitted in the case of the glass materials. Attempts to fit Zn-Zn scattering paths in isolation, or in combination with Zn-Si paths, resulted in implausible values of path degeneracies in the case of the glass materials.

Analysis of EXAFS data from glass materials points to the presence of ZnO_4 species participating in formation of the silicate glass network, independent of composition. The determined Zn-O contact distances, 1.95 ± 0.01 Å, are consistent with tetrahedral Zn species in oxide glasses [68; 69; 71; 137]; for ZnO_6 species, the Zn-O interatomic distance is generally greater than 2.0 Å. [137] Furthermore, the refined Zn-O path degeneracy and bond valence sum, are consistent with the presence of ZnO_4 species in all glasses, as shown in Table 4.4. The mean squared displacement parameters associated with the Zn-O path are similar for the hemimorphite and the glasses, indicating comparable structural disorder. The refined degeneracy associated with the Zn-Si path is significant for all glasses, within estimated precision, consistent with the presence of ZnO_4 species situated within the silicate network. The refined Zn-Si path lengths and mean squared displacement parameters are independent of glass composition, within precision, from which we conclude that Zn coordination environment is broadly similar in the glasses studied.

The simple soda lime zinc silicate (NCZS) and alkali zinc silicate (NZS) glass compositions investigated in this study were selected to enable comparison of the experimentally determined structural model with that derived from previous molecular dynamics simulation of the same materials. [130; 138] The Zn-O distance of 1.95 ± 0.02 Å determined from analysis of EXAFS data is identical to that predicted from molecular dynamics simulations, consistent with the presence of ZnO_4 species. Furthermore, molecular dynamics simulations demonstrated the network forming role of Zn, by sharing of oxygen atoms which bridge ZnO_4 and SiO_4 tetrahedra. However, the Zn-Si contact distance of ca. 3.58 ± 0.03 Å determined from analysis of EXAFS data is significantly greater than the weighted mean contact distance ~3.23 Å determined from molecular dynamics simulations of nominally identical glasses and that of 3.29 Å reported for hemimorphite. [132]

Molecular dynamics simulation of the glass with composition $Na_2ZnSi_3O_8$ identified the presence of edge sharing Si and Zn polyhedra, each with more than four coordinated oxygens. In the case of soda lime silica glass containing 14.5 mol% ZnO, clustering of ZnO_4 species was reported and the formation of edge-sharing polyhedra was apparent (see Figure 6 in Ref. (138)). The presence of such edge sharing polyhedra could be expected to increase the efficiency of atomic packing in the structures determined from molecular dynamics calculation which might offer an explanation for the shorter Zn-Si contact distance.

Attempts to fit a Zn-Zn scattering contribution to EXAFS data for the soda lime silica glass containing 14.5 mol% ZnO were unsuccessful. Such paths would be expected to contribute substantially to photoelectron scattering in the presence of significant clustering of ZnO_4 units, and we are, therefore, unable to confirm the presence of such clustering on the basis of the present data. Alternatively, the actual charge compensating role of alkali and alkaline species may differ between the experimental and modelled glasses, which could also lead to different Zn-Si contact distances. Figure 4.5 gives a proposed structure about zinc in the sodium zinc silicate glasses studied. The bond valence unit for Zn in Figure 4.5 is 2.1 ± 0.1. The dashed lines of the modifying cations of Na suggest that the alkali can compensate the charge of non bridging oxygen associated to either the Si or Zn.

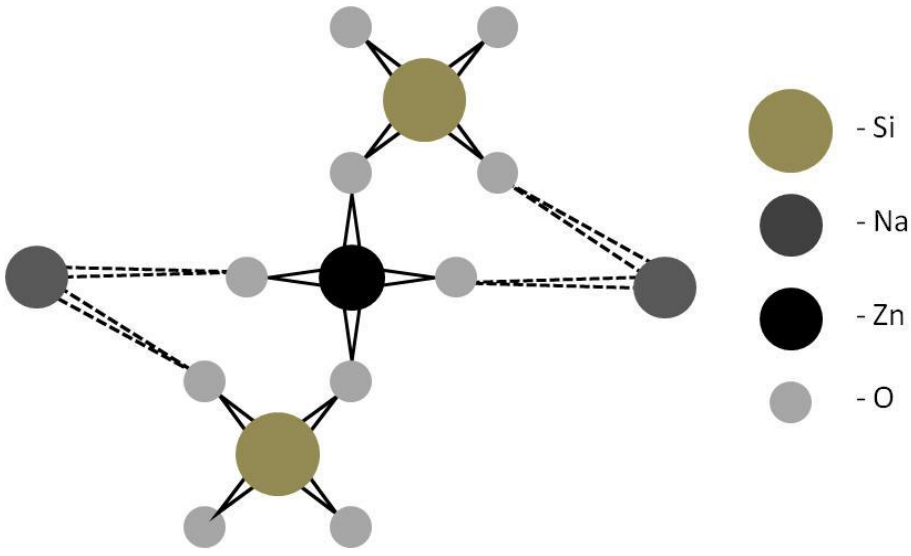

Figure 4.4 Proposed structure about Zn in sodium zinc silicate glasses.

4.4.3 Interpretation of the Property Measurements

The increase in T_g with the increase in ZnO for the NCZS glasses do not correlate to that of Lusvardi *et al.* where the T_g decreases with an increase in the mol fraction of ZnO. [67] Table 4.5 gives an increase in T_g for the NCZS glasses with an increase in ZnO. This could be due to Lusvardi *et al.* melting their glasses at 1550 °C which would increase the volatilisation of alkali within the melt. [67] The compositions given in their paper did not state they were the as analysed compositions, but the "experimental compositions" (i.e. nominal batched compositions) which likely explains the difference in the T_g of the glasses studied by Lusvardi *et al.* and the glasses in this study. [67] The density of the NCZS glasses are similar,

within ± 0.1 g cm^{-3}, to that of Lusvardi *et al.* suggesting an alkali zinc silicate glass within a similar composition range as the glasses in this study. (67)

The increase in T_g as given in Table 4.5 does; however, suggest that the clustering of the ZnO_4 tetrahedra decreases with less alkali in the nominal (batched) composition of the glass. The densities of the glasses in this study are all identical (within error), which implies that the clustering of the ZnO_4 tetrahedron may be similar for all alkali zinc silicates.

Although this study has made a considerable advance in validating molecular dynamics simulations of glass structure, by providing conclusive evidence for the presence of ZnO_4 polyhedra in a network forming role, it is clear that further investigation is required to resolve apparent differences in the geometry of the local cluster formed.

4.5 Conclusions

Zn K edge X-ray absorption spectroscopy was applied to determine the Zn coordination environment in model inactive UK HLW glasses. Comparison of XANES data between crystalline hemimorphite and glass materials, pointed to the presence of Zn^{2+} in tetrahedral coordination by oxygen, based on consideration of the precise energy of the absorption edge and similar post-edge features, which were damped in the case of the glass materials consistent with an amorphous structure. Quantitative analysis of EXAFS data provided conclusive evidence for the presence of ZnO_4 species participating in network formation, linking, on average, to 2 ± 1 SiO_4 units *via* bridging oxygen atoms. Excellent quantitative agreement was observed between the Zn-O contact distance and coordination number determined from EXAFS and previous Molecular Dynamics simulations of glasses with the same nominal composition. Our analysis also provides evidence in support of the network forming role of Zn as predicted from Molecular Dynamics simulation, but we were unable to confirm the predicted clustering of Zn species at high Zn concentration in simple soda lime silica glasses.

5.0 Flow Through Durability Experiments of Simulated UK High Level Waste Glasses

5.1 Introduction

In order to predict the performance of nuclear waste glasses in repository systems, an understanding of the glass dissolution rate in the context of environmental surroundings is needed. Several methods are currently used for analysis of the glass dissolution rate (single pass flow through test, product consistency test, and monoliths exposed to water) and surface alteration product formation (vapour hydration test, and monoliths exposed to water). Reaction rates of glass dissolution are generally modelled using transition state theory (TST) which is applicable to surface reaction-controlled processes; however, for glass dissolution, modelling of the corrosion rate using a simplified TST rate law has been employed by several authors and is given by equation 5.1:

Equation 5.1 $$R_i = k_0 v_i e^{-E_a/RT} a_{H^+}^n \left[1 - \left(\frac{Q}{K}\right)^\sigma\right]$$

where R_i is the release rate of glass component *i*, k_0 is the intrinsic rate constant, v_i the stoichiometric coefficient for element *i*, E_a is the activation energy, RT the product of the gas constant and the absolute temperature, $a_{H+}{}^n$ the hydronium ion activity, Q the activity product of the rate-limiting reaction K the equilibrium constant for the reaction, and σ is the overall reaction order. [16] The final term in square brackets describes the thermodynamic reaction affinity which implies reactions governing dissolution are reversible (thermodynamic equilibrium is possible). However, it is well known that for glasses the overall dissolution process is irreversible and no overall equilibrium is attainable. [16] For the given equation, it is assumed there is a reversible microscopic reaction that is rate limiting, and, as suggested by Grambow, it is the hydrolysis of siloxane bonds. [85]

Studies investigating the dissolution rate of borosilicate glasses containing UK simulated nuclear wastes have been performed using the single pass flow through (SPFT) test method with the experiments geared towards studying the specific role of aqueous Si and Al species during glass dissolution, and also an inter-laboratory study of the reproducibility of the SPFT method. [16; 139] It is widely accepted that the corrosion rate of silicate glass is influenced by temperature, pH, and ion exchange. The main contributor to the dissolution rate of silicate glasses is; however, the concentration of Si in solution. Other components in solution may

also have an effect on the glass dissolution rate, and this is commonly referred to as solution feedback. [139]

The SPFT procedure was designed to measure glass dissolution rates with limited solution feedback effects using a continuous flow of fresh solution contacting the glass surface. The dissolution rate is determined by measuring the concentrations of soluble glass components in solution from a reaction cell and solution flow rate. Since there exists a minimum concentration of glass components required for determination of the glass dissolution rate, the SPFT cannot be conducted with complete exclusion of the effects from solution feedback.

Previous results for UK glasses have shown that at low pH, glass dissolution is governed by reactions at non-Si sites while B, Al and modifier cations are selectively leached from the bulk glass. [16] Gel-layers were also shown to develop at the glass surface and it was suggested that the rate of the congruent dissolution process is influenced by the activity of silicic acid. Further studies by Abraitis *et al.* have shown that the dissolution rate is influenced by dissolved Al and also that the very low 'long term' dissolution rates in static batch experiments, such as the PCT and MCC-1 test, reflect near saturation conditions not attained during the SPFT tests. [16] However, it should be noted that the glasses studied by Abraitis *et al.* were grossly phase separated, which can be seen in optical photomicrographs of the glass surface in Figure 3.5 of reference (14).

This study makes use of the SPFT test in order to gain valuable information on simulated UK HLW glasses considered for use in vitrification of UK HLW. The dissolution rate with changes in temperature and pH were analyzed with SPFT for both MW+25wt% Blend and MW+30wt% Blend simulated nuclear waste glasses. In this study only the high pH regime was studied due limited funding and time available for the SPFT experiments. It should be noted that in order to fully understand the mechanisms of dissolution at low pH one should perform the SPFT at low, neutral and high pH.

5.2 Experimental Procedure

Two glasses were used for the single pass flow through experiments; MW+25wt% Blend and MW+30wt% Blend simulated nuclear waste glasses. Glasses were prepared from a baseline glass frit and a blended simulated nuclear waste calcine of which both were supplied by National Nuclear Laboratory in Sellafield, UK. The calcine was added to the baseline glass frit to give compositions as tabulated in Table 5.1. After batching, the frit and calcine was mixed by hand in a HDPE bottle for 2 min and then half of the charged batch was added to a

pre-heated mullite crucible and placed in a furnace at 1060 °C. After ~10 min, the batch was melted and the second half of the batch added to the crucible and allowed to sit for 1 h. After 1 h batch free, a mullite stirrer was lowered into the melt and the melt stirred for 4 h. After stirring, the glass was cast into a block using a pre-heated stainless steel mould, annealed at 500 °C for one h, and then cooled at 1 °C min^{-1} to room temperature. Glasses were crushed and powdered using a manual percussion mortar and then size fractioned with a stainless steel sieve to 75 μm < X < 150 μm. After sieving a magnet was passed through the powdered glass to remove any steel contamination from the percussion mortar. This gave an average glass particle radius of 5.63 x 10^{-5} m. Density measurements of both glasses were performed using Archimedes method yielding a density of 2.77 ± 0.01 g cm^{-2} for both MW+25wt% Blend and MW+30wt% Blend simulated nuclear waste glasses. Glass powders were cleaned according to the ASTM standard for the product consistency test. [118]

Table 5.1 Analysed compositions in wt % of MW+25wt% Blend and MW+30wt% Blend simulated nuclear waste glasses used for the flow through durability experiments at Pacific Northwest National Laboratory.

	MW+25 wt% Blend	MW+30 wt% Blend
SiO_2	46.28	44.33
B_2O_3	18.30	17.74
Na_2O	8.12	7.74
Li_2O	4.81	4.34
Al_2O_3	1.87	2.35
BaO	1.22	1.38
CeO_2	1.24	1.38
Cr_2O_3	0.37	0.46
Cs_2O	1.61	1.99
Fe_2O_3	1.87	2.06
Gd_2O_3	3.86	4.17
La_2O_3	0.67	0.73
MgO	1.34	1.64
MoO_3	2.02	2.48
Nd_2O_3	1.81	1.86
NiO	0.28	0.47
Pr_2O_3	0.47	0.46
RuO_2	0.49	0.51
Sm_2O_3	0.28	0.33
SrO	0.32	0.36
TeO_2	0.28	0.30
Y_2O_3	0.10	0.10
ZrO_2	2.40	2.81
Total	100.0	100.0

Setup of the SPFT was performed using 1 L HDPE vessels to hold the buffer solutions for the test, Kloehn V6 syringe pumps, Savillex Teflon digestion vessels with lids having two ports and HDPE collection vessels all connected by PTFE tubing with a 1/8 in. inner diameter. Figure 5.1 gives pictures of A) the reaction vessels B) the Kloehn V6 Syringe pump and C) the actual setup after assembly.

Solutions used for the SPFT experiment were water based solutions buffered to a pH = 8.00 ± 0.05, 10.00 ± 0.05 and 12.00 ± 0.05 at room temperature (≈ 23 °C). For buffer solutions at pH = 8.00 ± 0.05 and 10.00 ± 0.05, Tris(hydroxymethyl)aminomethane (TRIS) was added to high purity H_2O to make 0.05 M TRIS which was pH adjusted with concentrated HNO_3 to either pH = 8.00 ± 0.05, or 10.00 ± 0.05 at 23 °C. For pH = 12.00 ± 0.05 at 23 °C, LiOH and LiCL were added to high purity H_2O to make a 0.01 M LiOH + 0.01 M LiCl solution which was pH adjusted with 0.01 M LiOH.

A 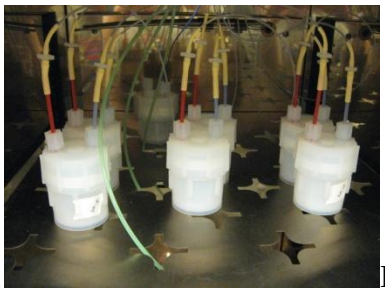 B  C 

Figure 5.1 A) reaction vessels used for SPFT tests B) Kloehn V6 syringe pumps used for controlling the flow rate through the reaction vessels and C) the actual SPFT setup after connecting the buffer solution, pump, reaction vessels and collection vessels with the PTFE tubing.

The procedure for SPFT experiments is described in detail in Chapter 3 and also in Reference (140). For each experiment, glass powder between 75μm < X < 150 μm was placed in the reaction vessel located in an oven at a pre-determined temperature. The buffer solution was continuously pumped from the buffer solution vessel, through the reaction vessel and into the collection vessel at a pre-determined rate. The first tests on MW+25wt% Blend and MW+30wt% Blend simulated nuclear waste glasses were at a flow rate of 10, 20, 40, 60, 80, and 125 mL/day to give flow rate, Q, per surface area of glass, S, at values: 6.00 x

10^{-7}, 2.40 x 10^{-6}, 6.00 x 10^{-6}, 1.60 x 10^{-5}, 4.80 x 10^{-5}, 9.60 x 10^{-5}, 3.20 x 10^{-4} [1] and 5.00 x 10^{-4} m s^{-1}, respectively. Sampling of each effluent was performed and the mass of the collection vessel was recorded at each sampling time to determine the flow rate after which aliquots of each sample were taken and acidified before being analysed by ICP. Each experiment ran for approximately 30 days in order for the glass in each reaction vessel to reach steady state dissolution.

5.3 Results

5.3.1 Q/S Measurements

Before performing experiments to understand steady state dissolution with changes in pH and temperature, the dependence of the dissolution rate with changes in flow rate (Q) to the sample surface area (S) was determined by varying either the flow rate or the mass of the sample powder used in the reaction vessel during the SPFT. By varying Q/S, one can change the chemical potential between the glass and solution. If Q/S is too low, effects from ion exchange become observable, as in the PCT or MCC-1 experiments, due to the higher concentration of solution species. Figure 5.2 gives the results of the Q/S measurement on MW+25wt% Blend simulated nuclear waste glass. The circled data points in Figure 5.2 at approximately Log Q/S = -8.1 and -8.4 do not correlate to Q/S data previously found by Abraitis *et al*. on MW+Magnox simulated waste glass in which there is a continuous increase in the normalised rate up to approximately Log Q/S = -7.5 where upon the normalised rate becomes constant. [(141)] If the highlighted data points in Figure 5.2 are set aside, the data appears to be similar to work by Abraitis *et al.* where there is a plateau in the normalised rate at values of Log Q/S ≥ -7.5. Previous Q/S results by McGrail *et al*. at approximately pH = 9 and 40 °C also became constant at values similar to MW+25wt% Blend simulated waste glass (Log Q/S = -7.5). [(142)] McGrail *et al.* also obtained a similar start of the plateau of the normalised rates near Log Q/S = -7.5. [(142)]

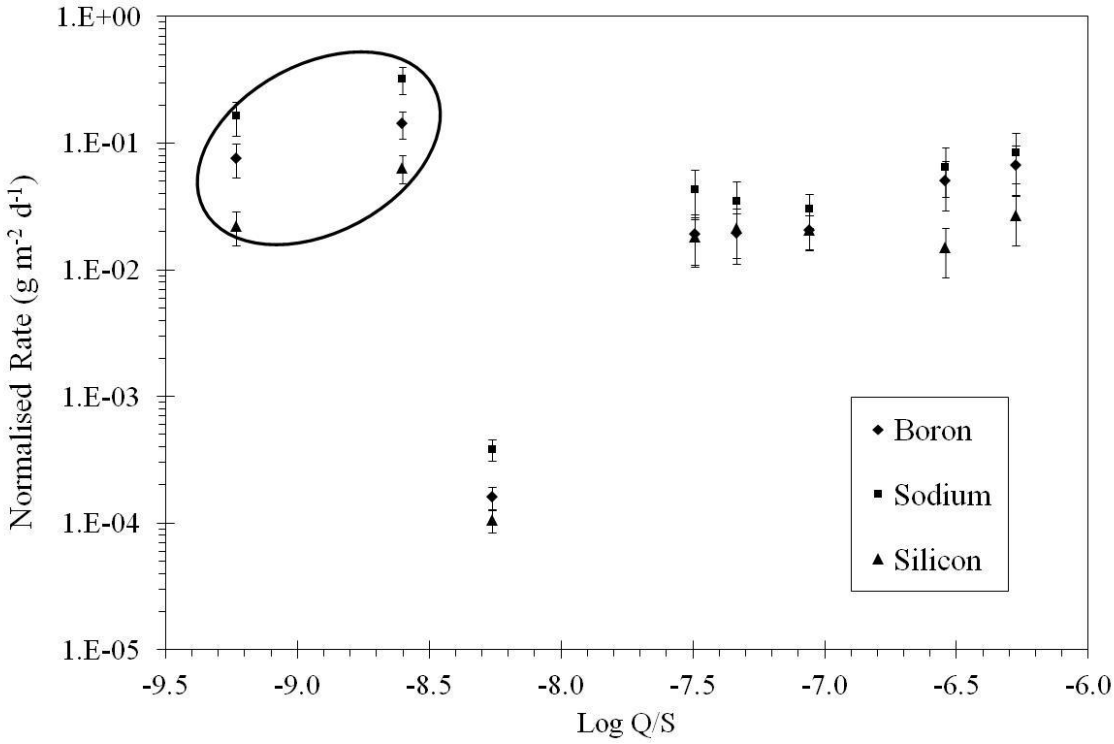

Figure 5.2 Flow rate of solution (Q) per sample surface area (S) results for MW + 25wt% Blend simulated waste glass at 40 °C.

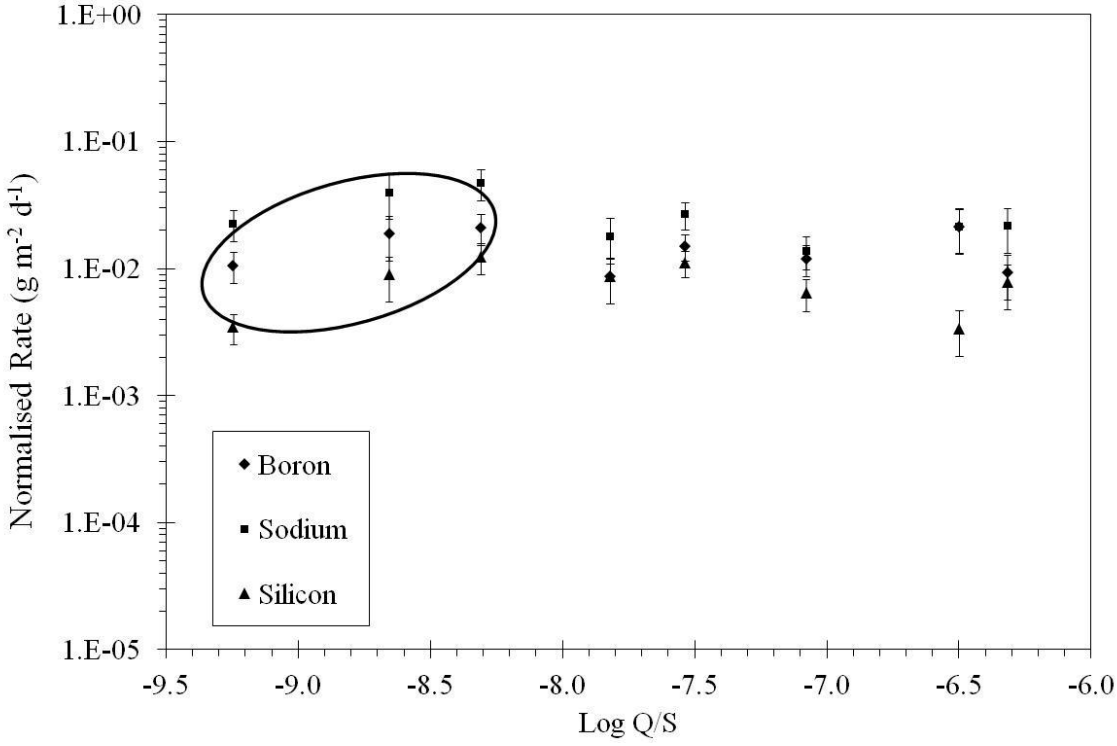

Figure 5.3 Flow rate of solution (Q) per sample surface area (S) results for MW + 30wt% Blend simulated waste glass at 40 °C.

The data points highlighted in Figure 5.2 which do not follow trends previously seen by Abraitis *et al.* and McGrail *et al.* can be attributed to problems with the syringe pumps during the experiment. [141; 142] The main issue with the pumps was air leaks that would not allow solution to be pumped at a consistent rate to the reaction vessel. This occurred several times for these two samples causing artificially high NR.

Figure 5.3 shows an increase of NR with an increase in Q/S for MW+30wt% Blend simulated waste glass. Again, pump problems occurred during the Q/S measurements for flow rates of Log Q/S < 8.0. Previous work by Abraitis *et al.* on a similar glass (MW+Magnox) and results by McGrail *et al.* at the same temperature of 40 °C, show that a constant NR is expected to occur above Log Q/S = -7.5. [141; 142]

At lower flow rates (Log Q/S < -8.0) for the MW+30wt% Blend simulated waste glass, there were again, problems with the pumps staying at the target flow rate as can be seen for the circled data in Figure 5.3. However, the Q/S measurements all appear to be constant above Log Q/S = -7.0 with a normalised rate of approximately 1.5 x 10^{-2} g m^{-2} d^{-1} as previously obtained on the similar glasses studied by Abraitis *et al*. (MW+Magnox), McGrail *et al*., and Pierce *et al*. [141; 142; 143] Since previous work shows similar regions of the Q/S plateau as the normalised rate in this study, Log Q/S = -6.5 ± 10% was used for the for MW+Blend (both 25 wt% and 30 wt%) simulated UK nuclear waste glass for studying changes to the dissolution rate with pH and temperature. By using a higher Q/S, one can account for increases in temperature which will increase the start of the Q/S plateau (increasing the independent rate regime) for steady state dissolution.

From personal communication with E. Pierce, it is a common experience for older syringe pumps and pump valves, such as the pumps used for the Q/S measurement in this study, to have problems keeping a constant vacuum during the experiment resulting in air leaks and inconsistent flow rates. [144] In order to minimize the issues seen during this study one must try to use new syringe pumps and pump valves which were not available at the time of this study. [144]

5.3.2 Effect of Temperature and pH

Several measurements of the normalised dissolution rate (NR) were performed at steady state conditions at different temperatures and pHs to study the effect different conditions have on the dissolution rate of MW+25wt% Blend and MW+30wt% Blend simulated waste glasses. Table 5.2 and 5.3 gives the power-law coefficients (η) and the intrinsic rate constant (*k*) as a

function of temperature based on steady-state dissolution of Al, B, Na and Si for both MW+25wt% Blend and MW+30wt% Blend simulated waste glasses, respectively.

The power-law coefficient was calculated by linear regression of the Log NR vs pH of Al, B, Na and Si at each temperature. The fit of the data, R^2, is also given in Table 5.2. Careful inspection of Table 5.2 for MW+25wt% Blend simulated waste glass gives an average B power-law coefficient (η_B) of 0.36 ± 0.5 (unitless), which is similar (within error) to the values reported by McGrail *et al.*, Abraitis and Pierce *et al.* calculated for their glasses. [14; 142; 143] The B power-law coefficient (η) for MW+30wt% Blend simulated waste glass resulted in a slightly higher value than MW+25wt% Blend of 0.38 ± 0.08 (unitless). The power-law coefficient of other ions for MW + 30wt% Blend as compared to MW+25wt% Blend simulated waste glass also showed a higher variability between temperatures than the results by Pierce *et al.* [144] The overall averages of η for both MW+25wt% Blend and MW+30wt% Blend simulated waste glass were similar (within error) to previous results and suggest that the power-law coefficient is not temperature dependent within the precision of this experiment.

Table 5.2. Estimate of the power-law coefficients (η) as a function of temperature based on the steady-state release of Al, B, Na and Si at a pH = 10 at 23 °C from MW+25wt% and MW+30wt% Blend Simulated waste glass.

MW + 25 wt% Blend Simulated Waste Glass												
T (°C)	η_{Al}	±	R^2_{Al}	η_B	±	R^2_B	η_{Na}	±	R^2_{Na}	η_{Si}	±	R^2_{Si}
23	0.45	0.05	0.91	0.37	0.04	0.90	0.40	0.04	0.78	0.47	0.05	0.93
40	0.51	0.05	0.93	0.38	0.04	0.91	0.46	0.05	0.89	0.48	0.05	0.93
70	0.61	0.13	0.86	0.34	0.07	0.98	0.54	0.71	0.99	0.42	0.06	1.00
MW + 30 wt% Blend Simulated Waste Glass												
T (°C)	η_{Al}	±	R^2_{Al}	η_B	±	R^2_B	η_{Na}	±	R^2_{Na}	η_{Si}	±	R^2_{Si}
23	0.52	0.10	0.93	0.40	0.08	0.86	0.44	0.09	0.83	0.49	0.10	0.89
40	0.49	0.10	0.95	0.36	0.07	0.92	0.50	0.10	0.97	0.50	0.10	0.99
70	0.56	0.11	0.96	0.36	0.07	0.99	0.42	0.08	0.98	0.35	0.07	0.70

Table 5.3 gives the intrinsic rate constant (*k*) for MW+25wt% Blend and MW+30wt% Blend simulated waste glasses. The intrinsic rate constant, k_i, was calculated from equation 5.2;

Equation 5.2 $$k_i = r / (10^{\eta[pH]})$$

Where k_i is the intrinsic rate constant base on element *i* (g m^{-2} d^{-1}), r is the dissolution rate (g m^{-2} d^{-1}) and η is the power-law coefficient (unitless). Inspection of Table 5.3 for

MW+25wt% Blend and MW 30wt% Blend simulated waste glasses shows a general increase in k_B from 5.8 ± 1.1 x 10^{-6} and 8.4 ± 1.7 x 10^{-6} g m^{-2} d^{-1} at 23 °C to 7.3 ± 2.3 x 10^{-4} and 6.6 ± 1.3 x 10^{-6} g m^{-2} d^{-1} at 70 °C, respectively, with an increase in temperature, which is similar to that of Pierce *et al.* [143] As shown in previous studies, there is a general increase in the dissolution rate with an increase in temperature. Since the power-law coefficient has been shown to not be temperature dependent for a pH that is nominally similar, there should be an increase in *k* with an increase in temperature according to Equation 5.2.

Table 5.3. Calculated intrinsic rate constants, *k* (g m^{-2} d^{-1}), as a function of temperature based on the steady-state release of Al, B, Na and Si at a pH = 10 at 23 °C from MW+25wt% and MW+30wt% Blend Simulated waste glass.

MW + 25 wt% Blend Simulated Waste Glass								
T (°C)	k_{Al}	R^2_{Al}	k_B	R^2_B	k_{Na}	R^2_{Na}	k_{Si}	R^2_{Si}
23	3.6 ± 0.7 x 10^{-6}	0.91	5.8 ± 1.1 x 10^{-6}	0.90	5.4 ± 1.1 x 10^{-6}	0.78	5.5 ± 1.1 x 10^{-7}	0.93
40	3.2 ± 0.6 x 10^{-6}	0.93	2.3 ± 0.2 x 10^{-5}	0.91	7.2 ± 1.3 x 10^{-6}	0.89	2.4 ± 0.6 x 10^{-6}	0.93
70	2.7 ± 0.5 x 10^{-5}	0.86	7.3 ± 2.3 x 10^{-4}	0.98	7.9 ± 1.6 x 10^{-5}	0.99	9.98 ± 2.1 x 10^{-4}	1.00
MW + 30 wt% Blend Simulated Waste Glass								
T (°C)	k_{Al}	R^2_{Al}	k_B	R^2_B	k_{Na}	R^2_{Na}	k_{Si}	R^2_{Si}
23	8.8 ± 1.8 x 10^{-7}	0.93	8.4 ± 1.7 x 10^{-6}	0.86	1.1 ± 0.2 x 10^{-5}	0.83	2.9 ± 0.6 x 10^{-7}	0.89
40	5.7 ± 1.1 x 10^{-6}	0.95	5.6 ± 1.1 x 10^{-5}	0.92	1.1 ± 0.2 x 10^{-5}	0.97	3.3 ± 0.7 x 10^{-6}	0.99
70	6.0 ± 1.2 x 10^{-5}	0.96	6.6 ± 1.3 x 10^{-4}	0.99	5.7 ± 1.1 x 10^{-4}	0.98	6.8 ± 1.4 x 10^{-3}	0.70

Figure 5.4 and 5.5 give the normalised dissolution rate with pH at each temperature based on Si and B release for MW+25wt% Blend simulated nuclear waste glass, respectively. Both Figure 5.4 and 5.5 show a general increase in the normalised dissolution rate with an increase in pH and Temperature. Figures 5.6 and 5.7 give the normalised dissolution rate with pH at each temperature based on Si and B release, respectively, for MW+30wt% Blend simulated nuclear waste glass. Both Figure 5.6 and 5.7, as expected, show a general increase in the normalised dissolution rate with an increase in pH and Temperature. The Log NR_{Si} and Log NR_B at pH = 10 at 23 °C for MW+25wt% and MW+30wt% Blend glasses are -2.1 ± 0.4, -1.9 ± 0.4 and -2.0 ± 0.4, -1.9 ± 0.4 g m^{-2} d^{-1}, respectively, which for Si, is similar (within error) to that of Abraitis who gives Log NR_{Si} = -2.07 g m^{-2} d^{-1} for pH = 9.9 at room temperature (23 °C). The NR_B for MW+25wt% Blend is identical to that reported by Abraitis (within error) at Log NR_B = -1.96 g m^{-2} d^{-1} for pH = 9.9 at room temperature (23 °C). [14]

Figure 5.8 gives the NR with respect to Al, Na, Si and B with changes in temperature at pH = 8, for MW+25wt% Blend simulated waste glass. As expected, the NR (for all elements) shows a general decrease with a decrease in temperature (increase in 1000 T^{-1}) for all pH ranges. Figure 5.9 and 5.10 gives NR vs temperature at pH = 10 and 12, respectively, for MW+25wt% Blend simulated HLW glass. Figures 5.11 through 5.13 show the normalised dissolution rate with temperature at pH values of 8, 10 and 12, respectively, for MW+30wt% Blend simulated waste glass. Again, the dissolution rate of all elements has a general decrease with a decrease in temperature for all pH ranges which is consistent with previous studies of Abraitis, Pierce *et al.* and McGrail *et al.* [14; 142; 143]

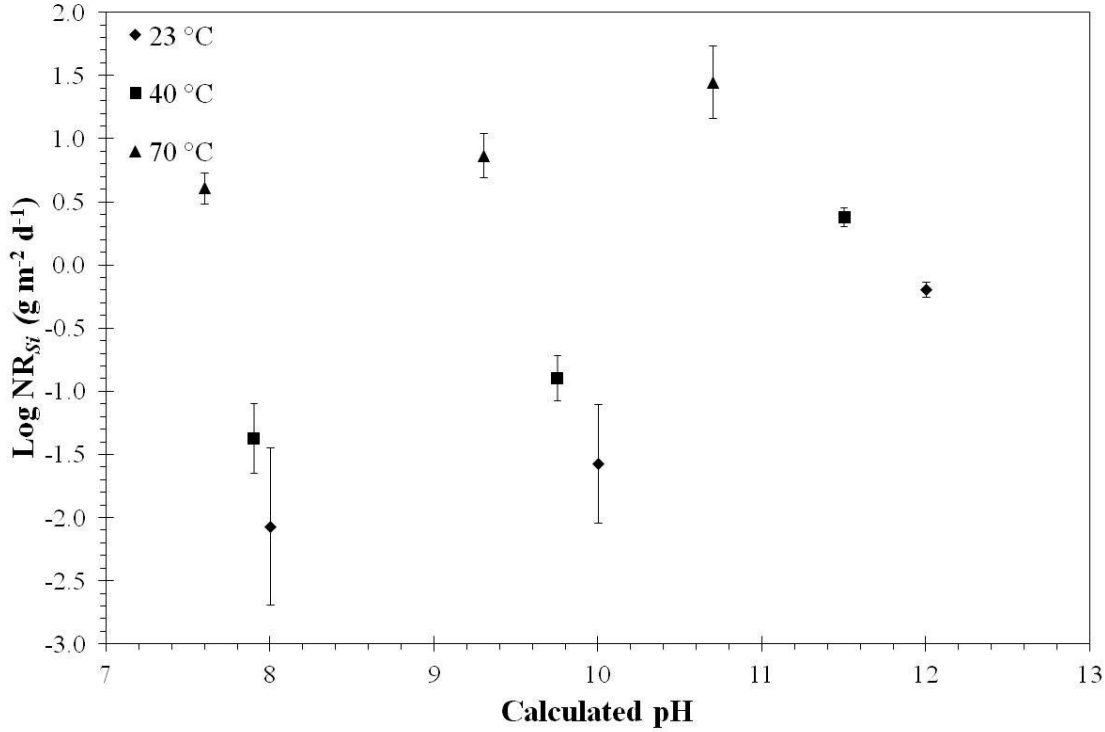

Figure 5.4 Normalised dissolution rate, based on Si release, as a function of calculated pH at different temperatures for MW+25wt% Blend simulated waste glass.

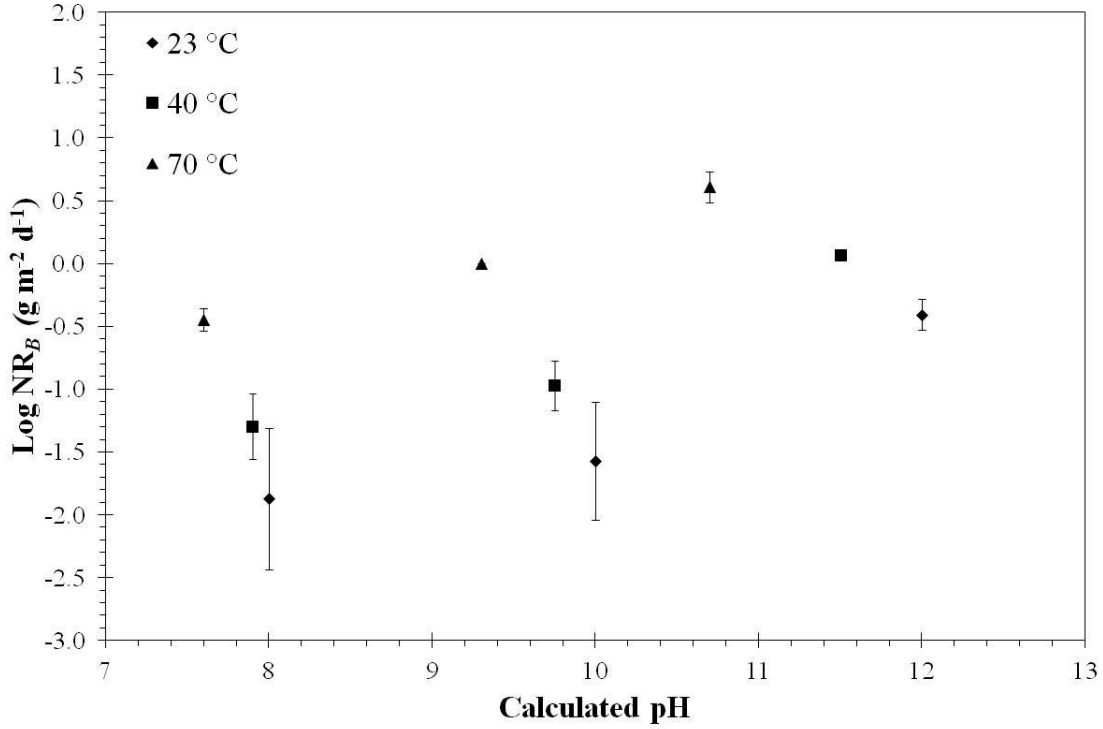

Figure 5.5 Normalised dissolution rate, base on B release, as a function of calculate pH at different temperature for MW+25wt% Blend simulated waste glass.

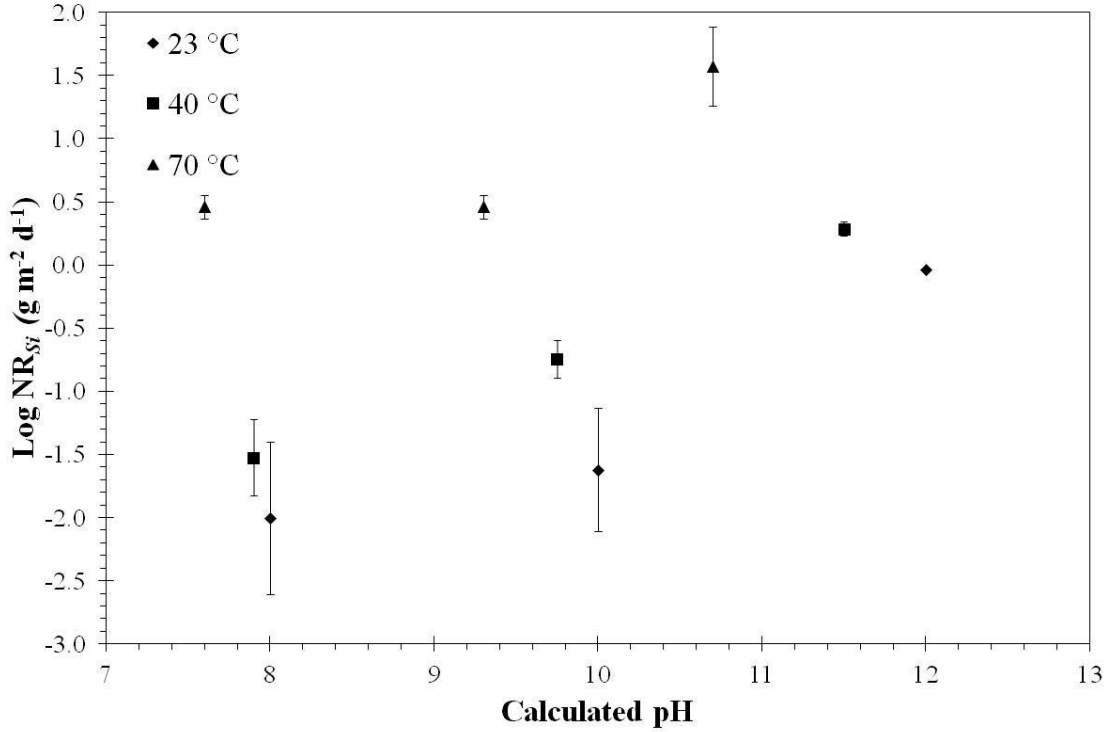

Figure 5.6 Normalised dissolution rate, based on Si release, as a function of calculated pH at different temperatures for MW+30wt% Blend simulated waste glass.

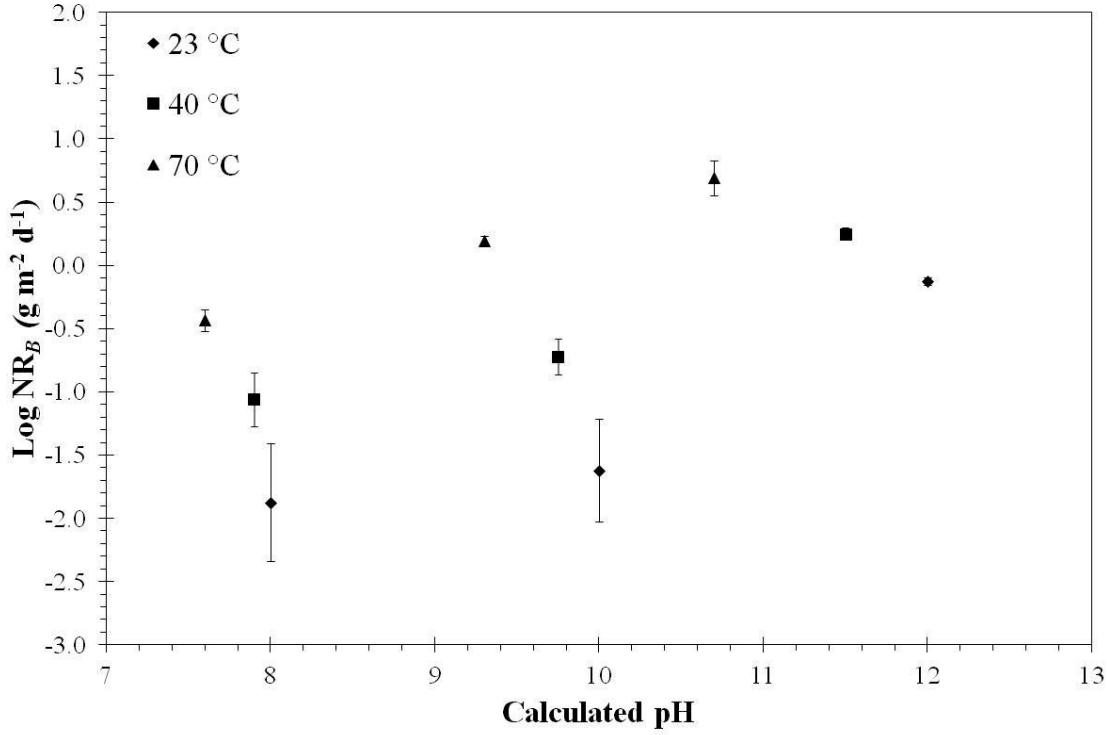

Figure 5.7 Normalised dissolution rate, based on B release, as a function of calculated pH at different temperatures for MW+30wt% Blend simulated waste glass.

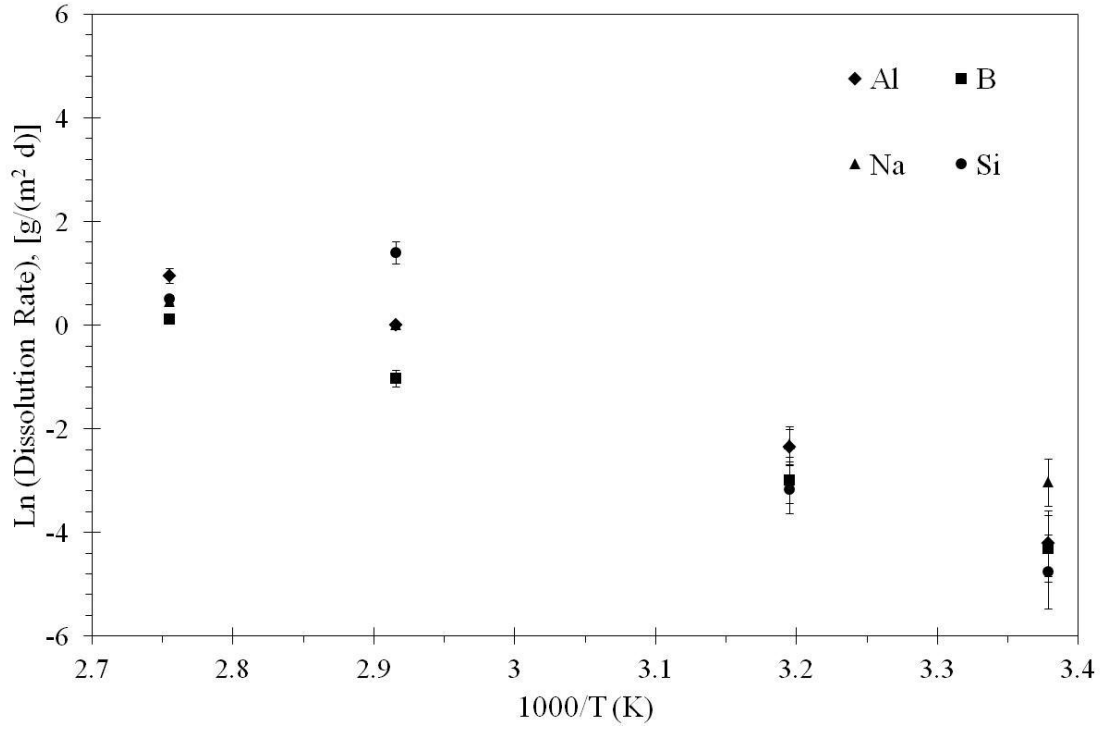

Figure 5.8 Normalised dissolution rate versus temperature at pH = 8 for MW+25wt% Blend simulated waste glass.

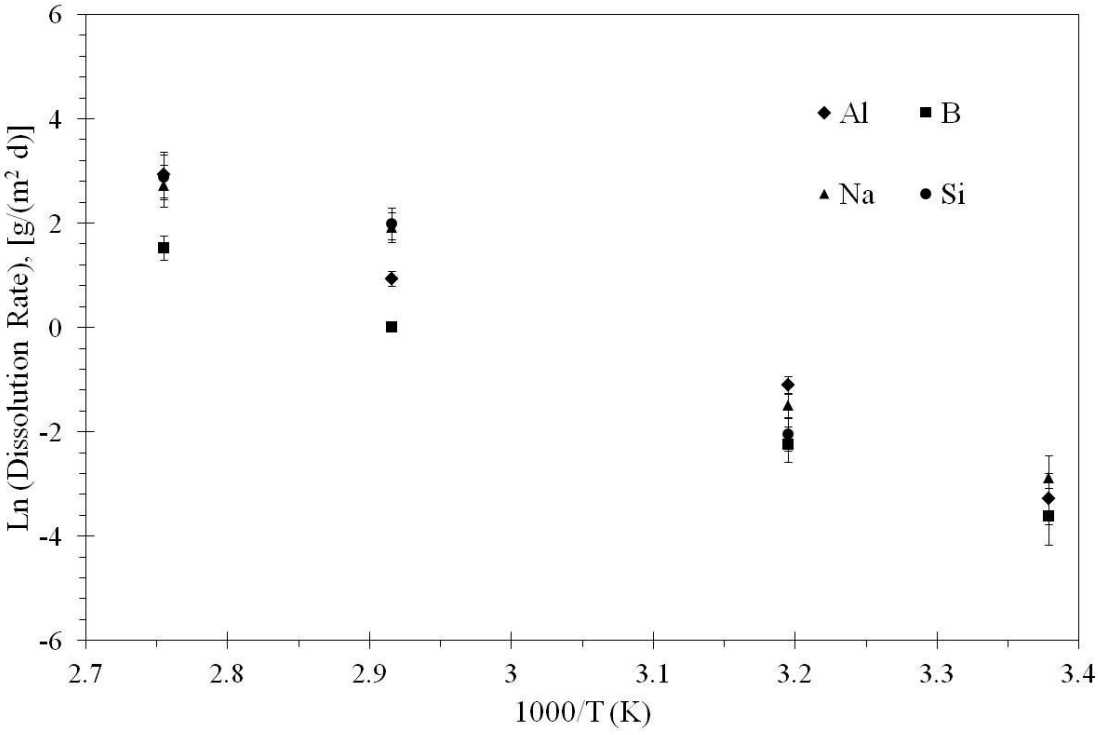

Figure 5.9 Normalised dissolution rate versus temperature at pH = 10 for MW+25wt% Blend simulated waste glass.

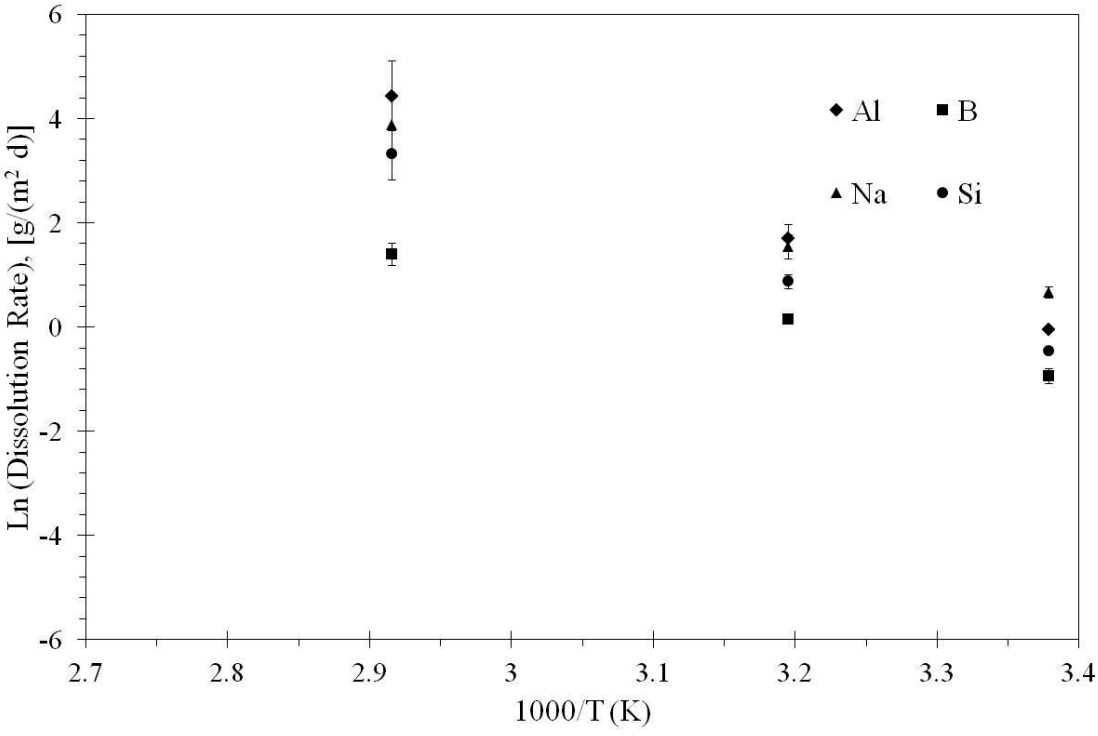

Figure 5.10 Normalised dissolution rate versus temperature at pH = 12 for MW+25wt% Blend simulated waste glass.

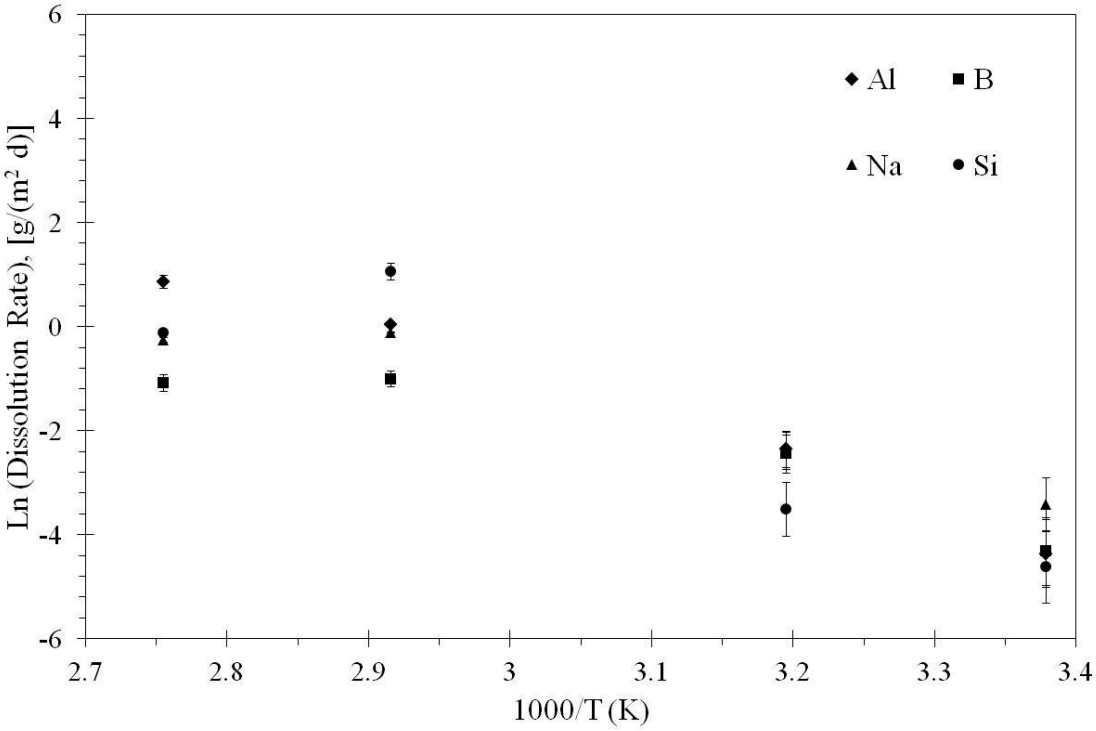

Figure 5.11 Normalised dissolution rate versus temperature at pH = 8.0 for MW+30wt% Blend simulated waste glass.

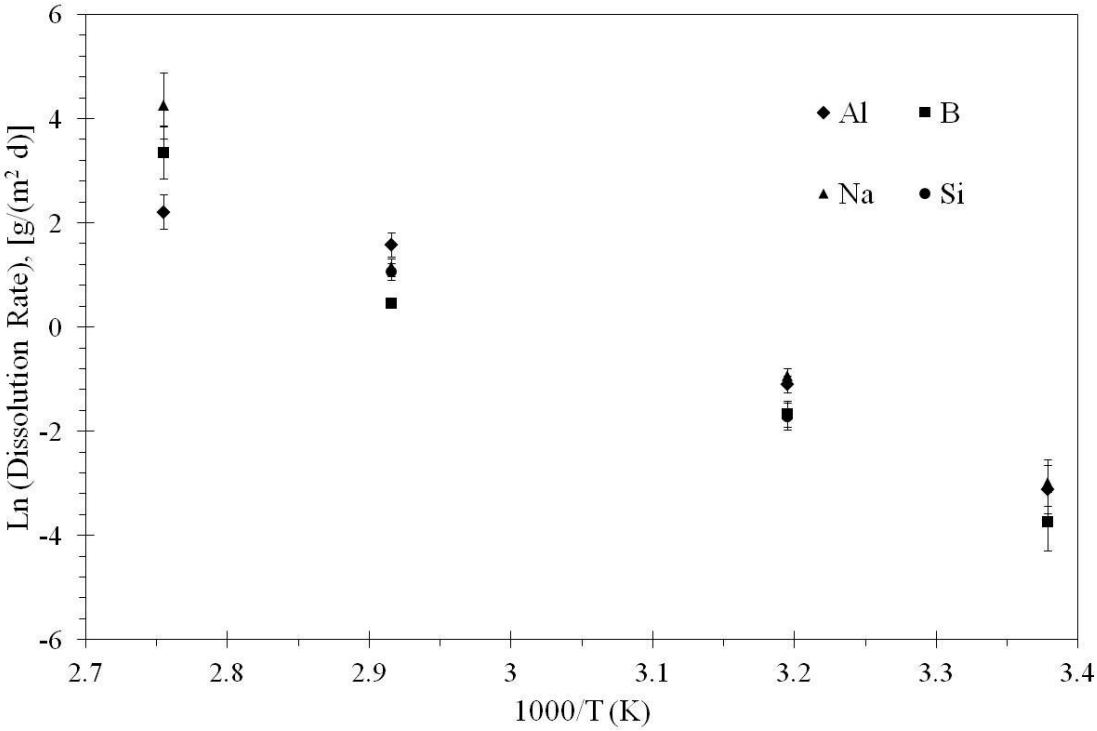

Figure 5.12 Normalised dissolution rate versus temperature at pH = 10.0 for MW+30wt% Blend simulated waste glass.

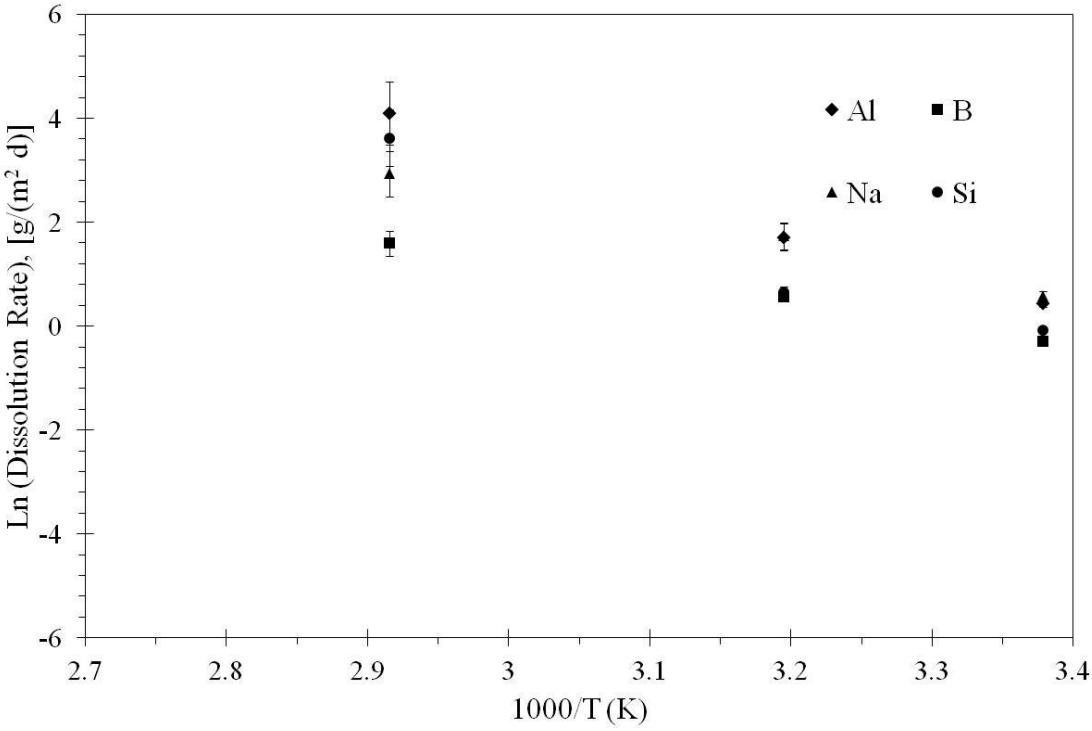

Figure 5.13 Normalised dissolution rate versus temperature at pH = 12.0 for MW+30wt% Blend simulated waste glass.

It was shown previously that there is a general increase in NR with an increase in temperature. [14; 15; 16; 141; 142; 143] The observed temperature dependence of the dissolution rate follows an Arrhenius curve which can be described by Equation 5.3.

Equation 5.3 $$r = Aexp\left(\frac{-E_a}{RT}\right)$$

Where r is the dissolution rate (g m^{-2} d^{-1}), A is the Arrhenius parameter (g m^{-2} d^{-1}), Ea is the activation energy (kJ mol^{-1}), R is the ideal gas constant (J mol^{-1} K^{-1}), and T temperature (K). Using the Arrhenius dependence of the dissolution rate with temperature, linear regression was performed using the dissolution rate vs temperature curve for Al, B, Na and Si in order to determine the activation energy (Ea) at each pH. Table 5.4 gives the activation energies associated to each regression curve and the associated correlations for Al, B, Na and Si for both MW+25wt% Blend and MW+30wt% Blend simulated waste glasses. The average activation energy (Ea) with respect to B and Si for MW+25wt% Blend is 52 and 84 kJ mol^{-1} K^{-1}, respectively. For MW+30wt% Blend simulated waste glass, Ea with respect to B and Si is 62 and 74 kJ mol^{-1} K^{-1}. The Ea with respect to B for both glasses are comparable to those for a surface-controlled reaction process that has an Ea between 41 and 84 kJ mol^{-1} K^{-1}. [145]

Table 5.4. Activation energies (Ea) for MW+25wt% Blend and MW+30wt% Blend simulated waste glass from regression analysis of the dissolution rate vs. temperature.

MW + 25 wt% Blend Simulated Waste Glass

pH	Ea_{Al} (kJ mol^{-1})	±	R^2_{Al}	Ea_B (kJ mol^{-1})	±	R^2_B	Ea_{Na} (kJ mol^{-1})	±	R^2_{Na}	Ea_{Si} (kJ mol^{-1})	±	R^2_{Si}
8	69	14	0.99	59	12	0.99	50	10	0.97	82	16	0.87
10	79	16	0.99	68	14	0.99	79	16	0.98	92	18	0.98
12	81	16	0.99	42	15	0.99	59	12	0.98	68	14	0.99

MW + 30 wt% Blend Simulated Waste Glass

pH	Ea_{Al} (kJ mol^{-1})	±	R^2_{Al}	Ea_B (kJ mol^{-1})	±	R^2_B	Ea_{Na} (kJ mol^{-1})	±	R^2_{Na}	Ea_{Si} (kJ mol^{-1})	±	R^2_{Si}
8	70	14	0.99	44	9	0.88	47	9	0.93	73	15	0.83
10	73	15	0.98	89	18	0.97	91	18	0.97	92	18	0.99
12	66	13	1.00	33	7	0.99	42	8	0.99	68	14	0.95

5.4 Discussion

The single pass flow through method is often used to measure the activation energy, ion-activity product along with the dissolution rate and is designed to measure reaction rates under tightly controlled, dilute solution environments. [142] In dilute solutions, dissolution of silicate glasses is subject to the common ion effect. This occurs when a solid precipitates in a solution containing the same ions released from the dissolving mineral. [142] It is widely accepted that saturation of common ions in solution will decrease the net rate of reaction relative to the rate in pure water. By removing solution and replacing it with pure water, the solution never reaches saturation and maintains the chemical affinity (Q/K value in Equation 5.1) at a value near zero. This allows determination of the intrinsic rate constant, *k*, and the activation energy, Ea. [142]

5.4.1 Steady State Dissolution of MW Blend

Determination of the dissolution rate at steady state conditions with respect to B and Si in this study had similar results as Abraitis, McGrail *et al*. and Pierce *et al*. where the plateau of the normalised rate occurred above Log Q/S = -8.0. [142; 143; 14] This is apparent at values of Q/S > Log = -7.5 in Figures 5.2 and 5.3. The Q/S measurements by Abraitis have a higher normalised dissolution rate at steady state conditions with a similar Q/S value as seen in Figure 5.2 and 5.3. This could be due to the heterogeneous glass samples which were tested by Abraitis. [14] If the samples were not completely homogenous, there could be regions of the glass that are of different composition and could result in a higher dissolution rate. Samples tested here were completely homogeneous; as confirmed by backscattered electron microscopy which is not shown here.

The two highlighted data points in Figure 5.2 which are higher than normalised dissolution rate at steady state conditions can be attributed to problems with the pumps used for the Q/S measurements where the solution in the reaction vessel became static for a period of time increasing the concentration of select elements in solution. In order to avoid issues with syringe pumps, one should use pumps which have been well maintained and cleaned correctly after each use. This will minimize issues with valves on the pump heads where the majority of air leaks occur, leading to decreased reliability.

Steady state conditions for glasses similar to MW+25wt% Blend and MW+30wt% Blend simulated waste glass as shown by McGrail *et al.*, Pierce *et al*. and Abraitis occurs near Log Q/S = -7.5. [14; 142; 143] Due to the compromised data shown in Figure 5.2 and 5.3, it is difficult to determine rate dependent/independent Q/S regimes due to compromised and limited data below Log Q/S = -7.5. The studies of rate dependence on flow rate from McGrail *et al.*, Pierce *et al*. and Abraitis using similar glass compositions as in this study give the author confidence that steady state conditions at 40 °C occur at Log Q/S ≥ -7.5. [14; 142; 144]

In order to determine which Q/S is needed for comparisons of temperature and pH of a glass sample, the flow rate per surface area needs to give a constant normalised release rate, NL in which no effects from ion exchange should be observable as was shown in Pierce *et al.* at Log Q/S < -8.5. [143] If there is a change in the NL with a change in Q/S, differences in pH and temperature cannot be compared to each other due to differences in the chemical affinity. At low values, such as Q/S < Log -7.5, NL decreases with a decrease in Q/S. As shown from previous results, at Q/S ≥ Log -7.5, NL becomes constant. [14; 142; 143] Due to the problems with the pumps used for the Q/S measurement in this study, a Q/S = Log -7.5 was used for measuring changes between the glasses with a change in temperature and pH.

The Q/S measurements in this study were performed at the same temperature (40 °C) but at a lower pH (approximately one pH unit) to Pierce *et al*. [143] It was shown previously by

McGrail *et al.* that a lower solution pH will increase the time needed to reach steady state dissolution at the same flow rate of solution. [142] In their study, a sample at pH = 5.9 had not reached steady state dissolution while the same samples in a solution of pH = 12.1 reached steady state conditions in less than 6 days. This suggests that the dissolution rate dependence on flow rate decreases at higher pH. It should also be noted that by decreasing the rate independence on Q/S at high temperature the rate will also be independent of Q/S at low temperatures.

It is generally assumed the dissolution rate is controlled by the breakdown of SiO_2 polymorphs. [142] When changing the concentration of Si in the composition of the pristine glass, one can assume the kinetic rate law parameters (η, *k* and Ea) will change due to the bonds available for hydration which can break up the glass network. With a higher concentration of network modifiers, such as Na, in the composition, the more non-bridging oxygens are available for hydration. This may cause an increase in the dissolution rate. Therefore, a change in the composition should result in a change in the minimum requirement for the dissolution rate to be independent of Q/S, albeit the observed differences could be small for families of similar glass compositions.

As stated previously, Abraitis performed the Q/S measurements on a glass composition related to the two glasses studied in this chapter: a British Magnox simulated HLW nuclear waste glass. [14] However, from inspection of the micrographs of the glass samples used for the SPFT measurements by Abraitis the British Magnox simulated HLW nuclear waste glass was heterogeneous and not homogenous as the glasses prepared in this study. [14] The heterogeneous samples could cause changes in the dissolution kinetics and cause the dissolution rate to increase due to changes in composition seen by the solution during congruent dissolution. Effecively, the dissolution rate will be dominated by the component of poorest durability. In a B rich environment, one could expect to see a more polymerised network as shown by the previous studies by Dell and Bray. [66] A polymerised network would increase the durability as compared to a network containing several non-bridging oxygen sites.

5.4.2 Temperature and pH Changes to MW Blend Dissolution

The forward or intrinsic dissolution rate in this study was determined by using SPFT dissolution studies in order to maintain steady-state conditions while comparing changes in pH and temperature for two different glass compositions. The intrinsic dissolution rate, R, as shown in Equation 5.1 above relates the effect of pH, temperature, saturation of solution and

the activities of solution species on glass dissolution and is essential in understanding mechanisms related to glass dissolution. Previous work by Bourcier *et al.* assigned the equilibrium constant to that of a simple silicate phase such as SiO_2, resulting in better agreement of the equilibrium constant for most silicate glasses. [146] This better agreement can be explained by the hydrated surface layer that is expected during glass dissolution for simple silicate phases. [99]

The simulated glasses in this study, MW+25wt% Blend and MW+30wt% Blend have a forward dissolution rate with respect to B at pH = 10 and 40 °C of 0.11 ± 0.03 g m^{-2} d^{-1} and 0.19 ± 0.08 g m^{-2} d^{-1}, respectively, as given in Table 5.2. Inspection of Table 5.2 illustrates that the difference between the NR_B for the glasses studied here is negligible, within error, suggesting the glasses do not show any significant changes in NR with a change in composition. This could be due to the subtle changes in the concentration for network forming constituents in this glass such as SiO_2, B_2O_3, and an intermediate of Al_2O_3 for these glasses. It is possible there is a slight increase in NR_B; however, the error associated with the values obtained make it difficult to confidently suggest any influence on the change in composition for the two glasses in this study. It is expected that larger changes in composition will directly influence the intrinsic dissolution rate.

Table 5.5 Normalized dissolution rate (g m^{-2} d^{-1}) for MW+25wt% and MW+30wt% Blend simulated UK HLW glasses with changing pH and temperatures.

pH	Temperature	MW+25wt% Blend		MW+30wt% Blend		ΔNR_B
	(°C)	NR_B (g m^{-2} d^{-1})	±	NR_B (g m^{-2} d^{-1})	±	(g m^{-2} d^{-1})
8	23	0.01	0.01	0.01	0.00	0.00
8	40	0.05	0.02	0.09	0.02	0.04
8	70	0.36	0.15	0.37	0.09	0.01
10	23	0.03	0.01	0.02	0.01	0.00
10	40	0.11	0.03	0.19	0.08	0.08
10	70	1.0	0.3	1.6	0.5	0.57
12	23	0.39	0.11	0.75	0.29	0.36
12	40	1.2	0.5	1.8	0.5	0.61
12	70	4.1	1.2	4.9	1.5	0.85

The dissolution rate at steady state conditions for B in this study (Table 5.5) are higher than results obtained by Pierce *et al.* who show a NR_B = 0.076 ± 0.017 g m^{-2} d^{-1} at pH = 8 and NR_B = 1.18 ± 0.26 g m^{-2} d^{-1} at pH = 12 for a low active glass (LAW). The composition of the LAW glass has a similar Wt% of SiO_2 (within 1-3 wt%); however, B_2O_3 is lower by over 8 Wt%. The concentration of Al_2O_3 is higher in the LAW glass by over 5 wt% giving

rise to Al possibly acting as a network former instead of a network modifier. By decreasing the amount of network modifiers, the glass network becomes more polymerised and there are less NBO's. Recent work by Gin *et al*. have shown that an increased concentration of Al along with Ca, which neither MW+25wt% Blend or MW+30wt% Blend contain, will result in the lowest intrinsic dissolution rates. [147] Abraitis obtained similar NR_B values of 0.16 ± 0.03 g m^{-2} d^{-1} on a British Magnox simulated waste glass at 40 °C and pH = 10, which is similar in the nominal composition to the glasses in this study.

The power-law coefficient gives an order of reaction of the dissolution kinetics and was calculated by regression analysis from Equation 5.2 using the NR_i at different pH's for both MW+25wt% and MW+30wt% Blend glasses. Previous work has shown that there is no temperature dependence (within error) as is seen for the glasses studied in this work in Table 5.2. [143; 142] The average η_B for MW+25wt% and MW+30wt% Blend simulated waste glass is 0.36 ± 0.05 and 0.38 ± 0.08, respectively, suggesting that there is no significant change with compositional differences for the two glasses in this study. However, as mentioned above, there is only a small difference in the overall change in the overall network former concentrations (SiO_2 and B_2O_3), which is consistent with no significant effect on η.

Other glasses that have been studied by McGrail *et al.* show similar η at 0.40 ± 0.03 as the glasses in this study further showing the power-law coefficient is not as dependent on composition as the intrinsic dissolution rate. The glass studied by McGrail *et al.* was an alumino-borosilicate, a similar family of glasses to the base glass in both MW+25wt% and MW+30wt% simulated waste glass in this study; however, the composition contained over 10 wt% more SiO_2 and Al_2O_3 and over 10 wt% less B_2O_3. [142] Another glass with much different concentrations of Al_2O_3 and B_2O_3 that resulted in similar η are the LAW glasses studied by Pierce *et al.* [143] The difference in compositions between the glasses of McGrail *et al.* and Pierce *et al.* while having similar values of η give the author confidence that the power-law coefficient, η, is not compositionally dependent within the borosilicate glass family.

The rate at which the surface of the glass hydrolyses is also known as the forward or intrinsic rate constant. The intrinsic rate constant, *k*, for MW+25wt% and MW+30wt% Blend simulated waste glass was modelled using the regressed power-law coefficients and Equation 5.2 and are given in Table 5.3. The results given in Table 5.3 show an increase in *k* with temperature, similar to Pierce *et al.* who show values of similar magnitude. [143] As suggested by Abraitis, the intrinsic rate constant in both acidic and basic solutions should take the form of an Arrhenius equation giving a dependency of *k* on temperature as shown in Equation 5.2. [14] It is suggested that as the temperature increases, the number of deprotonated Si sites available increases promoting further detachment of Si sites.

As given in Table 5.6, the intrinsic rate constant calculated from the normalised rates at 40 °C with the overall average η obtained from Table 5.2 (0.45 ± 0.1 (unitless)) does not show any significant trends in the data (within error). This is consistent with Grambow and Muller who show a general decrease in *k* with an increase in pH (all within the same magnitude of 10^{-1} g m^{-2} d^{-1}). [148] However, Grambow and Muller suggest that there are large errors associated to the correlation of acid consumption and release of B at pH > 9 (region of interest in this study) and that the small decrease seen in their study in the forward rate constant, *k*, may be an artefact due to the large errors. [148]

Table 5.6 Intrinsic rate constant for MW+25wt% and MW+30wt% Blend simulated waste glass at 40 °C with average η obtained from Table 5.2.

MW + 25 wt% Blend Simulated Waste Glass

pH	k_{Al} (g m^{-2} d^{-1})	k_B (g m^{-2} d^{-1})	k_{Na} (g m^{-2} d^{-1})	k_{Si} (g m^{-2} d^{-1})
8	$6.0 \pm 1.2 \times 10^{-6}$	$6.7 \pm 1.3 \times 10^{-5}$	$1.8 \pm 0.4 \times 10^{-5}$	$9.5 \pm 1.9 \times 10^{-6}$
10	$1.9 \pm 0.4 \times 10^{-6}$	$2.7 \pm 0.5 \times 10^{-5}$	$0.5 \pm 0.1 \times 10^{-5}$	$3.5 \pm 0.7 \times 10^{-6}$
12	$2.8 \pm 0.6 \times 10^{-6}$	$0.6 \pm 0.1 \times 10^{-5}$	$1.1 \pm 0.2 \times 10^{-5}$	$8.0 \pm 1.6 \times 10^{-6}$

MW + 30 wt% Blend Simulated Waste Glass

pH	k_{Al} (g m^{-2} d^{-1})	k_B (g m^{-2} d^{-1})	k_{Na} (g m^{-2} d^{-1})	k_{Si} (g m^{-2} d^{-1})
8	$6.2 \pm 1.2 \times 10^{-6}$	$8.7 \pm 1.7 \times 10^{-5}$	$2.3 \pm 0.5 \times 10^{-5}$	$8.0 \pm 1.6 \times 10^{-6}$
10	$2.0 \pm 0.4 \times 10^{-6}$	$3.4 \pm 0.7 \times 10^{-5}$	$1.2 \pm 0.2 \times 10^{-5}$	$6.2 \pm 1.2 \times 10^{-6}$
12	$2.9 \pm 0.6 \times 10^{-6}$	$5.6 \pm 1.1 \times 10^{-5}$	$2.2 \pm 0.4 \times 10^{-5}$	$8.5 \pm 1.7 \times 10^{-6}$

Inspection of Table 5.3 and 5.6 shows that the difference of the intrinsic rate constant between the glasses studied here is minimal. Again, this could be due to the small changes in the composition of the network formers of SiO_2 and B_2O_3 and the intermediate Al_2O_3. Pierce *et al.* also observed a lack of compositional dependency for glasses of a similar composition to each other which suggests that glasses of a similar family may not show a compositional dependency for both the power-law coefficient and the kinetic rate constant.

In a simplified transition state theory rate law, the activation energy, as given in Equation 5.1, is the energy associated of an elementary reaction to form an activated complex, which is a high energy, ground state species. This simplified transition state theory rate law was derived by Aagaard and Helgeson and applied to glasses by Grambow. [76; 85] The formation of an activated complex followed by its disintegration into products is a low energy path for the forward reaction. The formation of the activated complex is governed by

a reversible equilibrium; however, once it decomposes into products, it becomes irreversible and is dependent on the crosslink density of the reaction zone.

In this study, regression analysis from the normalised dissolution rate, NR, versus temperature was performed to compute the activation energy, Ea. This method was used by Abraitis, McGrail *et al.* and Pierce *et al*. in order to attain the activation energy and the other kinetic rate parameters; *k* and η. [14; 142; 143] Table 5.8 shows that there is no significant change in Ea (within error) with an increase in pH (with the exception of Ea_B at pH=10 for MW+30wt% Blend). The large difference in Ea_B for MW+30wt% Blend as shown in Figure 5.12 shows a higher trend due to the high dissolution rate at 90 °C as compared the other NL_B at pH's where NL_B at 90 °C are similar to the NL_B at 70 °C. The average Ea_i for MW+25wt% Blend are 76 ± 15, 56 ± 13, 63 ± 13 and 81 ± 16 kJ mol^{-1} for Ea_{Al}, Ea_B, Ea_{Na} and Ea_{Si}, respectively. For MW+30wt% Blend, the average Ea are 70 ± 14, 55 ± 11, 60 ± 12 and 78 ± 16 kJ mol^{-1} for Ea_{Al}, Ea_B, Ea_{Na} and Ea_{Si}, respectively. Within error, all of the activation energies are similar. The average of the Ea for MW+25wt% Blend and MW+30wt% Blend is 69 ± 14 and 65 ± 13 kJ mol^{-1}, respectively. These results (within error) are similar to that of Abraitis *et al.* who obtained an Ea between 56 and 64 kJ mol^{-1} suggesting the dissolution of these glass is through a surface-controlled reaction process. [15] According to Lasaga, a surface-controlled reaction process has an activation energy between 41 and 84 kJ mol^{-1}. [145] This is consistent with the previous suggestion where an increase in the number of deprotonated Si sites available at the surface of the glass will further promote the detachment of Si sites.

Excluding error, there is a slight decrease of 4 kJ mol^{-1} in the activation energy with an increase in the wt% of simulated waste in the base glass in this study. With a decrease in the activation energy, one should observe an increase in the dissolution rate with an increase in either temperature or pH. Close examination of Table 5.5 results in MW+30wt% Blend having a slightly higher NR_B for all pH ranges and temperatures (excluding error) indicating that MW+30wt% Blend does have a slightly lower Ea.

Pierce *et al.* suggests there is a relationship between the molar ratio of B_2O_3/Al_2O_3 with dissolution. [149] It was shown that with an increase in the molar ratio of B_2O_3/Al_2O_3 there in an increase in the normalised dissolution rate with respect to B. [149] The difference in the molar ratios of B_2O_3/Al_2O_3 between MW+25wt% and MW+30wt% Blend simulated waste glass is 4.8 with MW+25wt% Blend having a larger ratio. This is not consistent with the suggestion by Pierce *et al.* that an increase in the molar ratio of B_2O_3/Al_2O_3 increases NR_B. [149] The NR_B is shown to increase with a decrease in the molar ratio of B_2O_3/Al_2O_3 in this study (opposite of the results observed by Pierce *et al.*) suggesting that other components in

compositions used in this study may have more of an impact on the dissolution rate than just the ratio of B_2O_3/Al_2O_3. [149]

The traditional view on glass dissolution is that the local coordination has a large effect on the corrosion. Early work by Dell and Bray show that an alkali-borosilicate glass structure is polymerised by 4-coordinated B units ($B^{[4]}$), which will serve as a network former when charge compensated with a network modifying alkali. [66] When NBO sites are formed due to an excess of network modifying alkali, the formation of 3-coordinated B units ($B^{[3]}$) are formed which depolymerise the glass network. The depolymerisation of the glass network is suggested to lead to a decrease in the dissolution rate. Pierce *et al.* assume that an amount of Na equal to the amount of B + Al will fully charge compensate $B^{[4]}$ and $Al^{[4]}$ units in an alumina-borosilicate glass; however, for glasses where Na/(B+Al) = 1, there are still $B^{[3]}$ units that are observed. [149] MW+25wt% and MW+30wt% Blend glasses have a $Na_2O/(B_2O_3 + Al_2O_3)$ of 0.7 and 1.1, respectively. The lower NR_B for MW+25wt% Blend glass suggests that there are less depolymerising $B^{[3]}$ units than that of MW+30wt% Blend which is consistent with the suggestion by the earlier work of Dell and Bray. [66] In order to fully determine the concentration difference of $B^{[3]}$ and $B^{[4]}$ units between the MW glasses in this study, ^{11}B MAS-NMR will need to be performed. Until then, one can only speculate as to the concentrations of the tetragonal and trigonal B units in each glass, which lead to increased/decreased dissolution rates.

5.5 Conclusions

This study has shown that the steady state dissolution of MW+25wt% and MW+30wt% Blend simulated nuclear waste glasses is similar to that of previous studies. The SPFT Q/S results correlate to other results, with the exception of a few data points attributed to experimental error, on a very similar glass: a British Magnox simulated nuclear waste glass.

As expected, the NR with respect to B, Si, Na and Al of the glasses in this study have increased with an increase in solution pH. Previous results on different glass compositions have shown similar results where the NR of B, Si, Na and Al increased with an increase in pH.

The activation energy with respect to Si, Ea_{Si}, was shown to increase with an increase in pH. The average Ea in this study is consistent for a surface controlled reaction with these

glasses as was shown in previous studies. The Ea_B was also shown to have an average value similar to that of previous studies suggesting these glasses are controlled by surface reactions.

Changes in composition through the addition of 5 wt% simulated waste to the base glass did not show significant changes to the kinetic rate parameters for the dissolution rate of these glasses. This could be due to the small changes in compositions; however, it is suggested to perform nuclear magnetic resonance spectroscopy to determine the polymerisation of both Si and B polymorphs.

There were; however, several experimental errors (flow rate of pumps, and constant temperatures of the ovens) associated to these SPFT experiments. This suggests the need for further SPFT experiments on these glasses to support the data which has been given above.

6.0 Durability of Simulated UK High Level Waste Glass in Hyperalkaline Conditions

6.1 Introduction

Several methods have been proposed for disposal of nuclear waste; however, there is an international consensus for immobilisation of high level nuclear waste (HLW) by vitrification. The Radioactive Waste Management Directorate (RWMD) in the UK has also recommended immobilisation of HLW by vitrification. [4] Following vitrification, waste packages would be placed in an interim storage area awaiting final disposal in a geological repository. Currently in the UK, vitrification of the Magnox and Blend (25 wt % Magnox and 75 wt % ThORP waste) wastes are performed by the AVH process at the Sellafield site in Cumbria, UK. [2]

One of the suggested concepts for geological disposal in the UK, as selected by the RWMD, is a co-located intermediate level waste (ILW) and HLW geological repository. [3] This concept utilises a multi-barrier approach which includes; the waste form, waste container, the Nirex reference vault backfill (NRVB), sealing systems, and also the geology of the rock formations. The co-located conceptual site was proposed based on the information available from the opalinus clay concept from Nagra, Switzerland. [3] The consideration of a geological disposal repository containing both ILW and HLW immobilised packages in different regions of the facility requires quantitative, long-term durability experiments to further develop estimates on radionuclide release rates for high-quality safety assessments of the disposal facility site.

The Nirex reference vault backfill (NRVB) is one concept currently being considered for application in a geological disposal facility (GDF) for ILW to order to fill the voids between the waste packages within disposal vaults. The NRVB is a cementitious material derived from the hydration of a mixture of Ordinary Portland Cement (OPC), portlandite ($Ca(OH)_2$), and calcite ($CaCO_3$). The resulting substance is a highly porous material that allows migration of released gases from ILW packages, which also acts to retard the migration of actinides (and other radionuclides) that have a low solubility under the local hyperalkaline conditions imposed by the material. The co-located geological disposal repository may, at long times (> tens of thousands of years), allow ground water to flow from the ILW cement immobilised waste packages to contact the vitrified HLW products. Hence, there is a need to understand the dissolution behaviour of HLW glasses under conditions which simulate the infiltration of hyperalkaline groundwater migrating from the ILW to HLW disposal zones of

a co-located GDF. Since Grambow has shown that simulated waste glasses have an increased dissolution rate in acidic or alkaline solutions, the co-located geological disposal repository may not be a viable concept for the UK geological repository. [85]

The durability of nuclear HLW glasses is an important property for disposal in a geological repository. The use of glass as a host matrix for immobilisation of radioactive wastes is due to the ability of glass to sustain a suitable durability with a range of compositions of the HLW streams. Studies on the durability of simulated and radioactive HLW glasses have shown suitable corrosion rates in various environments. [15; 150; 151] Recent flow through experiments on UK simulated HLW glasses by Abraitis *et al*. have investigated the role of Al and Si in the dissolution process and suggest both Al and Si may suppress the final rate of corrosion. [15; 16] Further studies by Abraitis *et al*. also suggest that higher pH solutions will increase the final dissolution rate. [110]

This study was performed to determine effects of a high pH solution in contact with simulated UK HLW glasses. A semi-static dissolution test was used over a period of 168 days to determine the steady state dissolution rates for glass powders and glass monoliths containing UK simulated HLW in unbuffered deionized water and $Ca(OH)_2$ saturated solutions.

6.2 Experimental Procedure

The glass MW+25wt% Blend with the composition as given in Table 6.1 was made by mixing a 75 wt% borosilicate glass frit with 25 wt% simulated HLW calcine supplied by The National Nuclear Laboratory, UK. After mixing the frit and calcine together they were melted in a mullite crucible at 1060 °C for 1 h, stirred using a mullite stirrer for 4 h and cast into a block using a pre-heated stainless steel mould. After casting, the glass was annealed at 500 °C for 1 h and allowed to cool at 1 °C min^{-1} to room temperature.

The glass product was cut into 10.5 mm x 10.5 mm x 4.5 mm (± 1 mm) monoliths for the MCC-1 test (ASTM standard C 1220-98) and the rest of the glass crushed and size fractioned to 35 μm < X < 53 μm (fine, or high surface area to volume ratio powders) and 75 μm < X < 150 μm (coarse, or low surface area to volume ratio powders). [121] Glass monoliths were ground using SiC paper and polished to 10.0 mm x 10.0 mm x 4.0 mm (± 0.1 mm) with 3 μm diamond paste using ethanol as a lubricant. After polishing, the monolithic samples were cleaned by rinsing in high purity H_2O three times and then cleaning with an ultrasonicator in

high purity H_2O for 2 min and then cleaning with an ultrasonicator in ethanol for 2 min. After cleaning, the monoliths were placed in a drying oven at 90 °C overnight. All subsequent procedures were performed under a N_2 atmosphere in a glove box to avoid carbonation of $Ca(OH)_2$ solutions. Accelerated alteration experiments are typically conducted at 90 ^oC, in order to increase dissolution kinetics. However, as shown in Figure 6.1, the saturation of $Ca(OH)_2$ decreases with increasing temperature. [152] Therefore, in order to achieve a balance between measurable dissolution rate on the laboratory time scale and preservation of hyperalkaline conditions, experiments were conducted at 50°C.

Table 6.1 Analysed composition for MW25Blend used to make the glass powder and monoliths for the long term durability tests.

Oxide	**wt %**	**Oxide**	**wt%**
SiO_2	46.28	MgO	1.34
B_2O_3	18.3	MoO_3	2.02
Na_2O	8.12	Nd_2O_3	1.81
Li_2O	4.81	NiO	0.28
Al_2O_3	1.87	Pr_2O_3	0.47
BaO	1.22	RuO_2	0.49
CeO_2	1.24	Sm_2O_3	0.28
Cr_2O_3	0.37	SrO	0.32
Cs_2O	1.61	TeO_2	0.28
Fe_2O_3	1.87	Y_2O_3	0.1
Gd_2O_3	3.86	ZrO_2	2.4
La_2O_3	0.67	Total	100.0

For the MCC-1 test, the monoliths were placed on a Teflon cradle in Teflon reaction vessels with a N_2 de-aerated $Ca(OH)_2$ saturated solution (CSS), prepared with de-ionised H_2O; approximately 1.5 grams of $Ca(OH)_2$ was placed underneath the cradle before the solution was added and vessels were sealed and placed in an oven inside the glove-box which was set at 50 °C. Vessels were removed and sampled at 1, 3, 7, 14, 21, 28, 42, 56, 70, 84, 112, 140 and 168 days.

After size fractioning the glass powder, it was cleaned according to the PCT-B ASTM standard. [118] Once clean, the powder was placed in a desicator, in a glove-box under a N_2

atmosphere. Two solutions were prepared for the semi-static powder durability tests; a N_2 de-aerated unbuffered deionized water and a N_2 de-aerated $Ca(OH)_2$ saturated H_2O (CSS). 400 mL of solution were added to 500 mL HDPE vessels to contain the coarse and fine powders and a vessel for a blank solution. In order to buffer the CSS throughout the dissolution test, a USY-1 ultrafilter containing a $Ca(OH)_2$ slurry made from $Ca(OH)_2$ and unbuffered deionized water was connected to the lid and submersed in the solution. Glass powder was added to the solutions and the vessels were sealed and placed in the oven within the glove-box which was set at 50 °C. Aliquots of 5 mL were taken, for the coarse powder, at 1, 3, 7, 14, 21, 28, 35 and 42 days, while for the fine powders aliquots were taken at 1, 3, 7, 14, 21, 28, 42, 56, 70, 84, 112, 140 and 168 days. Solutions were analysed by ICP OES/MS for concentrations of ions in solution.

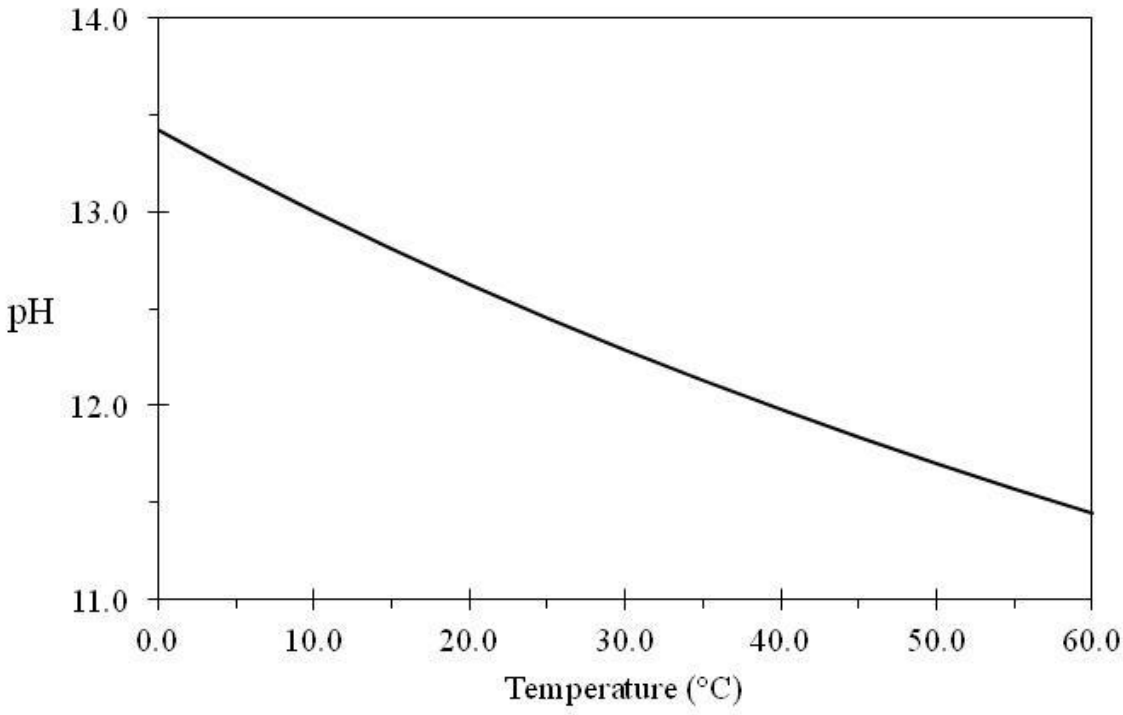

Figure 6.1 Change in pH of a $Ca(OH)_2$ saturated solution (CSS) with temperature. Based on data from (152).

6.3 Results

6.3.1 Powder Durability Test Results

Dissolution of glasses can be measured by the normalised mass loss of element *i* (NL_i). For the PCT-t tests, the normalised mass loss was calculated according to Equation 6.1,

Equation 6.1 $$NL_i = \frac{m_i}{f_i(\frac{SA}{V})}$$

where NL_i is the normalised mass loss of element *i* (g m^{-2}), f_i is the mass fraction of element *i* in the original glass, *SA* is the calculated surface area of the pristine glass in m^2, *V* is the volume of the solution in litres and m_i is the mass loss in g of element *i*, which was calculated by Equation 6.2,

Equation 6.2 $$m_i = (C_i - B_i)$$

where C_i is the concentration of element *i* in the aliquot in g L^{-1} and B_i is the concentration of element *i* in the blank in g L^{-1}.

6.3.1.1 Low surface area to volume powder dissolution test

Figure 6.2 shows the NL_B for powders with an initial surface area to volume (SA/V) ratio of 1200 m^{-1} in an unbuffered deionized water (UDW) and a $Ca(OH)_2$ saturated solution (CSS) at 50 °C. For powders in UDW, the NL_B is approximately three times higher than that measured in the CSS. It should be noted that B is generally accepted to be a good indicator of the extent of glass dissolution since this element generally does not participate in formation of an alteration layer or secondary precipitation. Both NL_B in UDW and CSS show a decrease in the rate of dissolution (NL_i / time) approaching 28 days which may signal steady state conditions corresponding to the apparent plateau in NL_B; however, longer dissolution times are needed to confirm that the powders have reached steady state conditions at this SA/V ratio. A similar trend is observed for NL_{Li} (Figure 6.3).

Figure 6.4 gives the concentration of Ca in solution for the experiments in CSS. The CSS Blank is CSS with no glass powder added to the solution. There is an observable decrease in the concentration of Ca for the CSS solution throughout the dissolution test (Figure 6.4), while for the CSS blank solution, there is no change (within error) during the experiment.

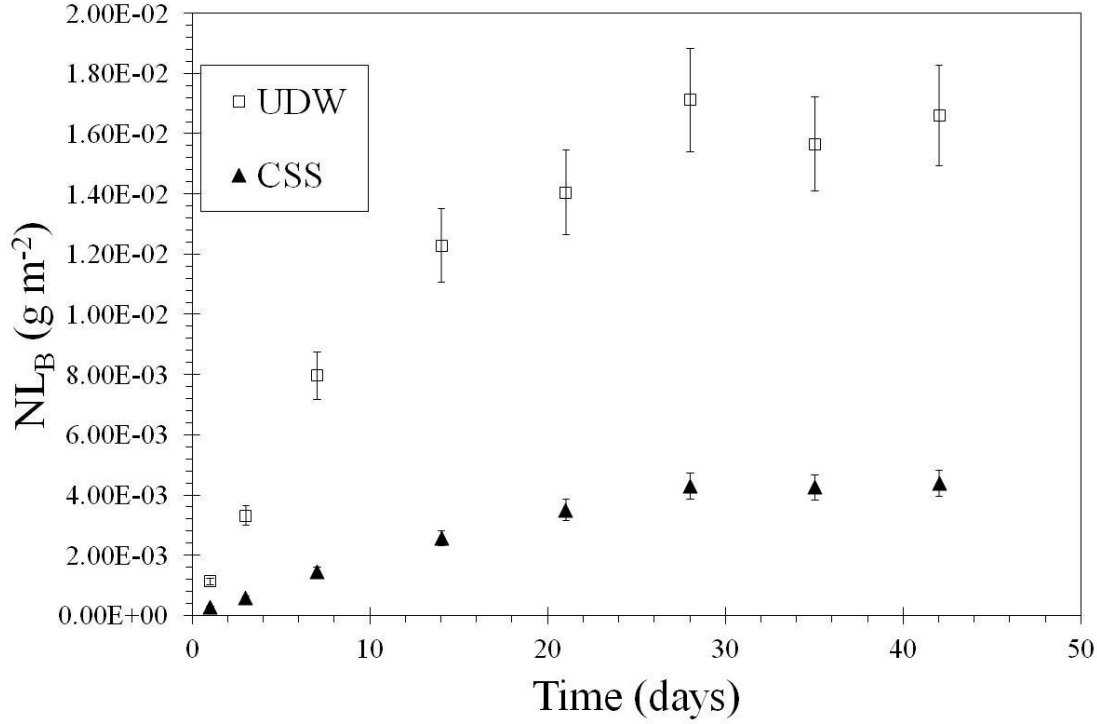

Figure 6.2 Normalised mass loss of B for glass powders with a surface area to volume ratio of 1200 m^{-1} in unbuffered deionized water (UDW) and the $Ca(OH)_2$ saturated solution (CSS) at 50 °C.

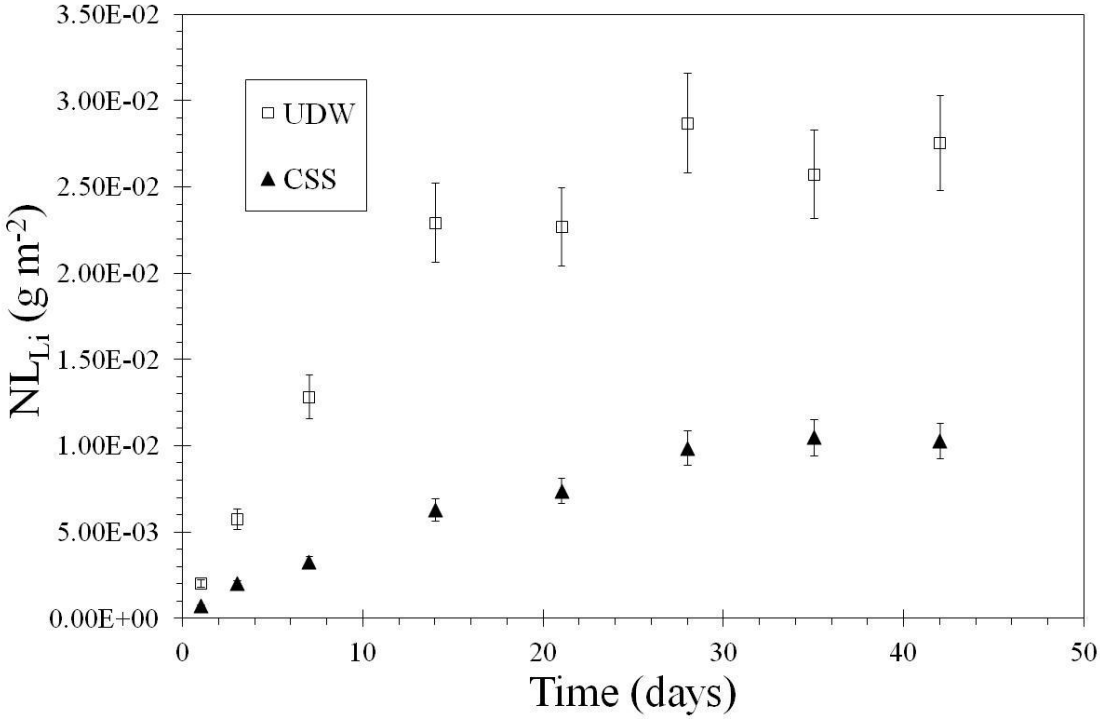

Figure 6.3 Normalised mass loss of Li for glass powders with a surface area to volume ratio of 1200 m^{-1} in unbuffered deionized water (UDW) and the $Ca(OH)_2$ saturated solution (CSS) at 50 °C.

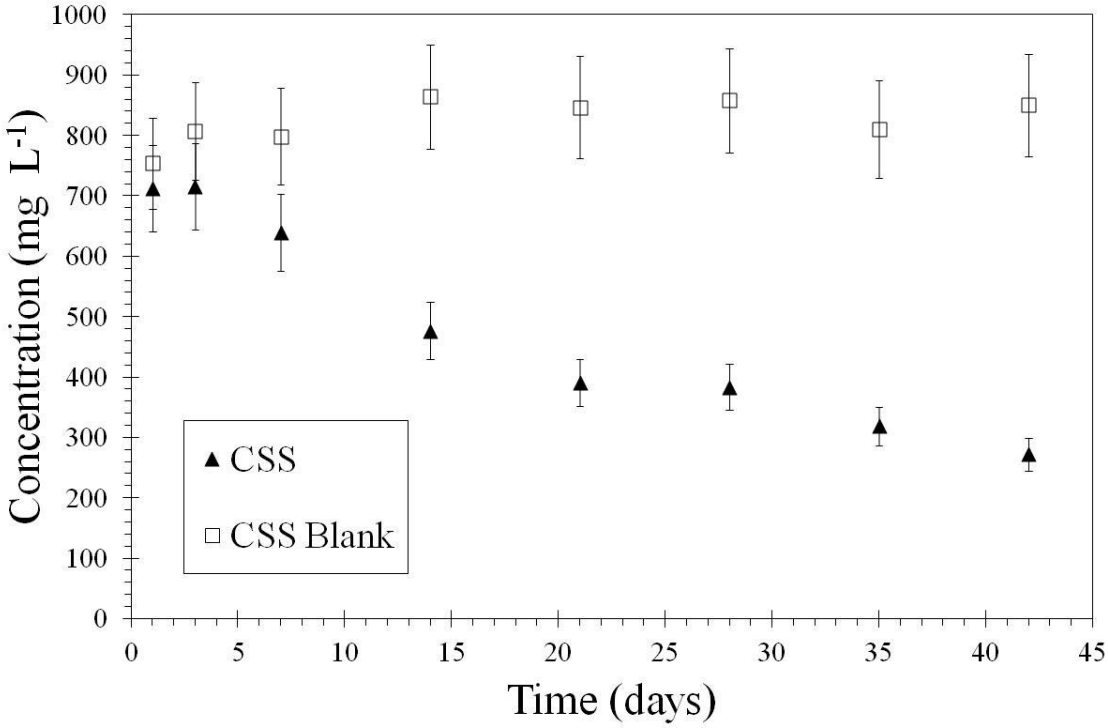

Figure 6.4 Concentration of Ca for glass powders in the $Ca(OH)_2$ saturated solution (CSS) for a SA/V = 1200 m^{-1}.

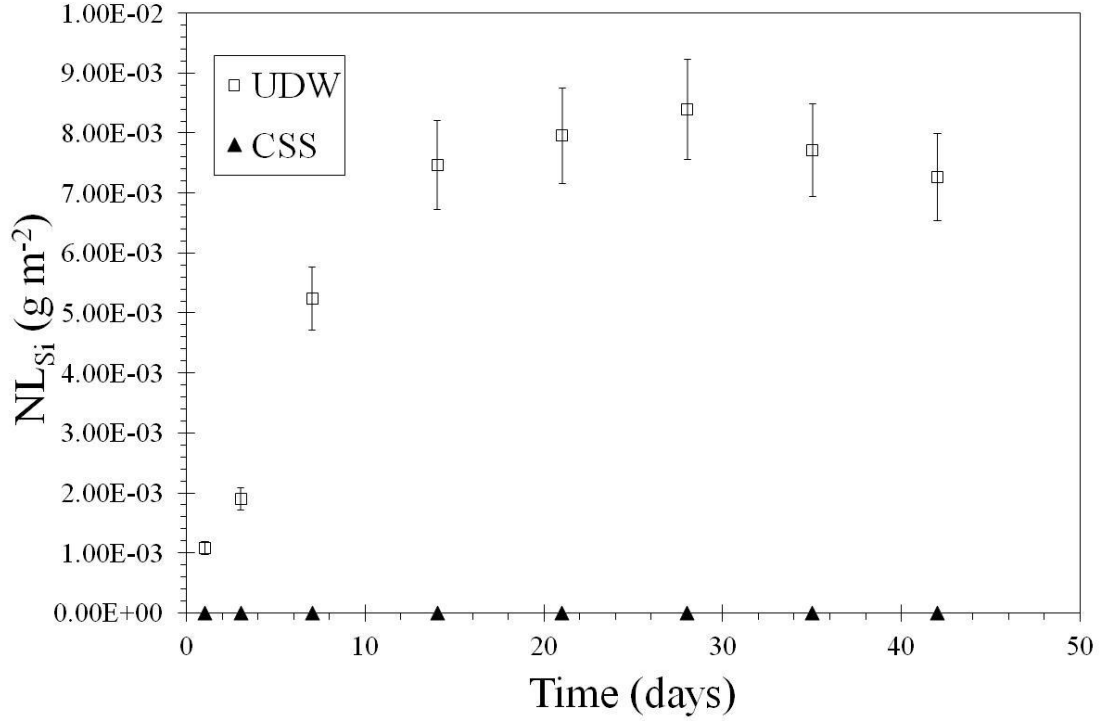

Figure 6.5 Normalised mass loss of Si for glass powders with a surface area to volume ratio of 1200 m^{-1} in unbuffered deionized water (UDW) and the $Ca(OH)_2$ saturated solution (CSS) at 50 °C.

The NL_{Si} for the glass powder with a SA/V = 1200 m^{-1} in solution is given in Figure 6.5. For the duration of the dissolution test, the concentration of Si in solution is below the detection limits for the powder in CSS. The initial NL_{Si} for the powders in UDW increases at a fast rate to a maximum of 8.4 ± 0.8 x 10^{-3} g m^{-2} at 28 days and then becomes constant (within error) for the remainder of the experiment.

The evolution of pH for powder in CSS and UDW is shown in Figure 6.6. There is a constant pH for powder in UDW at pH = 9.8 ± 0.1. However, there is a decrease in pH for the glass powder in CSS from a pH = 12.7 ± 0.1 at day 1 to pH = 11.8 ± 0.1 at 28 days. After 28 days, the pH for the CSS solution becomes stable at pH = 12 ± 0.2. It should be noted that the aim was to keep the CSS solution above pH = 11.5 in order to minimize precipitation of $Ca(OH)_2$ during the experiment, which was accomplished, as shown in Figure 6.6. As mentioned previously, Abraitis *et al.* suggest that the dissolution rate will increase for glasses in high pH solutions which is in apparent disagreement with the results in this study. [15] The pH for the CSS blank remained constant at pH = 12.5 ± 0.25.

The NL_{Na} is given in Figure 6.7, and similar to NL_B, dissolution in UDW is approximately 3 times higher than powders in CSS at 168 days. There is an overall increase in NL_{Na} in both UDW and CSS; however, the NL_{Na} for the glass powder in UDW becomes variable after 14 days. The NL_{Na} for the CSS after 14 days is linear (within error).

Figures 6.8 and 6.9 give the NL_{Al} and the NL_{Mg}, respectively. It is generally difficult to determine dissolved Al due to low concentrations of Al in solution for dissolution experiments. Inspection of Figure 6.8 does not reveal any significant conclusions for NL_{Al} for powders in both UDW and CSS due to the low Al concentrations in solution. It is also visible from Figure 6.9 that the low concentrations of Mg in solution make it difficult to determine significant trends of NL_{Mg} for powders in CSS; however, there is a clear increase of the NL_{Mg} to 3.0 x 10^{-3} g m^{-2} at 7 days whereupon the NL_{Mg} becomes constant.

Figure 6.10 gives the NL_{Fe} for the powders in UDW and CSS. Again, due to the low concentration of Fe in solution it is difficult to ascertain any significant information from NL_{Fe}. However, the powders in CSS the NL_{Fe} is initially higher than that in deionised water and then declines at day 3 to a normalized mass loss of zero.

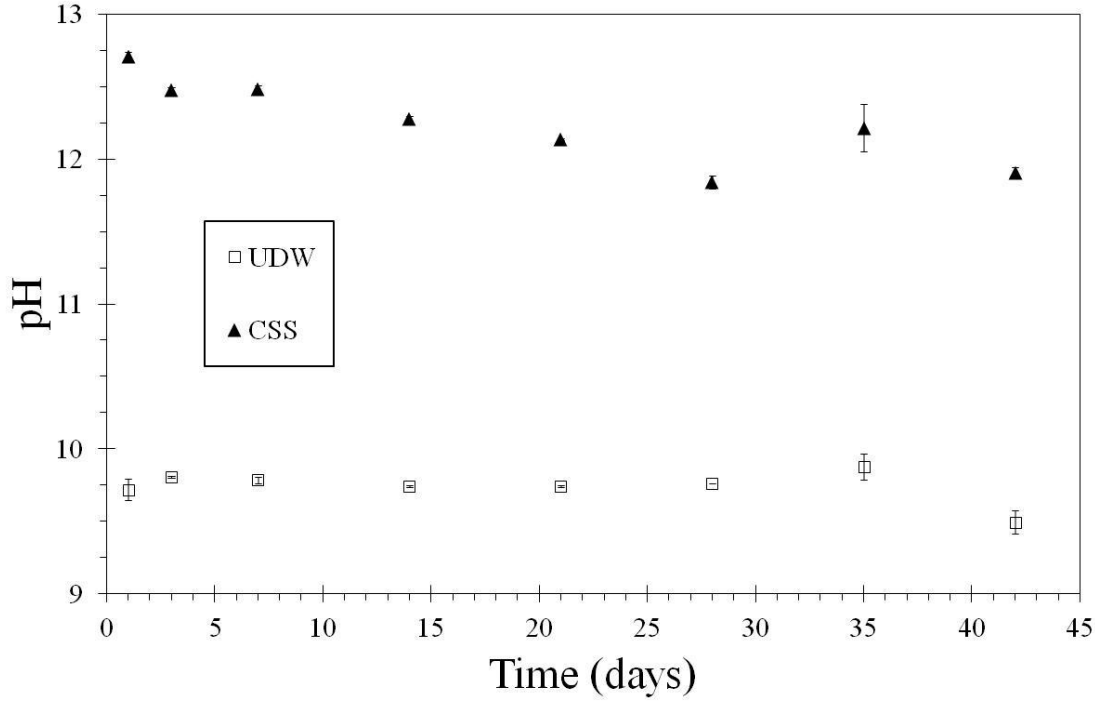

Figure 6.6 Solution pH of the glass powders in unbuffered deionized water (UDW) and the $Ca(OH)_2$ saturated solution (CSS) at 50 °C with a SA/V = 1200 m^{-1}.

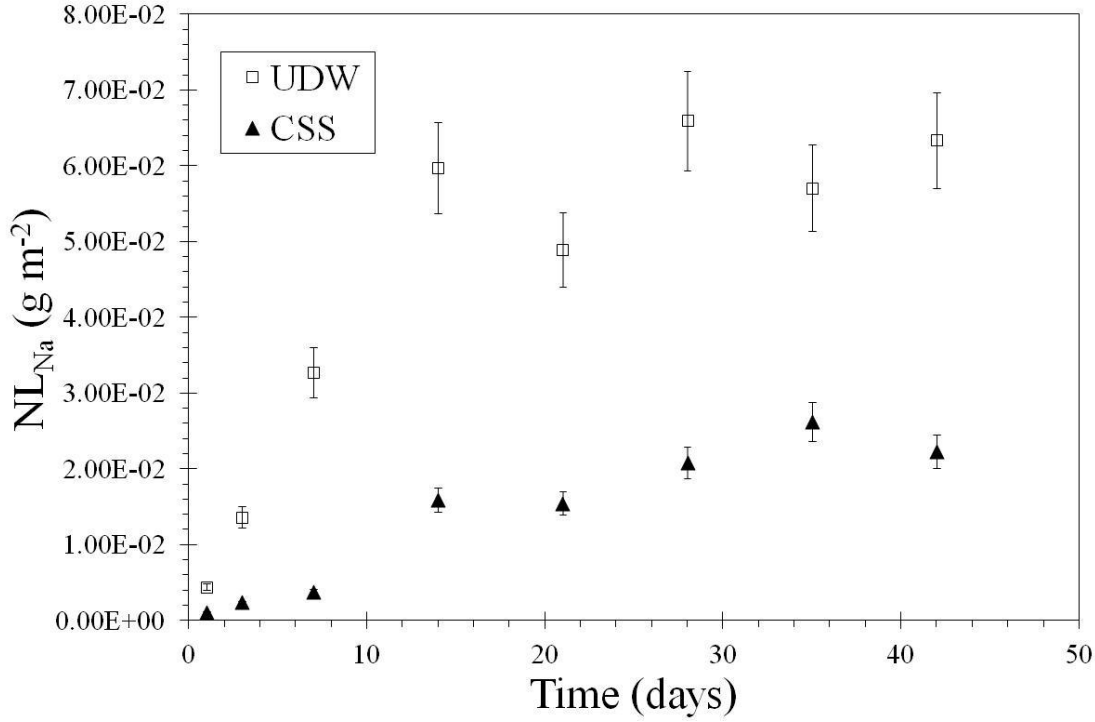

Figure 6.7 Normalised mass loss of Na for glass powders with a surface area to volume ratio of 1200 m^{-1} in unbuffered deionized water (UDW) and the $Ca(OH)_2$ saturated solution (CSS) at 50 °C.

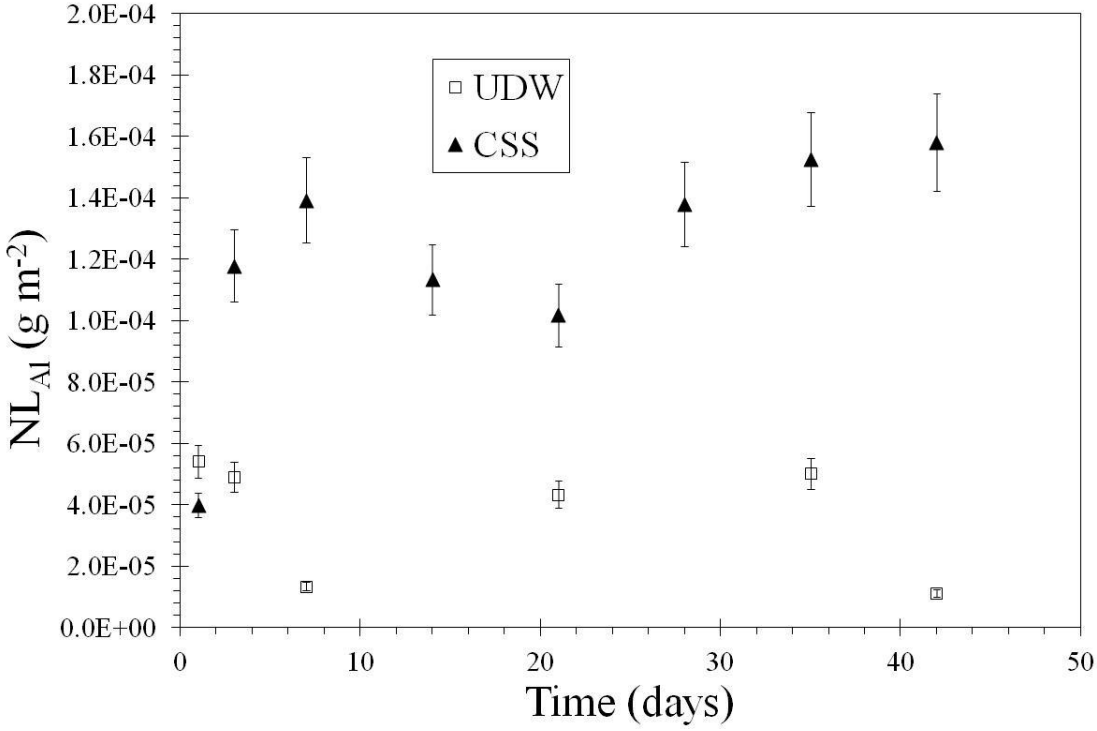

Figure 6.8 Normalised mass loss of Al for glass powders with a surface area to volume ratio of 1200 m^{-1} in unbuffered deionized water (UDW) and the $Ca(OH)_2$ saturated solution (CSS) at 50 °C.

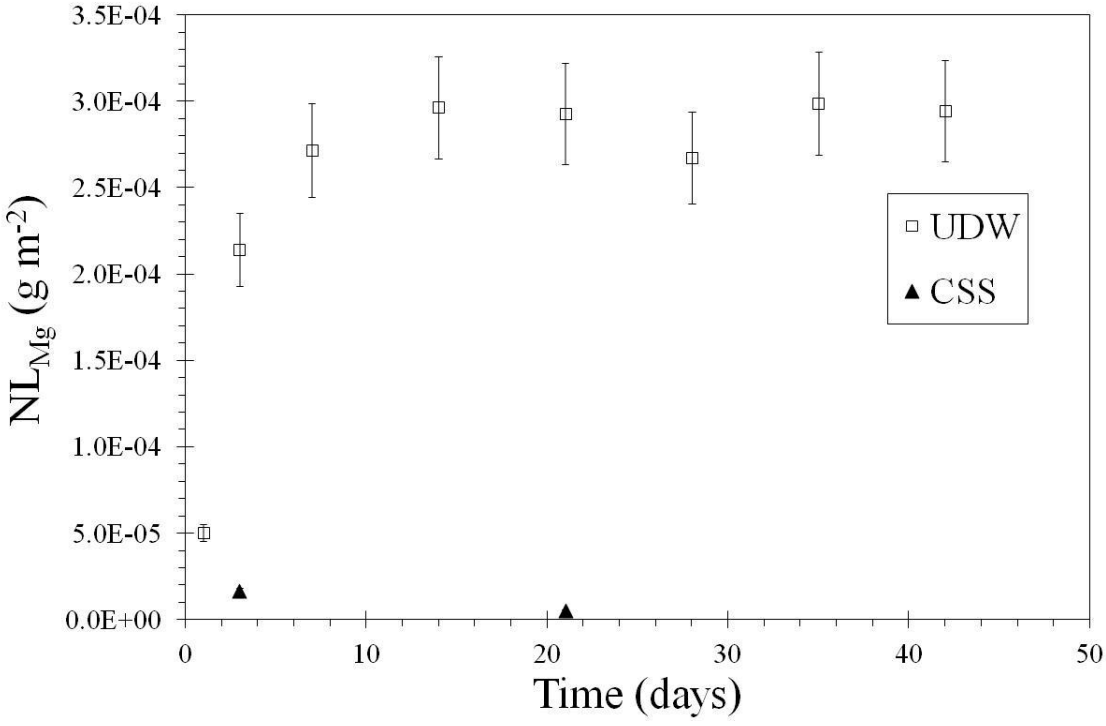

Figure 6.9 Normalised mass loss of Mg for glass powders with a surface area to volume ratio of 1200 m^{-1} in unbuffered deionized water (UDW) and the $Ca(OH)_2$ saturated solution (CSS) at 50 °C.

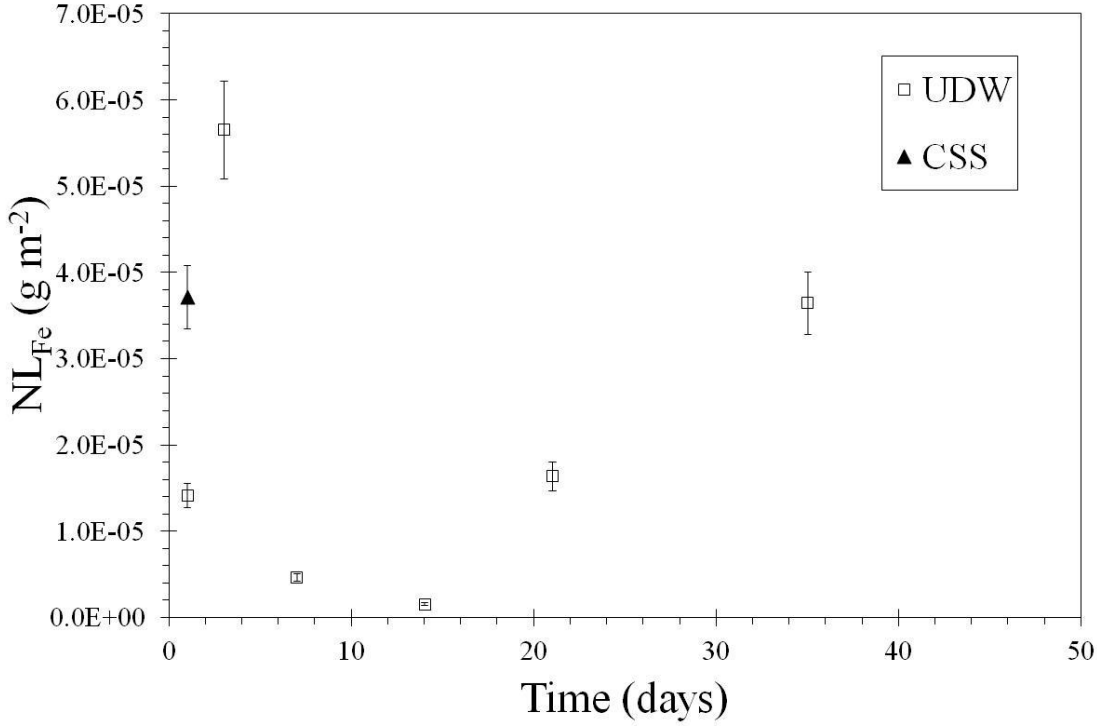

Figure 6.10 Normalised mass loss of Fe for glass powders with a surface area to volume ratio of 1200 m^{-1} in unbuffered deionized water (UDW) and the $Ca(OH)_2$ saturated solution (CSS) at 50 °C.

6.3.1.2 High Surface Area to Volume Ratio Powder Dissolution Test

Durability experiments were also completed for powders with a SA/V = 10,000 m^{-1} in both UDW and CSS. The NL_B for the high SA/V powder durability test is plotted in Figure 6.11. The rapid saturation of solution as observed for the high surface area powder is more representative of "final rate" dissolution. After 168 days, the powders in CSS appear to have reached steady state dissolution where there is a constant NL_B as compared to the NL_B at 142 days. However, further data is required in order to reach a definitive conclusion on whether or not "final rate" dissolution has been achieved. Powders in UDW show an overall increase in the NL_B to 168 days up to approximately 6.5 x 10^{-3} g m^{-2}. Between 21 and 28 days for powder in UDW, there is a decrease in the dissolution rate from approximately 2.0 x 10^{-4} g m^{-2} d^{-1} to near steady state conditions, which correspond to the plateau in NL_B. After 56 days, the dissolution rate with respect to B increases, again, to approximately 2.0 x 10^{-5} g m^{-2} d^{-1}. This second increase in the NL_B may possibly be due to precipitation of secondary phases. The NL_{Li} for the powders in UDW and CSS with a SA/V = 10,000 m^{-1} gave similar trends to that of the NL_B,, as expected, due to B and Li not generally being involved with secondary phase formation. This is shown in Figure 6.12.

When aliquots were removed from solution, visual observations of the powder in UDW revealed that the powders agglomerated, at short times. There was also agglomeration of the powders in CSS as observed from the top during sampling of the solution; however, agglomeration of the powder on the surface occurred after a longer time period.

The concentration of Ca in CSS, as plotted in Figure 6.13, decreases from approximately 700 mg L^{-1} until day 84 where the concentration of Ca becomes steady at approximately 50 mg L^{-1}. When the concentration of Ca becomes less than 150 ppm (Figure 6.13), the NL_{Si} increases significantly for powder in CSS, as shown in Figure 6.14. The NL_{Si} for the fine powder (SA/V = 10,000 m^{-1}) in UDW becomes constant at approximately 1.0 x 10^{-3} g m^{-2} after 14 days. The NL_{Si} of the coarse glass powder (SA/V = 1,200 m^{-1}), as shown in Figure 6.5, in UDW is constant (within error) near 8.0 x 10^{-3} g m^{-2}. When the total concentration of Si in solution is plotted for each glass powder in CSS and UDW (Figure 6.15), the concentration of Si in the UDW is the same (within error) for both glass powders. The similar concentration of silicon for both glass powders leads to a lower NL_{Si} as is seen for this study.

A plot of the pH for both solutions with the fine glass powder is given in Figure 6.16. The decline in the pH in the CSS is consistent with that of the Ca concentration where both the pH and Ca concentration become constant at 84 days (within error) at a pH of 10.5 ± 0.2. The pH for powders in UDW is constant throughout the dissolution test at a pH = 9.8 ± 0.1.

Figure 6.17 illustrates the NL_{Na} for the fine glass powder in UDW and CSS. As expected, the NL_{Na} in UDW is higher than in CSS. As observed for the fine powder in CSS, the NL_{Na} becomes constant (within error) after 140 days. The NL_B for the fine glass powder, as shown in Figure 6.11, continues to increase after 140 days suggesting the final dissolution rate has not been reached. The initial dissolution rate with respect to Na of the fine glass powder in UDW is 5.5 x 10^{-4} g m^{-2} d^{-1}, but the dissolution rate becomes constant after 28 days to what appears to be steady state conditions (within error). The possible dissolution rate increase after 84 days could be due to precipitation from secondary phases.

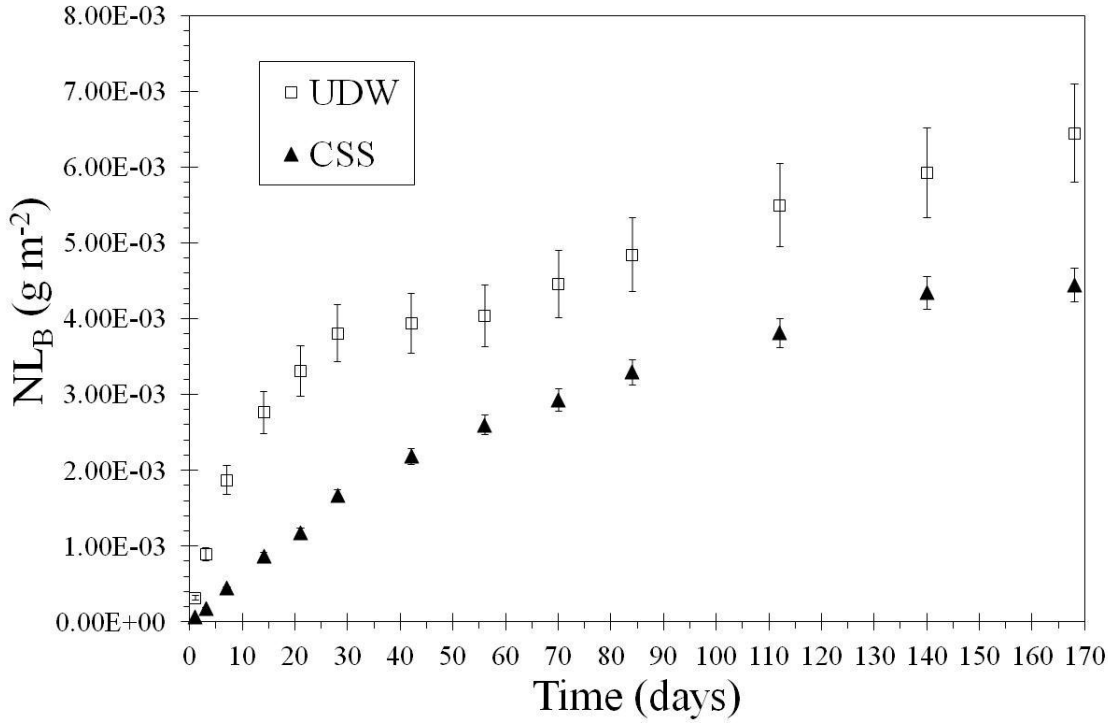

Figure 6.11 Normalised mass loss of B for glass powders with a surface area to volume ratio of 10,000 m^{-1} in unbuffered deionized water (UDW) and the $Ca(OH)_2$ saturated solution (CSS) at 50 °C.

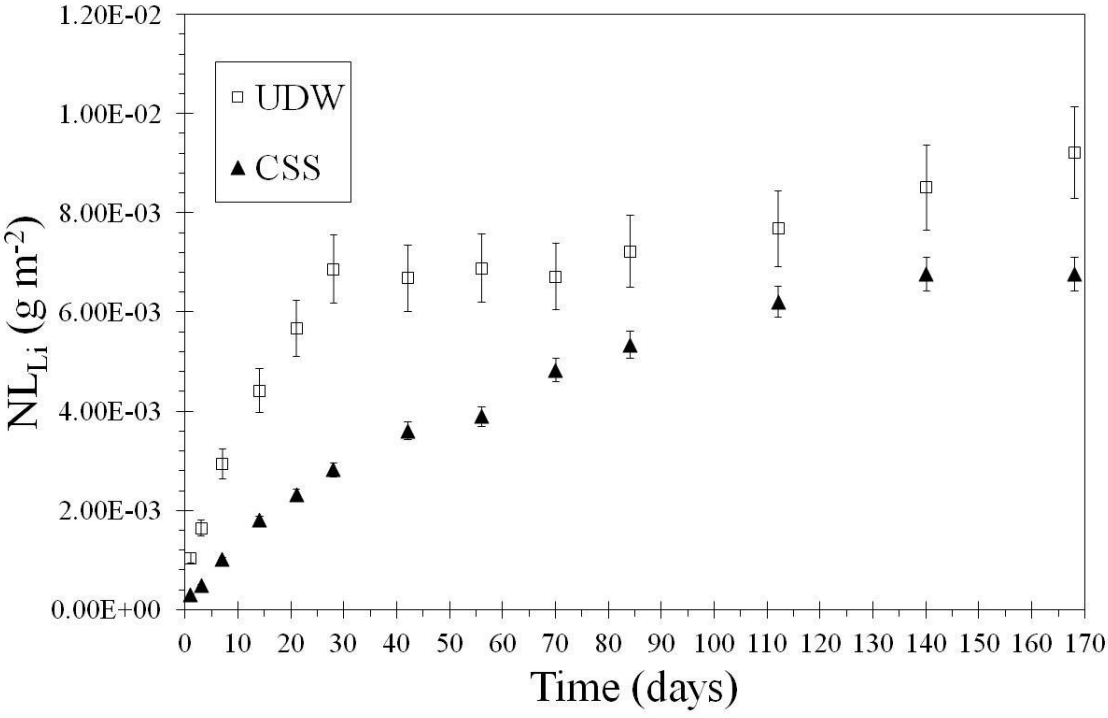

Figure 6.12 Normalised mass loss of Li for glass powders with a surface area to volume ratio of 10,000 m^{-1} in unbuffered deionized water (UDW) and the $Ca(OH)_2$ saturated solution (CSS) at 50 °C.

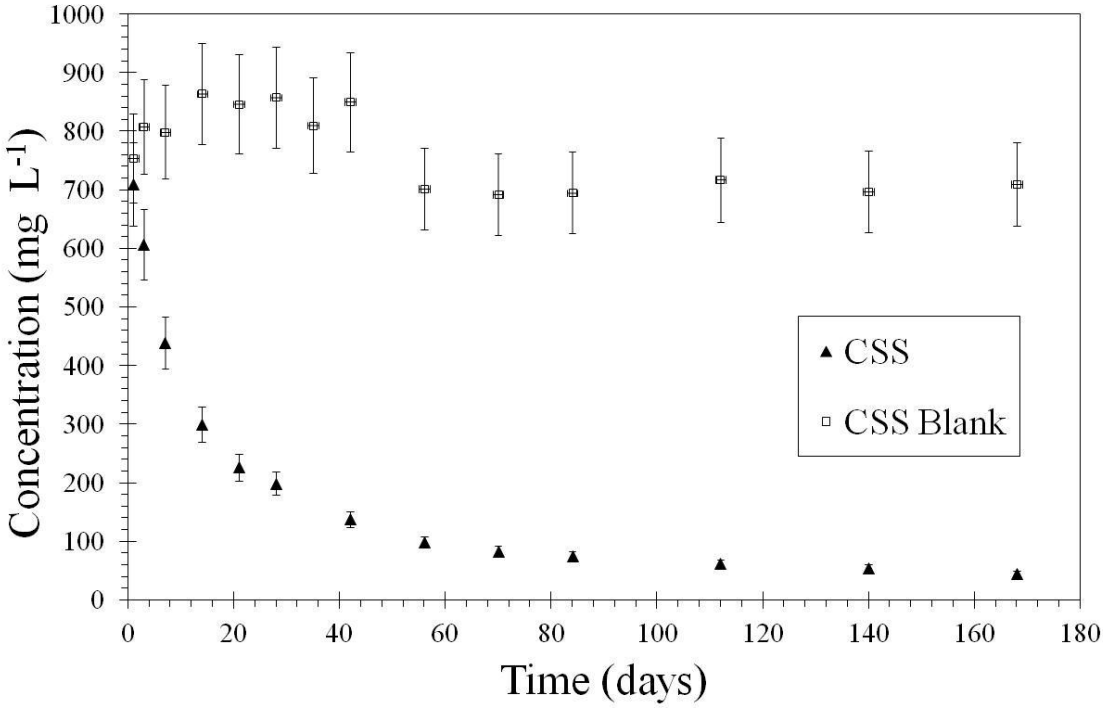

Figure 6.13 Concentration of Ca for glass powders in $Ca(OH)_2$ saturated solution (CSS) for a SA/V = 10,000 m^{-1}.

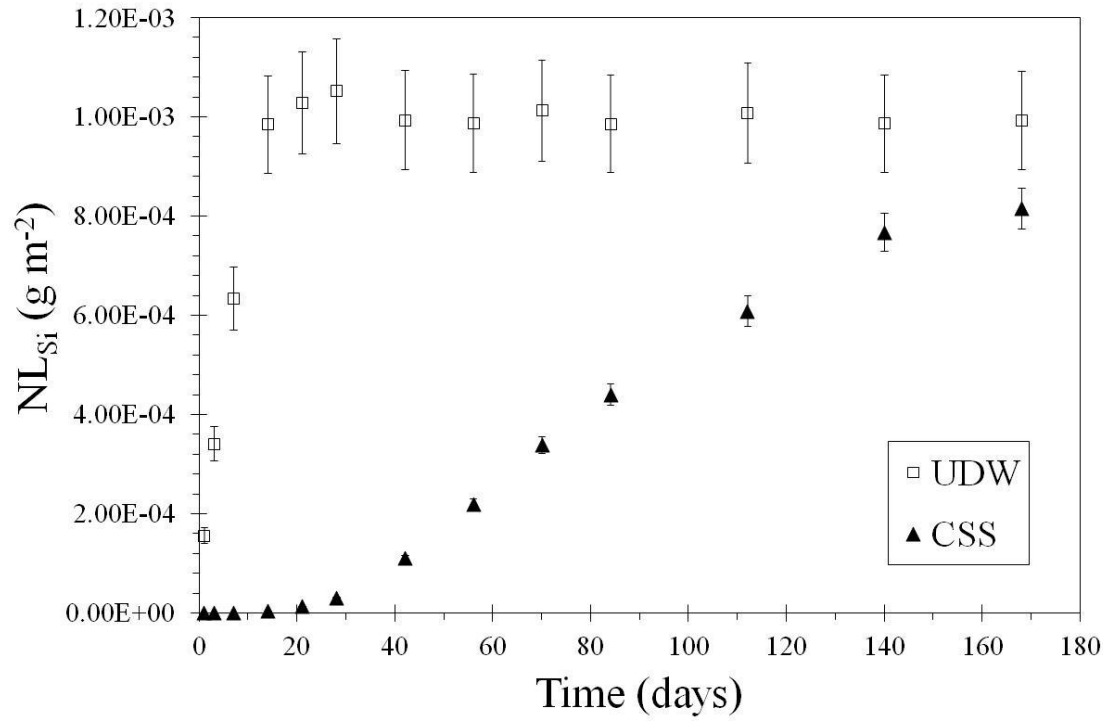

Figure 6.14 Normalised mass loss of Si for glass powders with a surface area to volume ratio of 10,000 m^{-1} in unbuffered deionized water (UDW) and the $Ca(OH)_2$ saturated solution (CSS) at 50 °C.

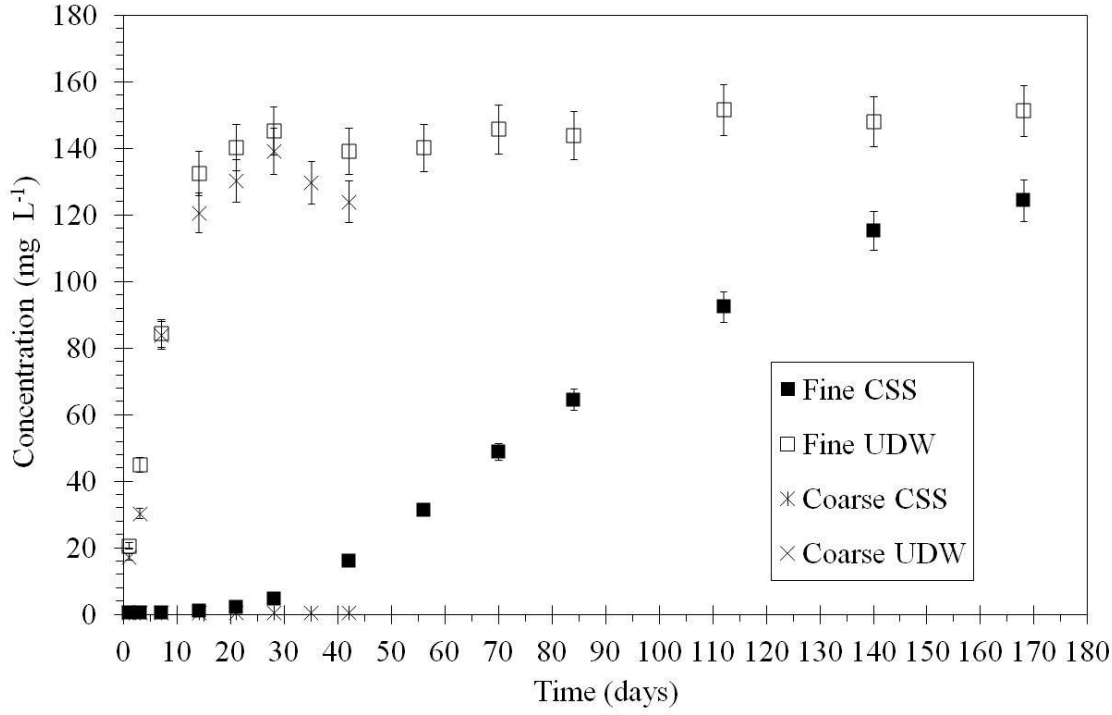

Figure 6.15 Concentration of Si for glass powders in unbuffered deionized water (UDW) and the $Ca(OH)_2$ saturated solution (CSS) for both the fine glass powder (SA/V = 10,000 m^{-1}) and coarse glass powder (1,200 m^{-1}).

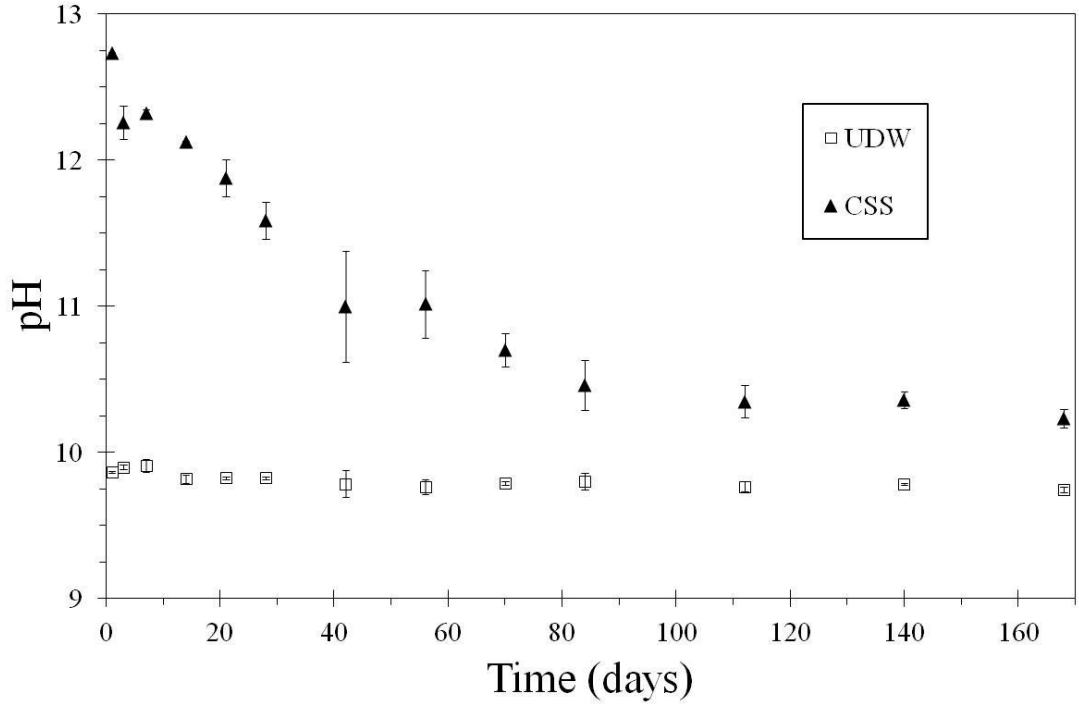

Figure 6.16 Solution pH of the glass powders in unbuffered deionized water (UDW) and the $Ca(OH)_2$ saturated solution (CSS) at 50 °C with a SA/V = 10,000 m^{-1}.

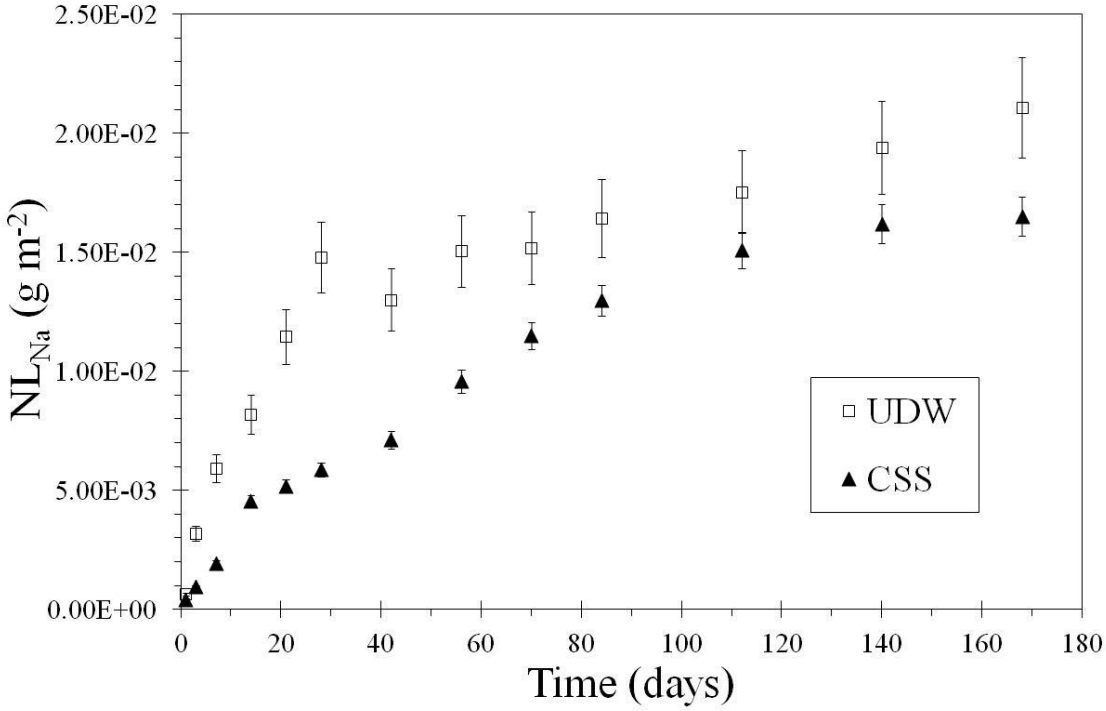

Figure 6.17 Normalised mass loss of Na for glass powders with a surface area to volume ratio of 10,000 m^{-1} in unbuffered deionized water (UDW) and the $Ca(OH)_2$ saturated solution (CSS) at 50 °C.

There is a clear difference between the NL_{Al} for the fine glass powder in UDW and CSS, as shown in Figure 6.18. The NL_{Al} for powder in UDW decreases over the duration of this study, while the NL_{Al} in CSS increases to 4.5 x 10^{-5} g m^{-2} at 14 days and is constant until 28 days where it begins a slow decrease to a constant value of approximately 4.0 x 10^{-5} g m^{-2} after 84 days.

The NL_{Mg} for the fine glass powders in UDW shows the opposite trend as compared to the NL_{Al}, while the NL_{Mg} for glass powder in CSS shows no significant change for the duration of the dissolution experiment. The NL_{Mg} for the glass powder in the UDW shows an increase to a maximum of about 5.5 x 10^{-5} g m^{-2} at 7 days and then a decrease to a constant value of approximately 3.0 x 10^{-5} g m^{-2} at 14 days. After 42 days, there is a decrease in the NL_{Mg} to approximately zero where the NL_{Mg} remains for the duration of the dissolution test.

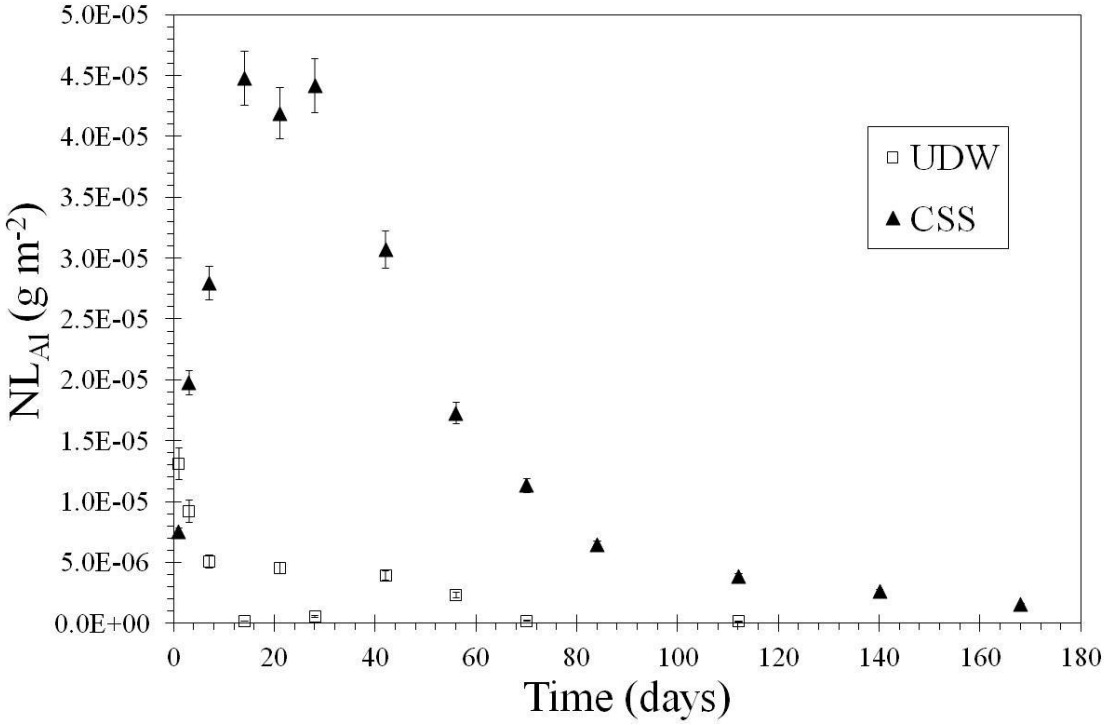

Figure 6.18 Normalised mass loss of Al for glass powders with a surface area to volume ratio of 10,000 m^{-1} in unbuffered deionized water (UDW) and the $Ca(OH)_2$ saturated solution (CSS) at 50 °C.

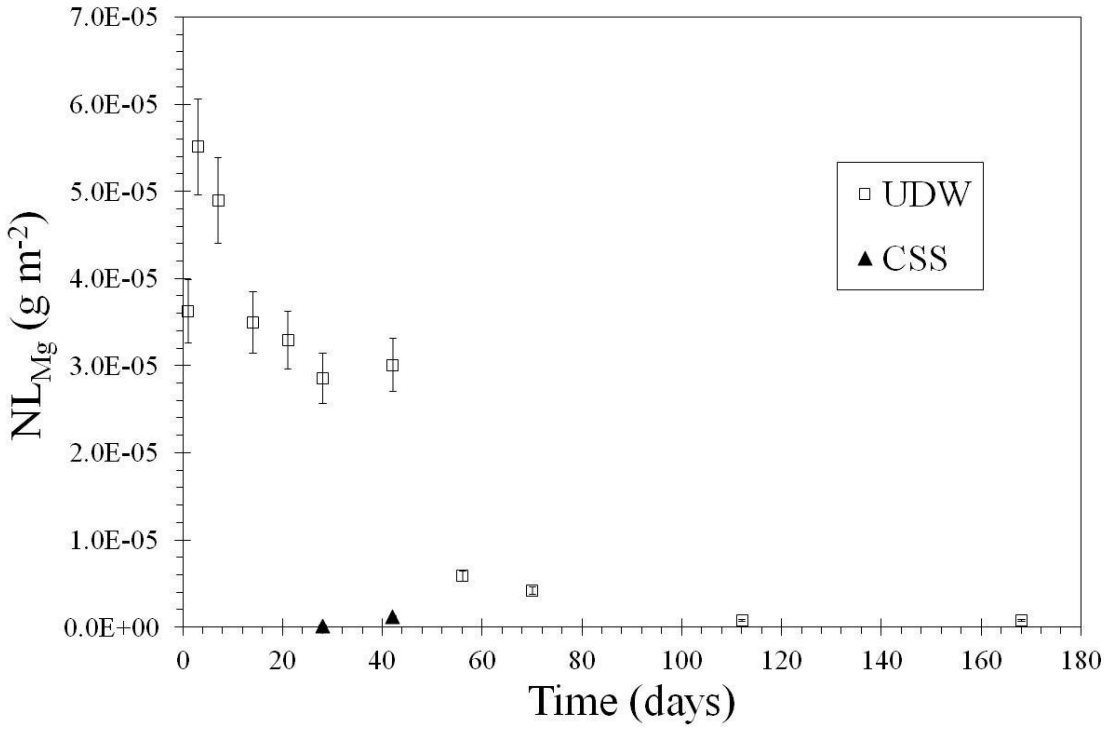

Figure 6.19 Normalised mass loss of Mg for glass powders with a surface area to volume ratio of 10,000 m^{-1} in unbuffered deionized water (UDW) and the $Ca(OH)_2$ saturated solution (CSS) at 50 °C.

6.3.2 Monolithic Durability Test Results

Monolithic durability tests (MCC-1) were performed using a similar process to the ASTM standard C 1220-98 but instead of UDW, the CSS was used at a temperature of 50 °C was used instead of 90 °C. The NL for B, Li, Si and Na for the monoliths are given in Figure 6.20. The NL_B initially decreases until 7 days, whereupon it is seen to increase until day 112 to 3.0 x 10^{-2} g m^{-2}. The NL_{Li} follows a similar trend as that of the $NL_{B,}$ as is expected. The concentration of Si was below the detection limits throughout the duration of experiments. There was also a general increase in NL_{Na} to 7.0 x 10^{-2} g m^{-2} during the experiment with possibly a slight reduction in the dissolution rate at 112 days. The maximum NL_B of the MCC-1 monoliths (Figure 6.20 A) at 140 days is approximately 10 times higher than the maximum NL_B of the coarse glass powder, as shown in Figure 6.2. The same is observed when comparing the NL_{Li} of the MCC-1 monoliths and the coarse glass powder plotted in Figure 6.3. These trends are consistent with the difference between the coarse and the fine glass powders where a higher SA/V ratio resulted in a lower NL due to the faster saturation of ion *i* in solution.

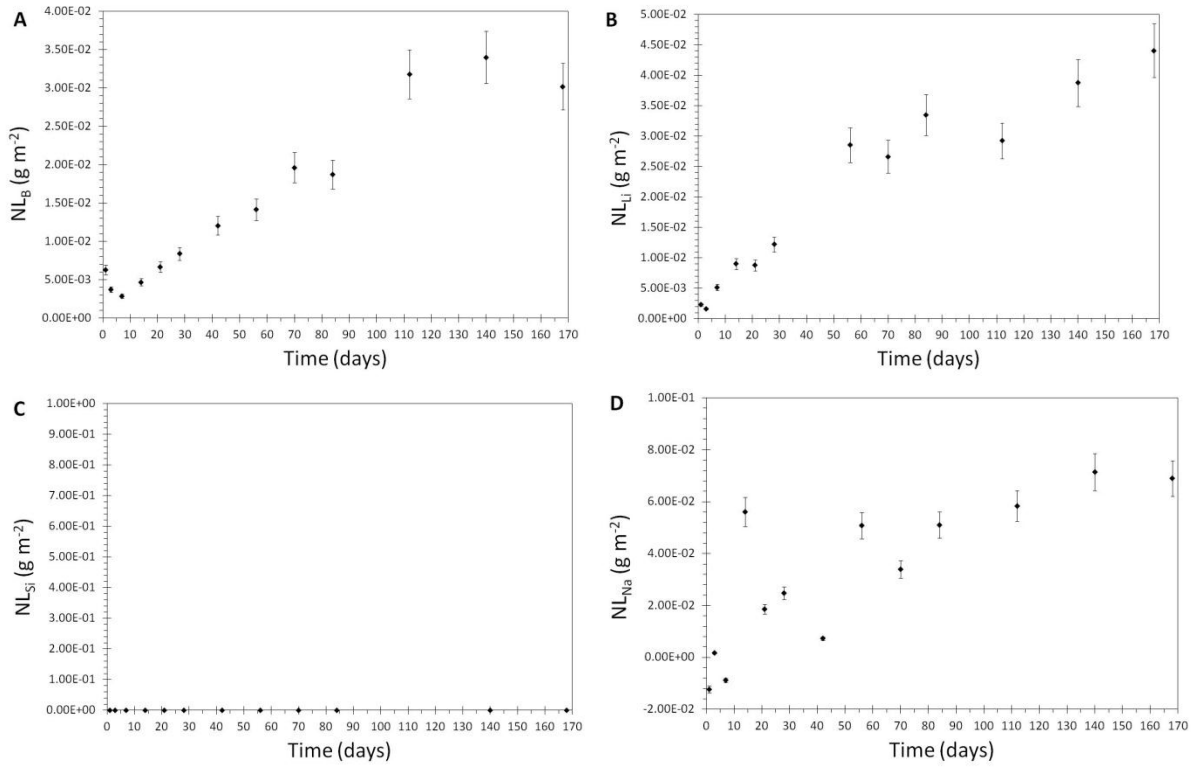

Figure 6.20 Normalised mass loss of A) B, B) Li, C), Si and D) Na for the MW+25wt% Blend glass monolith in $Ca(OH)_2$ saturated solution (CSS) at 50 °C.

Figure 6.21 gives the pH of the leachant used in the MCC-1 test and it can be seen that the pH throughout the entire test was 12.5 ± 0.3. The concentration of Si in solution being below the detection limits of the ICP (Figure 6.20 C) along with the high pH is consistent with the glass powder dissolution tests where Si is detected in solution above pH = 12.

Figure 6.22 plots the XRD traces for each monolith sample for each time period during the MCC-1 test. Analysis of the pristine glass by XRD resulted in three peaks which correspond to RuO_2, as shown in Figure 6.22. After 3 days, one peak can be seen near $2\theta = 23°$ and a second peak is observed at 21 days at approximately $2\theta = 18°$ on in the XRD traces. Fitting the peaks for the monolith corroded in CSS at 50 °C for 168 days, Figure 6.23, resulted in peaks at $2\theta = 13°$ and $2\theta = 23°$. These peaks possibly correlate to antigorite with the chemical composition of $Mg_{3-x}[Si_2O_5](OH)_{4-2x}$. The peak at $2\theta = 18°$ can be attributed to portlandite – $Ca(OH)_2$. Ruthenium oxide is also apparent in the diffraction pattern as shown in Figure 6.23.

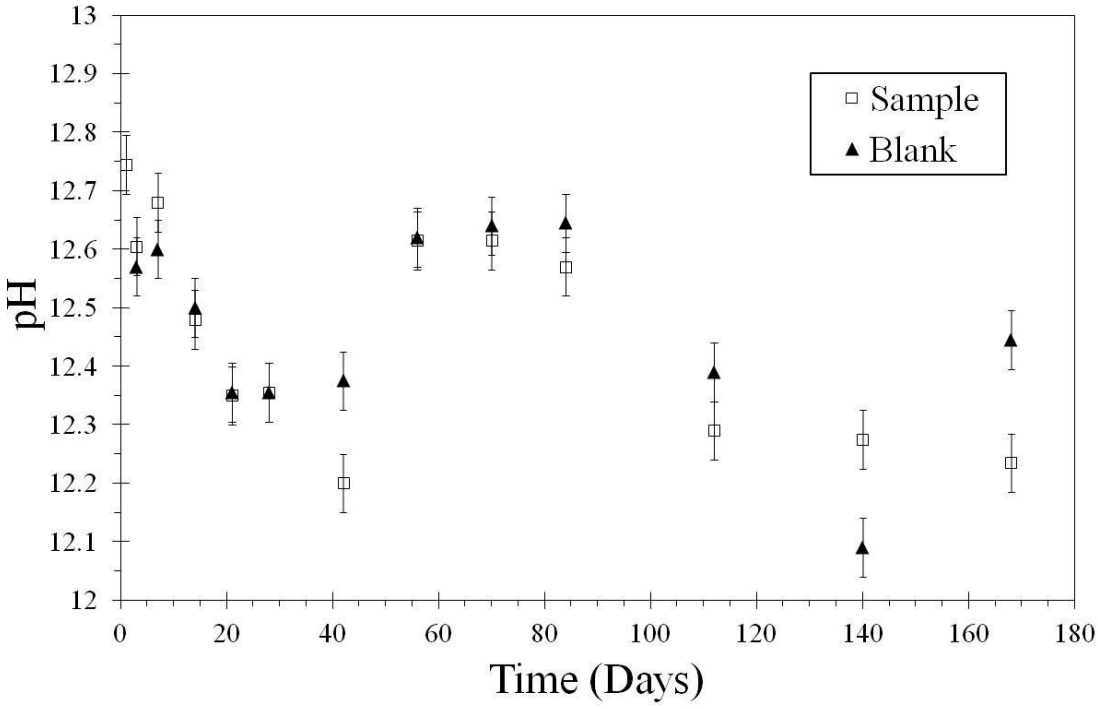

Figure 6.21 Solution pH for the MW +25wt% Blend MCC-1 test in $Ca(OH)_2$ saturated solution (CSS) at 50 °C.

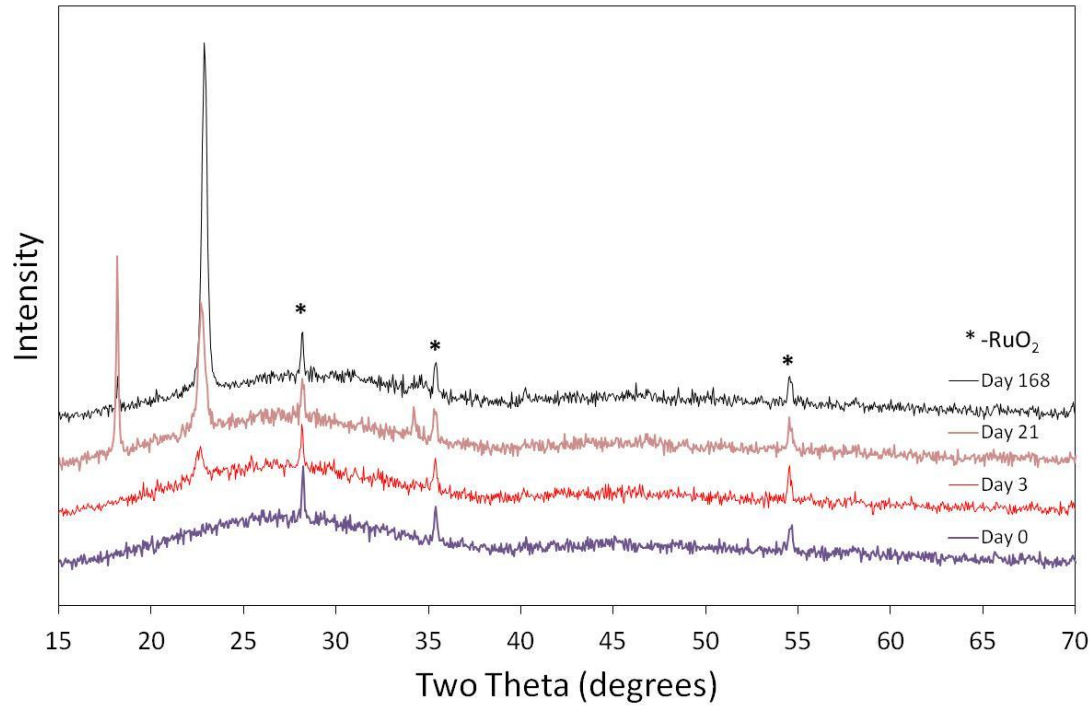

Figure 6.22 XRD patterns for the MW + 25 wt% Blend glass from a pristine surface and corroded up to 168 days in a $Ca(OH)_2$ saturated solution (CSS) at 50 °C.

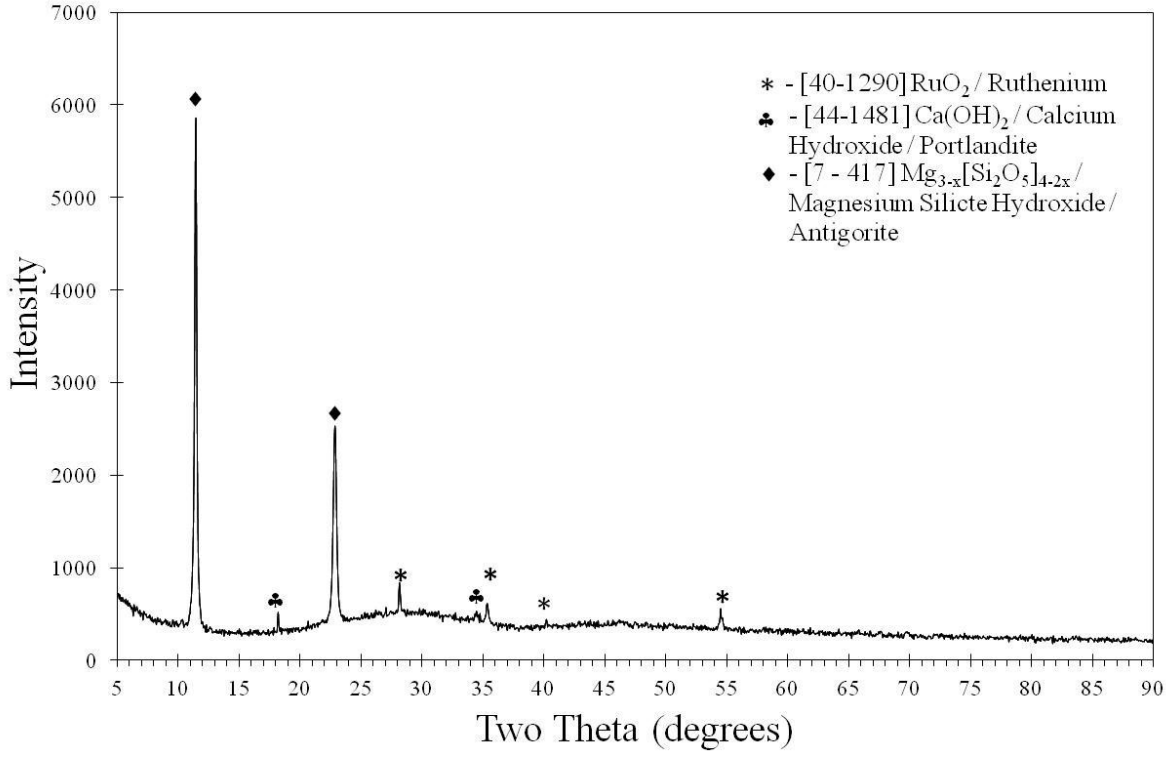

Figure 6.23 XRD pattern for the MW + 25 wt% Blend glass corroded for 168 days in a $Ca(OH)_2$ saturated solution (CSS) at 50 °C.

Secondary and backscatter electron images of the 3 day and 168 day MCC-1 monoliths in the CSS solution are shown in Figure 6.24 and 6.25, respectively. The images in Figure 6.24 are secondary electron images of the surface topography of the 3 day sample and the 168 day sample (Figure 6.24 A and Figure 6.24 B, respectively). It can be seen that for the 3 day sample there is possible formation of an alteration layer on the surface of the sample, while visual observation of the 168 day sample suggests there is a well defined alteration layer on the surface of the pristine glass. Observation of the same regions for the 3 and 168 day samples under backscatter electron imaging, Figure 6.25 A and Figure 6.25 B respectively, show that it is difficult to determine any significant alteration layer on the surface of the sample except for one region in the upper right region of the backscatter image on the 168 day sample, Figure 6.25 B.

Further analysis of the surfaces of the 3 day and 168 day MCC-1 samples revealed small precipitates that have formed on the surface, as shown in Figure 6.26 A and B, respectively. In Figure 6.26 A, the precipitates appear to be sphere like shapes; however, the precipitates formed on the surface of the 168 day sample have an acicular (needle like) morphology. Backscatter images of the both the 3 day and 168 day samples were also taken and are shown in Figure 6.27 A and B, respectively. Alteration products were observed to form after three days on the surface of the glass. For the 168 day sample, the precipitates have two distinct compositions as is apparent from the difference in contrast within the backscatter image. It should also be noted that there are also two different secondary alteration products shown in this image; spherical and rod like particles.

A 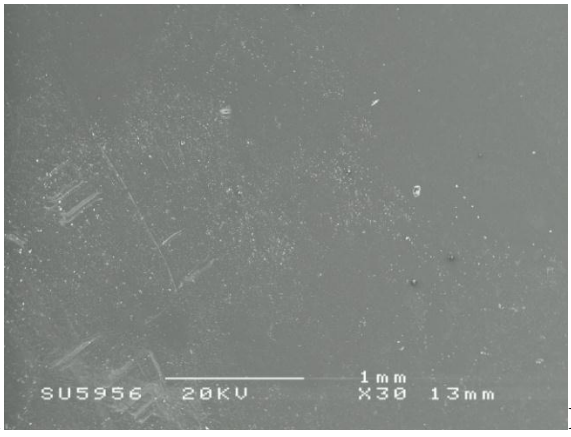

B 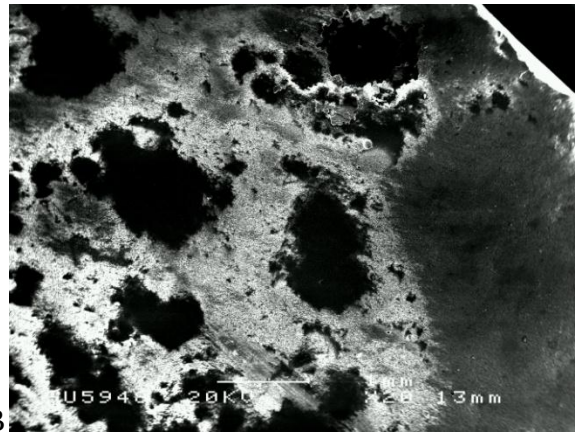

Figure 6.24 Secondary electron images of the surface topography of A) 3 day sample and B) 168 day monolith in $Ca(OH)_2$ saturated solution (CSS) at 50 °C.

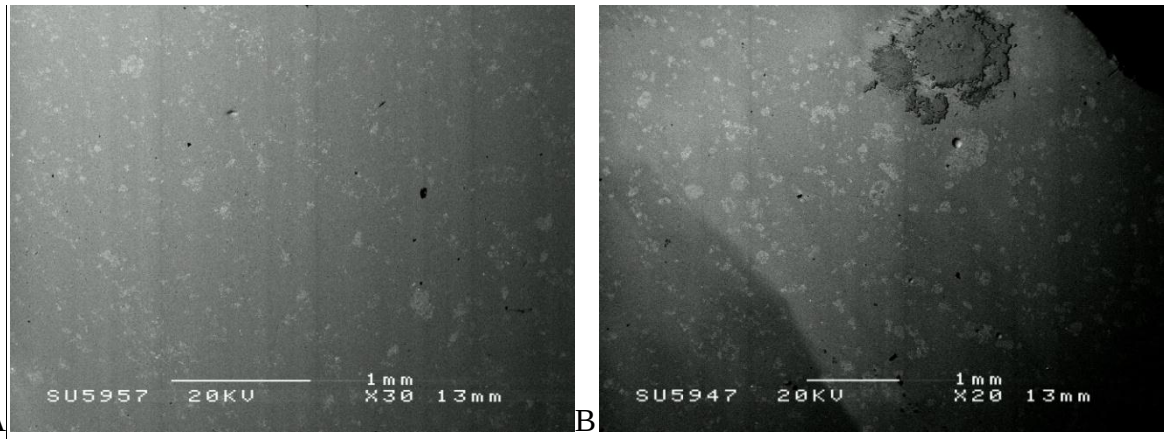

A B

Figure 6.25 Backscatter electron images of the surface of A) 3 day sample and B) 168 day monolith in $Ca(OH)_2$ saturated solution (CSS) at 50 °C.

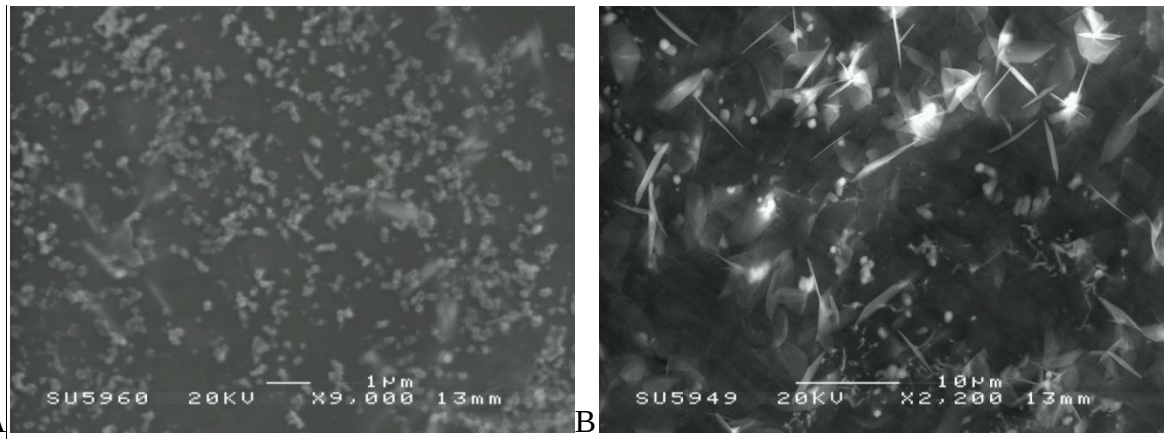

A B

Figure 6.26 Secondary electron images of the surface topography of A) 3 day sample and B) 168 day monolith in $Ca(OH)_2$ saturated solution (CSS) at 50 °C.

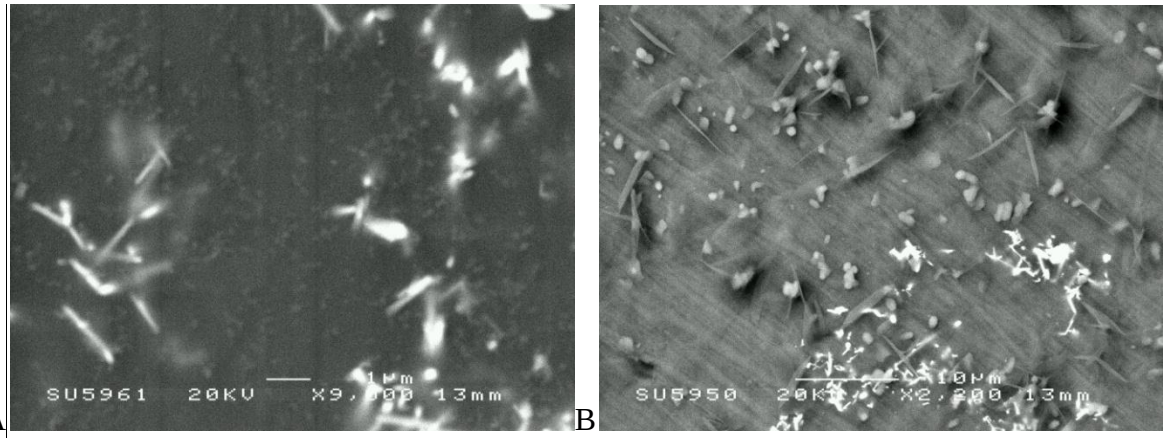

A B

Figure 6.27 Backscatter electron images of the surface of A) 3 day sample and B) 168 day monolith in $Ca(OH)_2$ saturated solution (CSS) at 50 °C.

Further examination of the precipitates on the 3 and 168 day sample by EDS analysis revealed that some were rich in Ru. Figure 6.28A and B gives backscatter electron images

for the surface of the 3 and 168 day samples, respectively, and shows the points that were analyzed by EDS. Only single points were utilized as shown in the image. In order to decrease the interaction volume and decrease the amount of the bulk glass analyzed, a smaller spot size with a lower KeV could be utilized; however, this also decreases the signal received. The regions of the EDS analysis were selected to analyse the bulk glass along with qualitative analysis of the alteration products.

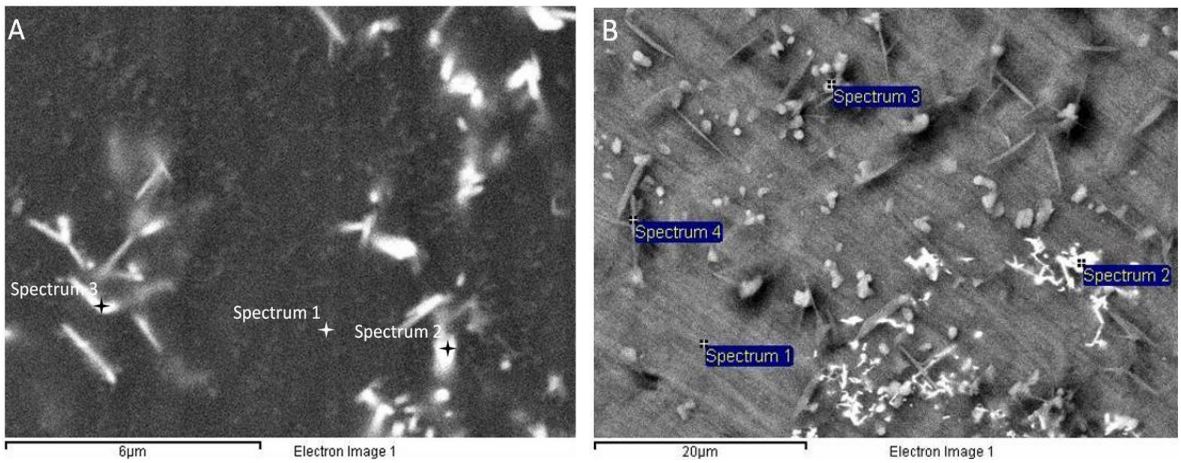

Figure 6.28 Backscatter electron image of A) the 3 day sample and B) the 168 day sample showing the regions of EDS point analysis.

Figure 6.29 gives EDS spectra of the images given in Figure 6.28 A. Spectrum 1 is of the bulk glass and spectra 2 and 3 are taken from the crystalline precipitates. Spectrum 2 and 3 of the 3 day sample, given in Figure 6.29, show a higher concentration of Ru as compared to spectrum 1 in which the counts of Ru are below the background level. The concentration of calcium also increases from the bulk glass (spectrum 1) to the crystalline precipitate analysed in spectrum 2. The concentration of Ru is similar between the two crystalline precipitates analysed in the 3 day sample (spectrum 2 and 3). A close examination of the three spectrum reveals that the concentration of Fe also increases from spectrum 1 (bulk glass) to spectrum 2 (crystalline precipitate).

Figure 6.28 B shows the locations of the four EDS point spectra for the 168 day sample shown in Figure 6.29. All four spectra contain a high concentration of Ca as compared to the three EDS spectra for the three day sample. The bulk glass (spectrum 1) is very similar to the alteration products analysed in spectrum 3 and 4, which is not surprising since the majority of the interaction volume is within the bulk glass. The alteration product in spectrum 2; however, shows that the concentration of Al is below the background of the signal and there

is a high concentration of Ru in the surface of the glass. This provides evidence that the Ru crystallites in the pristine glass do not corrode.

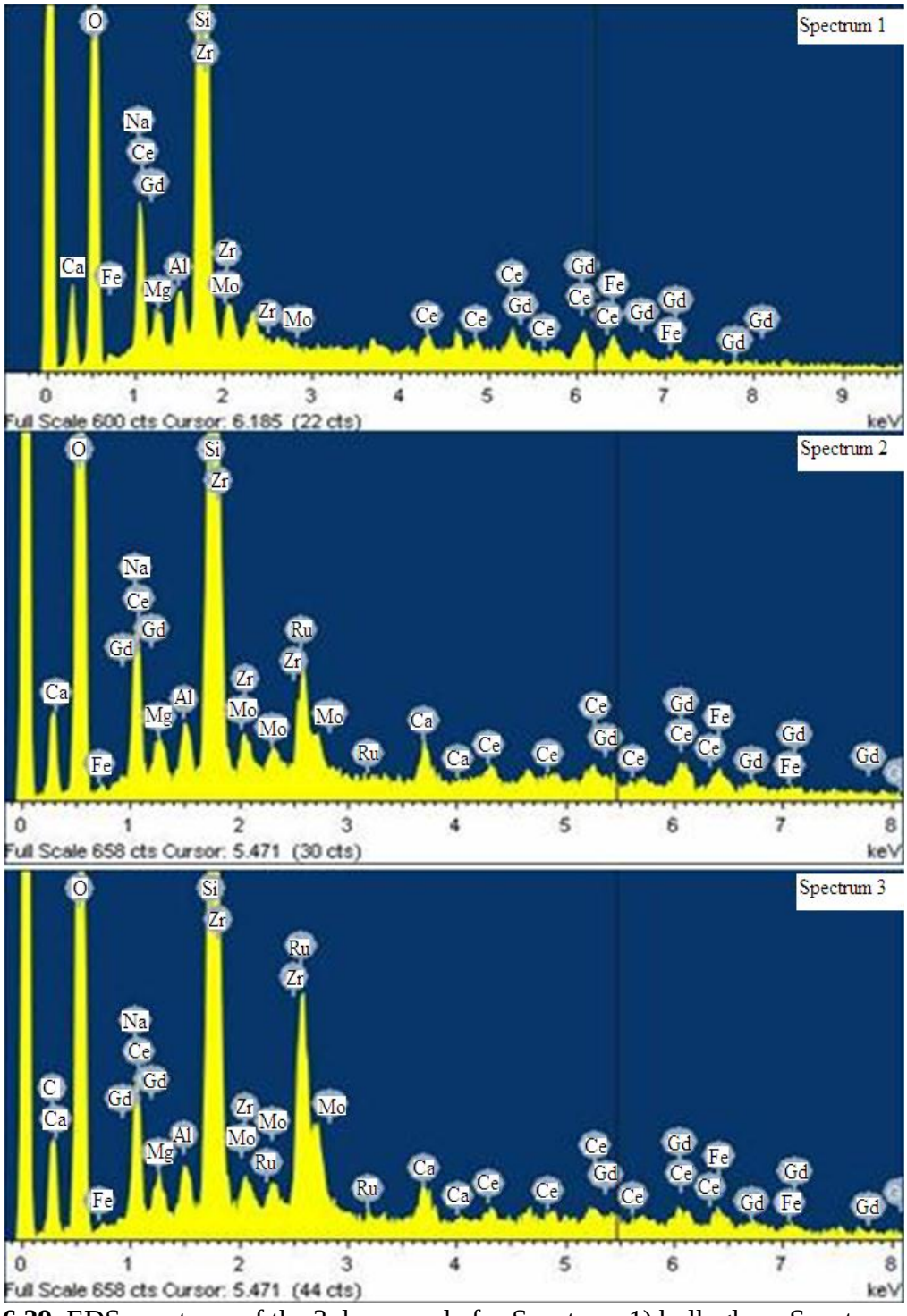

Figure 6.29 EDS spectrum of the 3 day sample for Spectrum 1) bulk glass, Spectrum 2) precipitate, and Spectrum 3) precipitate, of the image in Figure 6.28.

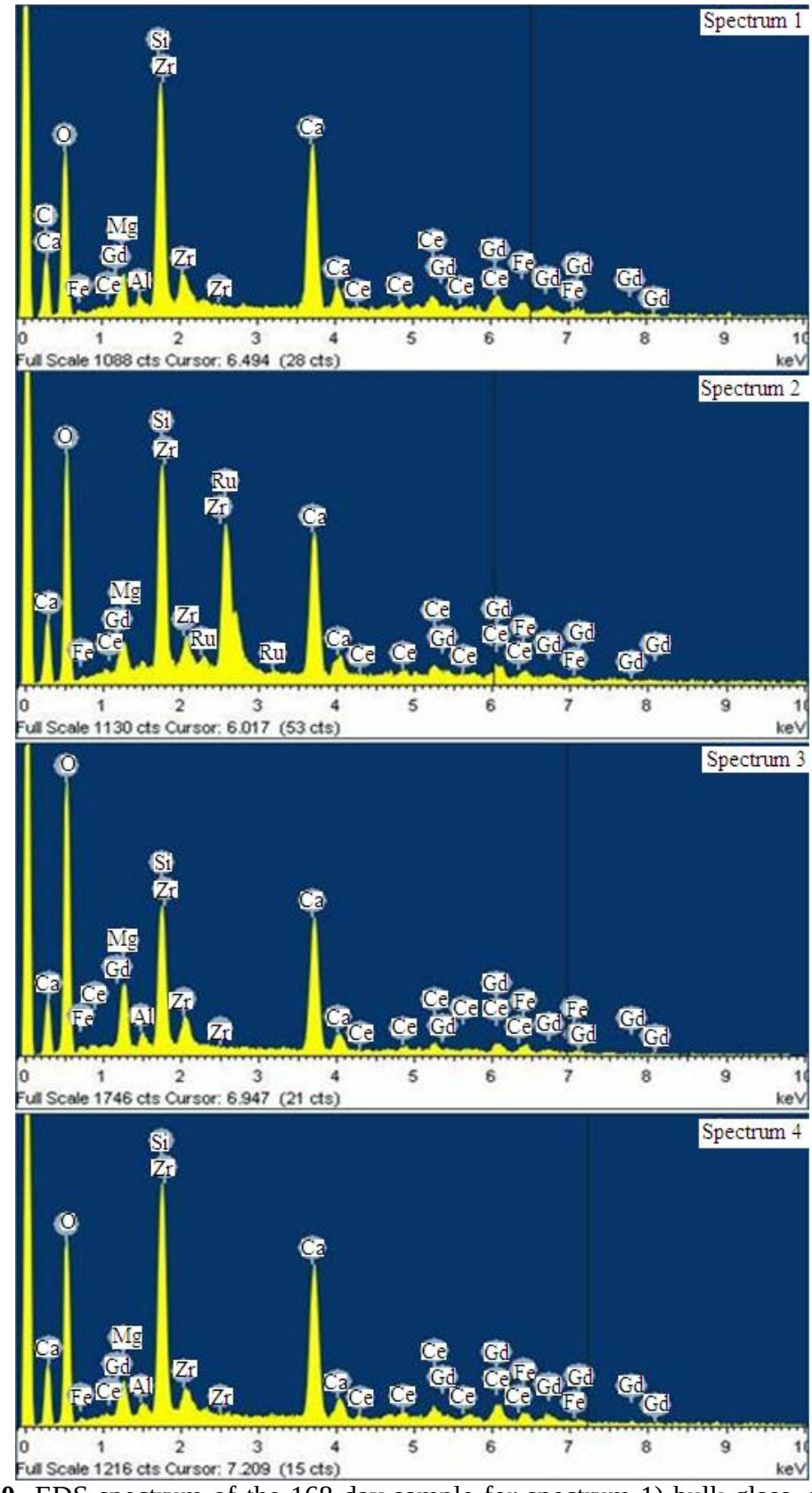

Figure 6.30 EDS spectrum of the 168 day sample for spectrum 1) bulk glass, spectrum 2) precipitate, spectrum 3) precipitate, and spectrum 4) precipitate, of the image in Figure 6.28B.

An analysis of the cross section of the 168 day sample, shown in Figure 6.31, reveals an alteration layer approximately 3 μm in thickness. This can be seen in the backscatter electron image in Figure 6.31A; which shows the bulk glass on the right side of the image, the alteration layer in the middle of the image and the epoxy resin which is the black region on the left of the image along with a white line showing where the EDS linescan was performed. The EDS line scan for Si, Na, Mg, Al, Zr, Fe, Ce and Mo is given in Figure 6.31. The concentration of Si on the alteration layer surface shows a local maximum between 0 – 3 μm from the surface of the gel layer and then a large increase at the surface of the bulk glass. Other elements, with the exception of Fe, also show that there is the formation of an alteration layer of the surface of the bulk glass due to the local maximum in concentration between 0 – 3 μm before their concentrations increase at the surface of the bulk glass.

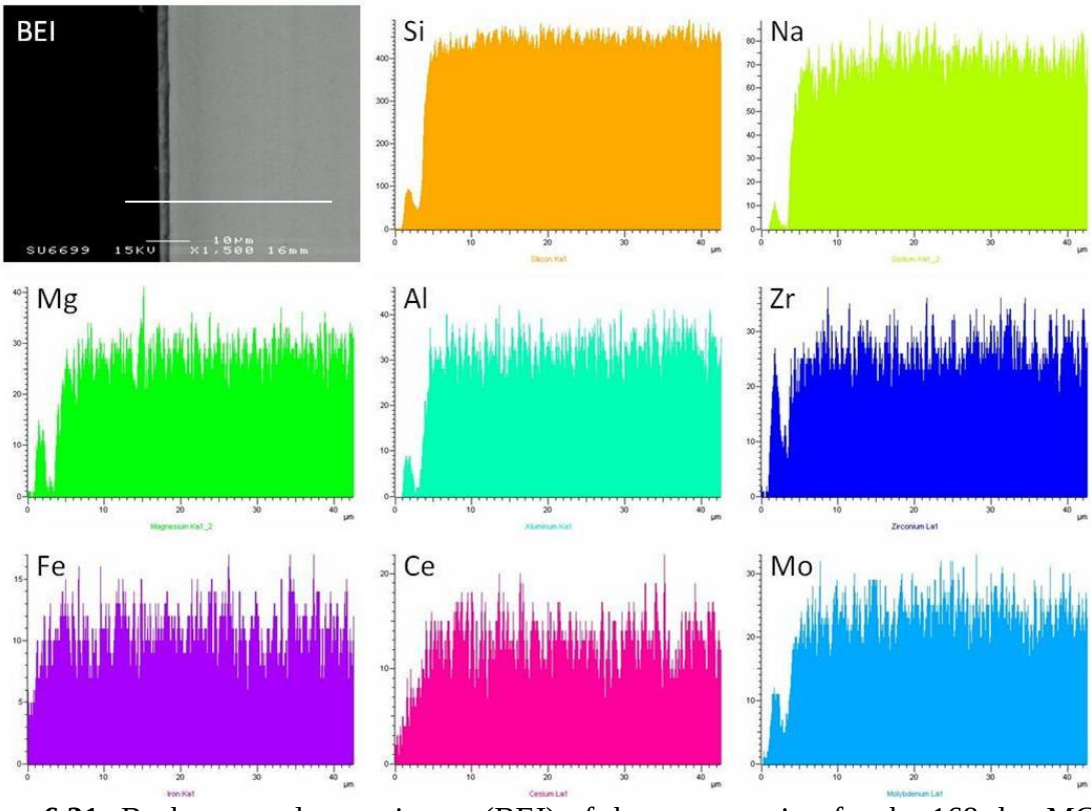

Figure 6.31 Backscatter electron image (BEI) of the cross section for the 168 day MCC-1 sample in $Ca(OH)_2$ saturated solution (CSS) along with the EDS line scans of Si, Na, Mg, Al, Zr, Fe, Ce and Gd.

6.3.3 PHREEQC Modelling of the PCT-t and MCC-1

The results of the PCT-t and MCC-1 were used for geochemical modelling using the PHREEQC code, a thermodynamic aqueous speciation and solubility modelling tool. [153] Modelling of the aqueous data from these experiments resulted in the apparent super-saturation with respect to several mineral phases, which suggest their possible precipitation during the dissolution. Due to the abundance of mineral phases available to be modelled by PHREEQC, a smaller number of possible phases were selected for discussion.*

The saturation index of several minerals was calculated in the modelling results from PHREEQC; however, only the most relevant were chosen for discussion due to the quantity of phases modelled. The minerals chosen for this study were originally modelled by Abraitis *et al.* in addition to analcime ($Na_{0.96}Al_{0.96}Si_{2.04}O_6{:}H_2O$), which is a known precipitate from silicate glasses, and tobermorite ($Ca_5Si_6(O,OH)18{\cdot}5H_2O$), which is a hydrated calcium silicate mineral. [141] The saturation indices of these minerals are plotted with time in Figure 6.34 to Figure 6.36 for the fine glass powder in CSS. Figure 6.34 illustrates the saturation index for Ca-bearing phases: $Ca(OH)_2$, diopside ($CaMgSi_2O_6$), tobermorite ($Ca_5Si_6(O,OH)18{\cdot}5H_2O$) and phillipsite-Ca ($CaAl_2Si_5O_{14}{\bullet}5H_2O$). As observed from Figure 6.34, at 21 days when $Ca(OH)_2$ becomes nearly constant after 85 days in solution, all the Ca-bearing phases become supersaturated and start to precipitate.

The saturation indices of the Si bearing phases; amorphous silica, analcime ($Na_{0.96}Al_{0.96}Si_{2.04}O_6{:}H_2O$),sepiolite ($Mg_2Si_3O_{7.5}OH{\bullet}3H_2O$) and talc ($Mg_3Si_4O_{10}(OH)_2$); are all plotted in Figure 6.35. It can be seen from a comparison of Figure 6.34 and 6.35 that analcime ($Na_{0.96}Al_{0.96}Si_{2.04}O_6{:}H_2O$) along with diopside become saturated in solution before 168 days. Analcime saturation corresponds to when $Ca(OH)_2$ becomes relatively constant after 80 days.

A key observation in Figure 6.34 is that for $Ca(OH)_2$ the saturation index is initially supersaturated and then at 21 days decreases below saturation. This correlates to the data where the concentration of Si in solution is below the detection limits of the ICP until 21 days. The saturation index of $Ca(OH)_2$ continues to decrease until 84 days where it then becomes stable.

It should be noted that the Si phases are also host to Mg, Al and Na for which there is plausible evidence that they are present in the precipitates that can be seen in the in the EDS linescans shown in the previous section; however, the normalised loss of Si, Mg, Al, and Na

* For a full list of mineral phases modelled in this study by PHREEQC, see Appendix A.

are not consistent with the phases modelled in this data. From the EDS linescans there is evidence of Mg, Al, and Na; however, from EDS spot analysis, it is difficult to say with confidence there is substantial evidence from this. This could be due to the electron interaction volume which will include much of the bulk glass. This gives a good indication that the corrosion process may be due to complex diffusion processes that are outside the scope of this work or that the solubility of these phases in solution is controlled by other phases that were not modelled in this work.

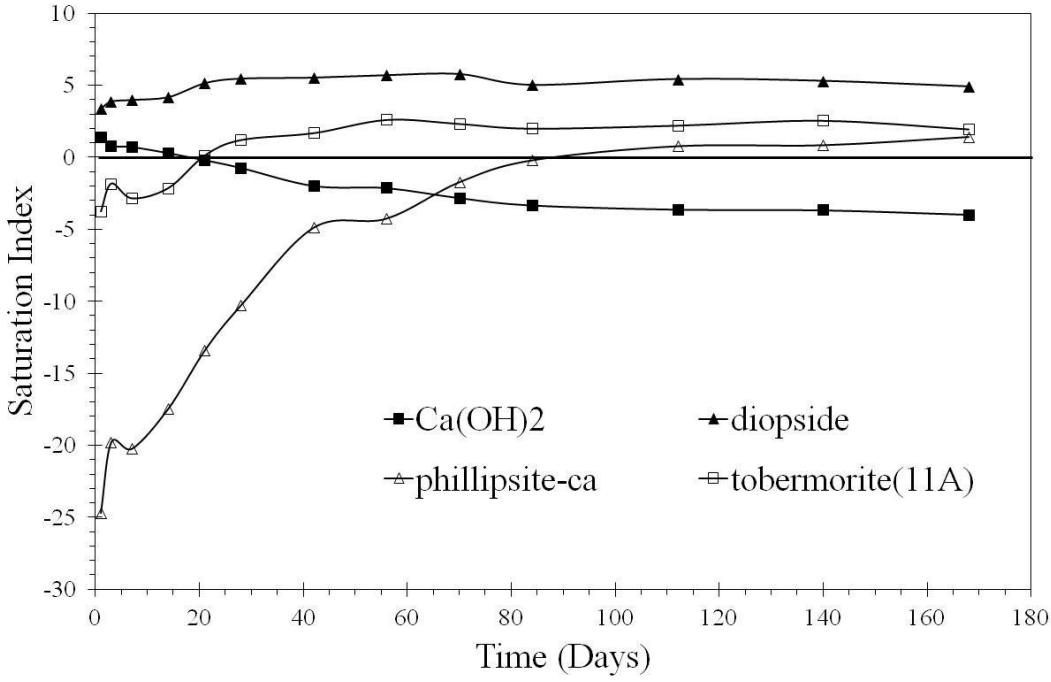

Figure 6.34 Saturation index of the Ca phases modelled with PHREEQC for the fine glass powder in $Ca(OH)_2$ saturated solution (CSS) at 50 °C; $Ca(OH)_2$, diopside ($CaMgSi_2O_6$), tobermorite ($Ca_5Si_6(O,OH)18{\cdot}5H_2O$) and phillipsite-Ca ($CaAl_2Si_5O_{14}{\bullet}5H_2O$).

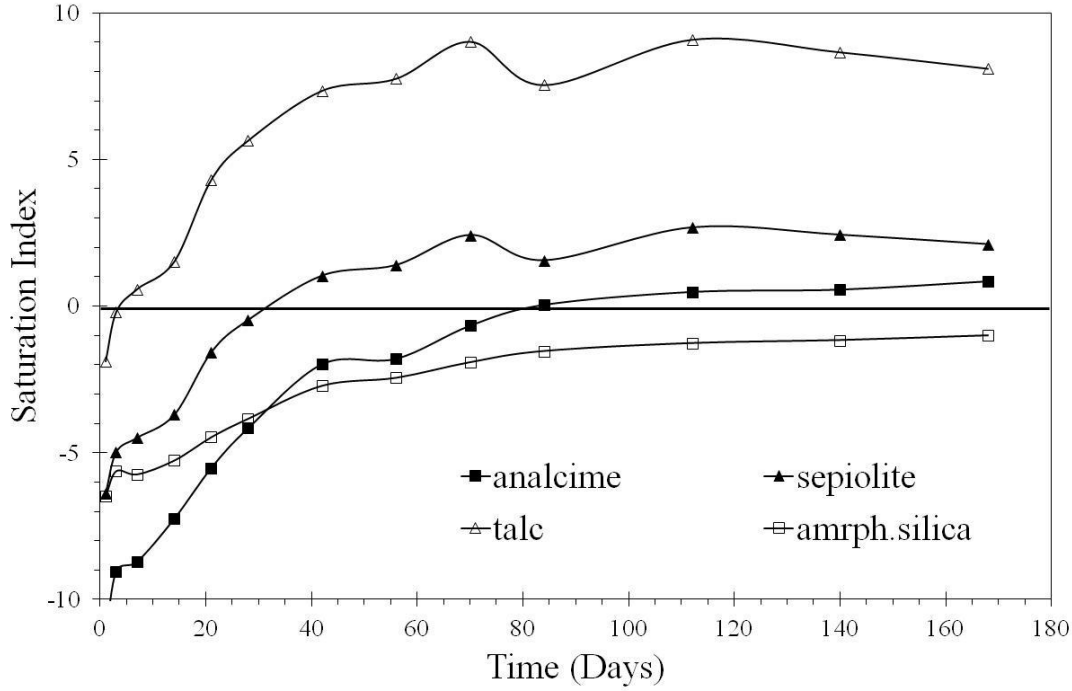

Figure 6.35 Saturation index of the Si-bearing phases modelled with PHREEQC for the fine glass powder in $Ca(OH)_2$ saturated solution (CSS) at 50 °C; amorphous silica, analcime ($Na_{0.96}Al_{0.96}Si_{2.04}O_6{:}H_2O$), sepiolite ($Mg_2Si_3O_{7.5}OH{\bullet}3H_2O$) and talc ($Mg_3Si_4O_{10}(OH)_2$).

Figure 6.36 models the saturation index for Al and Fe-bearing phases: diaspore ($AlO(OH)$), $Fe(OH)_3$, gibbsite ($Al(OH)_3$), and goethite ($FeOOH$). Both goethite and $Fe(OH)_3$ are supersaturated in solution during the dissolution experiment and show an overall increase in saturation. Both gibbsite and diaspore are undersaturated during the entire dissolution test; however, there is an initial increase in the saturation index up to a maximum at 42 days where the saturation index stabilises.

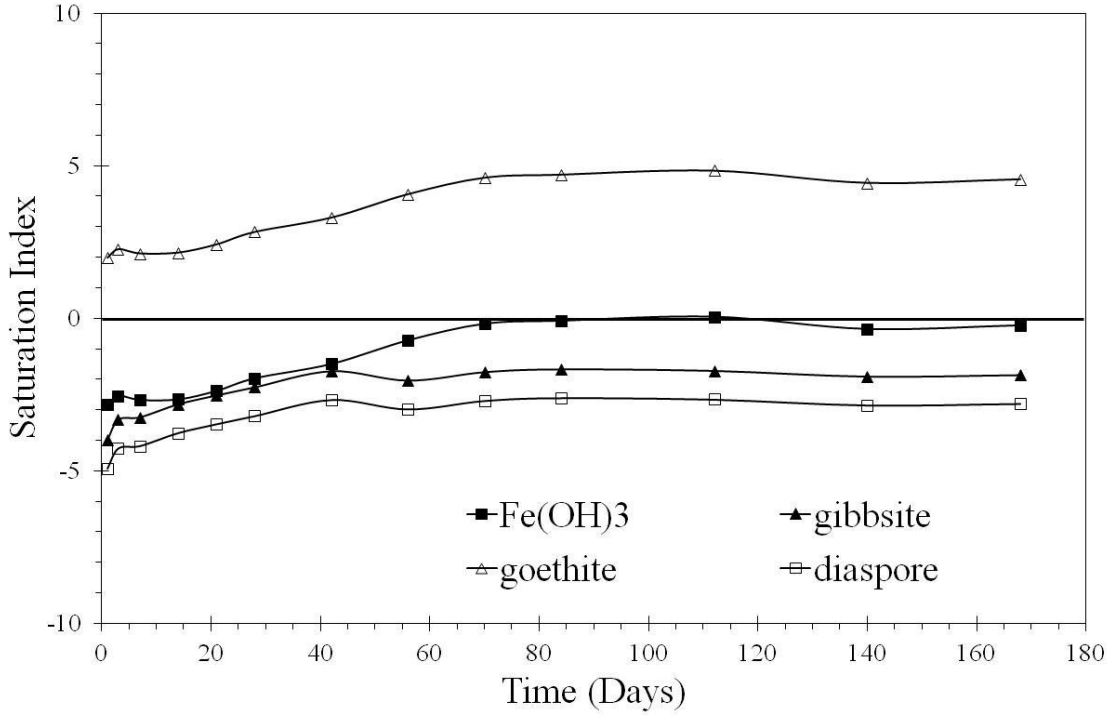

Figure 6.36 Saturation index of the Al and Fe-bearing phases modelled with PHREEQC for the fine glass powder in $Ca(OH)_2$ saturated solution (CSS) at 50 °C; diaspore (AlO(OH)), $Fe(OH)_3$, gibbsite ($Al(OH)_3$), and goethite (FeOOH).

Other minerals such as; phillipsite-ca ($CaAl_2Si_5O_{14}{:}5H_2O$), sepiolite ($Mg_2Si_3O_{7.5}OH{:}3H_2O$), talc ($Mg_3Si_4O_{10}(OH)_2$) and tobermorite-11A ($Ca_5Si_6(O,OH)18{\cdot}5H_2O$), all show an initial increase in their saturation index. With the exception of talc, they all become constant at 84 days. Whereas for talc, its saturation index becomes constant at approximately 56 days. After 42 days, both sepiolite and tobermorite are both supersaturated in solution and have a constant saturation index for the duration of the dissolution test.

The saturation index of the minerals becoming constant at approximately 84 days correlates to the concentration of Ca in solution and the pH of solution becoming constant (Figures 6.13 and 6.16, respectively). At 84 days, analcime (a known mineral phase which precipitates out of solution for silicate glasses) becomes supersaturated. Tobermorite becomes supersaturated in solution when $Ca(OH)_2$ becomes undersaturated, at 21 days, which also correlates to the concentration of Si in solution being above detection limits of the ICP instrument. At 84 days when analcime becomes supersaturated, the saturation index of the rest of the minerals, which may be present in solution, become constant. However, the NL_{Si} still increases up to 140 days where it appears to become constant. A close examination of the saturation index of Al containing phases (Figure 6.36) to the NL_{Al} in Figure 6.18 suggests that the increase in the saturation index of the Al minerals correlates to the NL_{Al}.

There does not appear to be any correlation between the saturation index of the minerals containing Mg to the NL_{Mg} for the glass powder in CSS as mentioned previously.

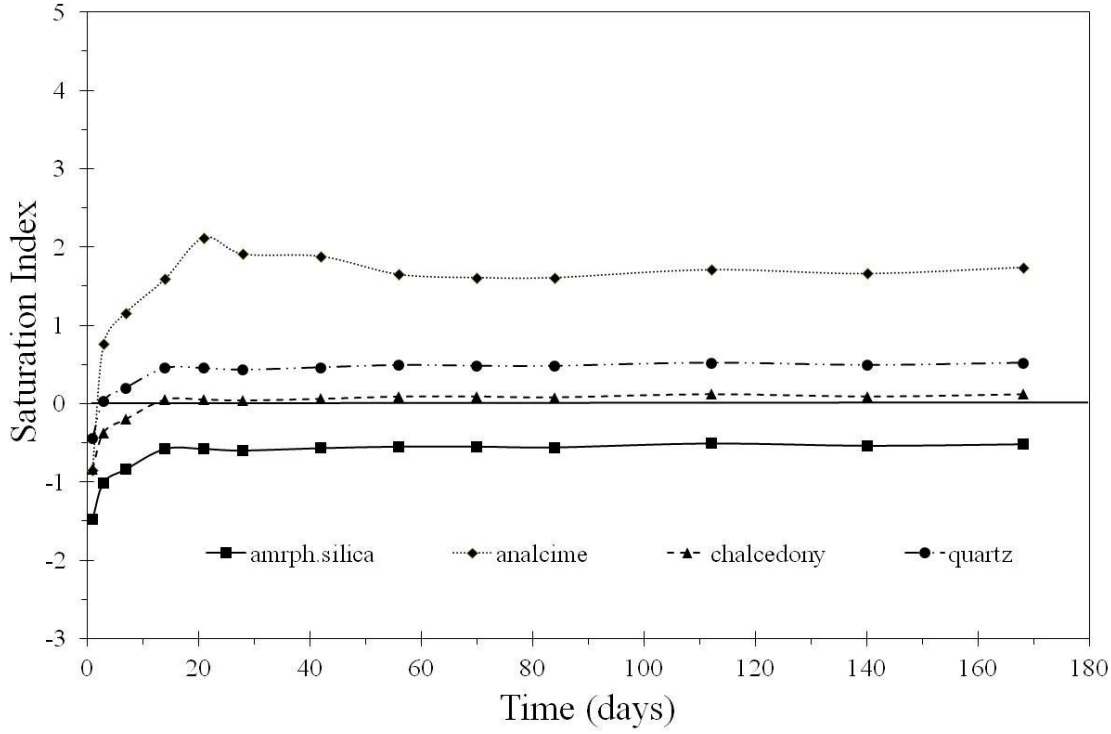

Figure 6.37 Saturation index of Si containing phases modelled with PHREEQC for the fine glass powder in unbuffered deionized water (UDW) at 50 °C; amorphous silica (SiO_2), analcime ($Na_{0.96}Al_{0.96}Si_{2.04}O_6{:}H_2O$), chalcedony ($SiO_2$) and quartz ($SiO_2$).

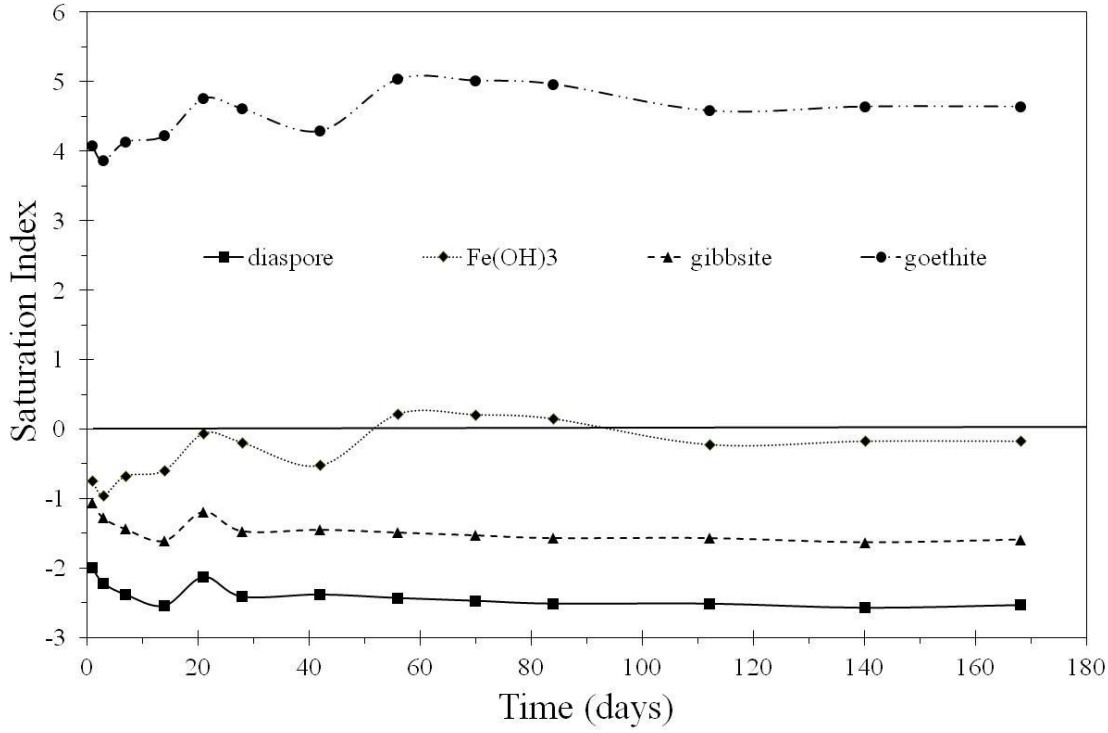

Figure 6.38 Saturation index of select phases modelled with PHREEQC for the fine glass powder in unbuffered deionized water (UDW) at 50 °C; diaspore (AlO(OH)), $Fe(OH)_3$, gibbsite ($Al(OH)_3$) and goethite (FeOOH)

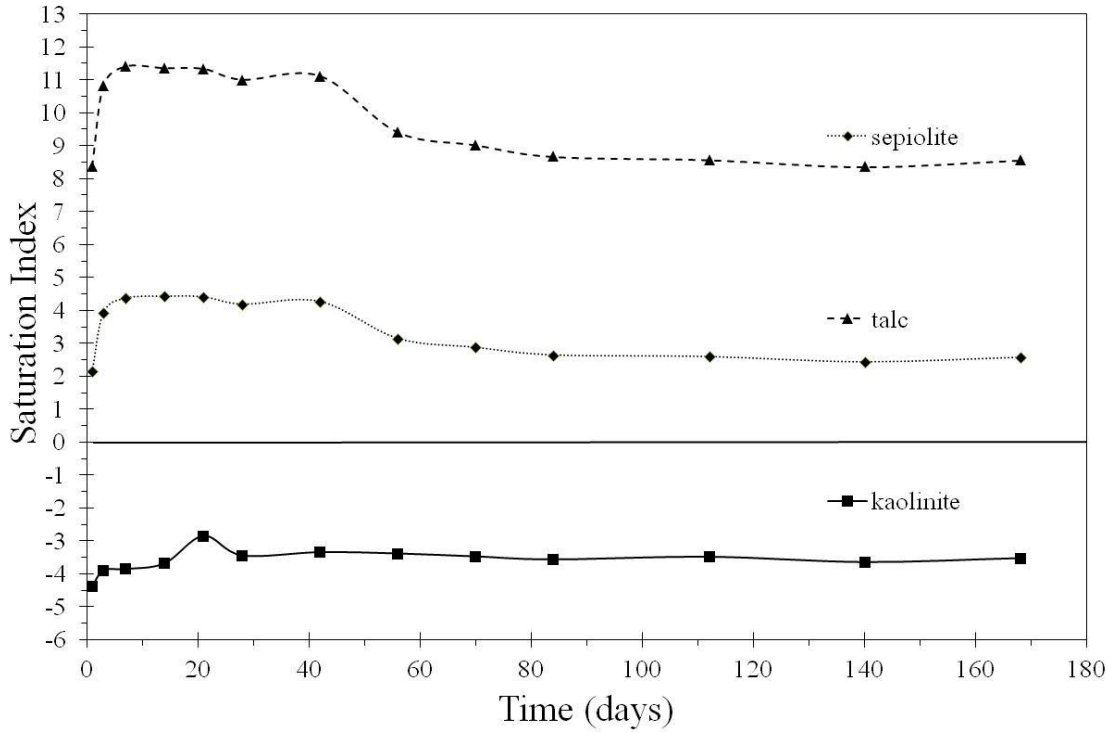

Figure 6.39 Saturation index of Mg and Al containing phases modelled with PHREEQC for the fine glass powder in unbuffered deionized water (UDW) at 50 °C; sepiolite ($Mg_2Si_3O_7$•5OH•$3H_2O$), talc ($Mg_3Si_4O_{10}(OH)_2$) and kaolinite ($Al_2Si_2O_5(OH)_4$).

Further modelling of the saturation index of minerals for the fine glass powder in UDW was performed and the results are presented in Figure 6.37 to Figure 6.39. Due to the absence of Ca in solution, phases containing Ca were not modelled. Examination of Figure 6.36 reveals an increase in each of the minerals and amorphous silica which follows the trend of the NL_{Si} where there is an increase of Si in solution up until 14 days where the NL_{Si} becomes constant. From day 14 all of the minerals are supersaturated in solution for the duration of the dissolution test. Only analcime continues to increase in saturation, until day 21, before it decreases and becomes constant at day 56.

Figure 6.38 plots the saturation index of diaspore (AlO(OH)), $Fe(OH)_3$, gibbsite ($Al(OH)_3$) and goethite (FeOOH) in UDW at 50 °C. Both $Fe(OH)_3$ and goethite show an increase in the saturation index until day 56 where they become constant, and $Fe(OH)_3$ becomes supersaturated in solution. Both diaspore and gibbsite are initially undersaturated and then decrease until 28 days where they become constant until the end of the dissolution test. Figure 6.39 only plots three minerals; sepiolite, talc and kaolinite. Both sepiolite and talc, as expected, follow the trend of NL_{Mg} (Figure 6.19) where there is a fast increase at short times and then a decrease after 42 days until it becomes constant near 56 days. There is only a slight overall increase in the saturation index of kaolinite. This is expected, due to no significant change in NL_{Al} for glass powder in UDW during the dissolution test as can be seen in Figure 6.18.

6.4 Discussion

6.4.1 Durability of the MW25Blend Glass

The decrease in the pH for glass powder in the low SA/V solution, as given in Figure 6.6, correlates to the OH^- being consumed causing the pH of the solution to decrease. It is proposed that below a neutral pH, Ca does not react with a silicate gel layer; however, above pH = 10, hydrated calcium silicate precipitates will form as shown in the modelling. [103] Other studies on the co-precipitation of Ca and Si by Nieto *et al.* suggest that there is a two step process that depends on an activated complex for the formation of silica bonds. [154; 76] Initially, Ca bonds to a non-bridging $Si\text{-}O^-$ bond as shown in Equation 6.3.

Eq. 6.3 $\equiv Si\text{-}O^- + Ca^{2+} \rightarrow \equiv Si\text{-}O\text{-}Ca^+$

The positive charge on the Ca forms an activated complex which then acts as a bridge between two silicate species. This leads to the formation of a siloxane bond as illustrated in Equation 6.4.

Eq. 6.4 $\equiv Si\text{-}O\text{-}Ca^{+} + {}^{-}O\text{-}Si\equiv + H_2O \rightarrow \equiv Si\text{-}O\text{-}Ca\text{-}O\text{-}Si\equiv \rightarrow \equiv Si\text{-}O\text{-}Si\equiv + Ca^{2+} + 2OH^{-}$

The formation of the siloxane bond along with the high concentration of Ca and pH of the solution explain the enhancement of the condensation kinetics of Si. [103]

The concentration of Si in solution for the coarse glass powder in CSS does not reach detection limits during the 42 day test. During the dissolution test, the concentration of Ca in solution, as shown in Figure 6.4, only decreases from about 700 ppm to approximately 250 ppm. A comparison of the concentration of Ca and Si in solution for the fine glass powder in CSS (Figure 6.13 and 6.15, respectively) reveals that the concentration of Si in solution does not reach detection limits until the concentration of Ca in solution is less than 250 ppm. After the concentration of Ca in solution becomes low enough, Si in solution is detected and the NL_{Si} increases as is shown in Figure 6.14.

Chave *et al.* demonstrates that the presence of calcium in solution decreases the rate of dissolution for the French reference high level waste (HLW) glass, as was the case in this study. [103] It was further suggested by Chave *et al.* that when the concentration of Ca in solution is higher than 50 ppm it forms a Passivating Reactive Interphase (PRI) which decreases the growth rate of a hydrated surface layer on the pristine glass surface. [103] The formation of a PRI on the surface of the glass could also react with additional Al in solution. If there are a limited number of reaction sites at the glass surface, Al in solution could react with these sites decreasing the overall dissolution rate. The decrease in the concentration of Ca in solution can be attributed to the low saturation index of Al where the available Al in solution reacts with Ca at short times due to the activity of $Al(OH)_4^-$ and $Ca(OH)^+$ being saturated in solution until 21 days for the PCT-t in CSS according the modelled data. [103] Further modelling of the data, as given in Table 6.2, shows that the saturation index of Al-Ca minerals, chabazite ($CaAl_2Si_4O_{12}\bullet 6H_2O$) and epidote ($Ca_2FeAl_2Si_5O_{12}OH$) both become supersaturated in solution, giving further evidence of Al performing as a dissolution inhibitor.

The correlation between the Al concentration at short times and the decrease in Ca concentration, seen in Figure 6.4, was also observed by Chave *et al.* where they suggest that the hydrated layer does not act as a protective barrier. [103] This was shown by Chave *et al.* when Si was far from steady state conditions as is also seen in this study. [103]

Table 6.2. Saturation indices of chabazite ($CaAl_2Si_4O_{12}•6H_2O$) and epidote ($Ca_2FeAl_2Si_5O_{12}OH$).

Time (days)	Saturation Index	
	Chabazite	Epidote
1	-19.61	-1.37
3	-15.53	1.52
7	-15.87	1.07
14	-13.56	2.52
21	-10.3	4.77
28	-7.78	6.53
42	-3.5	8.92
56	-3.15	9.6
70	-1.16	10.91
84	-0.01	11.28
112	0.69	11.56
140	0.66	10.97
168	1.08	11.04

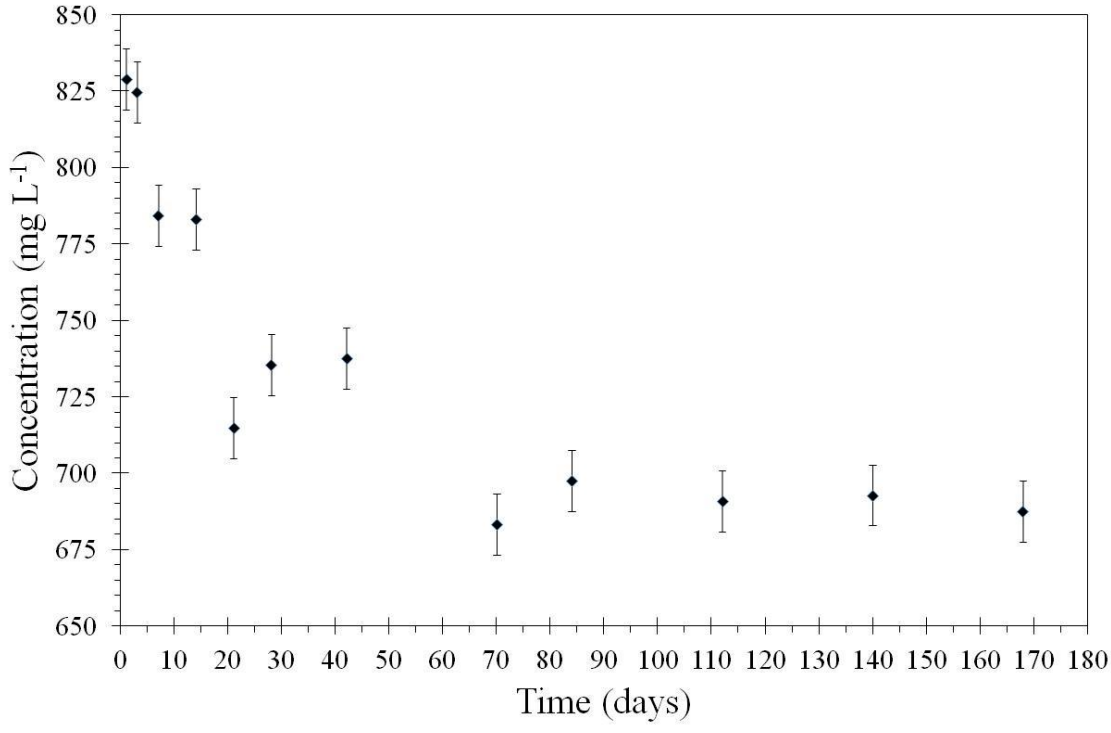

Figure 6.40 Concentration of Ca for the monolithic durability test in $Ca(OH)_2$ saturated solution (CSS) at 50 °C.

The MCC-1 tests were also performed using a CSS similar to that of the PCT-t dissolution test. The concentration of Ca, as plotted in Figure 6.40, during the MCC-1 test only decreases to just below 700 ppm at 70 days where it becomes constant. This gives further evidence of co-precipitation of Ca with Si since there is no measureable NL_{Si} during the entire MCC-1 test.

The surface area to volume (SA/V) ratio is also shown to control the dissolution rate. This is evident by comparisons of the NL_i given in Table 6.3. For the low SA/V ratio powder dissolution test, the NL_B is approximately four times higher than the NL_B for the high SA/V ratio glass powder in UDW at 42 days. Because B, generally, does not participate in secondary phase formation, it is useful for determination of the dissolution rate. The addition of an alkaline buffer decreases the effect of the SA/V ratio, as is apparent when comparing the NL_B in CSS to UDW at 42 days (Table 6.3). The addition of a $Ca(OH)_2$ buffer to UDW to make the CSS solution for the corrosion tests, decreased the overall dissolution for the glass powders in both the low and high SA/V ratio for this study. Both the UDW and CSS dissolution tests show similar trends in the NL, with the exception of Si in CSS, as is evident from Table 6.3.

The concentration of Si in solution for both the low and high SA/V ratio dissolution tests is the same (within error) at 42 days (Figure 6.15). This can be explained by the concentration of Si increasing to saturation quicker for the high SA/V ratio powders allowing the rate of dissolution to reach steady state conditions faster than that of the low SA/V ratio glass powders.

Table 6.3 Approximate NL_i at 42 days for the low and high SA/V ratio glass powder dissolution PCT-t experiments in unbuffered deionized water (UDW) and $Ca(OH)_2$ saturated solution (CSS) for selected elements.

Element	NL_i for UDW ($g\ m^{-2}$)		NL_i for CSS ($g\ m^{-2}$)	
	Low SA/V	High SA/V	Low SA/V	High SA/V
B	1.60E-02	4.00E-03	4.00E-03	2.00E-03
Li	2.70E-02	7.00E-03	1.00E-02	3.50E-03
Si	7.25E-03	1.00E-03	0.00E+00	1.00E-04
Na	6.00E-02	1.30E-02	2.00E-02	7.00E-03
Al	1.50E-04	3.00E-05	2.50E-05	5.00E-06
Mg	3.00E-04	3.00E-05	0.00E+00	0.00E+00

The NL_B and NL_{Al} given in this study, for both the low and high SA/V ratio tests, are consistent with the suggestion by Abraitis *et al*. that a high $Al(OH)_4^-$ (aq) activity will act as an inhibitor to dissolution. [16] At short times, NL_{Al} is high for the glass powder in CSS and low for powder in UDW. The lower extent of dissolution for glass powder in CSS seen from the NL_B is consistent with that of Abraitis *et al.* who have shown that the dissolution rate of a Magnox waste glass, similar to the glass used in this study, depends on the activity of both silicic acid and aqueous aluminate species. [16] Earlier studies by Abraitis *et al.* have shown lower leach rates for glass in an alkaline solution, which is consistent for results in this study, where the pH of the CSS was consistently higher than that of the UDW, as shown in Figure 6.5. [110]

Comparisons of the NL between the monoliths, the coarse glass powder and the fine glass powder show that as the SA/V ratio increases, the NL decreases over a specific time. This is evident of the saturation of solution of species, which directly influences the dissolution rate. As the surface area increases, the saturation of solution is faster, thereby decreasing the dissolution rate or NL.

6.4.2 PhreeqC Modelling of the Powder Durability Results

The saturation index trends of Ca and Si phases that are present in solution suggest co-precipitation of Ca and Si. This is seen for phillipsite-Ca ($CaAl_2Si_5O_{14}•5H_2O$) and tobermorite-11A ($Ca_5Si_6(O,OH)18·5H_2O$), both of which have Ca and Si in the composition, increase from below saturation in solution to being supersaturated by the end of the dissolution test. The saturation index of tobermorite-11A increases quickly to supersaturation after 21 days. This corresponds with the concentration of Ca and Si in solution where the concentration of Ca drops below 250 ppm at 21 days and the concentration of Si becomes detectable in solution at 21 days. Other phases, such as Al and Mg, also show similar trends in the data.

The Ca can also react with the surface of the glass, as suggested by Chave *et al*., and become a passive reactive interface. Evidence to this is from the electron images of the 3 and 168 day MCC-1 samples. [103] Figure 6.28, 6.29 and 6.30 reveals that there are definite Ca rich phases present on the surface of both the 3 and 168 day MCC-1 samples. Figure 6.31 shows a possible indication of a small, < 1 μm thick, alteration layer on the surface of the glass which is rich in Al and Mg. Further tests will need to be performed in order to confirm this layer.

The modelling of the PCT-t data using PHREEQC is consistent to the work by Chave *et al.* and Abraitis *et al.* [16; 15; 103] Chave *et al.* demonstrate that ". . . calcium is incorporated in the hydrated surface layer . . . [which] induces a drastic change of the hydrates surface layer composition, [and] a strong modification of its passivation properties is therefore all the more understandable." [103] Abraitis *et al.* suggest that the activity of silicic acid and an aluminate ion both affect the dissolution rate of UK HLW glasses. [16] It was shown by Abraitis *et al.* that Al species play an inhibitory role when the activity of the Al species is high, as is seen at short times in Figure 6.33. [15] It is suggested that with high concentrations of Al in solution the dissolution rate is not fully dependent on the activity of $Al(OH)_4^-$, which can be explained by the number of reaction sites at the glass surface that may react with dissolved Al. The saturation index of minerals containing Al, Figure 6.35, increases up to 40 days where they become relatively constant, which is similar to what Abraitis *et al.* found for a similar glass (MW Magnox). [16]

It is suggested that Al plays an inhibitory role of dissolution of the glasses. As seen in Figure 6.18, the NL_{Al} at short times is quite high for glass powder in CSS; however, for glass powder in UDW the NL_{Al} is negligible. The saturation index of Al containing minerals; diaspore, gibbsite and kaolinite, all show similar trends where there is an initial increase in the saturation index, but at longer times, the saturation index becomes constant (below saturation). Mg and Si containing minerals; sepiolite and talc, show similar trends as diaspore, gibbsite and kaolinite; however, the saturation index becomes positive for both after 21 days. The NL_{Mg} for the glass powder in CSS, Figure 6.19, suggests there is no mass loss of Mg; however, this could be due to the quick saturation of Mg in solution which complexes with Si and precipitates out of solution at short times.

Saturation indices of several minerals suggest that Ca and Si are co-precipitating during early stages of dissolution (hence no NL_{Si} at short times for the fine glass powder). After longer times, the phases precipitate out of solution allowing the concentration of Si in solution to increase giving rise to the increase in the NL_{Si} seen in Figure 6.14.

The existence of an alteration layer on the MCC-1 168 day sample allows speculation about the formation of a possible PRI on the surface of the pristine glass. Further tests and analysis on the glass powders during a dissolution test in both UDW and CSS will need to be performed in order to understand the formation of alteration products during the dissolution of these glasses at these SA/V ratios.

6.5 Conclusions

It has been shown from both the work presented here and previous work that the surface area to volume ratio has a large effect on the overall normalised mass loss. The difference between the concentration of Si in solution for the low and high SA/V ratio samples was explained by saturation effects of Si in solution.

The addition of an alkali buffer to the UDW was shown to result in a decrease of the dissolution rate for MW Blend glass. The concentration of Si in solution for all of the samples correlates to suggestions that Ca and Si are co-precipitating, possibly with Al, Mg and Na. This is evident from the large decrease in Ca concentrations at short times which are consistent with the NL_{Si}. It is suggested that the high concentration of Ca in solution forms a PRI which decreases the rate of formation of a hydrated surface layer, which in turn decreases the final dissolution rate.

At short times it was evident that the concentration of Al in solution is consistent to that of the concentration of both Ca and Si. It was discussed that the dissolution rate is dependent on the activity of $Al(OH)_4^-$ and silicic acid along with the solution pH. Both the PCT-t and the MCC-1 solution pH's show that the dissolution rate will remain low until the pH decreases past the point of zero net charge.

Modelling results are in agreement to previous studies which show that Ca and Si are co-precipitating at short times decreasing the NL_i. This is evident from the Ca and Si phases which are most probable to precipitate out of solution as suggested by the modelling results.

The alteration layer on the MCC-1 168 day sample is indicative of the possible formation of a PRI on the surface of the pristine glass. Previous work along with the results presented here give further evidence to the formation of the PRI; however, further work is needed in order to understand the alteration layer chemistry on the powder to determine the phases which have formed on the surface of the glass.

7.0 Secondary Product Formation on Simulated UK HLW Glasses

7.1 Introduction

Several studies on the mechanisms of the formation of alteration products on the surface of a corroding glass have been performed; however, there are contrary theories on the role of the gel layer. [148; 91; 93; 95; 97; 98; 102; 109] Initial studies of the dissolution rate law and the role of the gel layer by Grambow and Muller in 2001 resulted in a model which described corrosion of a nuclear waste glass in experimental and geological repository conditions. [148] This model allowed a comparison of various hypotheses, with several parameters in a single model, and allowed a combination mechanism for glass corrosion involving glass hydration and (possibly) a protective effect from the formation of an alteration layer. [148]

Other studies suggest that the decrease in the dissolution rate at longer times is attributed, in part, to the formation of alteration products on the surface of the glass. [92] Advocat *et al.* has observed a decrease in the dissolution rate for both radioactive and non-radioactive glasses; however, they observed a significantly different behaviour between active and inactive glasses with similar compositions. [94] It is suggested that the alteration layer on the surface of the radioactive glass is less protective due to a difference in the microstructure allowing enhanced diffusion as compared to the non-radioactive glass. [94] Contrasting studies suggest either the alteration layer on the surface, or saturation effects in the solution are responsible for the decrease in the dissolution rate of nuclear waste glasses. Xing *et al.* suggest that there is a large range of glass composition that vary in corrosion rates and thicknesses of the gel layer and that the reaction rate is strongly affected by the formation of the gel. [13]

Early work by Gin suggests that a gel layer formed under a saturated solution acts as a diffusion barrier and controls the kinetics of the glass corrosion. [95] Recent studies on the French simulated nuclear waste glass, SON68, suggest that a passivating reactive interface (PRI) influences the dissolution rate. [102; 109] The PRI, as Frugier *et al.* suggest, is an alteration layer which is characterised by a gradient of elements that limit the formation of crystalline phases. [102] The mechanisms by which the PRI are formed were modelled using the Glass Reactivity with Allowance for the Alteration Layer (GRAAL).*

* For an overview of the GRAAL model, see section 2.7.

Alteration layer studies have previously been performed on simulated UK HLW glasses by Hyatt *et al.* [97; 98] However, these studies were inconclusive regarding the formation mechanisms of the gel layer. This same work by Hyatt *et al.* also indicated that the durability, according to the generalised Avrami equation, is less than that of the French SON68 glass. [97]

The work below was performed in order to study the structure of the alteration layers which form during corrosion of glasses and also to gain an understanding of the mechanisms of the formation of the gel layer. This was achieved by vapour hydration tests performed on simulated UK HLW glasses followed by analysis using XAS, XRD, and SEM/EDS.

7.2 Experimental Procedure

Five glasses were used for the VHT study; MW Base, MW 25 Blend, CaZn Base, CaZn Blend, and FeZnZr. The composition of these glasses is given in Table 7.1. All glasses were prepared by using a glass frit supplied by National Nuclear Laboratory (NNL) with the nominal composition of MW Base. The addition of other oxides was performed by adding a calcine, also supplied by NNL or by raw oxides supplied by Alpha Aesar with >99.0% purity.* The batch added to a mullite crucible and placed in a furnace at 1060 °C for one hour before being stirred with a mullite crucible for three hours. After stirring, the glass was cast in a block using a pre-heated stainless steel mould and then annealed at 500 °C for one hour before being cooled to room temperature at 1 °C min^{-1}.

After annealing, the glass the VHT monoliths of 10 mm x 10 mm x 1.5 mm (± 0.1 mm) were prepared. This was performed by cutting the annealed glass with a diamond impregnated saw and then polishing the samples to a 600 grit surface finish with SiC polishing paper and rinsing in deionised water. Once rinsed, the samples were cleaned ultrasonically for 2 min in deionised water two times. A second cleaning of the samples was performed ultrasonically for 2 min in ethanol two times. After cleaning, the samples were placed in a drying oven overnight and then placed in a desicator until further use.

* Only the FeZnZr glass was batched with the MW Base frit and raw oxides.

Table 7.1 Analysed compositions of the glasses used for the VHT experiments in wt%.

	CaZn Base	MW Base	FeZnZr Glass	CaZn Blend	MW 25 Blend
SiO_2	56.10	60.27	48.17	46.44	46.28
B_2O_3	21.54	24.11	19.38	18.95	18.3
Na_2O	11.48	10.88	8.10	9.32	8.12
Li_2O	2.92	4.75	3.84	2.27	4.81
CaO	1.94	--	--	1.54	--
Al_2O_3	--	--	--	0.11	1.87
BaO	--	--	--	1.67	1.22
CeO_2	--	--	--	1.28	1.24
Cr_2O_3	--	--	--	0.19	0.37
Cs_2O	--	--	--	1.42	1.61
Fe_2O_3	--	--	12.34	0.49	1.87
Gd_2O_3	--	--	--	2.62	3.86
La_2O_3	--	--	--	0.71	0.67
MgO	--	--	--	0.11	1.34
MoO_3	--	--	--	2.41	2.02
Nd_2O_3	--	--	--	1.69	1.81
NiO	--	--	--	0.18	0.28
Pr_2O_3	--	--	--	0.46	0.47
RuO_2	--	--	--	0.46	0.49
Sm_2O_3	--	--	--	0.28	0.28
SrO	--	--	--	0.43	0.32
TeO_2	--	--	--	0.12	0.28
Y_2O_3	--	--	--	0.11	0.1
ZnO_2	6.03	--	3.53	4.28	--
ZrO_2	--	--	4.64	2.48	2.4
Total	100	100	100	100	100

7.2.1 Vapour Hydration Test

There were two VHT experiments performed in this study; the first was performed in order to determine reproducibility of the VHT method, and the second was performed to examine alteration layer formation with increasing time. The VHT experiment is performed by exposing a glass monolith to a saturated water vapour atmosphere for a pre-determined amount of time. For the studies below, this was performed by placing a glass monolith, as prepared above, into stainless steel vessels and exposing them to a water vapour atmosphere at 200 °C. The amount of water added to the vessel was low enough to create a 100% relative humidity atmosphere but not have condensed water from the sample driping to the bottom. This prevents migration of elemental species from the surface of the sample. Once the samples were removed from the vessel they were examined by XRD and SEM/EDS.

7.2.1.1 Reproducibility of the VHT

A simple borosilicate glass (CaZn Base) doped with small additions of ZnO and CaO was used for the reproducibility VHT experiments. The glass, supplied as a frit by National Nuclear Laboratory Ltd. with the composition given in Table 7.1 was melted in a platinum crucible for 4 h at 1060 ºC and stirring for 3 h using a platinum stirrer. The melt was cast into a pre-heated stainless steel mould, annealed at 500 ºC for 1 h and cooled at 1 ºC min^{-1} to room temperature. After annealing, the glass was sectioned into 10 x 10 x 1.5 mm (± 0.1 mm) sections using a diamond impregnated blade in a Buhler low speed saw.

The reproducibility VHT experiments were performed using both as cut and polished sections of the glass with either one or two samples mounted on a stainless steel specimen holder inside the VHT vessel. Both the as-cut and polished samples were tested per the matrix given in Table 7.2. Two vessels were used in order to test differences between the surface roughness and mounting either one or two samples in a single vessel.

Table 7.2 Matrix of experiments for the reproducibility of the VHT for both the as cut and polished samples.

	Vessel 1		Vessel 2	
	Sample 1	Sample 2	Sample 1	Sample 2
Test 1	x	x	x	--
Test 2	x	--	x	x
Test 3	x	x	x	x
Test 4	x	--	x	--

Vessels used for reproducibility VHT experiments were tested for water retention. Water retention of each vessel was tested by adding ~2 mL high purity H_2O to the vessel and measuring the mass before and after placing the sealed vessel in an oven at 200 ºC for 5 days. The two vessels were within 0.01 g for the initial and final mass for the retention test.

The vessels and samples were cleaned using distilled H_2O and acetone before each VHT experiment. Once the remaining alteration product from the previous VHT experiment was removed from the sample support, the samples, vessels, vessel lids, and sample supports were rinsed with distilled H_2O twice. After rinsing, they were submersed in distilled H_2O and cleaned ultrasonically twice. The samples, vessels, vessel lids, and sample supports were submersed and cleaned ultrasonically in acetone twice before being placed in a drying oven

at 90 ºC for 1 h. After drying everything was placed in a desicator until further use. During and after the cleaning process only latex gloves and tweezers were used for handling in order to keep samples free from contamination.

Samples were attached to the supports using a stainless steel wire (0.002 in diameter), inserted into the vessels and then placed in an oven at 90 ºC for 1 hour prior to the addition of high purity H_2O. This allowed for slight thermal expansion of the vessel prior to sealing. After pre-heating, 200 μL of high purity H_2O (18.2 MΩ cm at 25 ºC) were added to the vessel before sealing and being placed in an oven at 200 ºC for 5 days. The amount of high purity H_2O used gives a complete H_2O vapour atmosphere in the vessel. This procedure followed the same procedure as Jiricka *et al.* [155] The pH of the high purity H_2O was measured before and after each VHT using litmus paper in order to determine if solution condensed on the sample(s) and then dripped causing species migration from the surface of the sample. Figure 7.1 gives a representation of the vessel, vessel support, and sample attached to the support.

Figure 7.1 The vapour hydration test vessel with support and sample. The 20 pence piece is shown to indicate the size of apparatus.

Each vessel, once removed from the oven, was placed in ~1 cm depth of tap water in order to condense the high purity H_2O within the VHT vessel at the bottom and not on the sample. The vessel was unsealed and the support holding the sample was removed. The stainless

steel keeping the specimen attached to the support was removed and the sample(s) mounted in epoxy resin for analysis.

Once set, the epoxy moulds were polished back to expose the altered glass in cross section using a 1 μm median grit. This was performed by using SiC polishing paper from P600 to P1200 and then diamond paste at 6, 3 and 1 μm median grit size. Samples were subsequently analyzed using electron microscopy and backscatter electron images taken of each sample to measure the average alteration layer thickness and differences of the gel-layer structure.

Alteration thickness measurements were performed by placing the glass monolith into epoxy after it was removed from the vessel following the VHT experiment. The sample was polished with 1 μm diamond paste in order to view a cross section of the monolith in an SEM. Backscatter electron images were taken at two locations along each side and at the edge of the sample. After printing the images, the gel layer thickness was measured at five locations on each image and the thickness calculated. Figure 7.2 is a backscatter image illustrating five locations on the image which were used to calculate the average thickness of the alteration layer. The locations on each image were spaced evenly apart in order to account for any variation of thickness across the alteration layer.

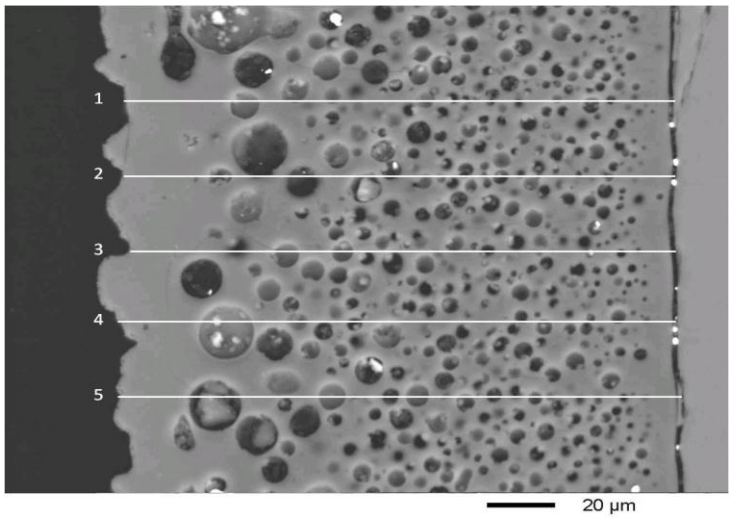

Figure 7.2 Backscatter electron image with five lines across the alteration layer illustrating the regions used to calculate the thickness of the gel. The bulk glass is on the right (light grey), the gel layer in the centre and the epoxy resin on the left (black region).

7.2.1.2 Alteration Layer Formation of Pristine Glass from VHT

Five compositions were used to study the formation of alteration layers during corrosion of glass. These glasses were; MW Base, MW Blend, CaZn Base, CaZn Blend, and FeZnZr. The analysed compositions are given in Table 7.1. After sample preparation as in section 7.2, glass monoliths were placed in the VHT vessel for 10, 20 and 30 days with the exception of CaZn Base which also included a 5 day sample from the reproducibility test. Once removed, the vessel was cooled to room temperature by placing the vessel in a shallow bath of cold water and the samples removed for analysis. Condensing the steam within the reaction vessel in this way permitted measurement of the solution in the vessel, which if basic, is an indicator of 'dripping' conditions, and hence, mass transport. After the VHT test, one sample was analysed by XRD and the other sample was placed in epoxy to examine the cross section of the monolith under SEM/EDS.

7.3 Results

7.3.1 Reproducibility of the Vapour Hydration Test

After several VHT experiments with varied results, it was determined that the reproducibility of the VHT method needed to be examined. Sample preparation was one possible cause to the variability of the results from the previous VHT experiments. A reproducibility VHT experiment was performed using as-cut and polished samples and either one or two specimen within the reaction vessel while keeping the time, and environment of the VHT experiment constant.

Early results of the VHT experiment for the MW Base glass showed a change in the alteration layer thickness with a difference in the polished surface of a sample. This is apparent in Figure 7.3 which gives the backscatter electron images of three different polished VHT samples exposed to a water vapour atmosphere for 5 days. The samples shown in Figure 7.3 A were polished with P800 SiC paper that has a median grit size of 22 μm. The alteration layer thickness was 5 ± 2 μm. Decreasing the median grit size to 15 μm resulted in an alteration layer thickness of 25 ± 5 μm, as shown in Figure 7.3 B. The thickest alteration layer resulted from a polish of a median grit size of 1 μm. This is seen in Figure 7.3 C where the average thickness of the alteration layer is 160 ± 15 μm. Other differences between the samples are formation of precipitates in the two higher polished surface samples. There is also substantial porosity within the thickest alteration layer sample. A close observation of

Figure 7.3 C also shows a change from a high number of small pores near the bulk glass to a few large pores near the surface of the alteration layer. Figure 7.4 plots the alteration layer thickness with a change in the median grit size for polishing samples. It clearly shows that the higher the median grit size the thinner is the alteration layer.

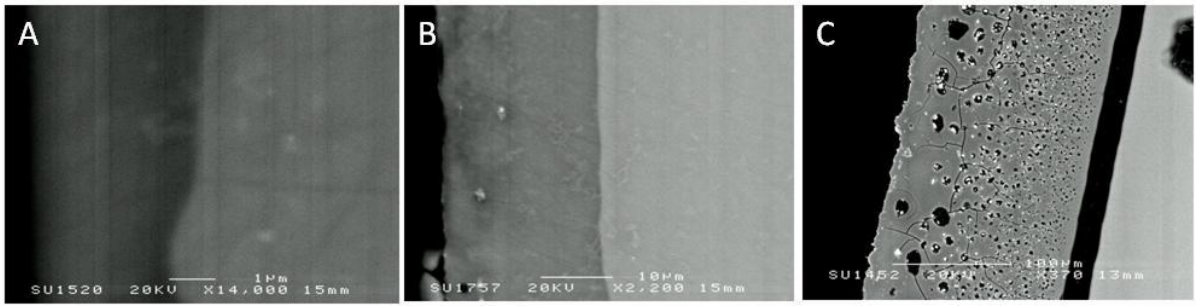

Figure 7.3 Vapour hydration test samples exposed for 5 days with different polished surfaces at A) 22 μm B) 15 μm and C) 1 μm median particle size for polishing.

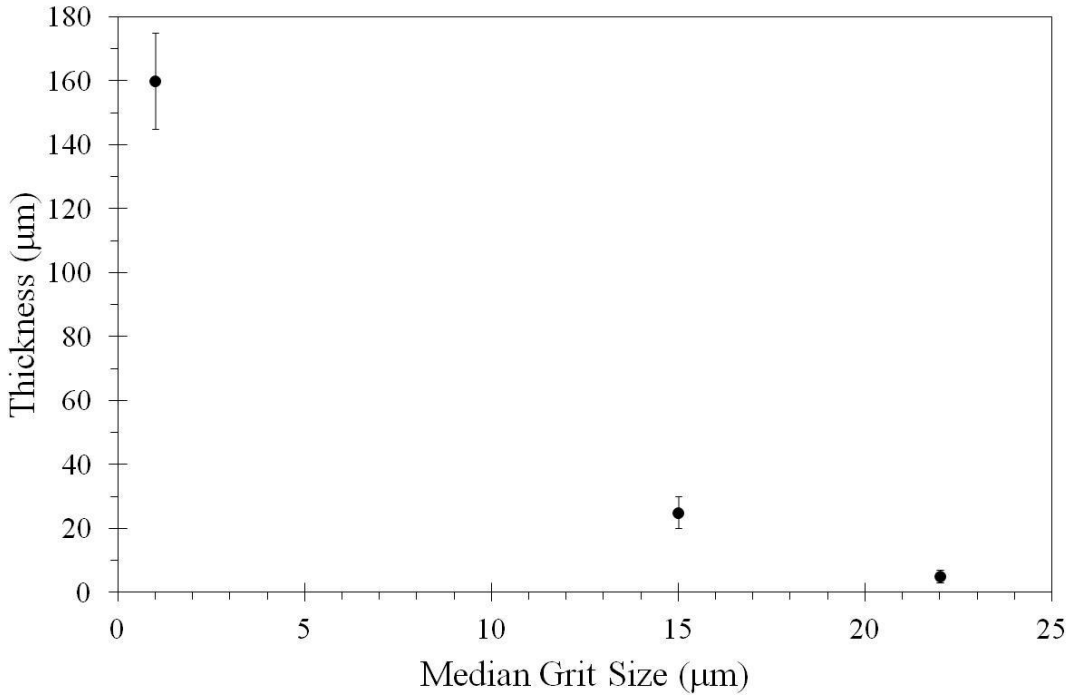

Figure 7.4 Alteration layer thickness for each median grit size polish for sample preparation of the VHT.

These early results were in contradiction to the findings of Jiricka *et al.* where they suggest the alteration layer decreases with a decrease in the polishing median grit size. [(155)] A possible explanation for this observation could be that the overall surface area to volume ratio

of the finer polished sample is less than that of the coarser polished sample. A finer polished sample is a sample that has a surface that is closer to a flat surface than that of a coarser polished sample which may resemble a jagged surface. An increase in the surface area will increase the concentration of ion *i* in solution allowing it to reach saturation quicker than that of the finer polished sample, which decreases the overall dissolution rate.

In order to investigate to what extent the VHT method is reproducible, a study was performed on a similar glass to earlier results, the CaZn Base glass. This study incorporated two changes. The first was the sample preparation where the surface finish of the glass monolith was changed. The second was that the number of samples in the VHT vessel was varied to examine the difference between having just one or two samples in the same vessel. To study these changes, several samples were analysed under backscatter electron microscopy to measure the thickness of the alteration layer after 5 days under a water vapour atmosphere.

The thickness of the alteration layers, which was used as an indication of reproducibility of the VHT method, is given in Table 7.3 for each sample. This table shows alteration layer thicknesses for both as cut and polished samples with either one or two samples in a reaction vessel. For the as cut samples in vessel 1; test 1 has two samples in the reaction vessel, while test 2 had only 1 sample (hence the absence of data for sample 2 in test 2). The error, σ, for each alteration layer thickness is given in the column after the thickness, t. Close observation of Table 7.3 reveals that there is a higher variability in alteration layer thicknesses for the as cut samples as compared to the polished samples.

A different perspective of the data presented in Table 7.3 is plotted via a box plot of the alteration layer thicknesses in Figure 7.5. For the as cut samples (first and second column) the "whiskers" give a visible representation of a higher variability in the alteration layer thickness as compared to the polished samples. However, the difference between mean thickness (round dot with the box) of the alteration layers for one or two as cut samples in a reaction vessel is higher than for one or two polished samples. The mean value of the alteration layer thickness for one or two polished samples in a reaction vessel is similar at ~190 μm. The box plot also shows that there is no significant difference between the mean values of one or two polished samples due to the large overlap between the second and third quartile of data. However, there is statistical difference between the mean values of the as cut samples, which is shown from the large difference between the second and third quartiles of either one or two samples in a reaction vessel.

Table 7.3 Gel layer thickness of the VHT reproducibility test after 7 days at 200 °C.

As Cut Samples								
	Vessel 1				Vessel 2			
	Sample 1		Sample 2		Sample 1		Sample 2	
	t (μm)	σ	t (μm)	σ	t (μm)	σ	t (μm)	σ
Test 1	134	14	140	11	185	19	--	--
Test 2	229	39	--	--	107	10	104	13
Test 3	190	25	183	29	95	24	116	10
Test 4	197	27	--	--	227	44	--	--
Polished Samples								
	Vessel 1				Vessel 2			
	Sample 1		Sample 2		Sample 1		Sample 2	
	t (μm)	σ	t (μm)	σ	t (μm)	σ	t (μm)	σ
Test 1	176	8	177	17	177	13	--	--
Test 2	206	21	--	--	175	13	205	66
Test 3	193	12	195	12	186	15	172	5
Test 4	197	32	--	--	184	5	--	--

Backscatter electron images also illustrate a difference between having one or two samples in the vessel during the VHT experiment, as shown in Figure 7.6 and 7.7. Figure 7.6 A is a representative backscatter electron image of the case with only one as cut sample in a reaction vessel during the VHT experiment and Figure 7.6 B is representative of the case

with two as cut samples. When only one as cut sample is in the vessel during the VHT experiment, both pores and precipitates can be seen within the alteration layer. On the surface of the alteration layer there is a change in the microstructure which is indicative of secondary precipitation after saturation of solution. When two samples are placed in the vessel, as shown in Figure 7.6 B, the secondary precipitation layer is much thinner; however, there are still pores and precipitates seen in the middle of the alteration layer.

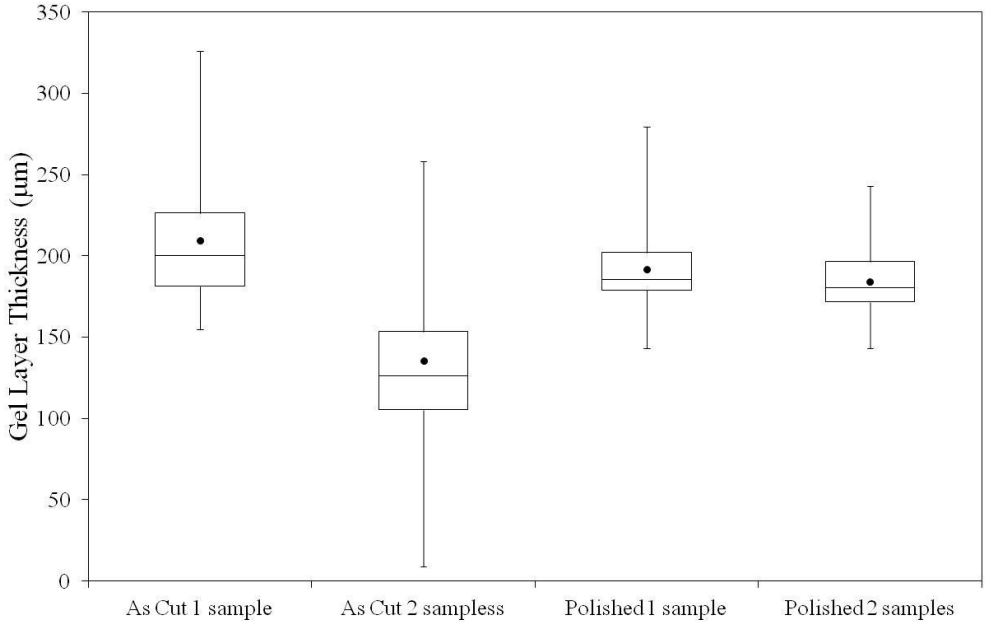

Figure 7.5 Box plot of gel layer thickness for the VHT reproducibility test.

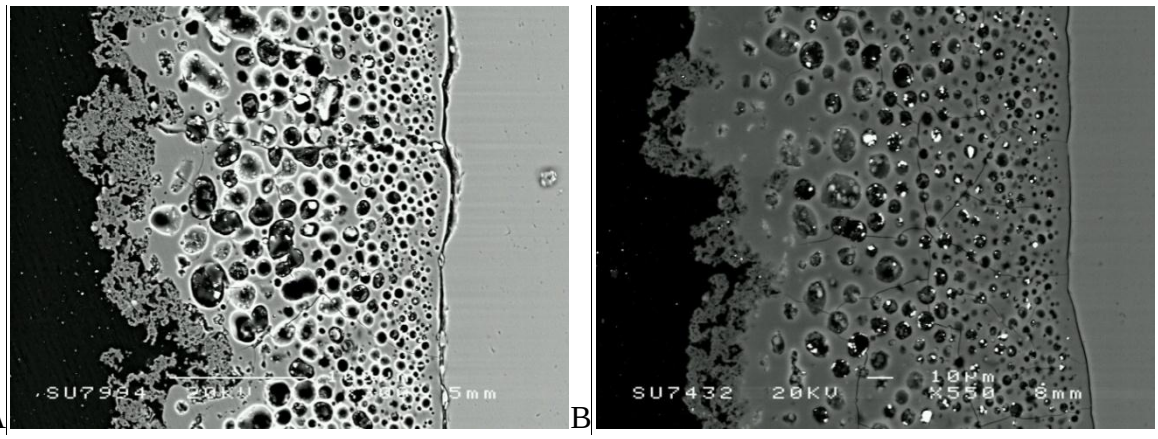

A B

Figure 7.6 Representative backscatter electron images of as cut samples for A) 1 sample in the vessel and B) 2 samples in the vessel during the VHT experiment.

Comparing the differences between only one or two samples in the VHT vessel for the polished samples in Figure 7.6, one can see that there is a slight difference between the two representative backscatter electron images. For instance, with only one sample in the vessel during the VHT test, the pores in the alteration layer appear to be much larger and contain larger precipitates; however, the porosity in the image for two polished samples in the VHT vessel shows that the pores are smaller in diameter and appear not to go all the way to the surface of the alteration layer (Figure 7.6 B).

Inspection of Figure 7.7 reveals that the alteration layers have less secondary precipitation compared to the as cut samples (Figure 7.6) for both 1 and 2 samples in the vessel.. When two polished samples are placed in the reaction vessel, the surface of the alteration layer does not exhibit such a change in the microstructure indicating the solution does not become saturated in leached elements causing secondary precipitation on the surface of alteration layer. Both Figure 7.7 A and B show porosity and precipitates within the alteration layer similar to the as cut samples. The precipitation within the pores seen in both images in Figure 7.7 show there is secondary precipitation occurs; however, this is only for precipitates rich in zinc. These precipitates are known to be rich in Zn from EDS point analysis that is not shown here. This, along with the results from the proceeding section showing Zn precipitates, suggests that within the pores, there is an increased concentration of zinc in solution leading to secondary precipitation within the pores for the CaZn Base glass..

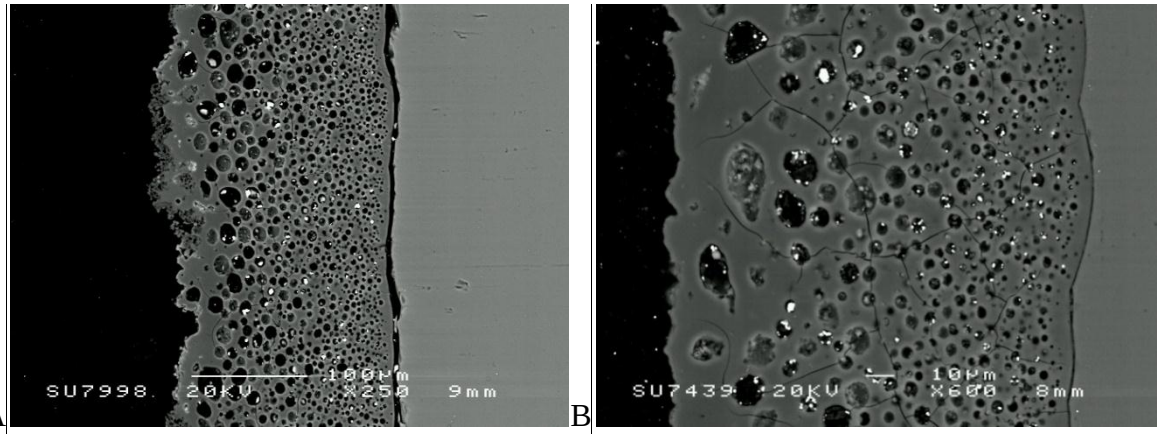

A B

Figure 7.7 Representative backscatter electron images of polished samples for A) 1 sample in the vessel and B) 2 samples in the vessel during the VHT experiment.

There is also an absence of secondary phases on the surface of the alteration layer for two polished samples in the VHT vessel. The secondary phase on the surface of the alteration layer is clearly shown on the surface of the alteration layer with only one polished sample,

Figure 7.7 A. Both representative images for the polished samples in Figure 7.7 show precipitates located within the pores.

As a result of the reproducibility tests, further VHT evaluations were performed using two samples polished with P1200 SiC paper. This is discussed below in section 7.4.1.

7.3.2 Alteration Layers in UK HLW Glasses

7.3.2.1 Vapour hydration tests of UK HLW glasses

7.3.2.1.1 CaZn Base glass

Five glasses were prepared for a time dependence study of the VHT method; CaZn Base, CaZn Blend, MW Base, MW Blend and FeZnZr glasses. As shown in Figure 7.8, the CaZn Base glass exhibits an increase in alteration layer thickness with time together with a change in the microstructure of the alteration. At short times, the CaZn Base glass has a very different alteration layer microstructure compared to longer alteration periods. The 5 day VHT sample has both pores (dark regions within the gel layer) and precipitates (bright spots within the pores of the alteration layer) which are clearly observed in the backscatter electron image. The 10 day sample exhibits a change in the microstructure of the alteration layer which does not contain any porosity. However, the precipitates within the pores seen in image of the 5 day sample appear to have increased in number and size after 10 days. The structure on the surface of the alteration layer of the 10 day VHT sample appears to be different compared to the bulk of the gel.

At longer times, for the CaZn Base 20 day VHT sample, the phase on the surface of the alteration layer appears to be broken up, as shown in Figure 7.8. This was seen throughout the sample when viewed under the electron microscope. This is apparent from the different microstructure of the alteration layer at the surface of the sample. The bulk of the alteration layer has less porosity for the 20 day VHT sample as compared to both the 5 and 10 day samples. The precipitates that were visible in the 5 and 10 day VHT samples are still present in the bulk of the alteration layer of the 20 day sample; however, there is no apparent porosity. The 30 day sample does not show the broken material on the surface of the alteration layer, but the precipitates visible in the other samples are larger near the surface of the alteration layer and decrease in size closer to the surface of the pristine glass.

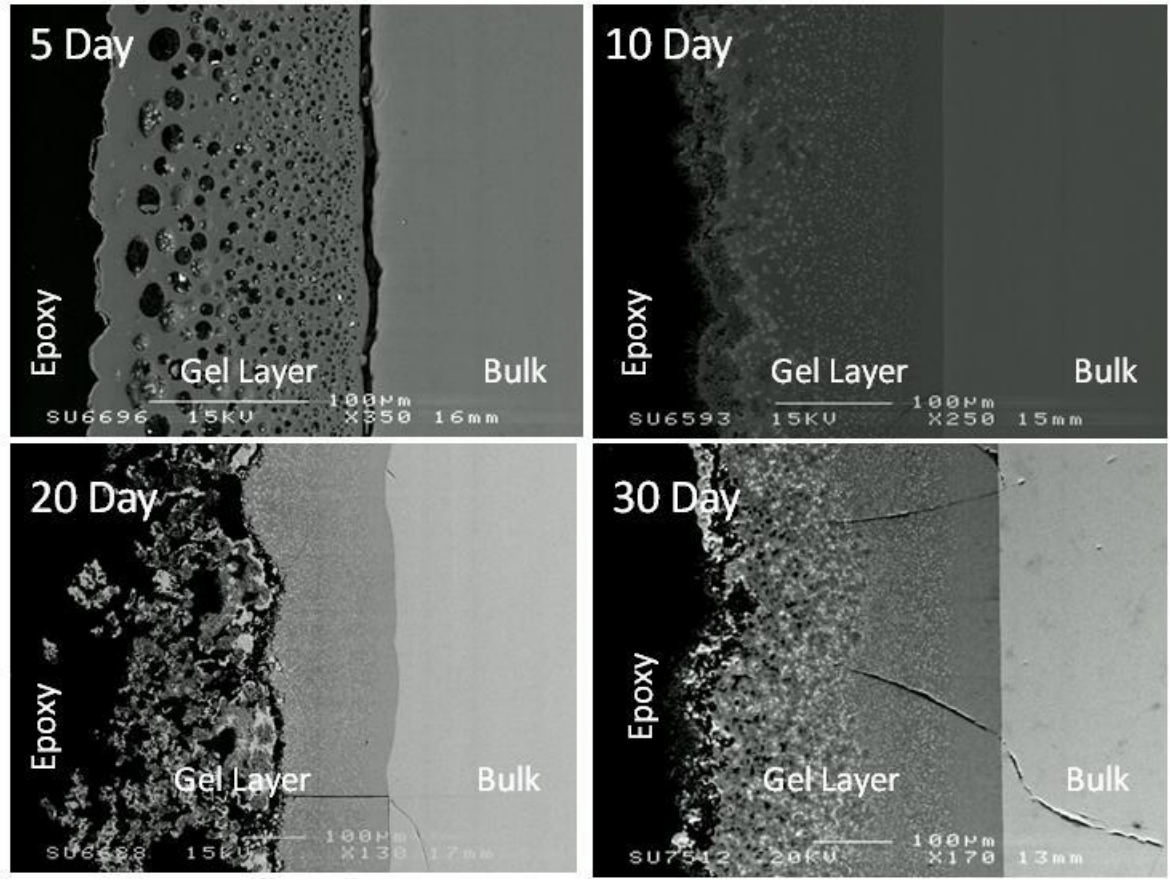

Figure 7.8 Backscatter electron images of CaZn Base for the VHT time dependent study. Times were 5, 10, 20 and 30 days at 200 °C in a high purity H_2O vapour atmosphere.

X-ray diffraction (XRD) of each of the CaZn Base glass VHT samples was performed in order to compare changes in the crystallinity of the alteration layer. Figure 7.9 shows the XRD traces of the CaZn Base samples. The crystallinity of the alteration layer of the VHT samples increases up to 20 days for the VHT test. The 20 and 30 day VHT samples appear to have similar peak intensities suggesting similar crystallinity in the alteration layer. The pristine glass, as expected, exhibits diffuse scattering. The 10, 20, and 30 day samples all exhibit peaks associated with crystalline materials in their respective diffraction patterns. The 10, 20, and 30 day samples all appear to contain phases of hemimorphite ($Zn_4Si_2O_7(OH)_2 \cdot H_2O$), calcium silicate hydroxide ($CaO \cdot SiO_2 \cdot H_2O$), and cristobalite ($SiO_2$). Previous studies have shown that cristobalite forms in lower temperature hydrothermal environments. [156; 157] Both the 20 and 30 day samples show higher peak intensities for hemimorphite and calcium silicate hydrate than the 10 day VHT sample.

A closer examination of the alteration layers seen in the backscatter electron images of the VHT samples was also performed using EDS X-ray mapping and line scans in order to determine changes in the microstructure and/or composition with an increase in time. At

short times, as can be seen in the Si EDS X-ray map for the 10 day CaZn Base glass, there is a concentration gradient of Si within the alteration layer, Figure 7.10 C. The concentration gradient of Si within the alteration layer shows that there is a higher concentration of Si at the surface of the alteration as compared to the region next to the pristine glass. This gives possible evidence of secondary precipitation after saturation of Si within solution. It is; however, difficult to verify any concentration gradients for Na, Ca, or Zn which would suggest diffusion of species through the alteration layer.

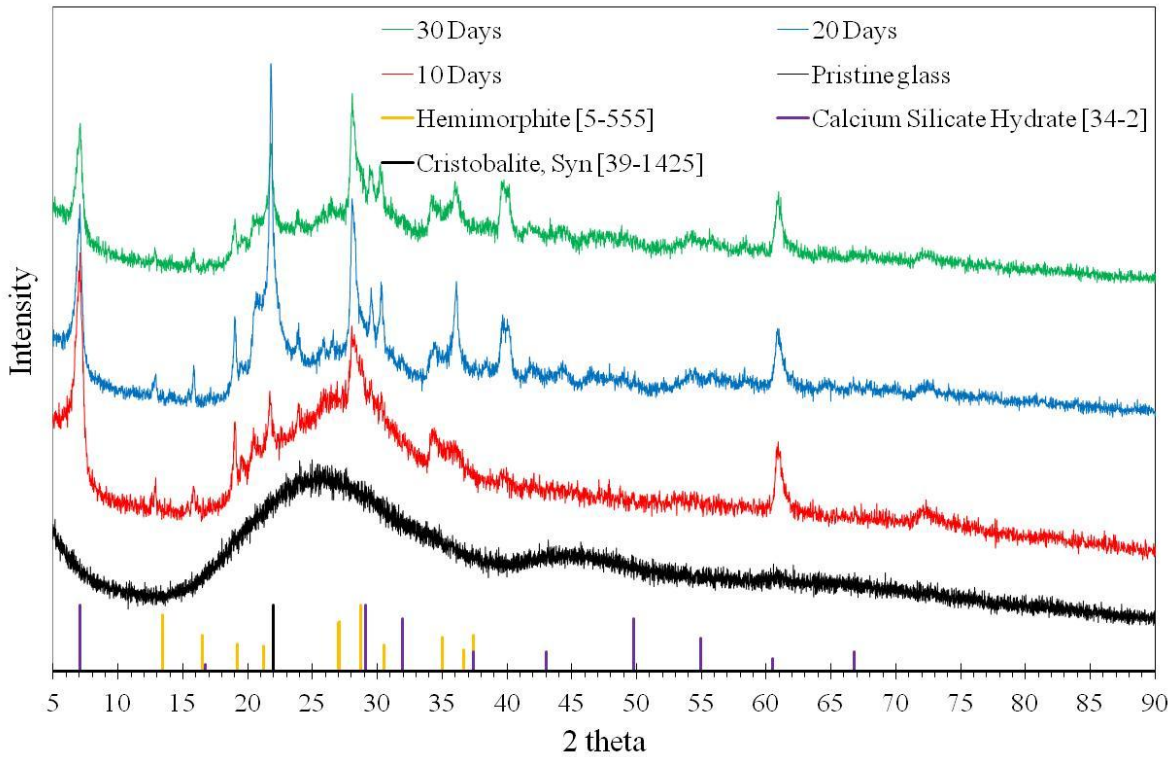

Figure 7.9 X-ray diffraction traces of the pristine glass, 10 day, 20 day, and 30 day VHT samples of the CaZn Base glass at 200 °C in high purity H_2O.

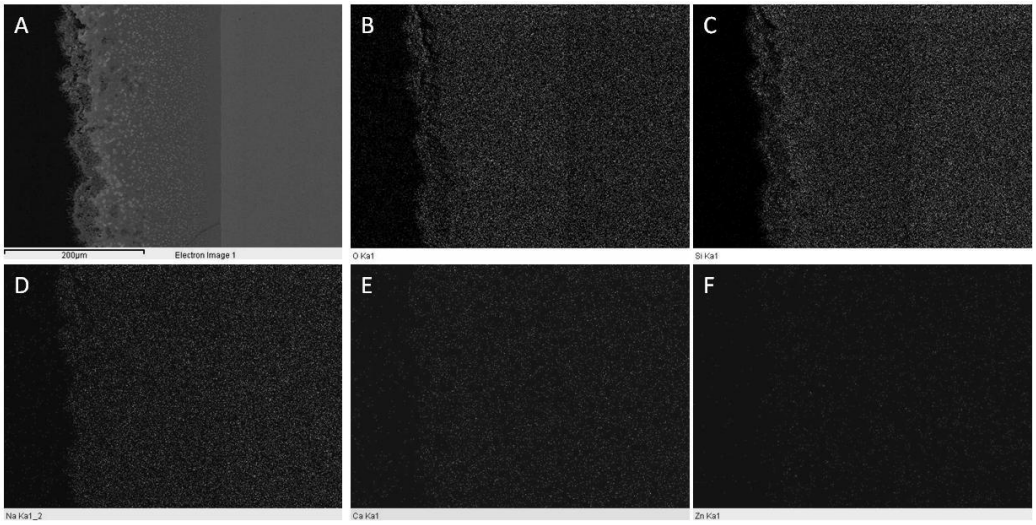

Figure 7.10 EDS dot map showing A) backscatter image B) O C) Si D) Na E) Ca and F) Zn for the CaZn Base 10 day VHT sample.

As shown in Figure 7.8, there is a change in the microstructure of the alteration layer with time; Figure 7.11 gives the EDS X-ray map of the 20 day CaZn Base glass VHT sample. It is clearly visible from the change in contrast of the images that there is a large difference in concentration of Si, Na and Ca between the alteration layer and the pristine glass. A closer observation of the EDS X-ray maps of Si shows that the different microstructure on the surface of the alteration layer has higher concentrations of Si as compared to the bulk of the alteration layer next to the pristine glass.

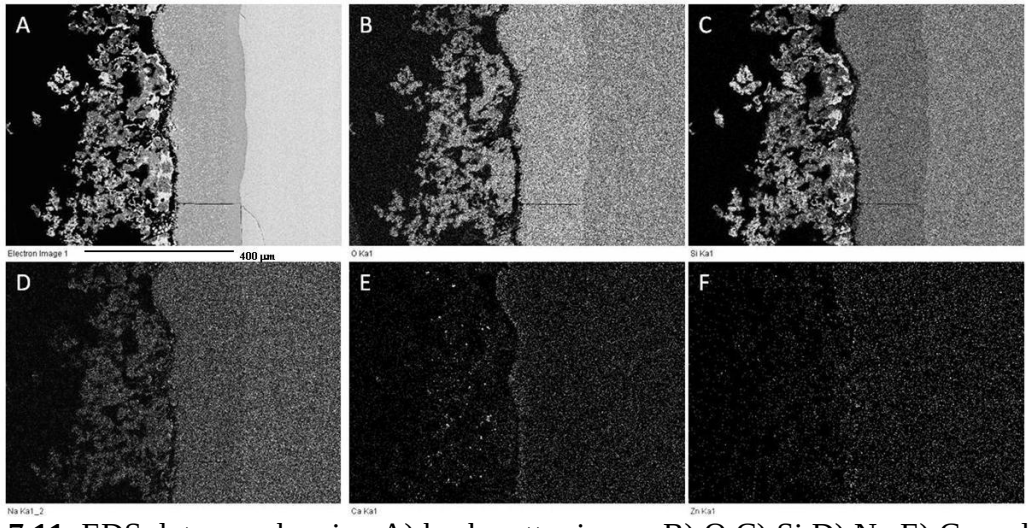

Figure 7.11 EDS dot map showing A) backscatter image B) O C) Si D) Na E) Ca and F) Zn for the CaZn Base 20 day VHT sample.

There is also a large difference in the microstructure between the 10 day sample as compared to the 20 day sample. The concentration gradient of Si that is visible due to the changing contrast of the alteration layer shown in the 10 day sample (Figure 7.10 C) appears to be absent in the 20 day sample (Figure 7.11 C). The different microstructure on the surface of the alteration layer in the 20 day sample appears to have regions rich in Si where there is a gradient with a small region on the surface of the alteration layer that is rich in Si. The EDS map of Ca for the 20 day sample also shows a region rich in Ca between the bulk alteration layer and the different microstructure on the surface of the alteration layer.

Figure 7.12 C confirms the gradient of Si within the alteration layer for the 10 day sample from the EDS line scan concentration profile. Examination of the EDS X-ray dot map (Figure 7.13 E) does not show any significant changes in the contrast of the image suggesting there is no real change in the concentration of Ca.

A comparison between the Si line scans of the 10 day and 20 day samples (Figure 7.12 and 7.13) shows that there is a distinct difference in the concentration gradients of the elements between the two samples. The concentration of Si in the alteration layer of the 10 day sample has an overall decrease from the surface of the alteration layer to the pristine glass. The line scan of the 20 day sample shows local enhancements in the concentration profile of Si in the different microstructure on the surface of the alteration layer, while the concentration is generally constant through the bulk of the alteration layer next to the pristine glass.

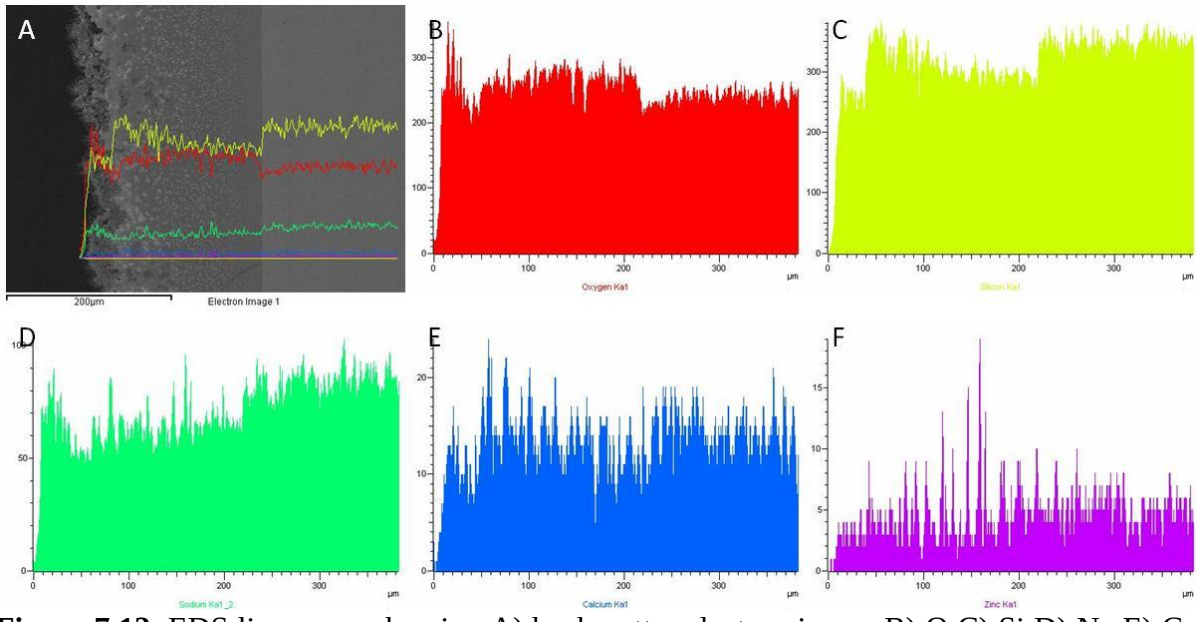

Figure 7.12 EDS line scans showing A) backscatter electron image B) O C) Si D) Na E) Ca and F) Zn for the CaZn Base 10 day VHT sample.

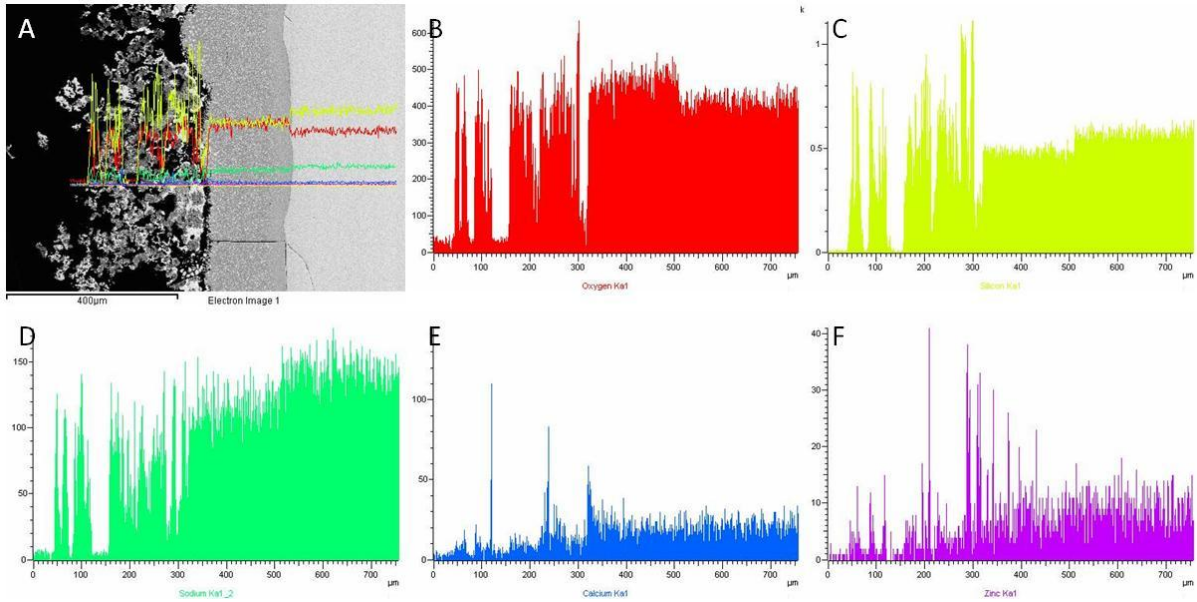

Figure 7.13 EDS line scans showing A) backscatter image B) O C) Si D) Na E) Ca and F) Zn for the CaZn Base 20 day VHT sample.

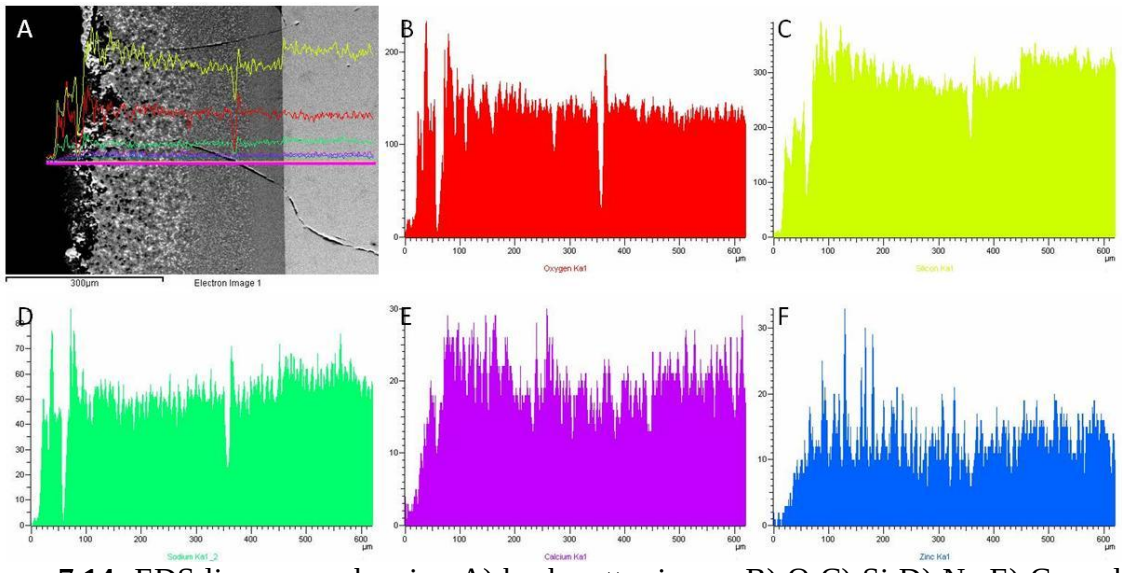

Figure 7.14 EDS line scans showing A) backscatter image B) O C) Si D) Na E) Ca and F) Zn for the CaZn Base 30 day VHT sample.

The 30 day VHT sample of the CaZn Base glass also has a different profile in the EDS line scans as compared to the 10 and 20 day VHT samples. It is clearly observed in Figure 7.14 that there are two distinct phases in the alteration layer of the 30 day VHT specimen. Inspection of the Si EDS X-ray map (Figure 7.14 C) indicates that there is a decrease in the

concentration of Si from the surface of the alteration layer to the inner pristine glass. This is similar to the 10 day VHT sample where there is a concentration gradient of Si in the alteration layer.

The EDS X-ray map of Si (Figure 7.15 C) shows that the microstructure on the surface of the alteration layer of the 30 day sample is different than the 10 and 20 day samples. This is apparent from the large change in the contrast of the image where the surface of alteration layer is rich in Si, while the bulk alteration layer has a general decrease in brightness correlating to a decrease in Si concentration. The concentration of Na appears to be constant throughout the bulk alteration layer; similar for both the 10 day and 20 day samples of the CaZn Base glass. The concentration of Ca and Zn both show higher concentrations on the surface of the alteration layer, similar to that exhibited by the 20 day VHT sample.

The EDS line scans of the 30 day VHT CaZn Base glass (Figure 7.14) show a distinct concentration gradient for Si, Na and Ca; however, there is an enhancement in the concentration at the surface of the alteration layer for Na. This is similar to the 10 day VHT sample where there is an overall gradient with the surface of the alteration layer showing a high concentration of Na. Both Si and Ca show a gradual decrease in their concentration with a decrease in the distance to the pristine glass while Na has a gradual increase (not including the surface of the alteration layer). Again, the 20 day VHT sample is different in that there is no significant gradient in the concentration profiles of the EDS line scans, with the exception of Na within the bulk alteration layer. The concentration of Zn exhibits local enhancements whenever the line scan is associated with a precipitate within the alteration layer, as is evident from Figure 7.13 A and F; this is similar to the 10 day sample.

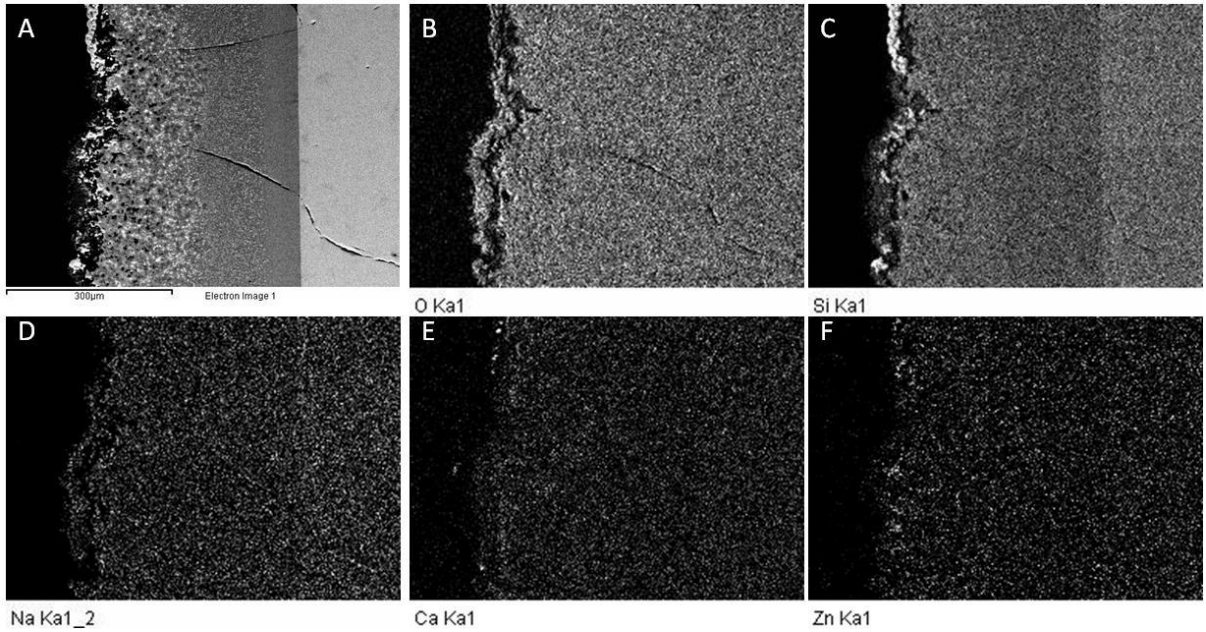

Figure 7.15 EDS dot map showing A) backscatter image B) O C) Si D) Na E) Ca and F) Zn for the CaZn Base 30 day VHT sample.

7.3.2.1.2 CaZn Blend

Figure 7.16 gives the backscatter electron images (BEI) of the 10, 20 and 30 day VHT samples for the CaZn Blend glass. The alteration layer thickness of the 10 day sample is approximately 2 ± 1 μm. At 20 days, the alteration layer thickness increases to approximately 5 ± 1 μm. Similar to the 10 day VHT sample, the 20 day sample also shows a banded structure within the alteration layer. The banded structure is visually similar to the 30 day VHT sample of the CaZn Base glass where the specimen has a region rich in Si of a different microstructure on the surface of the alteration layer. The 30 day sample of the CaZn Blend glass has an alteration layer thickness of ~10 ± 2 μm and a banded microstructure within the alteration layer as is visible from the different contrast within the BEI which is also apparent in the 10 and 20 day VHT samples. The banding structure for all three VHT samples of the CaZn Blend glass suggests the mechanism for alteration layer formation is the same at all time frames for this glass. This is different to the CaZn Base glass where the microstructure of the alteration layer changes with an increase in alteration time.

Figure 7.17 gives the XRD traces of the CaZn Blend glass VHT samples at 10, 20 and 30 days. It can be seen that the pristine glass only has diffuse scattering, characteristic of a homogenous glass. The alteration layers at 10, 20 and 30 days show evidence of a different alteration layer as compared to the CaZn Base glass where hemimorphite is not present, but

zircon, a zirconium silicate ($ZnSiO_4$) is present in the XRD pattern. Although zircon is generally formed at high temperatures, a recent study has found evidence of the formation of zircon from amorphous ZrO_2-SiO_2 powders which may show similarities to the formation of zircon in the VHT experiments in this study. (158)

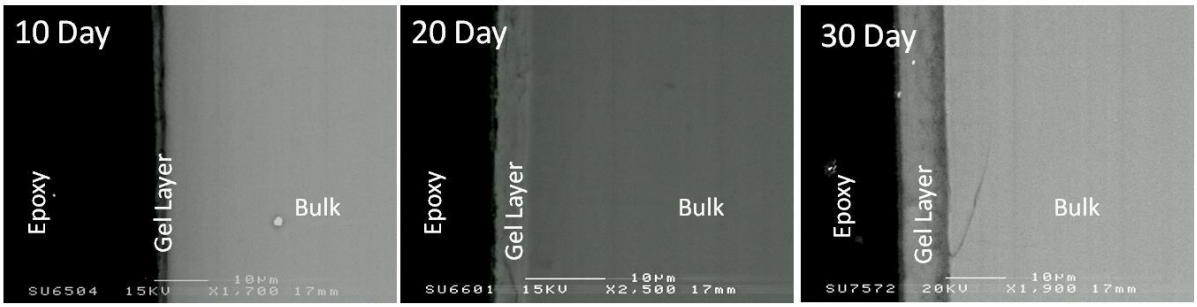

Figure 7.16 Backscatter electron images of CaZn Blend for the VHT time dependent study. Times were 10, 20 and 30 days at 200 °C in a high purity H_2O vapour atmosphere.

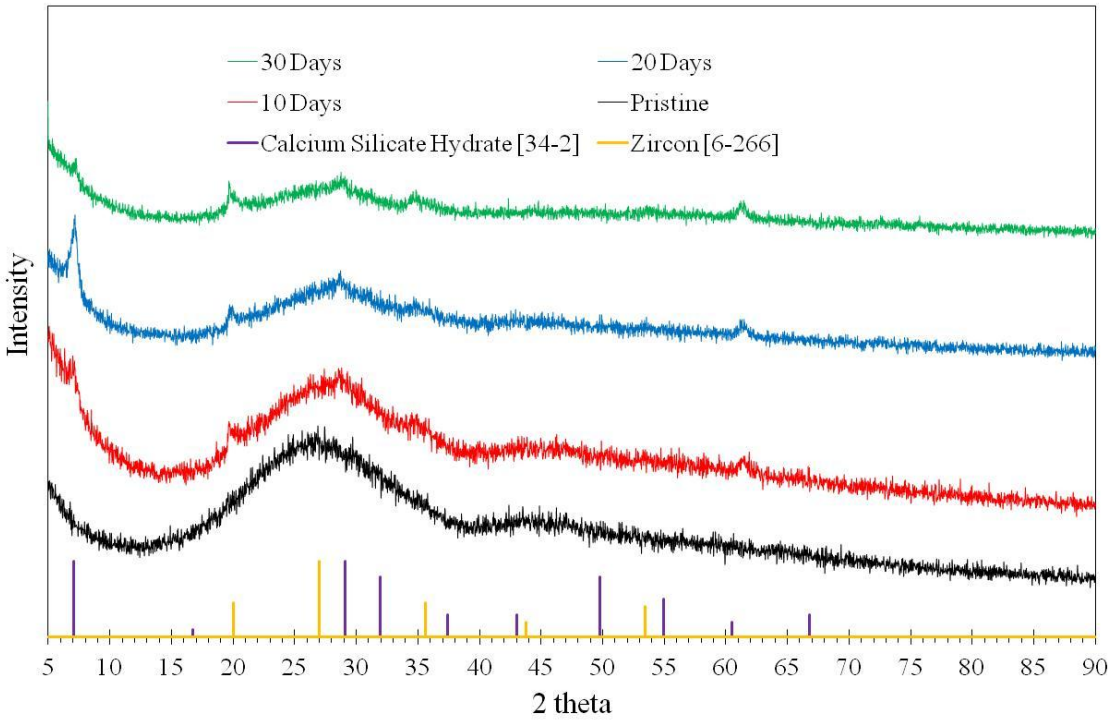

Figure 7.17 X-ray diffraction traces of the pristine glass, 10 day, 20 day, and 30 day VHT samples of the CaZn Blend glass at 200 °C in high purity H_2O.

Further analysis of the CaZn Blend glass under EDS X-ray mapping in Figure 7.18 provides evidence of a different alteration layer as compared to the CaZn Base glass samples. An increased concentration of Zn is not present as in the CaZn Blend glass; however, there is

an increased concentration of Ca within the alteration layer near the surface of the pristine glass. The concentration of Si in the alteration layer is lower than the concentration in the pristine glass for the 10 day VHT sample. This is apparent from the change in the contrast of the image in Figure 7.18 C, where the pristine glass is bright and the alteration layer on the surface of the pristine glass is slightly darker. The contrast change for the EDS X-ray map of Na is consistent with observations of the CaZn Base glass where the concentration of Na is lower in the alteration layer as compared to the pristine glass for the CaZn Blend glass. Mg, Al, and Zr do not show any changes in contrast in the EDS dot map in Figure 7.18 for the CaZn Blend 10 day VHT sample, suggesting there is no change in the concentration.

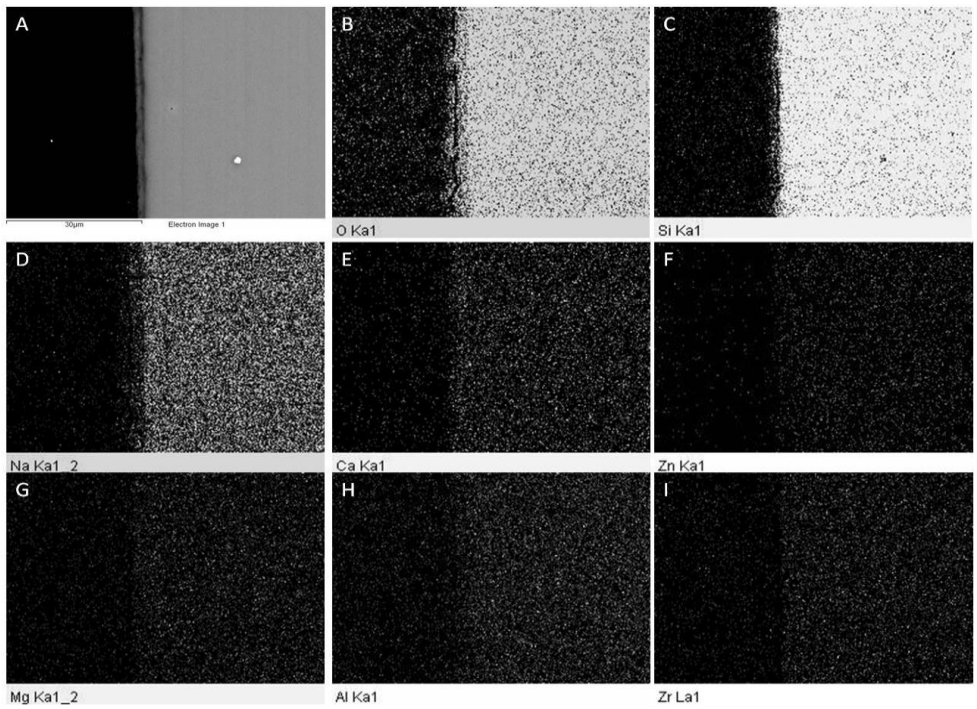

Figure 7.18 EDS dot map showing A) backscatter electron image B) O C) Si D) Na E) Ca F) Zn G) Mg H) Al and I) Zr for the CaZn Blend 10 day VHT sample.

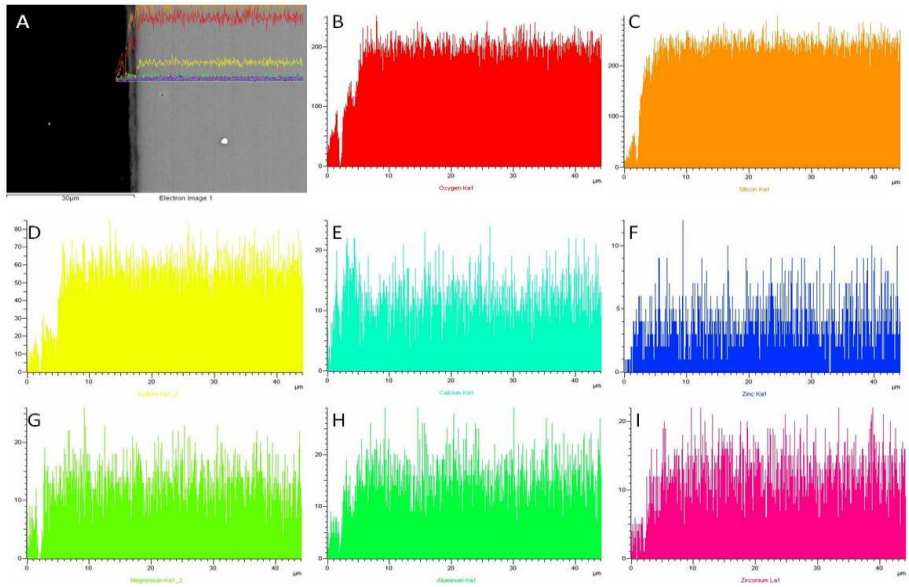

Figure 7.17 EDS line scans showing A) backscatter electron image B) O C) Si D) Na E) Ca F) Zn G) Mg H) Al and I) Zr for the CaZn Blend 10 day VHT sample.

EDS line scans of the CaZn Blend 10 day VHT sample verifies the formation of an alteration layer on the surface of the glass, as illustrated in Figure 7.17 from the concentration profiles of each element. The concentration profiles follow the EDS X-ray mapping where the concentration of Si and Na is lower in the alteration layer as compared to the pristine glass, while Ca has a possible increased concentration within the alteration layer (Figure 7.17 C).

Figure 7.18 illustrates the EDS line scans for CaZn Blend after a 20 day VHT at 200 °C. It can be seen from a comparison of the EDS line scans for the 10 and 20 day VHT of CaZn Blend that the alteration layer is similar in elemental concentration profiles and the only significant difference is the thickness of the alteration layer. There is an increase in the concentration of Si from the surface of the gel to the pristine glass. There is also a higher concentration of Ca in the alteration layer as compared to the bulk glass for the 20 day sample, confirming the concentration of Ca being higher in the alteration layer for the 10 day sample.

An EDS X-ray map for CaZn Blend after a 30 day VHT at 200 °C is given in Figure 7.19. A banded structure, as seen in the BEI of the 10 and 20 day VHT samples, is clearly visible from the changes in contrast of the selected mapped elements. The banded structure appears to contain high concentrations of Si, Na, Mg and Zr from visual observations in the changes in contrast in the images.

A closer examination of the CaZn Blend 30 day VHT sample using EDS line scans (Figure 7.20) show concentration gradients similar to those observed in the 10 and 20 day

VHT samples. This gives more evidence that the mechanism for the formation of alteration layers do not change with time for the CaZn Blend glass. Observation of Figure 7.20 clearly shows a region of the alteration layer adjacent to the pristine glass deficient in several elements. Zn does not show any significant change in the concentration from the surface of the alteration layer through the bulk glass as shown in Figure 7.20 F.

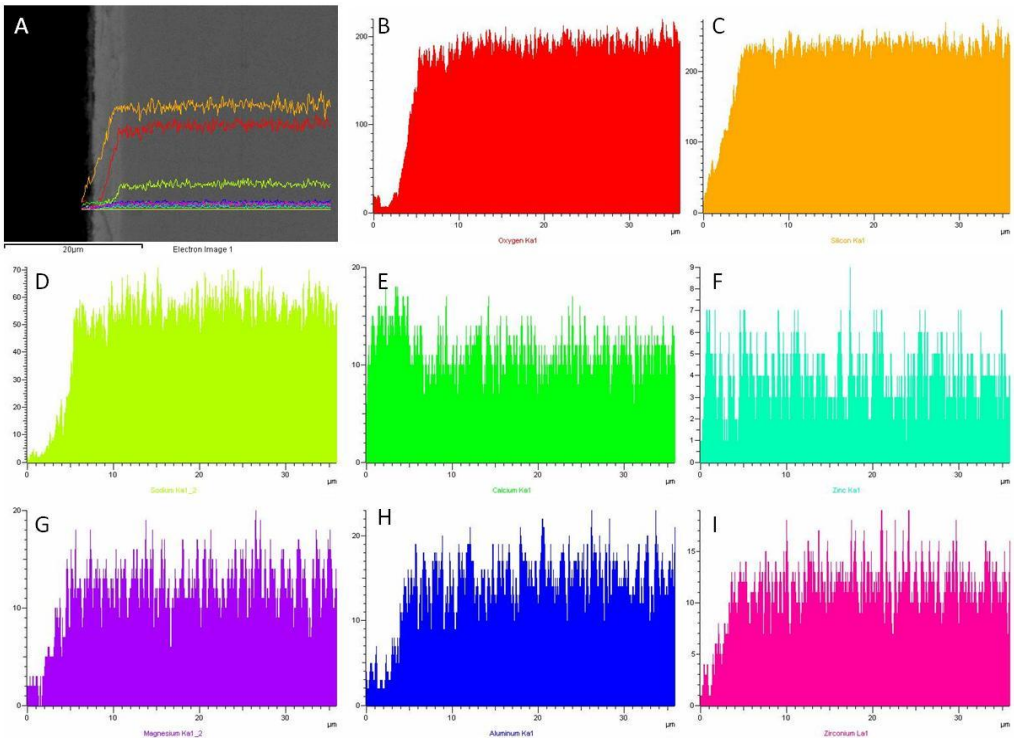

Figure 7.18 EDS line scans showing A) backscatter electron image B) O C) Si D) Na E) Ca F) Zn G) Mg H) Al and I) Zr for the CaZn Blend 20 day VHT sample.

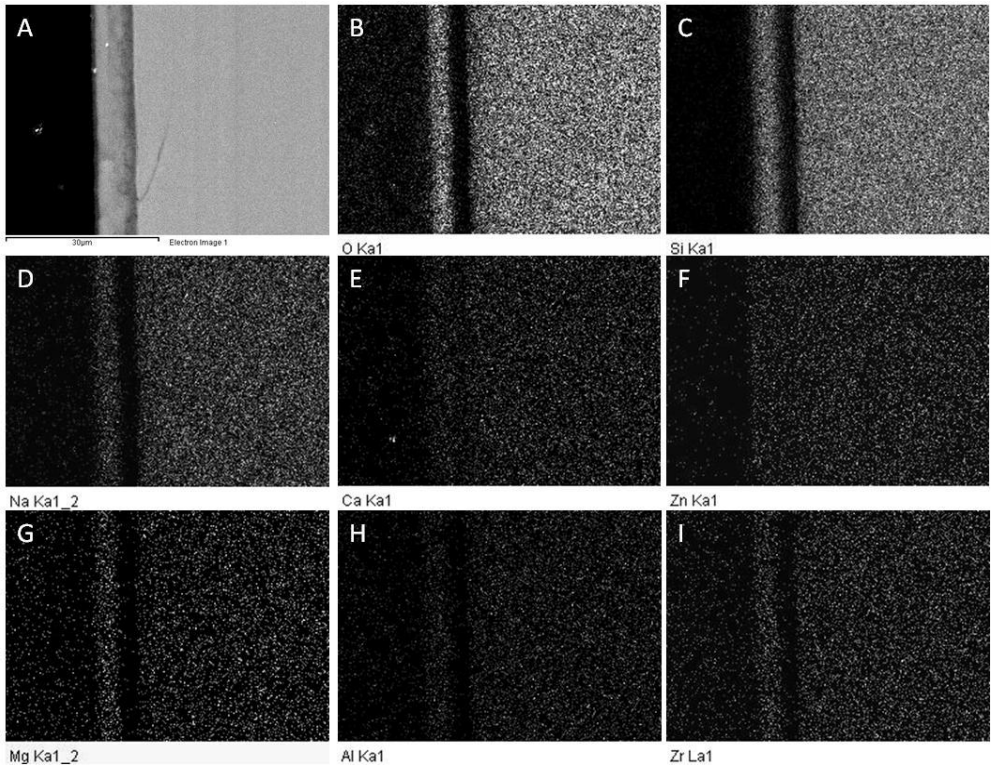

Figure 7.19 EDS dot map showing A) backscatter electron image B) O C) Si D) Na E) Ca F) Zn G) Mg H) Al and I) Zr for the CaZn Blend 30 day VHT sample.

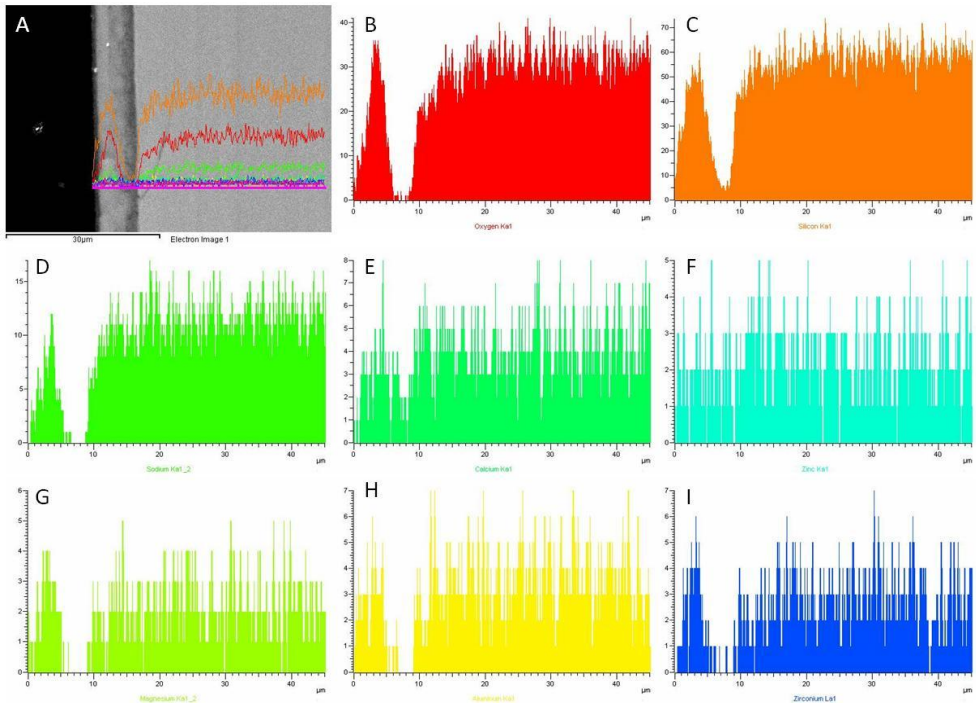

Figure 7.20 EDS line scans showing A) backscatter image B) O C) Si D) Na E) Ca F) Zn G) Mg H) Al and I) Zr for the CaZn Blend 30 day VHT sample.

7.3.2.1.3 MW Base

MW Base, a simple borosilicate glass used for vitrification of UK's nuclear waste, was also studied using the VHT method. Backscatter electron images of MW Base after 10, 20 and 30 day VHT experiments are given in Figure 7.21. The alteration layer thickness of each sample appears to be dense and thicker as compared to the CaZn Base glass as shown in Figure 7.8. The MW Base glass composition is similar to CaZn Base, but does not have additions of Ca and Zn to the composition. The thickness of the alteration layer for MW Base increases with time from >300 μm at 10 days to >1000 μm at 30 days. As shown in the BEI images in Figure 7.21, there is also no banding structure for any sample. This is different from CaZn Blend where the banded layers are visible in the BEIs. The vertical lines seen for the 10 and 30 day sample are artefacts from the instrument used and do not correlate to changes in the alteration layer. A close examination of the 20 day sample reveals a difference on the surface of the alteration layer as compared to both the 10 and 30 day sample.

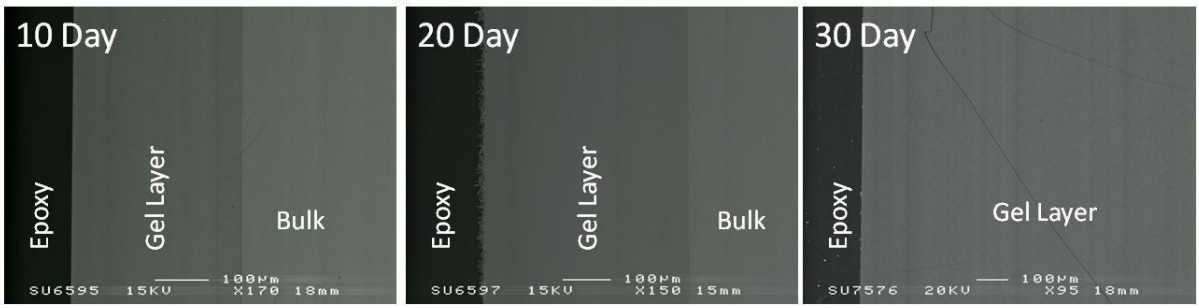

Figure 7.21 Backscatter electron images of MW Base for the VHT time dependent study. Times were 10, 20 and 30 days at 200 °C in a high purity H_2O vapour atmosphere.

The crystallinity of the alteration layers for MW Base can be seen to increase with time as shown in the XRD traces plotted in Figure 7.22. Two possible silica phases along with a sodium silicate phase for the 20 and 30 day VHT samples are plotted below the XRD traces. The 10 day VHT sample exhibited predominantly diffuse scattering with little to no crystalline peaks as is shown in Figure 7.22.

EDS line scans were performed on the 10, 20 and 30 day VHT samples of the MW Base glass in order to determine concentration profiles. Figure 7.23 shows that the thickness of the alteration layer to be 300 μm ± 10 μm due to the sharp changes in the concentration profiles. The concentration of both Si and Na do not show any significant variation within the alteration layer of the 10 day VHT. The alteration layer for the 20 day VHT, as seen in Figure 7.24, illustrates a possible decrease in the concentration of Si from the surface to the

surface of the pristine glass. The alteration layer thickness, as expected, increased from the 10 day VHT to the 20 day VHT to 450 μm ± 15 μm as is confirmed in Figure 7.24. The concentration profile of the gel layer of the 30 day sample in Figure 7.25 is similar as the 10 and 20 day sample by not having any significant change in the concentration of either Si or Na in the line scan.

Close examination of the alteration layer surface on the 20 day VHT of the MW Base glass revealed a second microstructure as can be seen in the EDS X-ray map given in Figure 7.26. This surface was not present on either the 10 or 30 day VHT samples. What appear to be crystals are deficient in Si, but high in Na concentration and are shown to be forming on the surface of the alteration layer. This second microstructural feature is, generally, approximately 15 to 20 μm thick. The identified phase in the XRD trace of the 20 day VHT MW Base glass suggests a sodium silicate forming on the surface of the alteration layer.

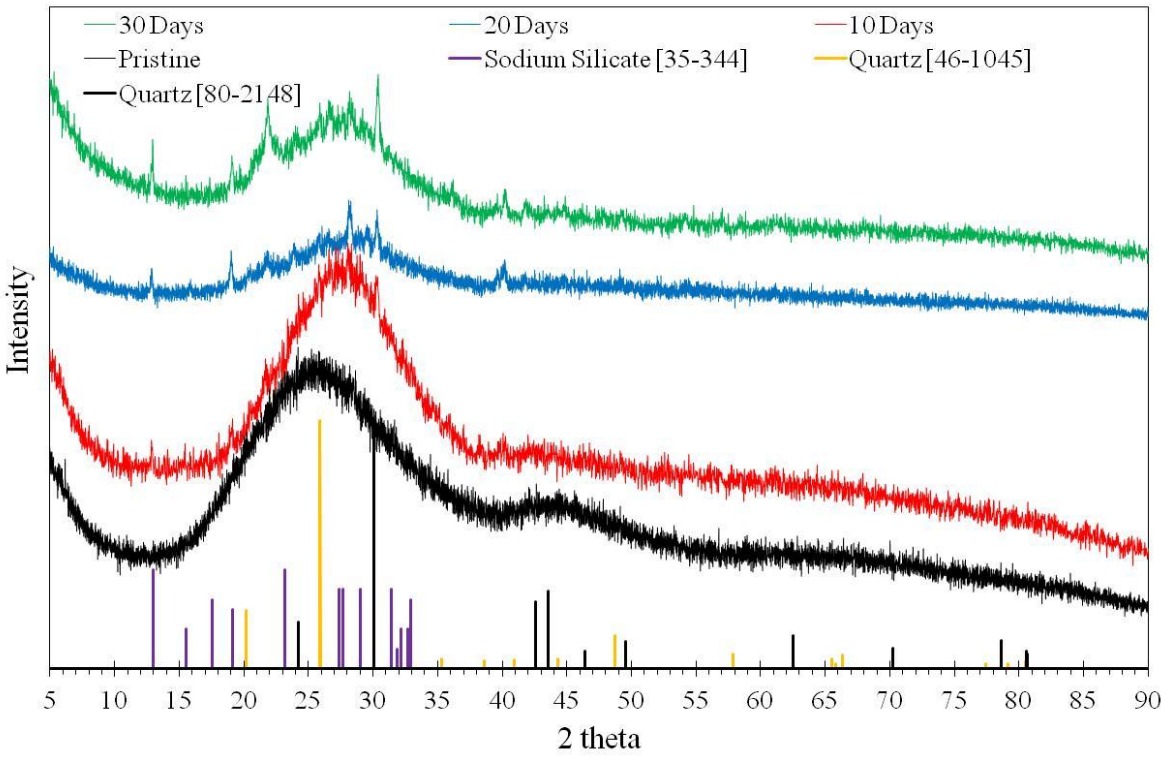

Figure 7.22 X-ray diffraction traces of the pristine glass, 10 day, 20 day, and 30 day VHT samples of the MW Base glass at 200 °C in high purity H_2O.

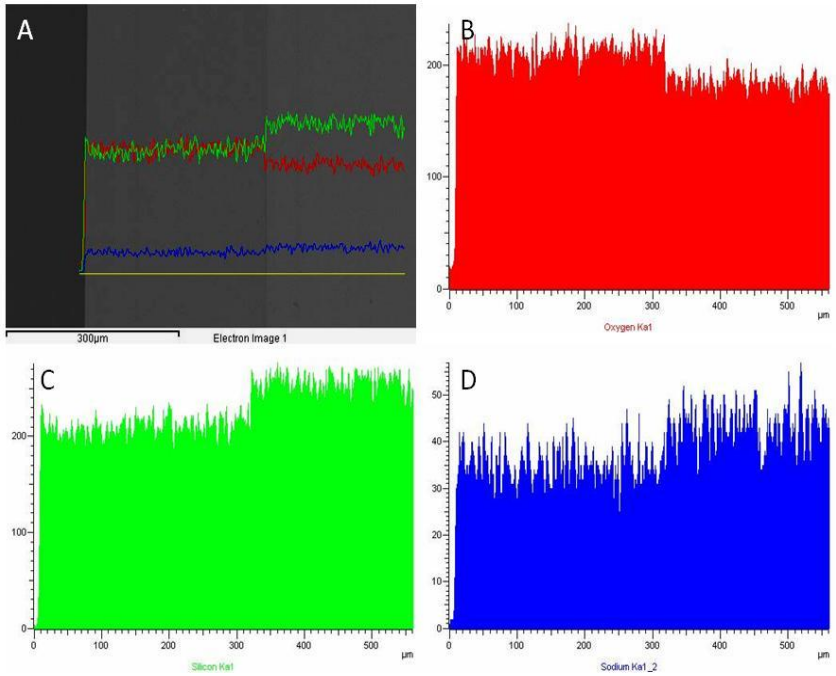

Figure 7.23 EDS line scans showing A) backscatter image B) O C) Si and D) Na for the MW Base 10 day VHT sample.

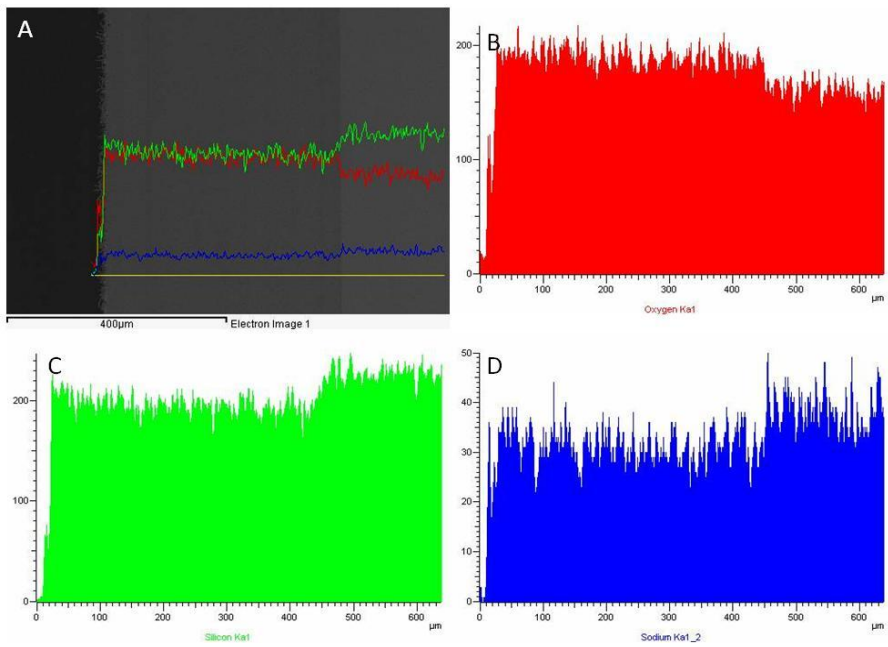

Figure 7.24 EDS line scans showing A) backscatter image B) O C) Si and D) Na for the MW Base 20 day VHT sample.

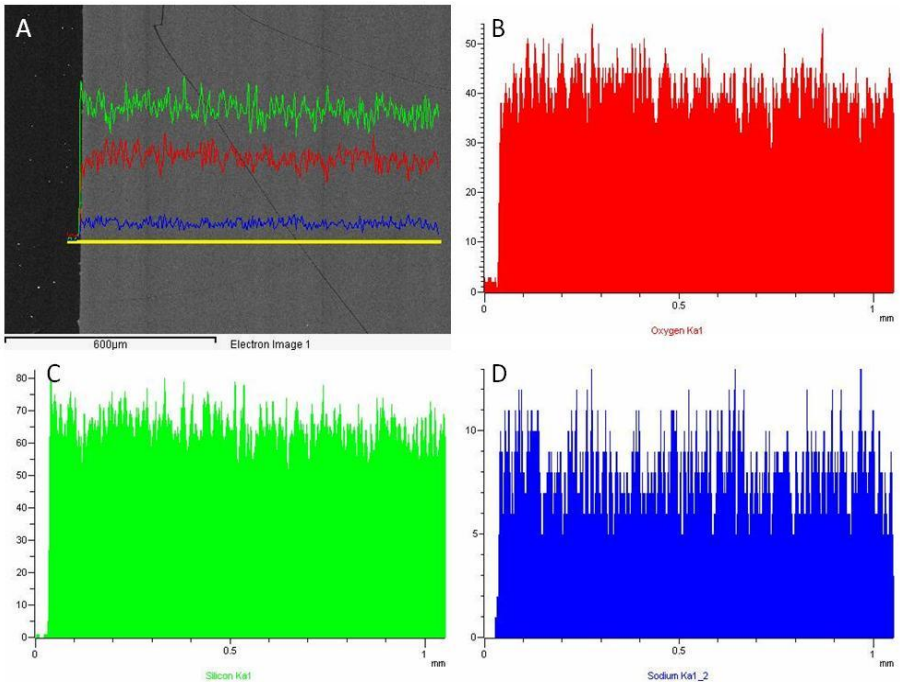

Figure 7.25 EDS line scans showing A) backscatter image B) O C) Si and D) Na for the MW Base 30 day VHT sample.

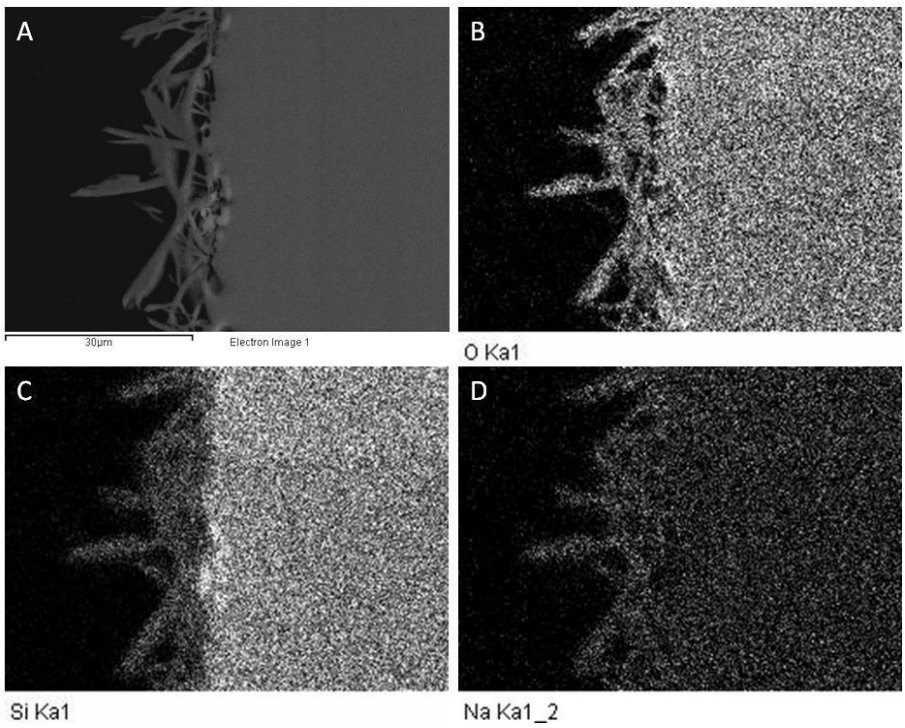

Figure 7.26 EDS dot map showing A) backscatter image B) O C) Si and D) Na for the surface of the alteration layer of the MW Base 20 day VHT sample.

7.7.2.1.4 MW Blend

The VHT of MW Base glass with the addition of simulated HLW, MW Blend, resulted in a banded structure, similar to CaZn Blend, within the alteration layer. The alteration layer is thinner as compared to MW Base as shown in Figure 7.27. The 10 day VHT of MW Blend resulted in an alteration layer 10 μm ± 3 μm in thickness. At 20 days, the alteration layer thickness increases to 17 μm ± 3 μm, followed by a thickness of 25 μm ± 3 μm at 30 days. Figure 7.27 clearly indicates a banded structure in each alteration layer from the changes in contrast of the backscatter electron images.

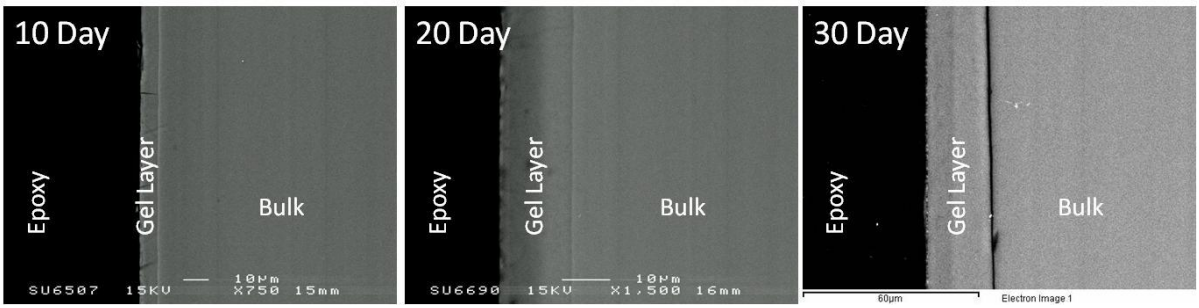

Figure 7.27 Backscatter electron images of MW Blend for the VHT time dependent study. Times were 10, 20 and 30 days at 200 °C in a high purity H_2O vapour atmosphere.

The XRD traces of the MW Blend VHT samples in Figure 7.28, reveals three plausible phases which formed during the VHT tests; revdite ($Na_2Si_2O_5 \bullet 5H_2O$) and a silicon dioxide zeolite (SiO_2). The 10 day VHT of MW Blend has diffuse scattering associated with a completely amorphous glass as illustrated for the pristine glass. With no crystalline peaks, the alteration layer that is seen in the BSI images suggests this layer may be amorphous at short times; however, this layer may be too thin to contribute to the scattering volume. Increasing the time of the VHT to 20 and 30 days increases the size of the peaks near 2θ = 20, 35 and 61 2θ in the XRD traces indicating an increase in the revdite structure in the alteration layer.

Figure 7.29 plots the EDS line scans for the 10 day VHT of the MW Blend glass. Only Si and Na show significant differences in concentration within the alteration layer as compared to the pristine glass. The 20 day VHT sample is different, as shown in Figure 7.30, and has a Si concentration that is possibly higher in the alteration layer than in the pristine glass. There is also a difference between the two samples for the concentration of Mg; there is a lower concentration in the alteration layer for the 10 day sample, but it is higher in the alteration

layer for the 20 day VHT sample. Both Na and Mo in the 10 and 20 day VHT samples have lower concentrations in the alteration layer than the pristine glass as is illustrated in Figure 7.29 and 7.30 in image D and H, respectively.

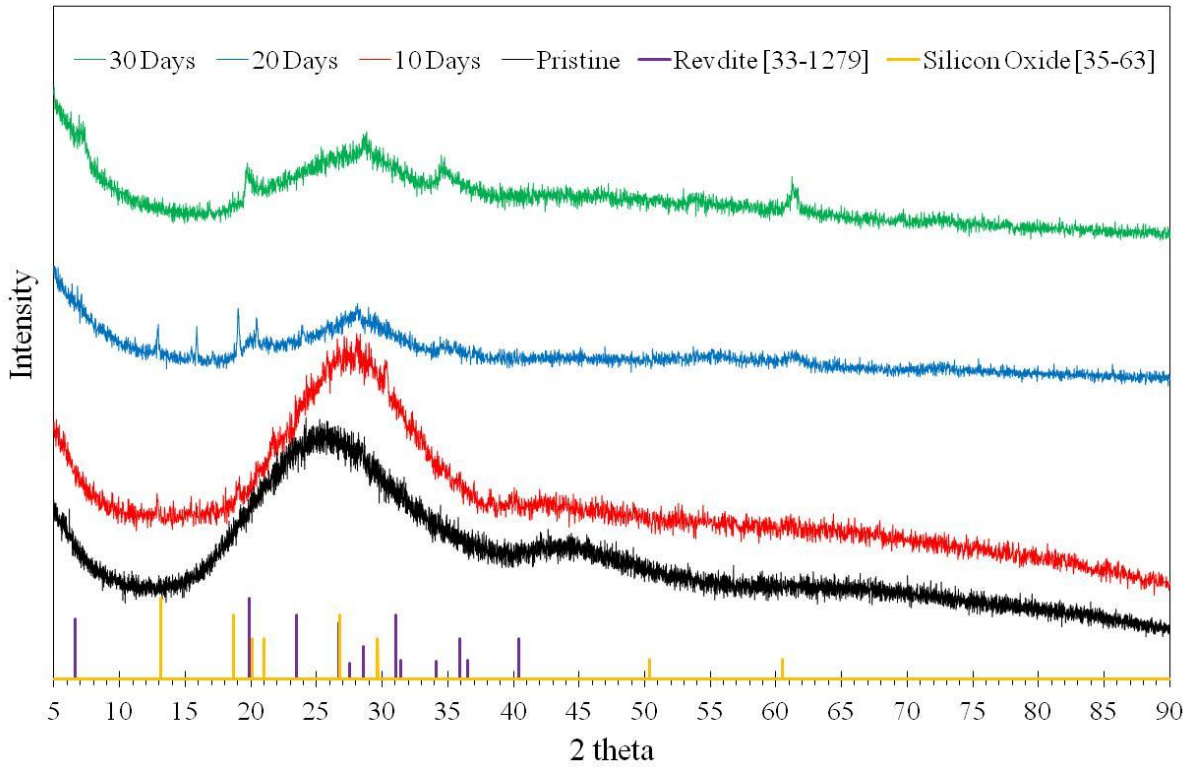

Figure 7.28 X-ray diffraction traces of the pristine glass, 10 day, 20 day, and 30 day VHT samples of the MW Blend glass at 200 °C in high purity H_2O.

The 30 day VHT MW Blend sample, as seen in Figure 7.31, has a high concentration of Si and Na at the surface of the pristine glass. The profiles of the EDS line scans for each element show that the alteration layer of the 30 day sample is different compared to both the 10 and 20 day VHT samples due to the increased concentrations of elements at the surface of the pristine glass that decreases with distance into the bulk glass. In the BEI, the banded structure of the alteration layer is more pronounced as compared to images for the 10 or 20 day VHT samples. The general concentration of Si and Na in the alteration layer of the 30 day VHT sample is lower than the pristine glass; however, Si and Na in the EDS line scans show a sharp change in concentration at the surface. Both Mg and Al have a higher concentration in the alteration layer, in general, as compared to the pristine glass. At the surface of the alteration layer, Zr has a high concentration which decreases sharply until approximately 5 μm ± 2 μm depth whereupon it becomes constant. Both the 10 and 20 day VHT samples do not show the decrease in concentration of Si and Na from the surface of the

pristine glass towards the centre of the bulk glass as is apparent in the 30 day sample. The higher concentration of Mg in the 30 day sample is also more apparent than in the 20 day VHT sample. The concentration of Zr is also different, which could be evidence of precipitation of a Zr phase starting to occur after 20 days.

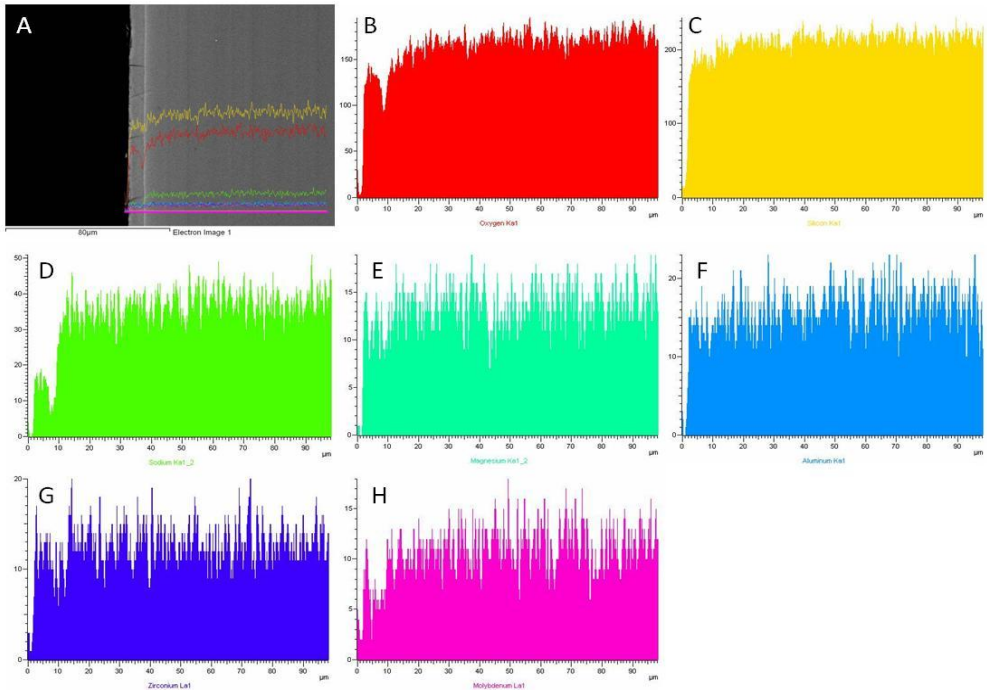

Figure 7.29 EDS line scans showing A) backscatter image B) O C) Si D) Na E) Mg F) Al G) Zr and H) molybdenum for the MW Blend 10 day VHT sample.

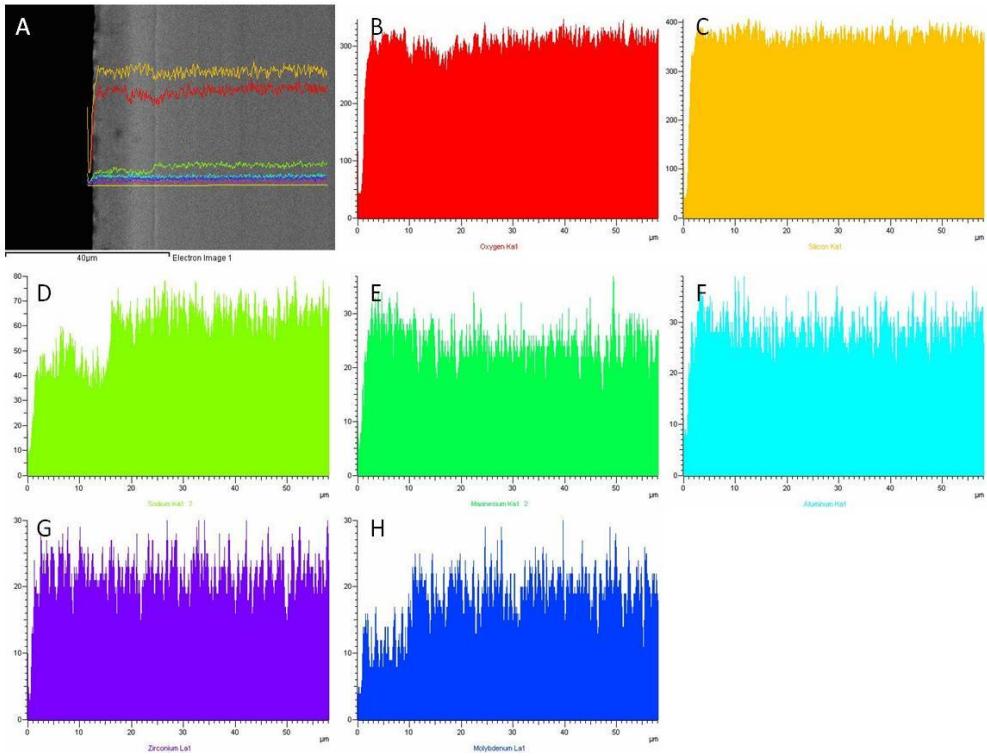

Figure 7.30 EDS line scans showing A) backscatter image B) O C) Si D) Na E) Mg F) Al G) Zr and H) molybdenum for the MW Blend 20 day VHT sample.

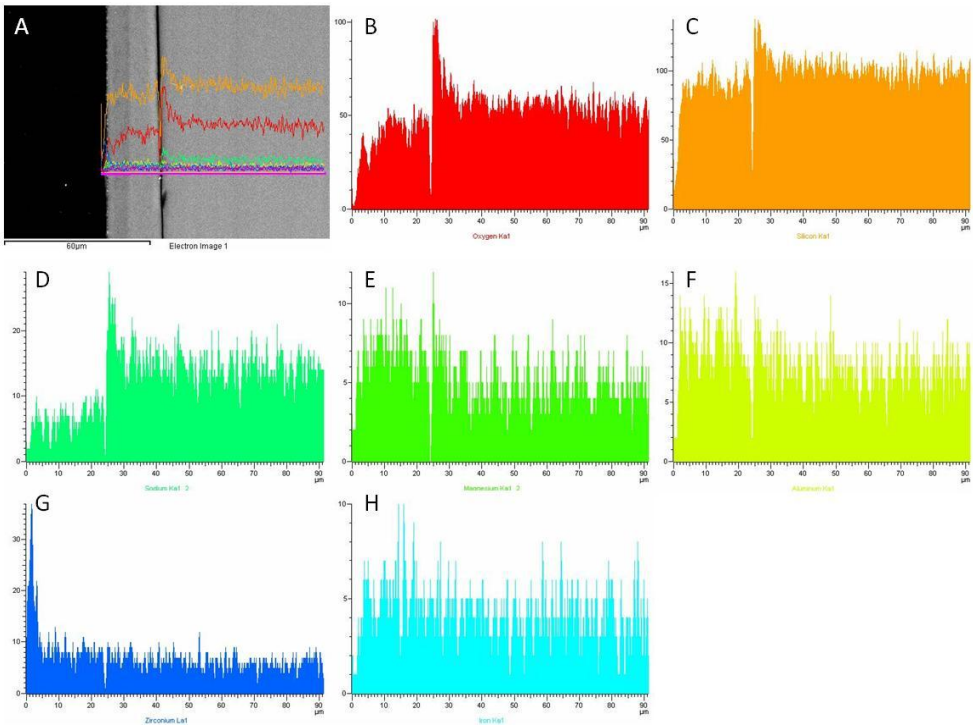

Figure 7.31 EDS line scans showing A) backscatter image B) O C) Si D) Na E) Mg F) Al G) Zr and H) iron for the MW Blend 30 day VHT sample.

7.3.2.1.5 FeZnZr

Backscatter electron images of the 10, 20, and 30 day VHTs of the FeZnZr glass are given in Figure 7.32. The changes in the contrast for the alteration layer show a banded structure similar to those seen in both the CaZn Blend and the MW Blend samples. As expected, the thickness of the alteration layer increases with time. The 10 day VHT sample has an alteration layer which is 12 μm ± 2 μm in thickness. Increasing the time to 20 days increases the alteration layer thickness to 15 μm ± 3 μm, followed by 18 μm ± 3 μm thick for the 30 day sample.

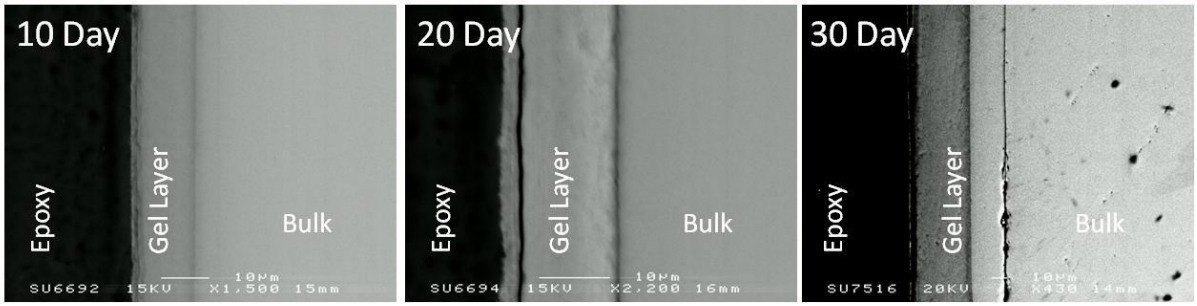

Figure 7.32 Backscatter electron images of FeZnZr for the VHT time dependent study. Times were 10, 20 and 30 days at 200 °C in a high purity H_2O vapour atmosphere.

The XRD traces of the FeZnZr pristine glass along with the 10, 20 and 30 day VHT FeZnZr glass samples are plotted in Figure 7.33. Indexing of the XRD traces resulted in four plausible phases present in the alteration layers of the FeZnZr VHT samples; revdite ($Na_2Si_2O_5 \bullet 5H_2O$), zircon ($ZrSiO_4$), quartz ($SiO_2$) and nontronite-15A ($Na_{0.3}Si_4O_{10}(OH)_2 \bullet 4H_2O$). All three VHT samples have the same peaks in the XRD trace while the pristine glass gives diffuse scattering, as expected, from a homogenous glass.

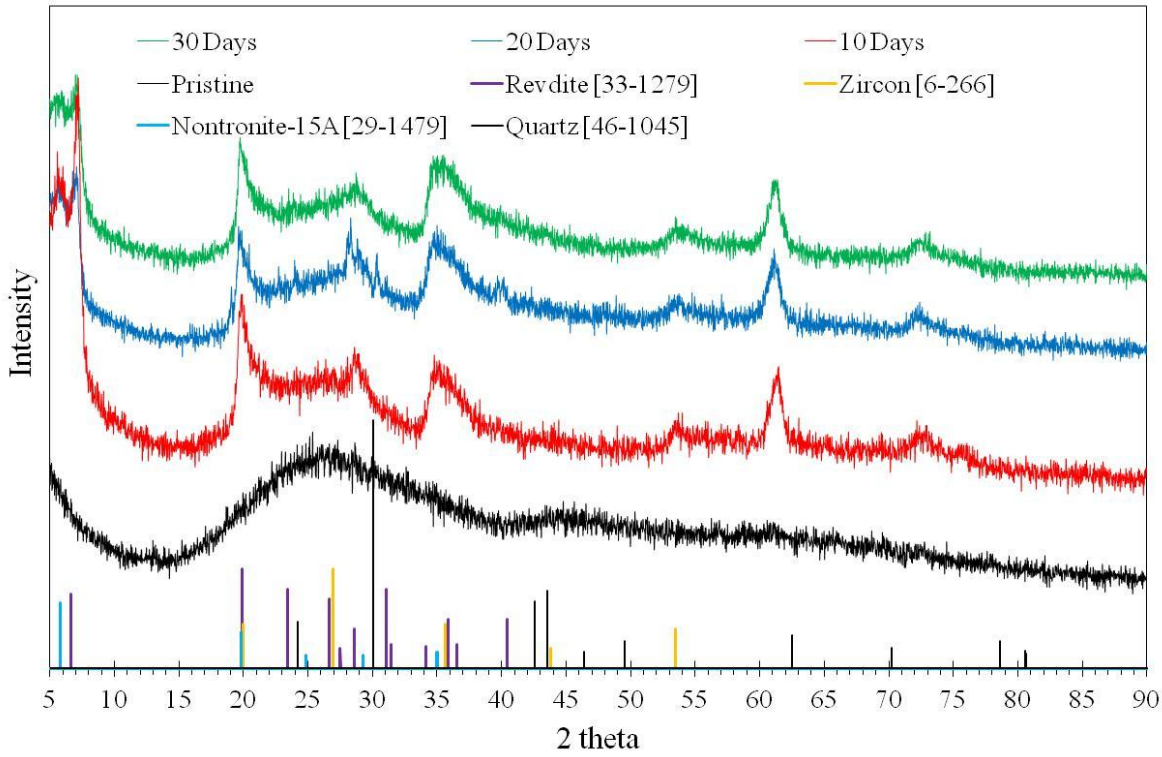

Figure 7.33 X-ray diffraction traces of the pristine glass, 10 day, 20 day, and 30 day VHT samples of the FeZnZr glass at 200 °C in high purity H_2O.

EDS X-ray maps of the 10 day VHT of the FeZnZr glass are shown in Figure 7.34. Only subtle changes are seen in the contrast of the EDS X-ray map for O while Na has a very distinct change in the contrast between the pristine glass and the alteration layer. Si, Zn, Fe and Zr do not show any significant changes in the contrast of their respective images. In the BEI of the FeZnZr glass, Figure 7.34 A, a band of a different contrast can be seen on the surface of the alteration layer suggesting that there is a different composition on the surface of the alteration layer as compared to the inner region of the alteration layer. The pristine glass does not show a change in the contrast indicative a homogenous glass.

EDS line scans were performed on the 10 day VHT of the FeZnZr glass in order to further analyse the alteration layer, Figure 7.35. The concentration of Si does not show significant changes in the composition between the alteration layer and the bulk glass, while Na and Zr show definite changes in their concentration profiles within the alteration layer.

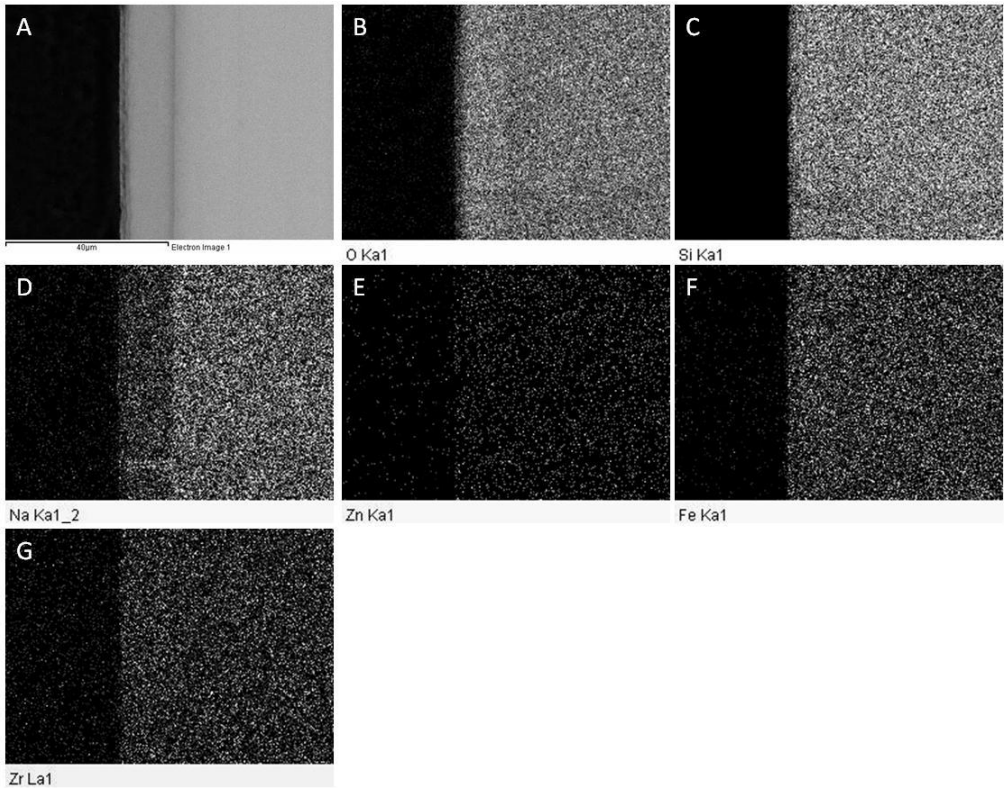

Figure 7.34 EDS dot map showing A) backscatter image B) O C) Si D) Na E) Zn F) iron and G) Zr for the FeZnZr 10 day VHT sample.

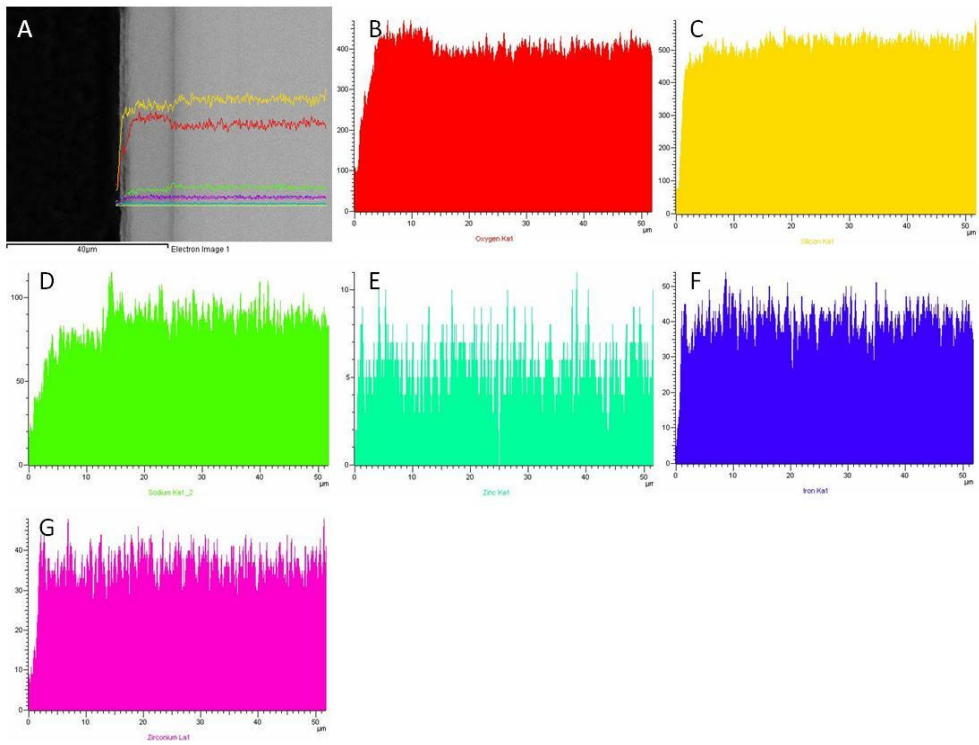

Figure 7.35 EDS line scans showing A) backscatter image B) O C) Si D) Na E) Zn F) iron and G) Zr for the MW Blend 10 day VHT sample.

The EDS X-ray maps of the 20 day VHT sample for the FeZnZr glass are given in Figure 7.36. It is clear from the changes in the contrast of the dot maps for Si, Na, Fe and Zr that a banded structure in the alteration layer has formed. This is different to the 10 day sample where there was no change in contrast of any element except O and Na. A further difference is a noticeable band on the surface of the alteration layer for the 20 day sample while on the 10 day VHT sample, this band is not visible from contrast differences in the EDS X-ray map images.

Further evidence of the banded structure is shown in the EDS line scans of the 20 day VHT sample for the FeZnZr glass, Figure 7.37. The EDS line scans show a more pronounced alteration layer as compared to the 10 day sample, Figure 7.35. There is a gradual increase in the concentration of O and Na in the alteration layer of the 20 day sample while Si exhibits a variation of concentrations within the alteration layer, which in general, is lower than the constant concentration of Si seen in the pristine glass. The concentration profile of Zn and Fe show a local minimum in the alteration layer that is higher than in the pristine glass. This is different as compared to the 10 day sample where Zn and Fe do not show any significant changes in their concentration. Zr, initially, has a very low concentration (outer band of the alteration layer), which increases to a steady concentration above that seen in the pristine glass for the 20 day VHT sample.

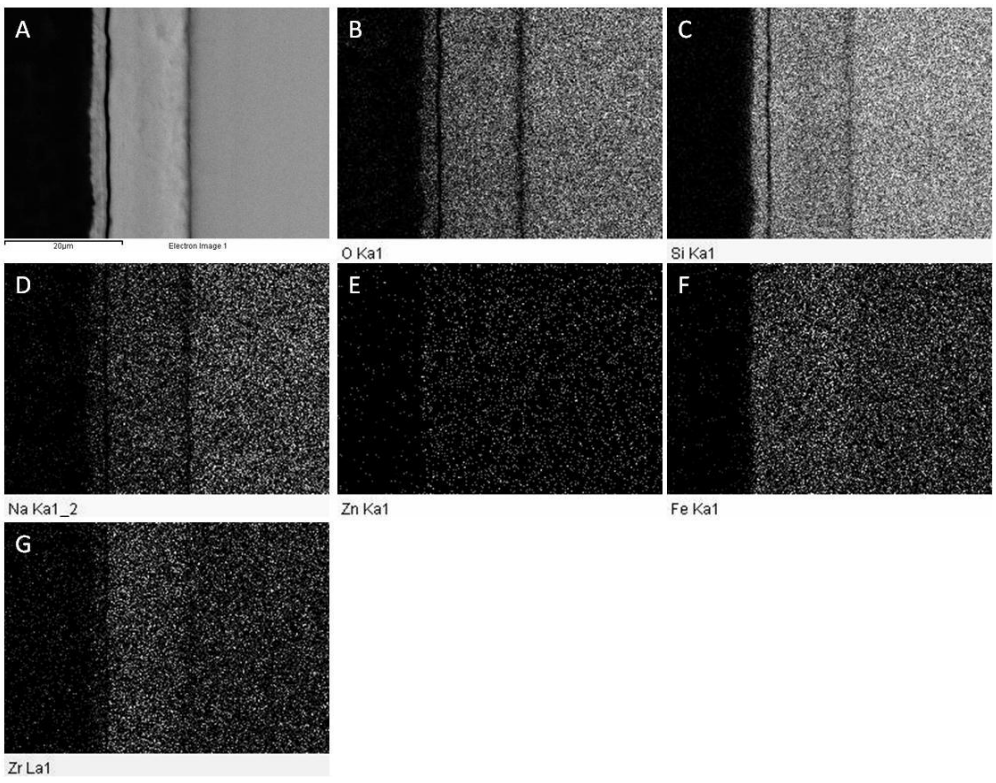

Figure 7.36 EDS dot map showing A) backscatter image B) O C) Si D) Na E) Zn F) iron and G) Zr for the FeZnZr 20 day VHT sample.

The 30 day VHT sample of the FeZnZr glass did not show any significant thickness increases with time as the previous glasses. The thickness is, within error, the same as the 20 day VHT sample. The banded structure of the alteration layer is; however, more prominent in the 30 day VHT sample as compared to the 20 day VHT sample. This is seen in the EDS X-ray maps for the 30 day VHT sample of the FeZnZr glass shown in Figure 7.38. A concentration gradient of Si, Na and Zr is evident from the changes in contrast of the X-ray map images in Figure 7.38 C, D and G, respectively. Both Zn and Fe do not show significant changes in their concentration in the EDS X-ray maps.

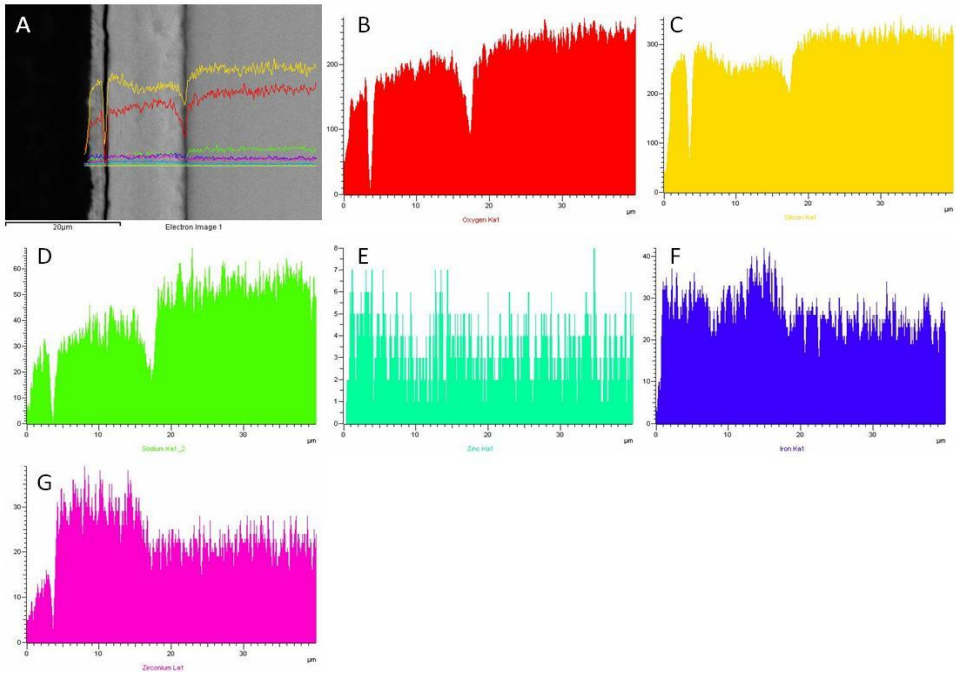

Figure 7.37 EDS line scans showing A) backscatter image B) O C) Si D) Na E) Zn F) iron and G) Zr for the MW Blend 20 day VHT sample.

The EDS line scans of the 30 day VHT FeZnZr glass are plotted in Figure 7.39. The surface of the alteration layer has a higher concentration of Si, Na and Zr as compared to the inner region of the alteration layer. The concentration profiles of the 20 and 30 day VHT samples are different for all elements in that their respective concentration profiles all show different trends. This suggests there are possible changes in precipitation of secondary phases between 20 and 30 days during a VHT. The concentrations of Si and Na show a minimum in the alteration layer for the 30 day sample while Na shows a maximum in the alteration layer in the 20 day sample. In the 30 day sample, both Fe and Zn show no significant changes in the concentration profile of the EDS line scans throughout the

alteration layer and the pristine glass which is different than the 20 day sample where their concentrations are higher in the alteration layer as compared to the pristine glass.

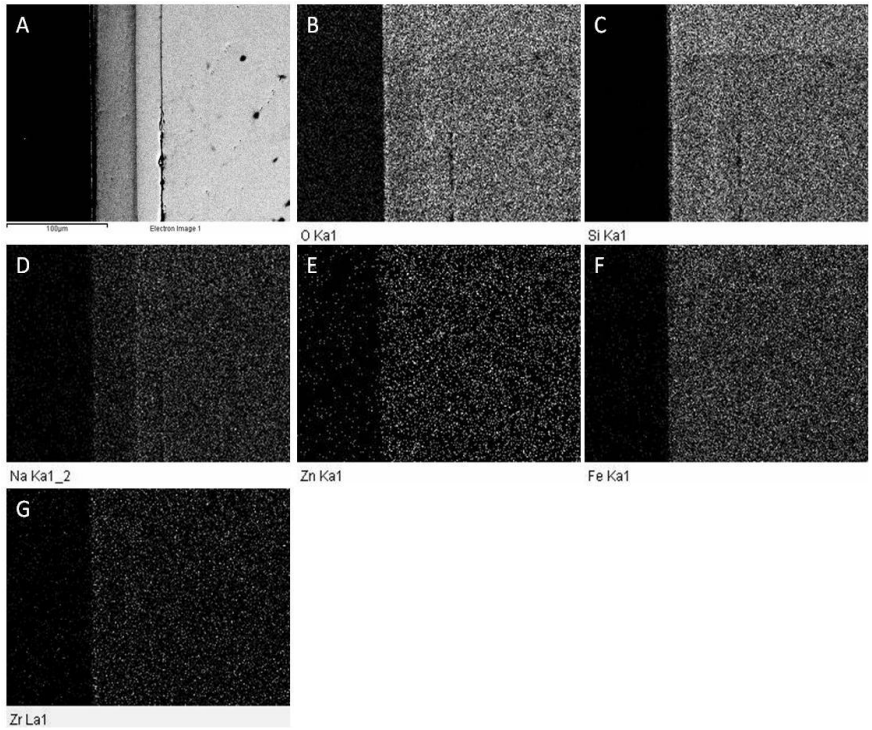

Figure 7.38 EDS dot map showing A) backscatter image B) O C) Si D) Na E) Zn F) iron and G) Zr for the FeZnZr 30 day VHT sample.

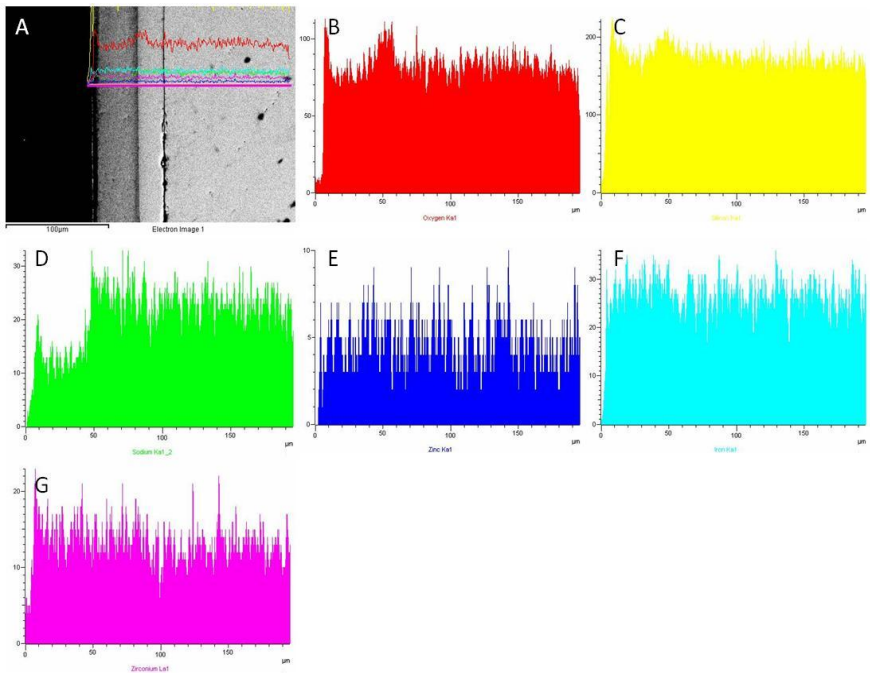

Figure 7.39 EDS line scans showing A) backscatter image B) O C) Si D) Na E) Zn F) iron and G) Zr for the MW Blend 30 day VHT sample.

7.4 Discussion

7.4.1 VHT Reproducibility

As shown in Figure 7.4, from the reproducibility VHT experiment, there is a larger variation in the alteration layer thickness for the as cut samples as compared to the polished samples. This can be attributed to the higher degree of variability in the surface finish of the as cut samples after cutting. After cutting samples, the blade needs to be dressed in order to cut the samples faster and in a more consistent cut; however, the blade was only dressed after several samples which would lead to a variability in the surface finish of the samples after cutting.

Polished VHT samples exhibit a lower variation in the alteration layer thicknesses as shown in the box plot of Figure 7.5. It is shown from Figure 7.5 that a finer polish of the surface of the sample will provide a more consistent (less variable) alteration layer thickness. The as cut samples have a variable surface roughness depending on the number of samples the saw blade cuts previous to getting re-sharpened (dressing the blade). A sample cut just after the saw blade is sharpened/dressed will have a less variable surface roughness as compared to a sample cut just before the blade is sharpened/dressed. This is due to wear on the saw blade. Further testing on the samples after cutting will need to be performed in order to prove or disprove this hypothesis.

Jiricka *et al.* suggest that the relative humidity within the vessel (i.e. amount of water added) will affect the time needed to achieve the same reaction extent. [155] With a smaller amount of water, it will take longer for the sample to reach the same reaction extent as a vessel with a higher amount of water. The change in volume associated with the addition of a second sample in the VHT vessel changes the effective relative humidity due to a decrease in the overall volume of the VHT vessel and therefore changing the time to reach the same extent of reaction. Vienna *et al.* performed VHT experiments with both one sample in a VHT vessel and 0.02 mL of high purity water and also two samples placed inside the reaction vessel with 0.025 mL of high purity water. [159] This was similar to this study where either one or two samples were used during the VHT experiment. Vienna *et al.* observed similar results where the thicker alteration layers were seen when only one sample is used during the VHT experiments.

There is also a variation in the alteration layer thickness depending on whether one sample or two samples are used in the reaction vessel during the VHT test. As shown in Figure 7.5, the average alteration layer thickness for only one sample in the VHT vessel during the test is

thicker than when two samples are placed in the VHT vessel. The mean alteration layer thickness for the polished samples is similar and within error. There is a slightly larger variation in the alteration layer thickness for polished samples when only one sample is used during the VHT experiment as compared to having two samples in the reaction vessel. As mentioned previously, the variation between only one or two samples in the VHT vessel during the test has an effect on the relative humidity due to the change in the overall volume within the VHT vessel during the test. (159)

It is currently recommended to use two samples polished with P1200 SiC paper in the VHT vessel during the alteration tests. This gives two samples for testing which have been exposed to the same exact environment. As long as there has been no reflux (dripping of solution from the sample to the bottom of the vessel) as measured with pH paper, this will give sufficient results to compare to other VHT studies. In the case of the study above, two samples were used; one sample was placed in an epoxy mould to study the alteration layer by electron microscopy while the second sample was used to study the alteration layer by X-ray diffraction.

7.4.2 Formation of Gel Layers on UK HLW Glasses

As seen from the EDS X-ray maps of the time dependant VHT experiment using CaZn Base glass, there are differences in the alteration layer microstructure at different times. After the 30 day VHT of the CaZn Base glass, four different phases formed; hemimorphite, CSH, and possibly two silicate phases. At short times, all four of the phases are present in the CaZn Base sample as shown in the XRD plot in Figure 7.9; however, the microstructure of the alteration layer changes with time.

The change in the alteration layers with time of the CaZn Base glass suggest pore ripening within the alteration layer. It was suggested by Cailleteau *et al.* that by substituting an insoluble oxide for a significant fraction of silica prevents the reorganization of the framework within the alteration layer leading to a high dissolution rate. (12) In the case of the CaZn Base glass, the Zn could become insoluble due to the increasing pH of the solution with an increase in the concentration of alkali in solution. It is known that the solubility of Zn decreases with an increase in solution pH. The addition of other oxides has been modelled and shown to decrease the dissolution rate due to densification of the alteration layer from pore ripening. (12) When pore ripening occurs, it transforms the rate of dissolution from being controlled by hydrolysis of the surface to being controlled by diffusion of species through the alteration layer. (12)

The CaZn Blend VHT samples only show quartz and CSH phases within the alteration layer during the VHT experiment. The formation of these phases was similar to the alteration layers that formed during the VHT of the CaZn Base glass. However, hemimorphite did not form in the CaZn Blend glass as it did in the CaZn Base glass. It is shown in the XRD trace for CaZn Blend that crystalline peaks could be associated to a hydrothermal zircon in the CaZn Blend 30 day VHT. Ruben *et al.* suggest three different categories of zircon formation in a hydrothermal environment; magmatic zircons hosted by intrusive igneous rocks, hydrothermal (or late magmatic) zircon overgrowths on magmatic zircons and hydrothermal zircons hosted by replacement bodies of fluorite in limestone. (160)

An inspection of the XRD patterns in Figures 7.9 and 7.17 show that there is less crystallization in the alteration layer of the CaZn Blend glass than compared to the CaZn Base glass. The wt % of Fe_2O_3 in the CaZn Blend glass could be sufficient enough to suppress the dissolution. As was shown by Cassingham *et al.*, the dissolution rate of MW Base glass decreased with an increase in the concentration of Fe_2O_3 in the overall glass composition. (150)

There is a large difference in the thickness of the alteration layers formed during the VHT as is seen between the simulated waste glasses and their respective base glasses. As shown in Table 7.4 below, the difference between CaZn Base and CaZn Blend alteration layer thickness after 10 days is significant, two orders of magnitude. The microstructure of the alteration layer of the 30 day VHT of CaZn Blend and MW Blend appears to be similar to that seen by Abrajano *et al.* where they have a banded structure. (161) According to Abrajano *et al.* the closest alteration layers to the pristine glass are more crystalline, which are the phases furthest from the reaction front. (161)

Table 7.4 Alteration layer thickness in micrometers for VHT samples after 10, 20 and 30 days at 200 °C in high purity H_2O vapour.

Sample	10 Day	20 Day	30 Day
CaZn Base	225 ± 25 μm	500 ± 100 μm	475 ± 50 μm
CaZn Blend	4 ± 2 μm	5 ± 2 μm	10 ± 2 μm
MW Base	300 ± 25 μm	450 ± 25 μm	> 1000 μm
MW Blend	10 ± 3 μm	17 ± 3 μm	25 ± 3 μm
FeZnZr	12 ± 2 μm	15 ± 3 μm	18 ± 3 μm

Crovisier *et al.* suggests that the alteration layers furthest from the reaction front contribute to the observable decrease in the dissolution rate of glass. (91) It is suggested that this occurs through an inhibition of Si diffusion observed during aqueous corrosion, similar

to that of SON68 under a high SA/V ratio test. [91] The addition of the simulated Blend waste in this study appears to contribute to a protective layer which decreases the alteration rate of the CaZn Blend glass as compared to the CaZn Base glass.

It is shown in the concentration profiles from the EDS line scans given in section 7.3 that the formation of alteration layers may initially be the direct result of hydration of the silicate frame work. The composition profiles of Na for the three VHT samples of CaZn Base also show that there is selective leaching of Na with an increase in time. This is evident from the depletion of Na in the alteration layer which is characteristic of a Type II glass described by Hench and Clark where the glass undergoes selective leaching of alkali on the surface of the glass which will act as a protective layer towards further dissolution of the pristine glass. [7] MW Base is also a Type II glass as is apparent from the slight increase in the Si concentration with an increase in the thickness of the alteration layer. There is also a higher concentration of Si at the surface of the alteration layer as compared to the inner portion adjacent to the pristine glass.

The addition of simulated waste to a base glass, CaZn Blend, resulted in dissolution characteristic of secondary precipitation following saturation of solution. Careful inspection of Figure 7.20 shows three regions of Si concentration within the alteration layer of the CaZn Blend 30 day VHT sample. The first, adjacent to the pristine glass, is similar to the 10 day sample and shows a slight decrease in the concentration of all the elements scanned (with the exception of Zn due to the low signal). The alteration layer has two regions; in the first region there is an absence of any element, the second region has an increase in concentration of select elements towards the surface of the alteration layer. The second region is similar to the 20 day sample which shows both the decrease in elemental concentration followed by a slight increase in concentration to the surface of the alteration layer. The third part of the alteration layer shows a decrease of all elements concentration to the surface of the sample. It is suggested by Gin *et al.* that glasses containing Si and Ca evolve to a significant extent which results in the glass having renewed glass alteration. They also show that the association of Zr and Ca is effective at decreasing glass alteration. [162]

An inspection of MW Blend reveals that the alteration layer may be participating in a decrease in the dissolution rate. This alteration layer may act as a diffusion barrier due to the high concentration of Si, Na and Ca at the surface of the pristine glass. According to Hench and Clark, this is a Type III surface which will have a dual protective layer and generally contain Al_2O_3. [7] Hench and Clark suggest that this dual protective layer contains a silica rich layer in between either an aluminoilicate or calcium phosphate layer. For this glass there are no additions of phosphate, and as shown from the CaZn Base and CaZn blend glass, only an aluminosilicate phase with a Si rich layer could form; however, this does not correlate

with the XRD traces plotted in Figure 7.28 which only show revdite, a hydrated sodium silicate phase, and silicon oxide phases being present.

Table 7.5 Mineral phases formed during the 30 day VHT of the five different glass compositions studied in this chapter.

Mineral Phases	Mineral Formula	PDF	MW Base	MW Blend	CaZn Base	CaZn Blend	FeZnZr
Hemimorphite	$Zn_4Si_2O_7(OH)_2 \cdot H_2O$	5-555			x		
Calcium Silicate Hydrate	$CaO \cdot SiO_2 \cdot H_2O$	34-2			x	x	
Cristobalite, Syn	SiO_2	39-1425			x		
Zircon	$ZrSiO_4$	6-266				x	x
Sodium Silicate	Na_4SiO_4	35-344	x				
Revdite	$Na_2Si_2O_5 \cdot H_2O$	33-1279		x			x
Silicon Oxide	SiO_2	35-63		x			
Nontronite-15A	$Na_{0.3}Fe_2Si_4O_{10}(OH) \cdot H_2O$	29-1479					x

During the 30 day VHT experiments of the five glass compositions in this study, a total of 9 different mineral phases formed. Table 7.5 lists the different mineral phases formed and the corresponding glass composition formed on during 30 day VHT experiment. Examination of Table 7.5 shows that during the 30 day VHT for each glass, there is a silicon dioxide mineral that forms. There are three different silicon dioxide phases that formed; cristobalite, quartz and silicon dioxide.

Cristobalite is a high temperature polymorph of silica; however, it can also form at lower temperatures. At higher temperatures, cristobalite is cubic while at lower temperatures (< 250 °C) the lattice is tetragonal and related to the high temperature by a static tilting of the tetragonal framework. As for the case of the VHT studies in this chapter, the cristobalite shown in the XRD plots is tetragonal which correlates to the formation of low temperature cristobalite. A study by Fischer *et al.* has shown evidence of the formation of surface cristobalite in hydrothermal environments in presence of a silica gel after drying. [157] The experiment by Fischer *et al.* was performed at 280 °C which is near the same temperatures of the VHT experiments in this study suggesting that cristobalite is a plausible phase that formed on the surface of these samples. [157] Hydrothermal conditions, such as those used in this study (the VHT vessel being similar to an autoclave) are similar to that used by Fischer *et al.* giving reason to believe the formation of a low temperature cristobalite is plausible.

SiO_2 is one polymorph of silicon dioxide which is one of the most common minerals and occurs in most mineral environments. SiO_2 has a trigonal crystal system and is often twinned in nature. As previously shown, SiO_2 plays a major role in the dissolution of glass and will generally precipitate on the surface of glass and possibly act as a protective layer. It is not

surprising that there are mineral layers of quartz which have formed during the 30 day VHT of 4 of the 5 glasses. There have been several authors such as Hench and Clark who show evidence of the formation of silicate species on the surface of glasses. [7] It has also been shown that SiO_2 can be grown in a hydrothermal process at lower temperatures (< 300 °C) with a water vapour atmosphere in an autoclave. [156]

Other silicates such as zircon, sodium silicate and calcium silicate hydrate were also formed during the 30 day VHT. Zircon, which is a widely distributed mineral, is generally associated with feldspars, amphibole, mica and quartz. [163] As mentioned previously, zircon has been shown to form in hydrothermal environments giving evidence that zircon is plausible phase formed during the VHT experiments. [160] The sodium silicate, which was only formed in the 30 day VHT of MW Base, is generally referred to as water glass. It is generally formed from the combination of silicon oxide and sodium carbonate to form the sodium silicate and carbon dioxide and is also generally stable in alkaline and neutral solutions; however, in acidic solutions, hydrogen ions break the Na from the silicate to form silicic acid.

Calcium silicate hydrate (CSH) is known to have several different structures which range from crystalline to amorphous. [164] The formation depends on the percentages of SiOH and CaOH bonds available during the reaction. [164] The CSH formed during the 30 day VHT in the CaZn glass samples is a structure related to tobimorite and jennite that have a Ca/Si ratio range from 0.8 to 1.3. Low temperature formation creates a gel CSH phase similar to what is seen in the VHT of the CaZn glass samples.

A hydrated sodium silicate, revdite ($Na_2(Si_2O_5)•5H_2O$), was formed during the 30 day VHT of MW Base and FeZnZr glass samples. The XRD pattern of revdite used was obtained from a mine on Mt. Karnasurt in Russia and is a hydrous analogue of natrosilite. Hemimorphite ($Zn_4Si_2O_7(OH)_2•H_2O$) is an orthorhombic zinc-sorosilicate with additional O, OH, F and H_2O. [163] It is generally found as a secondary mineral in the weathered portions of Zn deposits. This correlates to the Zn precipitates found in the CaZn and FeZnZr glass samples in a VHT at 200 °C.

The final phase which was formed on the surface of a 30 day VHT glass sample is nontronite-15A ($Na_{0.3}Fe_2Si_4O_{10}(OH)_2•4H_2O$). It is an iron rich member of the smectite clay minerals. The phase formed on the FeZnZr 30 day VHT sample is similar to a sample from Brazil that was formed in an environment with ~50% relative humidity (PDF [29-1497]). Nontronite forms from the precipitates of iron and silica rich hydrothermal fluids. The formation of nontronite in a VHT is very probable during the dissolution of an iron containing glass such as the FeZnZr sample used in this VHT study.

The simplest glass studied, MW Base, resulted in formation of a sodium silicate phase and SiO_2, Table 7.5. A close examination of Figure 7.26 shows precipitation of sodium silicate crystals on the surface of the glass after a 20 day VHT. At 30 days, these crystals were not present and there is a significantly larger thickness in the alteration layer of the 20 day VHT as compared to the 30 day VHT.

The VHT experiments of MW Base show that there were two possible different crystalline phases present in the XRD plot; revdite and a silicon oxide phase. The thickness of the alteration layers present in the MW Blend glass during the time dependant VHT experiment is also significantly different. This suggests there is a different mechanism of formation of the phases due to the presence of the simulated Blend waste that was added to the base glass. Figure 7.27 shows that there is a banded microstructure within the alteration layer. This suggests that precipitation of these different layers occurs at different times. As discussed previously in chapter 2, when the solution becomes saturated with element *i*, it may precipitate a phases containing element *i*. When the solution becomes saturated with element *i*, a second phase containing element *i* may precipitate. The banded microstructure of MW Blend that is observed in the backscatter electron images and the EDS X-ray maps suggests several different phases that have precipitated.

The alteration layer of the FeZnZr glass at 10, 20, and 30 days appears to be similar to that of MW Blend, in that the alteration layer thickness and the banded microstructure of the alteration layer is observed in both samples. Plausible phases present within the alteration layer of FeZnZr and MW Blend only share Revdite while other phases are present that differ between the two samples. Figure 7.33, the XRD plot of the alteration layers of FeZnZr glass at 10, 20 and 30 days, illustrates phases of zircon, quartz and nontronite present within the alteration layer. At 30 days, the alteration layer of FeZnZr shows the banded microstructure similar to that of the MW Blend glass giving more evidence of precipitation of phases at different times.

Giesler *et al.* suggest that under acidic conditions, glass undergoes congruent dissolution that is coupled to the precipitation of silica at the reaction interface. [165] Their results from dissolution studies show a banded microstructure of the alteration layer similar to what is seen in Figure 7.27 and 7.33; however, the banded microstructure on the glasses studied by Giesler *et al.* show much thinner bands within the alteration layer of their samples. [165] They show that there is an alternating layer rich in Si and Al, but depleted in Na and Ca. This is similar to what is shown in the EDS X-ray map of the 30 day VHT sample of CaZn Blend in Figure 7.29. The similar results between this study and that of Giesler *et al.* give strong support of an interface-coupled dissolution-reprecipitation mechanism. [165]

It should be noted that there is further work that could be done to further prove the interface-coupled dissolution-reprecipitation mechanism described by Giesler *et al.* [165] This work includes, but is not limited to, trying to obtain chemical analysis of the very small amount of reaction fluid used in the VHT vessel and secondary ion mass spectrometry (SIMS) analysis of the alteration layers to get a better resolution of the elemental depth profile of the glass/gel layer.

7.5 Conclusions

The results from the reproducibility test show that there is a method which allows for repeatable experiments. It is suggested that two 10 mm x 10 mm x 1.5mm samples polished using P1200 SiC paper (600 Grit) and then washed according to the procedure in 7.2 are prepared for VHT experiments. This allows one sample to be analysed using XRD and one sample to be analysed by microscopy, either optical or electron.

Results from the time dependant VHT experiments have shown changes in the mechanisms of alteration layer formation with the addition of the simulated Blend waste to the base glasses. This was apparent from the CaZn Blend and MW Blend glasses when compared to the respective base glasses after a 30 day VHT. It was also shown that iron may act as a suppressor to dissolution. Both the CaZn Blend and FeZnZr glasses do not show significant layers of zinc in the alteration layer as shown in the CaZn Base glass in both the reproducibility or time-dependant VHT experiments.

Giesler *et al.* have similar results as shown here which correlate to an interface-coupled dissolution-reprecipitation mechanism when simulated Blend waste is added to the base glasses. However, further work needs to be performed in order to prove this second mechanism of waste glass dissolution.

8.0 Concluding Discussion and Future Work

The current understanding of the British nuclear waste glasses, as compared to other nuclear waste glasses, is limited. This study expands the understanding of the UK glasses in open and closed systems by studying the structure and dissolution rates of UK simulated waste glasses. The structure of MW Base glass with the addition of ZnO has been shown to have a tetrahedral co-ordination about Zn through the use of XAS, as discussed in Chapter 4 above. In Chapter 5, the dissolution rate of a UK simulated nuclear waste glass, in an open system, was shown to increase with an increase in pH of the solution. In alkaline conditions in a closed system, the dissolution rate of MW Blend was shown to be lower than that of MW Blend placed in an initial solution of high purity H_2O. These glasses were shown to have different alteration layers from exposure to a water vapour environment at elevated temperatures.

As discussed in Chapter 4 above, Zn has a tetrahedral co-ordination with respect to O in these glasses and participates as a network former. As a network former, ZnO_4 will decrease the number of non-bridging oxygen (NBO) and polymerise the network, increasing the durability of the glass. As discussed in Chapter 2.5, NBO's will react with water on the glass surface which increases the rate of dissolution by breaking the Si-O-Si bond to form Si-OH, further breaking apart the glass network. Small additions of ZnO to the glass composition decreases the number of NBO's in the glass network which help to increase the durability of the glass as was observed during the VHT experiments. The increase in durability can be explained by the difference in the alteration layer thickness on the CaZn Base glass as compared to the MW Base glass.

During the VHT of the CaZn Base glass, precipitates rich in Zn were observed inside pores located in the alteration layer on the surface of the pristine glass. The addition of a simulated waste to the CaZn Base glass resulted in formation of a different alteration layer that did not contain any porosity or precipitates rich in Zn as the CaZn Base glass. This; however, suggests that the addition of the waste to the base glass has a greater effect on the dissolution rate than the addition of Ca or Zn alone. Comparisons of the alteration layer thickness at 30 days between the MW Base glass and CaZn Base glass show that the addition of Ca and Zn to the base glass decreased the thickness of the alteration layer by an order of magnitude giving evidence of a decrease in the dissolution rate with an addition of Ca or Zn to the glass composition.

During the VHT experiments, the CaZn Base glass had a thinner alteration layer as compared to the MW Base glass. The addition of Ca and Zn to the base glass could be an

effect from both Ca and Zn. As discussed in Chapter 4, small additions of ZnO to the glasses have been shown to decrease the dissolution rate and in Chapter 6, Ca in solution was shown co-precipitate with Si decreasing the dissolution rate. The alteration layers for the CaZn Base and CaZn Blend glasses after the VHT had a calcium silicate hydrate layer giving further evidence of Ca and Si co-precipitating and possibly forming a PRI or a diffusion boundary layer on the surface of the pristine glass. The addition of a simulated waste to the base glasses also decreased the dissolution rate of the glasses. Evidence of this comes from the thinner alteration layer on the simulated waste glasses as compared their respective base glasses.

It was suggested by Frugier *et al*. that a passive reactive interface (PRI) is a rate limiting step in the overall glass dissolution kinetics. [102] It has been known for several years that there is a boundary layer to consider during crystal growth from high temperature solutions. [166] This boundary layer is generally referred to as a diffusion or hydrodynamic solution and is diffusion-limited. The existence of this boundary layer during crystal growth may be analogous to a boundary layer that performs similar to the PRI during dissolution of glass. Frugier *et al*. suggest that the PRI is a soluble phase whose stability is directly dependent on the nature of the secondary phases likely to precipitate and on the solution renewal conditions. [102] During crystal growth, the boundary layer is diffusion limited and can be described by a solute concentration gradient increasing with increasing distance from the crystal up to the maximum concentration of the solute in solution. During dissolution of a glass in a closed system, the boundary layer may act as a diffusion barrier and become what is known as the PRI. However, dissolution in an open system, such as the SPFT, the boundary layer has less of an effect due to the solution never becoming saturated and limiting effects from solution feedback.

As discussed in Chapter 5, for the SPFT experiments, increases in solution pH lead to an increase in the normalised dissolution rate. However, the normalised mass loss in a closed system, such as those performed during the PCT-t experiments, was lower in a $Ca(OH)_2$ saturated solution (a higher pH) as compared to a solution that was initially high purity H_2O. The SPFT experiments were performed at steady state conditions in order to model long term dissolution without the effects of solution feedback, while the PCT-t and VHT experiments were in a closed system and allowed for precipitation of secondary products (solution feedback).

Current designs of a repository of UK nuclear waste include a co-located region of ILW and HLW wasteforms. At long times, after the repository is decommissioned, ground water interact with the ILW region and possibly flow to the region of the disposal facility containing the vitrified HLW wasteforms. The ground water may increase in pH and become

alkaline. As shown in Chapter 5, the intrinsic dissolution rate increases with an increase in pH at all temperatures. However, results from Chapter 6 where the dissolution rate was determined to be lower in a $Ca(OH)_2$ saturated solution (high pH) as compared to an initial solution of high purity H_2O. It was also determined that Ca and Si co-precipitate out of solution decreasing the overall dissolution rate. These findings suggest that ground water flowing from the ILW region of the repository, where the waste is contained in cemented packages, to the region where the vitrified HLW is located may not have a negative impact on the dissolution rate; however, further work will need to be performed in order to fully understand the impact on glass corrosion.

8.1 Future Work

It was confirmed from XAS that Zn acts as a network former in the glasses studied here. In order to determine how Zn affects the dissolution of these glasses, one could perform XAS of the alteration layers formed during dissolution. This could be performed by using the VHT and then analyzing the alteration layer that is formed by carefully removing the alteration layer and analyzing by XANES and EXAFS. Further tests should be performed in order to determine whether or not the Ca or Zn has a greater effect on the dissolution rate.

Further SPFT experiments need to be performed in order to fully understand the effect of pH on the dissolution rate of these glasses. This study only performed the SPFT at higher pH while low and neutral pH still need to be performed to determine how rate independence varies with pH. Further SPFT experiments should also be performed to determine changes in NR at steady state conditions at low and neutral pH with changes in temperature to determine if similar trends are exhibited in the lower pH regime.

After the PCT-t experiment in this study was completed solutions and powders were discarded instead of analyzed. In order to determine how the agglomeration of the powder during the test affects the normalized mass loss, the PCT-t should be performed under very slow stirring conditions. One could also perform the PCT-t for longer times in order to determine the long term durability and what the steady state dissolution rate of these glasses are in these solutions.

The VHT experiments in this study were quite comprehensive; however, there are still experiments that should be performed to further understand the mechanisms of alteration layer formation on these glasses. After the VHT, TEM images of the alteration layers will

give information on the crystallinity and will give better resolution of the interface between alteration layer and the pristine glass. This will help to determine the presence of a PRI as suggested by Frugier *et al*. [102]

9.0 Conclusions

Zn K edge X-ray absorption spectroscopy was applied to determine the Zn coordination environment in model inactive UK HLW glasses. Comparison of XANES data between crystalline hemimorphite and glass materials, pointed to the presence of Zn^{2+} in tetrahedral coordination by oxygen, based on consideration of the precise energy of the absorption edge and similar post-edge features, which were damped in the case of the glass materials consistent with an amorphous structure. Quantitative analysis of EXAFS data provided conclusive evidence for the presence of ZnO_4 species participating in network formation, linking, on average, to 2 ± 1 SiO_4 units *via* bridging oxygen atoms. Excellent quantitative agreement was observed between the Zn-O contact distance and coordination number determined from EXAFS and previous Molecular Dynamics simulations of glasses with the same nominal composition. Our analysis also provides evidence in support of the network forming role of Zn as predicted from Molecular Dynamics simulation, but we were unable to confirm the predicted clustering of Zn species at high Zn concentration in simple soda lime silica glasses.

This study has shown that steady state dissolution of MW+25wt% and MW+30wt% Blend simulated nuclear waste glasses is similar to that of previous studies. The SPFT Q/S results, with the exception of a few data points which can be attributed to experimental error, correlate to other results on a very similar glass; MW+Magnox simulated nuclear waste glass. The NR_i with respect to B, Si, Na and Al, of the glasses in this study, have increased with an increase in solution pH. Previous results on different glass compositions have shown similar results where the NR_i of B, Si, Na and Al has increased with an increase in pH.

The activation energy with respect to Si, Ea_{Si}, was shown to increase with an increase in pH. The average Ea_{Si} were consistent for a surface controlled reaction with these glasses as was shown in previous studies on MW+Magnox, a similar glass. The Ea_B of MW+25wt% and MW+30wt% Blend simulated nuclear waste was also shown to have an average value of 56 ± 13 kJ mol^{-1} and 55 ± 11 kJ mol^{-1}, respectively, which is similar to that of previous studies suggesting these glasses are controlled by surface reactions.

There are; however, several experimental errors (flow rate of pumps, and constant temperatures of the ovens) during the SPFT experiments. This suggests the need for further SPFT experiments on these glasses to further support data which has been analysed during this study.

It has been shown from both the work presented here and previous work that the surface area to volume ratio has a large effect on the overall normalised mass loss. The difference

between the concentration of Si in solution for the low and high SA/V ratio samples was explained by saturation effects of Si in solution. As the low SA/V ratio experiment, the concentration of Si in solution did not reach saturation as quick as that of the high SA/V ratio experiment. Differences in the normalised mass loss with respect to B for the PCT-t experiments also showed that the low SA/V ratio had a higher normalized mass loss than the high SA/V ratio dissolution tests by by an order of magnitude.

The addition of an alkali buffer to an initially high purity H_2O solution was shown to result in a decrease of the dissolution rate for the MW Blend glass. The concentration of Si in solution for all of the samples correlates to suggestions that Ca and Si are co-precipitating. This is evident from the large decrease in Ca concentrations at short times which correlate to the NL_{Si}. It is suggested that the high concentration of Ca in solution forms a PRI which decreases the rate of formation of a hydrated surface layer, which in turn, decreases the dissolution rate.

In a closed system and at short times, it was shown that the concentration of Al in solution decreased with an increase in the normalized mass loss of Si up to steady state conditions with respect to Si. It was discussed that the dissolution rate is dependent on the activity of $Al(OH)_4^-$ and silicic acid along with the solution pH. Both the PCT-t and the MCC-1 solution pH's show that the dissolution rate will remain low until the pH decreases past the point of zero net charge as was also suggested by Abraitis. (14)

Modelling results from the solutions of the PCT-t experiments are in agreement to previous studies which show that Ca and Si co-precipitate at short times decreasing the normalised mass loss. This is evident from the Ca and Si phases which are most probable to precipitate due to becoming saturated in solution during the experiment.

The alteration layer on the MCC-1 168 day sample is indicative of the possible formation of a PRI on the surface of the pristine glass. Previous work along with the results presented here give further evidence to the formation of the PRI; however, further work is needed in order to understand the gel layer chemistry on the surface of the glass monolith to determine the actual phases which have precipitated out of solution during the dissolution tests.

The results from the VHT reproducibility test show that there is a method which allows for repeatable experiments. It is suggested that two 10 mm x 10 mm x 1.5mm (± 0.1 mm) samples polished using P1200 SiC paper (600 Grit) and then washed according to the procedure in 7.2 are prepared for VHT experiments. This allows one sample to be analysed using XRD and one sample to be analysed by microscopy, either optical or electron.

Results from the time dependant VHT experiments have shown changes in the mechanisms of alteration layer formation with the addition of the simulated Blend waste to

the base glasses. This was apparent from the CaZn Blend and MW Blend glasses when compared to the respective base glasses after a 30 day VHT. It was also shown that iron is possibly a suppressor to zinc dissolution. Both the CaZn Blend and FeZnZr glasses do not show significant layers of zinc in the alteration layer as shown in the CaZn Base glass in both the reproducibility or time-dependant VHT experiments.

Giesler *et al.* have similar results as shown here which correlate to an interface-coupled dissolution-reprecipitation mechanism when simulated Blend waste is added to the base glasses. However, further work needs to be performed in order to prove this second mechanism of waste glasses.

9.0 References

1. **Donald, Ian W.** *Waste Immobilization in Glass and Ceramic Based Hosts: Radioactive, Toxic and Hazardous Wastes.* Chichester : John Wiley & Sons Ltd., 2010.

2. **Marples, J. A. C.**, *Glass Tech.*, 29 (1988) 230.

3. **Nuclear Decomissioning Authority,** *Geological Disposal: Steps towards implementation.* Radioactive Waste Management Directorate. March 2010. NDA/RWMD/013.

4. **Nuclear Decomissioning Authority,** *Radioactive Waste Management Directorate: Proposed Research and Development Strategy.* Didcot : Nuclear Decomissioning Authority, 2008.

5. **Nuclear Energy Agency.** *Radioactive Waste Management: Engineered Barrier Systems and the Safety of Deep Geological Repositories.* s.l. : Organization for Economic Co-Operation and Development, 2003.

6. **Penrice, Ch.; McGowan, B.; Garth, B.; Reed, J.; Sartelet, S.; Guerif, H. N.; Hollebecque, J. F.; Flament, T.; Prod'homme, A.**Tuscan, AZ, USA : s.n., 2008. Waste Management Symposia.

7. **Hench, L. L. and Clark, D. E.** *J. Non-Cryst Sol*., 28 (1978) 83.

8. **Grambow, B.** Geochemical Approach to Glass Dissolution. [ed.] David E. Clark and Bruce K. Zoitos. *Corrosion of Glass, Ceramics and Ceramic Superconductors: Principles, Testing, Characterization and Applications.* Park Ridge : Noyes Publications, 1992, 5, pp. 124-152.

9. **Vernaz, E. Y. and Dussossoy, J. L.,** *App. Geochem.*, (1992) 13.

10. **Short, R., Gribble, N. and Riley, A.** Phoenix, AZ : s.n., 2008. Waste Management Conference.

11. **Lemmens, K.**, *J. Nuc. Mat.*, 298 (2001) 11.

12. **Cailleteau, C.; Angeli, F.; Devreux, F.; Gin, S.; Jestin, J.; Jollivet, P.; Spalla, O.** s.l. : Nature Materials, 7 (2008) 978.

13. **Xing, S. B., Buechele, A. C. and Pegg, I. L.**, *Mat. Res. Soc. Symp. Proc.*, 333 (1994) 541.

14. **Abraitis, P. K.** *Dissolution Of a Simulated Magnox Waste Glass in Aqueous Solutions at Temperatures Below100 ºC.* Department of Earth Sciences, University of Manchester. 1999. Ph.D. Thesis.

15. **Abraitis, P. K.; Livens, F. R.; Monteith, J. E.; Small, J. S.; Trivedi, D. P.; Vaughan, D. J.; Wogelius, R. A.,** *App. Geochem.*, 15 (2000) 1399.

16. **Abraitis, P. K., McGrail, B. P. and Trivedi, D. P.** 1999, *Mat. Res. Soc. Symp. Proc.*, 556(1999) 401.

17. **B. Grambow, R. Muller.**, *J. Nuc. Mat.*, 298 (2001) 112.

18. **Bourcier, W. L.**, *Mat. Res. Soc. Symp. Proc.*, 333 (1994) 69.

19. **D. M. Strachan, T. L. Croak.**, *J. Non-Cryst Sol*., 272 (2000) 22.

20. **Dalton, J.** NDA Radioactive Waste Management Directorate. *Proposed Research and Development Strategy.* s.l. : NDA, 2008.

21. **E. Curti, J.L. Crovisier, G. Morvan, A.M. Karpoff.**, *App. Geochem.*, 21 (2006) 1152.

22. **E. Vernaz, S. Gin, C. Jegou, I. Ribet.**, *J. Nuc. Mat.*, 298 (2001) 27.

23. **Strachan, D.M.**, *J. Nuc. Mat.*, 298 (2001) 69.

24. **S. Mcloughlin, N. Hyatt, B. Lee.** FI6W-CT-2003-02389, s.l. : European Commission, 2005, Vols. NF-PRO.

25. **NDA RWMD.** *An Approach to Characterising a Site for a Co-Located Geological Disposal Facility.* Geosphere Characterisation Programme. s.l. : Nuclear Decomissioning Authority, 2009. B1092300.

26. **Newton, R.G.**, Glass Technology, 26 (1985) 21.

27. **Doremus, R.H.**, *J. Non-Cryst Sol.*, 48 (1982) 431.

28. **N.P. Bansal, R.H. Doremus.** *Handbook of Glass Properties.* London, UK : Acedemic Press, Inc. (1986) 500.

29. **T. Advocat, J.L. Crovisier, B. Fritz, E. Vernaz.,** *Mat. Res. Soc. Symp. Proc.*, 176 (1990) 241.

30. **Bates, J. K.; Bradley, C. R.; Buck, E. C.; Cunnane, J. C.; Ebert, W. L.; Feng, X.; Mazer, J. J.; Wronklewicz, D. J.; Sproull, J.; Bourcier, W. L.; McGrail, B. P.; Altenhofen, M. K.** High-Level Waste Borosilicate Glass: A Compendium of Corrosion Characteristics. [ed.] J. C. Cunnane. s.l., USA : U.S. Department of Energy: Office of Waste Management, March 1994. Vols. 1-3. DOE-EM-0177.

31. **Wilson, P. D., [ed.].** *The Nuclear Fuel Cycle: From Ore To Waste.* Oxford : Oxford University Press Inc., 2001.

32. Mawson Resources Ltd. *Uranium Industry Info: Uranium Mining.* [Online] Mawson Resources Ltd. [Cited: 19th October 2009.] http://www.mawsonresources.com/s/Uranium_Mining_Case_Histories.asp.

33. **Dahlkamp, Franz J.** *Uranium Deposits of the World.* London : Springer, 2009. ISBN: 978-3-540-78556-9.

34. **Peter Diehl.** WISE: Uranium Project. *Uranium Mining and Milling Wastes: An introduction.* [Online] World Information on Service Energy (WISE). [Cited: 19th October 2009.] http://www.wise-uranium.org/uwai.html.

35. No 2 Nuclear Power. *Uranium Suply and Mining.* [Online] [Cited: 19th October 2009.] http://www.no2nuclearpower.org.uk/reports/Uranium_Supply_and_Mining.pdf.

36. Manual of acid in situ leach uranium mining technology. *IAEA-TECDOC-1239.* Vienna, Austria : International Atomic Energy Agency (IAEA), August 2001. ISSN 1011-4289.

37. **Office of Environmental Cleanup: EPA Region 10.** Midnight Mine Superfund Site: Record of Decision. s.l. : EPA, September 2006. 415-2328-007 (025).

38. Yamatji Marlpa Aboringal Corporation. *Uranium Mining.* [Online] [Cited: 19th Octomber 2009.] http://www.yamatji.org.au/download.cfm?DownloadFile=B6B35936-1372-5CE6-24AB3F969145ACC9.

39. **IAEA.** *Minimization of waste from uranium purification, enrichment and fuel fabrication.* Vienna : s.n., 1999. IAEA-TECDOC-1115.

40. **Marshall, W., [ed.].** *Nuclear power technology.* London : Oxford University Press, 1983. Vol. 2: Fuel Cycle.

41. **Nirex.** *Radioactive Wastes in the UK: A summary of the 2001 Inventory.* 2002. DEFRA/RAS/02.003 or Nirex Report N/041.

42. **IAEA.** *Classification of Radioactive Waste: safety guide.* Vienna : s.n., 2009. ISBN 978-92-0-109209-0.

43. **U.S. NRC.** *Radioactive Waste: Troduction, Storage, Disposal.* Washington, DC : s.n., 2002. NUREG/BR-0216, Rev. 2.

44. **Kim, D., et al.**, *Cer. Trans.*, 143 (2002) 337.

45. **Connelly, A. J.** Vitrification of historic and future high level nuclear wastes in borosilicate glasses. *PhD Thesis.* Sheffield : s.n., February 2008.

46. **Zachariasen, W.H.**, *J. Chem. Soc.*, 54 (1932) 3841-3851.

47. **Varshneya, A.K.** *Fundementals of Inorganic Glasses.* New York : Academic Press, Inc., 1994.

48. **Cooper, A.R.**, *J. Non-Cryst Sol*., 49 (1982) 1.

49. **Warren, B.E.**, *J. Amer. Cer. Soc.*, 24 (1941) 256.

50. **Sun, K.-H.** *J. Amer. Cer. Soc.*, 30 (1947) 277.

51. **Randall, J. T., Rooksby, H. P. and Cooper, B. S.**, *J. Soc. of Glass Tech.*, 15 (1931) 54.

52. **Lebedev, A.A.**, *Trans. State Optic Inst.*, 10 (1921) 2.

53. **Bray, P. J.**, *J. Non-Cryst Sol*., 75 (1985) 29.

54. **Hägg, G.**, *J. Chem. and Phy.*, 3 (1935) 42.

55. **Greaves, G. N.; Fontaine, A.; Lagarde, P.; Raoux, D.; Gurman, S. J.**, *Nature*, 293 (1981) 611.

56. **Greaves, G.N.**, *J. Non-Cryst Sol*., 71 (1985) 203.

57. **Krogh-Moe, J.**, *Phy. and Chem. of Glasses*, 3 (1962) 101.

58. **Yun, Y. H. and Bray, P. J.**, *J. Non-Cryst Sol*., 27 (1978) 363.

59. **Krogh-Moe, J.**, *Phy. and Chem. of Glasses*, 1 (1960) 26.

60. **Krogh-Moe, J.**, *Phy. and Chem. of Glasses*, 3 (1962) 1.

61. **Bray, P. J.**, *Inorganica Chimica Acta*, 289 (1999) 158.

62. **Bray, P. J. and O' Keefe, J. G.**, *Phy. and Chem. of Glasses*, 4 (1963) 37.

63. **Gatterer, K.** The Bray model. *The Structure of Glasses.* [Online] [Cited: 30th September 2009.] http://www.ptc.tugraz.at/specmag/struct/braytab.htm.

64. **Yun, Y. H., Feller, S. A. and Bray, P. J.** 1979, *J. Non-Cryst Sol*., Vol. 33, p. 273.

65. **Xiao, S. Z.** 1981, *J. Non-Cryst Sol*., Vol. 45, pp. 29-38.

66. **Dell, W. J., Bray, P. J. and Xiao, S. Z.** 1983, *J. Non-Cryst Sol*., Vol. 58, pp. 1-16.

67. **Lusvardi, G, et al.** 2002, *J. Phy. Chem. B,* Vol. 106, pp. 9753-9760.

68. **Le Grand, M., et al.** 9, 2000, *J. Mat. Res. Soc.*, Vol. 15, pp. 2015-2019.

69. **McKeown, David A., et al.** 2000, *J. Non-Cryst Sol*., Vol. 261, pp. 155-162.

70. **Lusvardi, G., et al.** 2004, *J. Non-Cryst Sol*., Vol. 345 & 346, pp. 710-714.

71. **Rosenthal, A. B. and Garofalini, S. H.** 11, 1987, *J. Amer. Cer. Soc.*, Vol. 70, pp. 821-826.

72. **Minser, D. G., Walden, B. and White, W. B.** 1984, Communications of the American Ceramic Society, pp. C-47.

73. **Cassingham, N J, Stennett, M.C., Bingham, P.A., Hyatt, N.C., Aquilanti, G**., *Int. J. App. Glass Sci.*, 2 [4] (2011) 243.

74. **Jantzen, C. M.** Thermodynamic Approach to Glass Corrosion. *Corrosion of Glass, Ceramics and Ceramic Superconductors: Principles, Testing, Characterization, and Applications.* Park Ridge : Noyes Publications, 1992, pp. 153-217.

75. **Charles, R. J.**, *J. App. Phy.*, 29 (1958) 1549.

76. **Aagaard, P. and Helgeson, H. C.**, *Amer. J. Sci.*, 282 (1982) 237.

77. **Correns, C. W.**, *Nature*, 28 (1940) 369.

78. **Correns, C. W. and von Engelhaardt, W.**, *Chemi der Erde*, 12 (1938) 1.

79. **Petrovic, R., Berner, R. A. and Goldhaber, M. B.**, *Geochim et Cosmochim. Acta.*, 40 (1976) 537.

80. **R. A. and Holdren, G. R., Jr.**, *Geology*, 5 (1977) 369.

81. **Fung, P. C., Bird, G. W. and Sanipelli, G. G.**, *EOS*, 60 (1979) 975.

82. **Wollast, R.**, *Geochim. et Cosmochim. Acta*, 31 (1963) 635.

83. **Lagache, M., Wyart, J. and Sabatier, G.**, Acad. Sci. Paris, *Comtes Rendus*., 253 (1961) 2296.

84. **Sjöberg, E. L.**, *Geochim. et Comochim. Acta*, 40 (1976) 441.

85. **Grambow, B.**, *Mat. Res. Soc. Symp. Proc.*, 44 (1985) 15.

86. **Fueno, Takayuki, [ed.].** *The transition state: A theoretical approach.* Tokyo : Gordon and Breach Science Publishers, 1999.

87. **Temkin, M. I.** *Nauk SSSR Doklady*, 152 (19XX) 782.

88. **Dibble, W. E.** Non-equilibrium water-rock interactions: PhD dissertation. s.l. : Stanford University, (1980) 165.

89. **Dibble, W. E. and Tiller, W. A.**, *Geochim. et Cosmochim. Acta*, 45 (1981) 79.

90. **Lemmens, K.**, *J. Nuc. Mat.*, 298 (2001) 11.

91. **Crovisier, Jean-Louis, Advocat, Thierry and Dussossoy, Jean-Luc.**, *J. Nuc. Mat.*, 321 (2003) 91.

92. **Rebiscoul, Diane, et al.**, *J. Nuc. Mat.*, 326 (2004) 9-18.

93. **Gin, S., Ribet, I. and Couillard, M.**, *J. Nuc. Mat.*, 298 (2001) 1-10.

94. **Advocat, T.; Jollivet, P.; Crovisier, J. L.; del Nero, M.** *J. Nuc. Mat.*, 298 (2001) 55-62.

95. **Gin, S.**, *Mat. Res. Soc. Symp. Proc.*, 663 (2001) 207.

96. **Advocat, T.; Crovisier, J. L.; Vernaz, E.; Ehret, G.; Charpentier, H.** *Mat. Res. Soc. Symp. Proc.*, 212 (1991) 57.

97. **Hyatt, N. C.; Lee, W. E.; Hand, R. J.; Ojovan, M. I.; Abraitis, P. K.; Scales, C. R.**, *Mat. Res. Soc. Symp. Proc.*, 757 (2003) 83.

98. **Hyatt, N. C.; Lee, W. E.; Hand, R. J.; Abraitis, P. K.; Scales, C. R.**, *Mat. Res. Soc. Symp. Proc.*, 807 (2004) 181.

99. **Grambow, B.**, *Elements*, 2 (2006) 357.

100. **Vernaz, E., Advocat, T. and Dussossoy, J.**, *Cer. Trans.*, 9 (1990) 175.

101. **Grambow, B.** *JSS-A glass dissolution: mechanism, model and experiments.* Swedish Nuclear Fuel and Waste Management Co., SKB Tech. Stockholm : s.n., 1987. Rept 87-02.

102. **Frugier, P.; Gin, S.; Minet, Y.; Chave, T.; Bonin, B.; Godon, N.; Lartigue, J.; Jollivet, P.; Ayral, A.; De Windt, L.; Santarini, G.** *J. Nuc. Mat.*, 380 (2008) 8.

103. **Chave, T.; Frugier, P.; Gin, S.; Ayral, A.**, *Geochimica et Cosmochimica Acta*, 75 (2011) 4125.

104. **Ojovan, M., Pankov, A. and Lee, W.**, *J. Nuc. Mat.*, 358 (2006) 57.

105. **Oelkers, E. H.**, *Geochimica et Cosmochimica Acta*, 65 (2001) 3703.

106. **Gin, S., Godon, N. and Vernaz, E.** New York, NY : s.n., 1995. Proceeding of the Fifth International Conference on Radioactive Waste Management and Enviornmental Remediation 2nd Ed. p. 599.

107. **Grambow, B. and Strachan, D.**, *Mat. Res. Soc.*, 112 (1998) 713.

108. **Vernaz, E. Y.**, *C. R. Physique*, 3 (2002) 813.

109. **Frugier, P.; Chave, T.; Gin, S.; Lartigue, J.**, *J. Nuc. Mat.*, 392 (2009) 552.

110. **Abraitis, P. K.; Vaughan, D. J.; Livens, F. R.; Monteith, J.; Trivedi, D. P.; Small, J. S.**, *Mat. Res. Soc. Symp. Proc.*, 506 (1998) 47.

111. **Abraitis, P. K.; McGrail, B. P.; Trivedi, D. P.; Livens, F. R.; Vaughan, D. J.**, *J. Nuc. Mat.*, 280 (2000) 206.

112. **Hyatt, N. C.; Taylor, K. J.; Gibb, F. G.; Lee, W. E.** *Glass Tech.*, 45 (2004) 68.

113. **Nuclear Decommissioning Authority.** *The NDA's Research and Development Strategy to Underpin Geological Disposal of the United Kingdom's Higher-activity Radioactive Wastes.* s.l. : NDA, 2009. NDA/RWMD/011 - issue 1.

114. **SERCO.** *Interactions of Vitrified Wastes with NRVB.* s.l. : NDA, 2012.

115. **Institute of Theoretical Chemistry.** SciGlass -- The glass property information system. Newton, MA, USA : s.n., 2009.

116. **Kelly, S.D., Hasterberg, D. and Ravel, B.** Analysis of Soils and Minerals Using X-Ray Absorption Spectroscopy. *Methods of Soil Analysis. Part 5. Mineralogical Methods.* Madison : Soil Science Society of America, 14 (2008) 387.

117. **Ravel, B. and Newville, M.**, *J. Synch. Rad.*, 12 (2005) 537.

118. **ASTM International.** Standard test methods for determining chemical durability of nuclear, hazardous, and mixed waste glasses and muliphase glass ceramics: the product consistency test (PCT. West Conshohocken, PA, USA : ASTM International, 2008. DOI: 10.1520/C1285-02R08.

119. **Bassett, H.**, *J. Chem. Soc.*, Vol. 2 (1934) 1270.

120. **Taylor, H.F. W.** *Cement Chemistry.* Second Edition. London : Thomas Telford, 1997.

121. **ASTM Standards.** Standard test menthod for static leaching of monolithich waste forms for disposal of radioactive waste. 1998. C 1220 - 98.

122. **Short, R.; Turner, E.; Dunnett, B.; Riley, A.**, *Mat. Res. Soc. Symp. Proc.*, 1107 (2008) 261.

123. **Della Mea, G.; Gasparotto, A.; Bettinelli, M.; Montenero, A.; Scaglioni, R.** *J. Non-Cryst Sol*., 84 (1986) 443.

124. **Calestani, G.; Montenero, A.; Ferraguti, E.; Ingletto, G.; Bettineli, M** *J. Non-Cryst Sol*., 84 (1986) 452.

125. **Dumas, T. and Petiau, J.**, *J. Non-Cryst Sol*., 81 (1986) 201.

126. **Calas, G.; Cormier, L; Galoisy, L.; Jollivet, P.**, *C. R. Chimie*, 5 (2002) 831.

127. **Rosenthal, A. B. and Garofalini, S. H.**, *J. of Non-Cryst Sol*., (1987) 354.

128. **Hesse, K. F.; Liebau, F.; Bohm, H.; Ribbe, P. H.; Phillips, M. W.**, *Acta Crystallographica Section B*, 33 (1977) 1333.

129. **Viega, J. P. and Figueiredo, M. O.**, *X-Ray Spectrometry*, 37 (2008) 458.

130. **Sayers, D. E., Stern, E. A. and Lytle, F. W.**, *Phys. Rev. Lett*, 27 (1971) 1204.

131. The Chemical Database Service. *Inorganic Crystal structure Database.* [Online] 6th May 2010. http://cds.dl.ac.uk/cds/datasets/crys/icsd/llicsd.html.

132. **Libowitzky, E.; Kohler, T.; Armbruster, T.; Rossman, G.**, *Eur. J. Mineral*, 9 (1997) 803.

133. **Brown, I. D. and Altermatt, D.**, *Acta. Cryst.*, B41 (1985) 244.

134. **Brown, I. D. and Shannon, R. D.**, *Acta. Cryst.*, A29 (1973) 266.

135. **Connelly, A. J.; Hyatt, N. C.; Hand, R. J.; Travis, K. P.; Maddrell, E..** *Phy. Chem. of Glasses.*, 52 (2011) 64.

136. **Brese, N. E. and O'Keeffe, M.**, *Acta. Cryst.*, B47 (1991) 192.

137. **Elzinga, E. J. and Reeder, R. J.**, *Geochem. Cosmo. Acta*, 46 (2002) 3943.

138. **Stern, E.**, *Phys. Rev.*, B10 (1974) 3027.

139. **Ebert, W. L.** *Interlaboratory study of the reproducibility of the single pass flow through test method: Measureing the dissolution rate of LRM glass at 70 C and pH 10.* Department of Energy. s.l. : Argonne National Laboratories, 2005. ANL-05/33.

140. **ASTM Standards.** ASTM C 1662 - 10 Standard Practice for Measurement of the Glass Dissolution Rate Using the Single-Pass Flow Through Method. *ASTM C1662 - 10.* s.l. : ASTM International, 2010. DOI: 10.1520/C1662-10.

141. **Abraitis, P. K.; McGrail, B. P.; Trivedi, D. P.; Livens, F. R.; Vaughan, D. J.**, *J. Nuc. Mat.*, 280 (2000) 196.

142. **McGrail, B. P.; Ebert, W. L.; Bakel, A. J.; Peeler, D. K.**, *J. Nuc. Mat.*, 249 (1997) 175.

143. **Pierce, E. M.; Rodrigues, E. A.; Calligan, L. J.; Shaw, W. J.; McGrail, B. P.**, *App. Geochem.*, 23 (2008) 2559.

144. **Pierce, E.** *Issues with pumps for single pass flow through experiments.* [interv.] N. Cassingham. Pittsburgh, 10 October 2012.

145. **Lasaga, A. C.** Transition state theory. [ed.] A. C. Lasaga and R. J. Kirkpatrick. *Kinetics of Geochemical Processes. Reviews in Mineralogy.* 8 (1981) 135.

146. **Bourcier, W. L.; Peiffer, D. W.; Knauss, K. G.; McKeegan, K. D.; Smith, D. K.,** *Mat. Res. Soc.*, 176 (1990).

147. **Gin, S.; Beaudoux, X.; Ageli, F.; Jegou, C.; Godon, N.**, *J. Non-Cryst Sol.*, 358 (2012) 2559.

148. **Grambow, B. and Muller, R.**, *J. Nuc. Mat.*, 298 (2001) 112.

149. **Pierce, E. M.; Reed, L. R.; Shaw, W. J.; McGrail, B. P.; Icenhower, J. P.; Windisch, C. F.; Cordova, E. A.; Broady, J.**, *Geochimica et Cosmochimica Acta*, 74 (2010) 2634.

150. **Cassingham, N. J., Bingham, P. A. and Hand, R. J.**, *Glass Tech.*, 49 (2008) 21.

151. **Jantzen, C. M.; Kaplan, D. I.; Bibler, N. E.; Peeler, D. K.; Plodinec, M. J.**, *J. Nuc. Mat.*, 378 (2008) 244.

152. Lime Fact Sheet. *National Lime Association.* [Online] [Cited: 04 December 2012.] http://www.lime.org/documents/lime_basics/lime-physical-chemical.pdf.

153. **Parkhurst, D. L.** *Water-Resources Investigations Report.* U.S. Geological Survey. (1995) 95.

154. **Nieto, P.; Dron, R.; Thouvenot, R.; Zanni, H.; Brivot, F.**, *CR. l' Acad. Sci.*, 320 (1995) 485.

155. **Jiricka, A.; Vienna, J. D.; Hrma, P.; Strachan, D. M.**, *J. Non-Cryst Sol.*, 292 (2001) 25.

156. Hydrothermal Quartz. *The Image.* [Online] [Cited: 01 December 2012.] http://www.theimage.com/newgems/syntheticicanimate4.html.

157. **Fischer, E. H.; King, S. A.; Miller, J. B.; Ying, J. Y.; Benziger, J. B.; Schwartz, J.**, *Inorganic Chemistry*, 30 (1991) 4403.

158. **Tartaj, P.; Serna, C. J.; Moya, J. S.; Requena, J.; Ocana, M; De Aza, S.; Guitian, F.**, *J. of Mat. Sci.*, 31 (1996) 6089.

159. **Vienna, J. D.; Jiricka, A.; Hrma, P.; Smith, D. E.; Lorier, T. H.; Schulz, R. L.; Reamer, I. A.,** Hanford Immobilized LAW Product Acceptance Testing: Tanks Focus Area Results. December 2001. PNNL-13744.

160. **Rubin, J. N., Henry, C. D. and Price, J. G.**, *American Mineralogist*, 74 (1989) 865.

161. **Abrajano, T. A.; Bates, J. K.; Woodland, A. B.; Bradley, J. P.; Bourcier, W. L.**, *Clays and Clay Minerals*, 38 (1990) 537.

162. **Gin, S. and Jegou, C.** *Water-Rock Interaction Symposium*, (2001) 279.

163. Mindat.org. [Online] May 2012. www.minedat.org/min-1860.html.

164. **Chen, J. J.; Thomas, J. J.; Taylor, Hal F.W.; Jennings, H. M.**, *Cement and Concrete Research*, 34 (2004) 1499.

165. **Geisler, T.; Janssen, A.; Scheiter, D.; Stephan, T.; Berndt, J.; Putnis, A.**, *J. Non-Cryst Sol*., 356 (2010) 1458.

166. **Elwell, D. and Scheel, H. J.** *Crystal Growth from High-Temperature Solutions.* London : Academic Press, 1975.

Appendix A

Full list of mineral phases modelled by PHREEQC for the MW+25wt% Blend glass with SA/V = 10,000 m^{-1} in CSS at 50 °C.

Mineral Name	Composition	Mineral Name	Composition
(CaO)2.B2O3	(CaO)2B2O3	FeCr2O4	FeCr2O4
(CaO)3.B2O3	(CaO)3B2O3	diaspore	AlHO2
xonotlite	Ca6Si6O17(OH)2	Zr(OH)4(am,fresh)	Zr(OH)4
andradite	Ca3Fe2(SiO4)3	nepheline	NaAlSiO4
tremolite	Ca2Mg5Si8O22(OH)2	cronstedt.-7a	Fe4SiO5(OH)4
NiFe2O4	NiFe2O4	H3BO3	H3BO3
nontronit-ca	Ca0.165Fe2Al0.33Si3.67H2O12	BaOSiO2	BaOSiO2
nontronit-na	Na0.33Fe2Al.33Si3.67H2O12	boric	B(OH)3
nontronit-mg	Mg0.165Fe2Al.33Si3.67H2O12	rankinite	Ca3Si2O7
Cr2O3	Cr2O3	paragonite	NaAl3Si3O10(OH)2
RuO2	RuO2	beidellit-ca	Ca0.165Al2.33Si3.67O10(OH)2
epidote	Ca2FeAl2Si3O12OH	boehmite	AlO2H
epidote-ord	FeCa2Al2(OH)(SiO4)3	ca-p	CaAl2Si2.6O12.4H6.4
hematite	Fe2O3	beidellit-na	Na0.33Al2.33Si3.67O10(OH)2
saponite-ca	Ca0.165Mg3Al0.33Si3.67O10(OH)2	Ca3ZrSi2O9	Ca3ZrSi2O9
saponite-na	Na0.33Mg3Al0.33Si3.67O10(OH)2	anorthite	CaAl2(SiO4)2
saponite-mg	Mg3.165Al0.33Si3.67O10(OH)2	Ca2SiO4	Ca2SiO4
talc	Mg3Si4O10(OH)2	Ca(OH)2	Ca(OH)2
anthophyllite	Mg7Si8O22(OH)2	beidellit-mg	Mg0.165Al2.33Si3.67O10(OH)2
ferrite-ca	CaFe2O4	merwinite	MgCa3(SiO4)2
saponite-h	H0.33Mg3Al0.33Si3.67O10(OH)2	wairakite	CaAl2Si4O12:2H2O
petalite	Li2Al2Si8O20	HBO2	HBO2
chrysotile	Mg3Si2O5(OH)4	pyrophyllite	Al2Si4O10(OH)2
Ni2SiO4(olivine)	Ni2SiO4	NaFeO2	NaFeO2
ZrSiO4	ZrSiO4	kaolinite	Al2Si2O5(OH)4
okenite	CaSi2O4(OH)2:H2O	CaOB2O3	CaOB2O3
ferrite-mg	MgFe2O4	larnite	Ca2SiO4
mesolite	Na0.676Ca0.657Al1.99Si3.01O10:2.647H2O	colemanite	Ca2B6O11:5H2O
diopside	CaMgSi2O6	hedenbergite	CaFe(SiO3)2
RuO2:2H2O	RuO2:2H2O	csh(1.8)	Ca1.8SiO9H10.4
BaCrO4	BaCrO4	clinochl-7a	Mg5Al2Si3O10(OH)8
goethite	FeOOH	Na2CrO4	Na2CrO4
gyrolite	Ca2Si3O7(OH)2:1.5H2O	ripidolit-14a	Mg3Fe2Al2Si3O10(OH)8
Ni2SiO4(spinel)	Ni2SiO4	Sr(OH)2	Sr(OH)2
foshagite	Ca4Si3O9(OH)2:0.5H2O	ZrO2(am)	ZrO2
Ru(OH)3:H2O	Ru(OH)3:H2O	Na2Si2O5	Na2Si2O5
prehnite	Ca2Al2Si3O10(OH)2	margarite	CaAl4Si2O10(OH)2

tobermorite(14A)	Ca5Si6H21O27.5	hydroboracite	MgCaB6O11:6H2O
magnetite	Fe3O4	Cr(OH)3	Cr(OH)3
scolecite	CaAl2Si3O10:3H2O	ferrosilite	FeSiO3
Ni(OH)2(beta)	Ni(OH)2	ferrite-2-ca	Ca2Fe2O5
MgCr2O4	MgCr2O4	kyanite	Al2SiO5
grossular	Ca3Al2(SiO4)3	Na2MoO4:2H2O	Na2MoO4:2H2O
sepiolite	Mg2Si3O7.5OH:3H2O	CaO(B2O3)2	CaO(B2O3)2
ZrO2(monoclinic)	ZrO2	andalusite	Al2SiO5
afwillite	Ca3Si2O4(OH)6	borax	Na2B4O5(OH)4:8H2O
NiO	NiO	Na2MoO4	Na2MoO4
tobermorite(11A)	Ca5Si6H11O22.5	sillimantite	Al2SiO5
phillipsite-ca	CaAl2Si5O14:5H2O	Ba(OH)2:8H2O	Ba(OH)2:8H2O
hillebrandite	Ca2SiO3(OH)2:0.167H2O	wustite	Fe0.947O
wollastonite	CaSiO3	halloy	Al2Si2O9H4
heulandite-ca	CaAl2Si7O18:6H2O	corundum	Al2O3
stilbite-na,ca	NaCa2Al5Si13O36:14H2O	ca-al	CaAl2SiO6
chabazite	CaAl2Si4O12:6H2O	MgMoO4	MgMoO4
epistilbite	CaAl2Si6O16:5H2O	Ca2Al2SiO15H16	Ca2Al2SiO15H16
CaMoO4	CaMoO4	FeO	FeO
La(OH)3	La(OH)3	na-p_zeolite	Na2Al2Si2.6O12.4H6.4
analcime	Na0.96Al0.96Si2.04O6:H2O	stratlingite	Ca2Al2Si1O15H16
pseudo	CaSiO3	cr-ettringite	Ca6(Al(OH)6)2(CrO4)3:26H2O
monticellite	CaMgSiO4	ripidolit-7a	Mg3Fe2Al2Si3O10(OH)8
albite_low	NaAlSi3O8	Fe(OH)2	Fe(OH)2
NiMoO4	NiMoO4	gehlenite	Ca2Al2SiO7
natrolite	Na2Al2Si3O10:2H2O	spinel	Al2MgO4
Ce(OH)3	Ce(OH)3	H2MoO4	H2MoO4
spodumene-a	LiAlSi2O6	Sr2SiO4	Sr2SiO4
Sm(OH)3	Sm(OH)3	hercynite	FeAl2O4
quartz	SiO2	hydrotalcite	Mg4Al2O17H20
enstatite	MgSiO3	MoO3	MoO3
akermanite	Ca2MgSi2O7	katoite	Ca3Al2SiO12H8
Nd(OH)3	Nd(OH)3	CaO	CaO
B2O3	B2O3	FeMoO4	FeMoO4
Fe(OH)3	Fe(OH)3	Na2Cr2O7	Na2Cr2O7
cristobalite	SiO2	Na2Mo2O7	Na2Mo2O7
lawsonite	CaAl2Si2O7(OH)2:H2O	Ba2SiO4	Ba2SiO4
tobermorite(9A)	Ca5Si6H6O20	jennite	Ca9Si6O32H22
chalcedony	SiO2	Ru	Ru
SrCrO4	SrCrO4	Ca3Al2Si0.5O12H10	Ca3Al2Si0.5O12H10
BaO(SiO2)2	BaO(SiO2)2	cordier.hydr	Mg2Al4Si5O18:H2O
montmor-ca	Ca0.165Mg0.33Al1.67Si4O10(OH)2	fayalite	Fe2SiO4
zoisite	Ca2Al3(SiO4)3OH	Ca2Al2O13H16	Ca2Al2O13H16

laumontite	CaAl2Si4O12:4H2O	chamosite-7a	Fe2Al2SiO5(OH)4
yugawaralite	Ca0.5AlSi3O8:2H2O	cordier.anh	Mg2Al4Si5O18
crist.beta_amorph	SiO2	O2(g)	O2
montmor-na	Na0.33Mg0.33Al1.67Si4O10(OH)2	minnesotaite	Fe3Si4O10(OH)2
mordenite-na	NaAlSi5O12:3H2O	Ca3Al2O12H12	Ca3Al2O12H12
albite_high	NaAlSi3O8	greenalite	Fe3Si2O5(OH)4
phillipsite-na	Na2Al2Si5O14:5H2O	Ca3SiO5	Ca3SiO5
Zr(OH)4(am)	Zr(OH)4	hydrogarnet	Ca3Al2O6:6H2O
chs(0.8)	Ca0.8SiO5H4.4	MoO2	MoO2
amrph.silica	SiO2	CsOH	CsOH
montmor-mg	Mg0.495Al1.67Si4O10(OH)2	Ce2O3	Ce2O3
pargasite	NaCa2Al3Mg4Si6O22(OH)2	SrO	SrO
CrO2	CrO2	Ca4Al2O20H26	Ca4Al2O20H26
clinozoisite	Ca2Al3Si3O12(OH)	H2(g)	H2
forsterite	Mg2SiO4	BaO	BaO
Ru2O5	Ru2O5	RuO4	RuO4
SrSiO3	SrSiO3	MgMoO3	MgMoO3
BaMoO4	BaMoO4	Na4SiO4	Na4SiO4
csh(1.1)	Ca1.1SiO7H7.8	daphnite-14a	Fe5Al2Si3O10(OH)8
jadeite	NaAl(SiO3)2	CaMoO3	CaMoO3
Mg(OH)2	Mg(OH)2	daphnite-7a	Fe5Al2Si3O10(OH)8
Ba2Si3O8	Ba2Si3O8	Na6Si2O7	Na6Si2O7
gibbsite	Al(OH)3	amesite-14a	Mg2Al2SiO5(OH)4
clinochl-14a	Mg5Al2Si3O10(OH)8	Al2(MoO4)3	Al2(MoO4)3
SrMoO4	SrMoO4	Cs2O	Cs2O
eucryptite	LiAlSiO4	Mo(s)	Mo
antigorite	Mg24Si17O42.5(OH)31		